VERY HIGH MULTIPLICITY PHYSICS

Proceedings of the Third International Workshop

Joint Institute for Nuclear Research

VERY HIGH MULTIPLICITY PHYSICS

Dubna, June 3–5, 2002

Proceedings of the Third International Workshop

Dubna 2003

УДК 539.12.01 (063)
ББК [22.382 + 22.317] я 431
V51

The contributions are reproduced directly from the originals presented by the Organizing Committee.

V51 **Very** High Multiplicity Physics: Proceedings of the Third International Workshop (Dubna, June 3–5, 2002). — Dubna: JINR, 2003. — 243 p.

ISBN 5-9530-0014-6

The Proceedings collect the reports given at the Third International Workshop on Very High Multiplicity Physics. These include discussion of original investigations dedicated to the phenomenology of very high multiplicity processes, multiperipheral models, perturbative QCD predictions, low-x physics, fractal analysis, statistical physics approaches, collective phenomena, multiparticle Bose–Einstein correlations and perspectives of VHM experimental investigation.

Физика очень больших множественностей: Труды III Международного совещания (Дубна, 3–5 июня 2002 г.). — Дубна: ОИЯИ, 2003. — 243 с.

ISBN 5-9530-0014-6

В сборнике представлены доклады, прочитанные на III Международном совещании по физике очень больших множественностей. Он включает обсуждение оригинальных результатов исследования феноменологии процессов с очень большой множественностью, мультипериферические модели, предсказания пертурбативной КХД, физику малых x, фрактальный анализ, статистические подходы, коллективные явления, многочастичные бозе-эйнштейновские корреляции и перспективы экспериментального исследования процессов рождения очень большого числа адронов.

УДК 539.12.01 (063)
ББК [22.382 + 22.317] я 431

ISBN 5-9530-0014-6

CONTENTS

Status of very high multiplicity physics

J.Manjavidze, A.Sissakian

JINR, Dubna

Abstract

It is argued that investigation of the very high multiplicity processes at high energies will allow
(i) to check the pQCD in the infrared region,
(ii) to investigate the soft gluons role in the final state properties formation and of the 'cold' colored plasma creation,
(iii) to observe possibility of heavy pQCD jets creation,
(iv) investigate the collective phenomena.
The possibility of experimental investigation of the very high multiplicity events is discussed.

1 Introduction

The infrared region of soft color partons interaction is a mostly important field of high energy hadron dynamics. Such fundamental problems as the infrared divergences of perturbative QCD (pQCD), collective phenomena in the colored particles system, symmetry breaking are the phenomena of infrared domain. Just this general idea forces us investigate the very high multiplicity (VHM) physics.

Another reason of our interest was comparable simplicity of the VHM physics. This connected with presence of small parameter $(\bar{n}(s)/n) << 1$, where $\bar{n}(s)$ is the mean multiplicity at given CM energy $\sqrt{s}$. Another small parameter is the energy of fastest hadron ε_{max}. In the VHM region $(\varepsilon_{max}/\sqrt{s}) \rightarrow 0$. Having this small parameters we can organize the perturbation theory over them.

We wish discuss a set of problems, mostly interesting from our point of view. In the second part of paper the brief discussion of experimental status of the VHM problem will be given.

A. *Soft gluons problem*

The standard (mostly popular) hadron theory considers perturbative QCD (pQCD) at small distances (in the scale of $\Lambda \simeq 0.2$ *Gev*) as the exact theory. This statement is confirmed by a number of experiments, viz deep-inelastic scattering data, hard jets observation. The pQCD has finite range of validity since the non-perturbative effects should be taken into account at distances larger then $1/\Lambda$.

It is natural to assume, building the complete theory, that at large distances the non-perturbative effects *lay on*[1] the perturbative ones. In result pQCD lose its predictability, it becomes *shadowed* by the non-perturbative effects.

Exist another possibility. It should be noted here that the pQCD running coupling constant $\alpha_s(q^2) = 1/b\ln(q^2/\Lambda^2)$ becomes infinite at $q^2 = \Lambda^2$ and we do not know what happens with pQCD if $q^2 < \Lambda^2$. There is a few possibility. For instance, at $q^2 \sim \Lambda^2$ the properties are changed so drastically, i.e. the new vacuum appears, that even the notions of pQCD is *disappeared*. This means that pQCD should be truncated from below on the 'fundamental' scale Λ. Then it seems natural that this infrared cut-off would influence on the soft hadrons emission.

So, it is important to rise predictability of pQCD in the 'forbidden' area of large distances. For this purpose one should split experimentally the perturbative and non-perturbative effects at the large distances to check out quantitatively the role of soft color partons. One must realize for this purpose highly unusual condition that the non-perturbative effects must be negligible even if, formally, the distance among color charge is high.

It is a question of the leading non-perturbative effects in the multiple production process. Thus, the non-perturbative effect leads to the strong polarization of QCD vacuum and, in result, to the color charge confinement. This vacuum is unstable against creation of real quark-antiquark ($q\bar{q}$) pairs [2] if the distance among charges became large. This pairs are captured into the colorless hadrons and just emission of this 'vacuum' hadrons is the mostly important non-perturbative effect.

But, if the kinetic energy of colored partons is small, i.e. is comparable with hadron masses, creation of 'vacuum' hadrons should be negligible. Just this is the VHM process kinematics: because of the energy-momentum conservation law, produced (final-state) partons can not have high relative momenta and, if they was created at small distances, the production of 'vacuum' hadrons will be negligible (or did not play important role). Therefore, if the 'vacuum' channel is negligible, the pQCD contributions became "pure" [3, 4].

B. *Dissipation problems*

The multiple production process is the process of dissipation of the kinetic energy of incident particles into the created particles energies. From this point of view the VHM processes are highly nonequilibrium since the VHM final state is very far from initial one. It is known from statistics [5] that such process are close to the "stationary Markovian" ones.

In the pQCD terms last one means that the process of VHM formation should be enhanced, at least in asymptotics over multiplicity and energy, by jets. It is the general conclusion of nonequilibrium thermodynamics and it means that the very nonequilibrium initial state tends to equilibrium (thermalized) as fast as possible.

The entropy S of a system is proportional to number of created particles and, therefore, S should tend to its maximum in the VHM region [6]. But the maximum of entropy testify

[1]The corresponding formalism was described e.g. in [1].

the equilibrium of a system and it is well known that only a few parameter is enough to describe such system. For this reason the VHM events may be 'simple'. But, introducing the infinite-range correlations, the soft massless gluons may destroy our hope [7].

C. *Collective phenomena*

The connection of the equilibrium and relaxation of correlations is well known [8]. Continuing this idea, if the VHM system is in equilibrium one may assume that the color charges in the pre-confinement phase of VHM event form the plasma. One should note here that expected plasma is 'cold' and by this reason no long-range confinement forces would act among color charges. Then, being 'cold', in such system various collective phenomena may be important. For instance, the phase transition (*colored partons* $\rightarrow$ *colorless hadrons*) may be investigated.

We should underline that the collective phenomena may take place if and only if the particles interaction energy is comparable to the kinetic one. The considered VHM system is 'cold' and just for this reason the collective phenomena may be seen in it. The fundamental interest presents the problem of vacuum structure of Yang-Mills theory. For instance, if the process of cooling is 'fast', then one can consider a possibility of formation of domains with various chiral properties. As was mentioned above, the dissipation process of VHM final state formation should be as fast as possible [5]. Then decay of this domains may lead to large fluctuations, for instance, of the isotopic spin [10].

The paper is organized as follows. In the following Sec.2 we will give the list of problems with short comments. In the subsequent Sec.3 the the list of measurable predictions will be given. It should help read the Sec.4, where the experimental side of the VHM problem is described.

2 List of problems connected with VHM processes

It is not necessary to fix the multiplicity n exactly in the VHM domain: if the number n is too high, for example 10 000 then the physics should not changed drastically if, for instance, $n = 10000 \pm 100$. Therefore, it is natural to think that the theory prediction in the VHM domain should not exceed this accuracy.

Let us consider possible predictions for the topological cross sections σ_n asymptotics over multiplicity n from this point of view. We will expect that

$$\sigma_n(s) = \sigma_{tot}(s) P_n(s) e^{-n\mu'(n,s)}, \tag{2.1}$$

where $P_n = O(n)$ and $\mu'(n,s) = O(n)$ are some power functions of n. Then, the main quantity of investigations would be

$$-\frac{1}{n}\ln\left\{\frac{\sigma_n(s)}{\sigma_{tot}}\right\} = \mu'(n,s) - \frac{1}{n}\ln P_n(s) = \mu'(n,s) + O(\ln n/n). \tag{2.2}$$

So, with $O(\ln n/n)$ accuracy we may investigate in the VHM domain the value of $\mu'(n,s)$.

Considering the VHM events we will use the S-matrix interpretation of thermodynamics. In this interpretation the created particles are probes, i.e. measuring created particles energy, momentum, charge we reproduce investigated system of interacting particles (fields). So, if we assume that the temperature if interacting fields coincide with mean energy of created particles, then exist one-to-one coincidence among cross-sections of S-matrix theory and corresponding partition functions? [3].

Taking this interpretation into account, μ' has evident physical meaning. Consider the multiple production state as the statistical system with variable number of particles, $\sigma_n(s)/\sigma_{tot}$ may be considered as the partition function [3] with fixed number of particles. This quantity should be $\sim e^{-n\mu'}$, where μ' is the dimensionless chemical potential. It has natural connection with so called activity z: $\mu' = \ln z$ see also [11] and the papers cited therein.

The ordinary thermodynamical definition of the chemical potential measures μ in the term of the particles mean kinetic energy units, $1/\beta$, the temperature, i.e. $\mu' = \beta\mu$. The question of introduction of the canonical chemical potential into the theory will be considered.

We would like show now that investigation of the VHM events may help to look inside a number of interesting problems. We divide them on three groups:

(**A**) *Hard pQCD problems for VHM processes*

(**I**) *The dissipation process of highly nonequilibrium state is the stationary Markovian*;

(We may use the general statement of nonequilibrium thermodynamics that if the initial state is very far from equilibrium then the there is not fluctuations of flow to the equilibrium state [5]. One can say, that in this case the system tends to equilibrium as fast as possible. This means in the field-theoretical terms that the very high frequency phonons will only decay on the lower frequency modes and the inverse process is practically forbidden.)

In the considered hadrons collision process this statement is less evident since there is a two channel of incident energy dissipation. First one is dominate in the total cross sections and is connected to creation of 'vacuum' ($q\bar{q}$) pares. It can be shown [3] that corresponding multiplicity n distribution σ_n^s have following asymptotics over n:

$$\sigma_n^s < O(e^{-n}) \text{ at } n \to \infty, \tag{2.3}$$

i.e. σ_n^s decrease faster then any power of e^{-n}. So, if

$$\sigma_n^s < O(e^{-n}) \text{ then}: \ \frac{\partial}{\partial n}\mu'(n,s) > 0. \tag{2.4}$$

Noting that a chemical potential is a work needed to create one particle, thus the estimation (2.3) means that the vacuum of this model is stable against particles creation.

At the same time, for all evidence [12], for the stationary Markovian processes we may find:

$$\sigma_n^j = O(e^{-n}): \ \frac{\partial}{\partial n}\mu'(n,s) = 0, \tag{2.5}$$

i.e. no additional work (energy) is needed for particles creation in this case.

Comparing (2.3) and (2.5) we can conclude that one can find such high values of n that

$$\sigma_n^j >> \sigma_n^s. \tag{2.6}$$

It should be noted that the influence of the finite phase space boundary can prevent (2.6) from observation and by this reason the energy $\sqrt{s}$ should be high enough to have the maximal value of multiplicity at given energy

$$n_{max} = \frac{\sqrt{s}}{m} >> \bar{n}(s) \sim \ln s, \tag{2.7}$$

where $m \simeq 0.2$ Gev is the typical hadron mass.

(II) *The heavy QCD jets.*

The prediction (2.5) is natural for QCD jets [12]. The explicit for one jet production looks as follows:

$$\sigma_n^{(1j)}(M) = a^{(1j)}(M,n)e^{-c_j n/\bar{n}_j(M)},\ n \geq \bar{n}_j(M), \tag{2.8}$$

where $a^{(1j)}(n,M)$ is the polynomial function of n, $\bar{n}_j(M)$ is the mean multiplicity in the mass M jet and c_j is a positive constant.

The linearity of the exponent in (2.8) over n have important consequences. So, let us assume that the total energy M is divided on two jets of masses M_1 and M_2 equally: $M_1 = M_2 = M/2$. If, for instance, $M_2 << M_1 \simeq M$ then the distribution will coincide with (2.8), but the second jet distribution would reorganize coefficient $a^{(1j)}$.

Then the multiplicity distribution in the two-jet event would be

$$\sigma_n^{(2j)}(M) = a^{(2j)}(M,n)e^{-c_j n/\bar{n}_j(M/2)}, \tag{2.9}$$

where $n_1 + n_2 = n$ is the total multiplicity. (If, for instance, $M_2 << M_1 \simeq M$ then the distribution will coincide with (2.8), but the second jet distribution reorganizes $a^{(1j)}$.)

Comparing (2.8) with (2.9) we can see that with exponential accuracy:

$$\sim \exp\{-c_j \frac{\bar{n}_j(M) - \bar{n}_j(M/2)}{\bar{n}_j(M)\bar{n}_j(M/2)} n\}$$

the (2.8) would dominate in the VHM domain since the mean multiplicity $\bar{n}_j(M)$ increase with M.

The experimental observation of this phenomena crucially depends on the value of a^{1j}, a^{2j},... But if (2.6) is hold then one can expect that the events in the VHM domain would be enhanced by QCD jets and the mass of jets would have a tendency to be high with growing multiplicity.

(B) *The pQCD problems connected with soft massless gluons.*

(III) *The pQCD physics: BFKL Pomeron predictions*;

Wishing to describe the VHM domain in the pQCD frame one should take into account that

(a). Expected transverse momentum of created particle is, at least, larger then the Regge-pole model predicts;
(b). The longitudinal momenta of created particles are comparatively smaller (in the given frame) then the Regge-pole model predicts.
Validity of such kinematics follows from (I). One can say that the VHM are 'beyond' the standard Regge (multiperipheral) hadron kinematics.

The ATLAS detectors are unable to cover all 4π geometry and some number of particles is escape being undetected. By this reason our description is 'semi-inclusive': we can guarantee the (a) and (b) conditions in the restricted (central) range of rapidities.

In terms of pQCD the following kinematical variables are used: the $\tau = \ln(1/|x|) \geq 0$, where $|x| \leq 1$ is the fraction of longitudinal momentum and $\xi = \ln(|q^2|/\Lambda) \geq 0$, where the transverse momentum is $\sim q^2$. The logarithmic variables are natural for renormalizable quantum field theories assuming that the main theoretical contributions are calculated with logarithmic accuracy.

The multiperipheral kinematics assumes that

$$\xi << 1, \ \tau << 1, \tag{2.10}$$

i.e. in the multiperipheral processes the transverse momenta are restricted (by exponential factor) and the longitudinal momenta are high. Just in this kinematics the BFKL Pomeron parameters was calculated [13]. It describes creation of particles close to CM beams direction (either small angles $\Theta_i \sim (2m/\sqrt{s}) << 1$) [4].

VHM are beyond this kinematics:

$$\xi >> 1, \ \tau >> 1. \tag{2.11}$$

and particles angles Θ_i are high. Moreover, with rising n the tendency to hardness should conserved, see (II).

The natural attempt to generalize the BFKL Pomeron leader structure to include creation, at least, mini-jets means that the transverse momenta should be comparatively high and the longitudinal momentum low, i.e. the generalization of BFKL Pomeron kinematics on the case

$$\xi \sim \tau \sim 1 \tag{2.12}$$

is necessary. The naive attempts of such generalization shows the 'unstable' predictions .

We conclude, that we have not field theory formalism which be able to describe the soft hadron physics and can be continued in the VHM domain.

(IV)*pQCD physics: DIS kinematics*

To describe the hadron production in pQCD terms the parton-hadron duality is assumed. This means that the multiplicity, momentum etc. distributions of hadron and colored partons are the same. This reduce the problem practically on the level of QED.

Let us consider now n particles (gluons) creation the DIS. As usual, $D_{ab}(x, q^2)$ is the probability to find parton b with virtuality $q^2 < 0$ in the parton a. We always may chose q^2 and x so that the leading logarithm approximation (LLA) will be acceptable. Then $D_{ab}(x, q^2)$ described by ladder dyagrams.From qualitative point of view this means approximation of Markovian process of random walk over coordinate $\ln(1/x)$ and time is $\ln\ln|q^2|$. LLA means that the 'mobility' $\sim \ln(1/x)/\ln\ln|q^2|$ should be large

$$\ln(1/x) >> \ln\ln|q^2|. \qquad (2.13)$$

But, on other hand,

$$\ln(1/x) << \ln|q^2|. \qquad (2.14)$$

The leading contributions give integration over wide range $\lambda^2 << k_i^2 << -q^2$, where $k_i^2 > 0$ is the 'mass' of real gluon. If the time needed to capture the parton into the hadron is $\sim (1/\lambda)$ than, then the gluon should decay if $k_i^2 >> \lambda^2$. This leads to creation of (mini)jets. The mean multiplicity $\bar{n}_j$ in the QCD jets is high if the gluon 'mass' $|k|$ is high: $\ln\bar{n}_j \simeq \sqrt{\ln(k^2/\Lambda^2)}$. By this reason the jet creation should dominate in the VHM domain.

But rising multiplicity should rise mean value of gluon masses $< |k_i| >$ and this decrease the range of integrability over k_i^2. The quantitative analysis gives:

$$\ln D_{gg}(n;x,q^2) \propto \sqrt{\ln(1/x)\bar{t}(\mu'(n),q^2)}, \qquad (2.15)$$

where

$$\bar{t}(\mu,q^2) =. \int_1^{\tau}\frac{d\tau'}{\tau'}t(\mu,\tau'),\ \tau=\ln(-q^2/\lambda) \qquad (2.16)$$

and $t(\mu,\tau)$ is the probability of mass $-q^2=\lambda^2e^{\tau}$ jets formation if the number of particles in the jet is defined by the 'chemical' potential μ':

$$t(\mu',\tau)=\sum_n e^{n\mu'}t_n(\tau),\ t_n>0 \text{ for all } n. \qquad (2.17)$$

The estimation (2.15) assumes that

$$\ln(1/x) >> \bar{t}(\mu',q^2) \qquad (2.18)$$

i.e. $\bar{t}$ play the role of time.

By definition $t(\mu'=0,q^2)=1$ and in this case (2.18) coincide with (2.13). But with rising μ' or, it is the same, with rising n the 'time' $\bar{t}$ increase since t should increase with μ'm, see (2.17). So, increasing n we go out the validity of the LLA if $\ln(1/x)$ is fixed.

But if x is dynamical (fluctuating) variable, one can remain the LLA taking $x\to 0$. We may conclude, noting that the LLA gives main contribution, that the rising multiplicity leads to the infrared domain, where the soft gluons creation becomes dominant. Otherwise, if there is an infrared cut-off ($x > x_0$) the cross section should decrease and the next to leading order corrections should be taken into account.

(V) *The problem of long-range correlation.*

The S-matrix interpretation of the thermodynamics hides the assumption that the system can be described by few 'thermodynamical' parameter. Main of them is temperature $1/\beta_c$ and chemical potential μ_c. In thermodynamics this quantities have the fundamental character: the probability to find given state is defined just by the values of β_c and μ_c.

In particles physics the energies of particles, theirs number, etc. are fundamental parameters and the 'temperature', 'chemical potential' are secondary quantities. So, wishing to describe the multiple production state thermodynamically, one should be sure that the thermodynamical parameters are 'good' ones, i.e. they are able to describe whole system unambiguously.

This assumes that the fluctuations near β_c, μ_c should be Gaussian. This strong assumption [8, 14] leads to the smallness of particles energy correlations. Indeed, if the system is not in the thermal equilibrium, then there should be in it the macroscopic energy flows. It is evident, presence of energy flows would lead to the particles energy correlations. We expect that the entropy $S \sim n$ and in the VHM domain the system *relax* exceeding the entropy maximum. The same one may expect considering the relaxation over other parameters.

Otherwise the system would be unstable. The type of instabilities may be few. First of all the instability may be connected with the masslessness of gluons (one may distinguish few hundred instabilities in QED plasma) and may be seen in the color charge correlations. Another source of instability may be connected with complicated structure of Yang-Mills vacuum. So, the mostly interesting for us question is following: tend or not the VHM system to the equilibrium. As was explained this should be seen in the relaxation of energy, momentum, charge, jet-jet (i.e. color charge), etc. correlations.

(C) *The problems connected with collective phenomena in the 'pre-confinement' final state of VHM hadron collision.*

(VI) *The problem of cold color plasma (CCP) formation*;

We have a large number of colored particle in the preconfinement phase of VHM process and one may consider this system as a colored plasma state.

Indeed, by definition, the plasma is a *state* of $semi-free$ charged particles. The $semi-free$ condition means that the collision frequency is much less then the system characteristic frequencies. This means that particles are involved mostly into the collective motions.

The condition that the system of charges form a *state* means that the system should be 'describable', i.e. the only restricted number of parameters should be used for its complete description. Only in this case the system has a physical meaning. It is natural to describe the system introducing the correlation functions among particles (anyway, one can transform this description into arbitrary one [14]). It is known from thermodynamics that it is necessary and sufficient of correlations relaxation if the system tends to equilibrium [8]. In other words, the equilibrium is defined by correlation relaxation and the equilibrium state is described by few parameters; by temperature, chemical potential, density, pressure.

So, if we want to observe the plasma state, one should investigate the corresponding correlators. So, if we want to describe the system by the temperature, one should observe the energy correlations relaxation. This has evident physical meaning: if energy correlators are not small (in definite scale) then there should be energy flaws in the system. Such system can not be equilibrium in this sense (but, for instance, can be equilibrium in the charge distribution sense).

Noting that the entropy of system should rise with rising multiplicity one can expect the (cold) color plasma formation. The signal of this plasma would be relaxation of corresponding correlators.

(VII) *The first order phase transition.*

Let us assume that the VHM state is equilibrium. Being cold this state is mostly useful for investigation of collective phenomena, since in this case the particles kinetic energy becomes comparable or even less then the potential energy. There is the old standing problem of the transition of colored state into the colorless one.

We can offer in the VHM domain the direct investigation of this question. So, the first order phase transition assumes that some part of quark systems energy is hidden into the hadrons. This means that there should be discrepancy in energy spectrum of quarks in the preconfinement state and hadrons.

The experimental side of this problem would be considered later. Here we note, it is evident that the VHM kinematics is especially convenient to observe this discrepancy.

(VIII) *The vacuum instability against particles creation.*

This situation was described in [15, 16]. Let us consider the lattice gas model. In this models the down spin means absence of particle in this junction and creation of particle flips spin up. The energy of this system is $\sim \sigma_{\imath}\sigma_{\imath+\imath}$, where $\sigma_{\imath}$ is the spin in the $\hat{\imath}$-th junction, $\sigma_{\imath} pm1$. The external field $\mathcal{H}$ adds the energy $\sim \sigma_{\imath}\mathcal{H}$ and leads to polarization of the system. By this reason $\mathcal{H}$ has the meaning of the chemical potential μ.

Let us assume that at $\mathcal{H} = 0$ the ground state of this system degenerate. This means that the system (of dimension $d = 3$) is divided on the stable domains of up and down spins. The thermal fluctuations create subdomains (bubbles) of opposite for given domain spins, but this bubbles are unstable and dissipates with time. Let us switching on the external field in such a way that the domains with down spin becomes unstable.

This means that in this domains the bubbles are stable and grow with time. It is a typical first order phase transition. The stability of the bubble is defined by the its volume energy $E_v \sim R^3$ and surface energy $E_s \sim r^2$. So, if $E_v > E_s$ then the bubble grow with time and its boundary accelerate.

For our VHM physics acceleration of boundary means that less energy (work) is needed to add into bubble (i.e. to create) a particle. But searching VHM events we extract the bubbles with very high multiplicity of up spins, i.e. the very large dimension bubbles. So, we conclude that in considered model the increasing $n$should decrease our chemical potential μ':

$$\frac{\partial}{\partial n}\mu'(n, s) < 0. \tag{2.19}$$

Than, taking into account (2.2) we conclude, that in this case

$$\sigma_n > O(e^{-n}). \tag{2.20}$$

3 What must be measured

Following quantities should be measured:

a. *Multiplicity distributions*

It was shown in Sec.2I that the cross sections asymptotics over n gives important information. On Fig. we depict three type of possible asymptotics. One can conclude that in terms of pQCD

$$\frac{\partial}{\partial n}\mu'(n,s) \leq 0 \text{ at } s \to \infty,\ n \to \infty,\ \frac{n}{\sqrt{s}} << 1. \tag{3.1}$$

Last condition assumes that the finiteness of phase space should not influence on the particles creation dynamics. The inequality (3.1) means that, at least, jets creating govern cross sections asymptotics over n.

b. *One-particle distribution*

The estimation (3.1) means that the created particles transverse energy should rise with multiplicity.

c. *Correlation functions*

It is important to investigate the multiple correlation functions $C_k(X_1, X_2, ..., X_k; n, s)$, $k \geq 2$, where X_i is the dynamical variable in the i-th cell of measuring device; for example, if $X_i = \varepsilon_i$ this means that we investigate the energy correlations and i may be considered as the 3-(or 4-)coordinate of calorimeter cell, where the energy of particle (or group of particles) measured. So, if the mean value of correlation functions

$$< C_k(i; n, s) >= \int \prod_{i=1}^{k} dX_i C_k(X_1, X_2, ..., X_k; n, s) \tag{3.2}$$

tend to zero for given set i, in the VHM domain then one can expect tendency to equilibrium over corresponding parameter.

So, the smallness of energy correlations means that the energy ε fluctuation near some mean value $1/\beta_c(n,s)$ should be Gaussian. This spectra contradict to the Pomeron predictions. Therefore, with rising multiplicity we should see transition from Pomeron $d\varepsilon/\varepsilon$ energy spectra to the exponential $d\varepsilon e^{-\beta_c \varepsilon}$. If the created particles are nonrelativistic this distribution coincide with Maxwell distribution.

If $< C_k(i; n, s) >\approx 0$ for arbitrary i then the system is in equilibrium and in this case one may consider the set of color charges as the plasma state. One can consider the collective phenomena in this state.

References

[1] J.Manjavidze and A.Sissakian, Theor. Math. Phys., 130 (2002) 153

[2] A.Casher, H.Neuberger, S.Nassinov, Phys.Rev., D20 (1979) 179; E.Gurvich, Phys.Lett., B87 (1979) 386

[3] J.Manjavidze, El. Part. At. Nucl., 16 (1985) 101

[4] E.Kuraev, J.Manjavidze and A.Sissakian, hep-ph/0003074

[5] M.Kac in: Probability and Related Topics (Intersciens Publ., London, New York, 1957)

[6] E.Fermi, Progr. Theor. Phys., 4 (1950) 570, Phys. Rev., 81 (1950) 115, *ibid* 92 (1953) 452;
L.D.Landau, Izv. AN SSSR, 17 (1953) 85

[7] Selected papers of F.Dyson (AMS,1996)

[8] N.N.Bogolyubov, Studies in Statistical Mechanics, (North-Holland, Amsterdam, 1962)

[9] L.Van Hove, Phys. Lett. B245 (1990) 605

[10] J.D.Bjorken, Acta Phys. Polon., B28 (1997) 2773, hep-ph/9712434; A.Anselm and M.G.Ryskin, Phys. Lett. B266 (1991) 482

[11] J.Manjavidze and A.Sissakian, Phys. Rep. 346 (2001) 1

[12] K.Konishi, A.Ukawa and G.Veneziano, Phys.Lett., B80 (1979) 259; A.Basseto, M.Ciafaloni and G.Marchesini, Nucl.Phys., B163 (1980) 477; see also J.Taylor, Phys. Lett., 83B (1979) 207

[13] E.Kuraev, L.Lipatov and V.Fadin, Sov. Phys. JETP, 44 (1976) 443; Zh. Eksp. Teor. Fiz., 71 (1976) 840; L.Lipatov, Sov.J. Nucl. Phys., 20 (1975) 94; V.Gribov and L.Lipatov, Sov.J. Nucl. Phys., 15 (1972) 438, 675; G.Altarelli and G.Parisi, Nucl. Phys., B126 (1977) 298; I.V.Andreev, Chromodynamics and Hard Processes at High Energies (Nauka, Moscow, 1981)

[14] J.Manjavidze and A.Sissakian, Proc. of Bogol. Conf. Physics of Elementary Particles and Atomic Nuclei, 31,(2000) 104.

[15] C.G. Callan, Jr. and S.R. Coleman, Phys.Rev.D16 (1977) 1762

[16] T.D.Lee and C.N.Yang, Phys.Rev., 87 (1952) 404, 410; J.S.Langer, Ann.Phys., 41 (1967) 108

Wavelet analysis of angular distributions of secondary particles in high energy nucleus-nucleus interactions

Irregularity of particle pseudorapidity distributions

V.V.Uzhinskii, V.Sh.Navotny[1], G.A.Ososkov, A.Polanski, M.M.Chernyavski[2]

Joint Institute for Nuclear Research,
Laboratory of Information Technologies

Experimental data on sulphur and oxygen nuclei interactions with photoemulsion nuclei at the energies of 200 and 60 GeV/nucleon are analyzed with the help of a continuous wavelet transform. Irregularities in pseudorapidity distributions of narrow groups of the secondary shower particles in the mentioned interactions are observed at application of the second order derivative of Gaussian as a wavelet. The irregularities can be interpreted as an existence of the preference emission angles of groups of particles. Such an effect is expected at emission of Cherenkov gluons in nucleus-nucleus collisions. Some of the positions of the observed peculiarities on the pseudorapidity axis coincide with those found by I.M.Dremin et al. (I.M.Dremin et al. Phys. Lett., 2001, v. B499, p. 97).)

In the last decade a new type of mathematical analysis of data, the so-called wavelet analysis has become very popular in various branches of science and engineering [1]–[4]. Mainly, it is applied for analysis of time series coming from geophysics, meteorology, astrophysics, and so on (applications in aviation, medicine and biology see in [5]).

The wavelet decomposition or wavelet transform of a function $f(x)$ is its decomposition on an orthogonal functional family of special form [6];

$$W_\Psi(a,b)f = \frac{1}{\sqrt{C_\Psi}} \int_{-\infty}^{\infty} f(x)\Psi_{a,b}(x)dx, \tag{1}$$

$$\Psi_{a,b}(x) \equiv a^{-1/2}\Psi\left(\frac{x-b}{a}\right),$$

where Ψ is called a wavelet, b – a translation parameter, a – a dilation parameter or a scale, and C_Ψ – a normalizing constant

$$C_\Psi = 2\pi \int_{-\infty}^{+\infty} |\tilde{\Psi}(\omega)|^2 |\omega|^{-1} d\omega,$$

where $\tilde{\Psi}(\omega)$ – Fourier transform of $\Psi(x)$.

The derivatives of the Gaussian function are often used as wavelets

$$\Psi(x) \equiv g_n(x) = (-1)^{n+1}\frac{d^n}{dx^n}\mathrm{e}^{-x^2/2}, \quad n > 0, \quad C_{g_n} = 2\pi(n-1)!.$$

The first two wavelets are well known:

$$g_1(x) = -x\mathrm{e}^{-x^2/2}, \quad g_2(x) = (1-x^2)\mathrm{e}^{-x^2/2}.$$

[1]FTI, Tashkent, R. Uzbekistan
[2]FIAN, Moscow, Russia

The second one is called Mexican Hat wavelet (MHAT).

As seen, the wavelet transform puts in correspondence to the function of one variable, $f(x)$, the function of two variables, $W_\Psi(a,b)$. Until recently, a presentation and an analysis of a function of two variables was quite a difficult job, and only modern computers with their 3D-graphics allowed one to implement completely the method of wavelet analysis.

There is a discrete analogy of the continuous wavelet transform (see [6]). It was used in elementary particle physics for the study of events of cosmic rays interactions with materials – at the analysis of particle pseudorapidity distributions [7]. The wavelet coefficients ($W_\Psi(a,b)$) of energy distributions predicted by different models of multi-particle production were studied in [8]. Possibilities of the wavelet analysis in searching for manifestation of the disoriented chiral condensate in the pseudorapidity distributions of neutral particles fraction were considered in [9].

In papers [10] the wavelet transform was used for pattern recognition in $Pb+Pb$-interactions at the energy of 158 GeV/nucleon. Structures were found in the angular distributions of secondary particles that can be interpreted as irradiation of Cherenkov gluons. The last publications in this research are devoted to experimental search for the disoriented chiral condensate in nucleus-nucleus interactions [11].

Most of the mentioned papers suffer from the apparent lack of quantitative results which caused either by uniqueness of nature phenomenon or low statistics of analyzed data. It is connected partly with specific properties of the wavelet analysis itself (see [12]). A regular method of wavelet analysis application in particle physics is needed. Our paper presents experience of using the wavelet transform for analysis of more than 2000 interactions of nuclei with nuclei at high energies.

Experimental data were obtained at horizontal irradiation of NIKFI BR-2 nuclear photoemulsion by sulfur and oxygen nucleus with the energies of 200 and 60 GeV per nucleon at the CERN SPS. The sensitivity of emulsion was about 30 grains per unit length of 100 μm for single charged particles with minimal ionization.

Primary interactions were found by along-the track double scanning: fast in the forward direction and slow in the backward direction. Fast scanning was made with a velocity excluding any discrimination of events in the number of heavily ionizing tracks, slow scanning was carried out to find events, if any, with little changed and unbiased projectile nucleus. Upon rejecting events of electromagnetic dissociation and purely elastic scattering in the total sample, 884 events of $S+Em$ and 504 events of $O+Em$ at the energy of 200 GeV/nucleon, and 884 $O+Em$ interactions at the energy of 60 GeV/nucleon were selected for a further analysis. In each event the polar angles θ and azimuthal angles φ were measured.

Shower particles, or the so-called s-particles – single charged particles with a velocity $\beta = v/c \geq 0.7$, are considered in this study. The s-particles consist mainly of produced particles and single charged nuclear fragments. A special separation of single charged fragments was not done.

According to Ref. [10], a distribution of the secondary particles on the pseudorapidity $\eta = -\ln(\tan(\theta/2))$ in an event was presented as

$$f(\eta) = \frac{dn}{d\eta} = \frac{1}{N}\sum_{i=1}^{N}\delta(\eta - \eta_i), \qquad (2)$$

where N is multiplicity of s-particles in the event, and η_i is pseudorapidity of i-th particle.

A wavelet transform of the function (2) gives

$$W_\Psi(a,b) = \frac{1}{N}\sum_{i=1}^{N} a^{-1/2}\Psi\left(\frac{x-b}{a}\right). \tag{3}$$

So, the function of two variables is brought into correspondence with each particle. Wavelet spectra of the event ($W_\Psi(a,b)$) is a sum of such functions.

As an example, Fig. 1 presents wavelet spectra of event with 6 particles having pseudorapidities $\eta_1 = 1$, $\eta_2 = 2.75$, $\eta_3 = 3.25$, $\eta_4 = 5$, $\eta_5 = 6$, $\eta_6 = 7$. The values of translation parameter b are put on the X-axis, dilation parameter, a – on Y-axis. The values of the wavelet coefficients are depicted in a gray-level scale: the high values of the coefficients are of light shade while the lower ones are darker. As seen, in g_2 wavelet spectra at the scale lower than 0.3 all particles are distinguished. At the scale larger than 0.5, the particles 2 and 3 can not be resolved. At $a > 1$ particles 4, 5, 6 can not be resolved. At $a > 2$ one could expect a fusion of particles 1, 2, and 3. However, this does not take place due to small yield of particle 1 in the wavelet spectra at a large scale. So, the wavelet transform of g_2 allows one to study the particle clusterization.

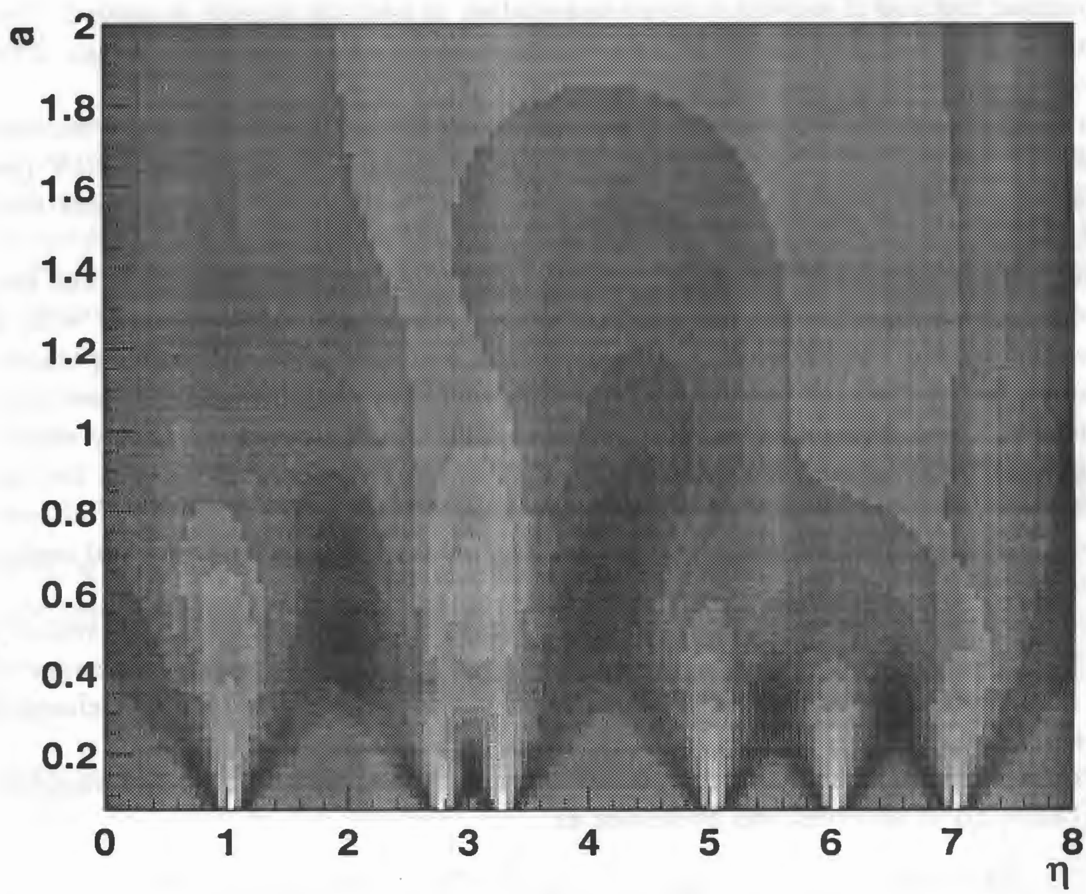

Figure 1: Wavelet spectra, energy densities, and scalogramms

Let us note that the positions of the local maximums of $W_\Psi(a,b)$ ($a \simeq 0.5$ and $b = 3$, $a \simeq 1$ and $b = 6$) on the b-axis are connected with positions of the centers of the groups of particles 2, 3 and 4, 5, 6. The corresponding scales reflect the width of the groups on the pseudorapidity axis. Positions of the local minimums give the centers of the pseudorapidity splits between the groups.

There are a lot of wavelets. Different representations of the 6 particles of the test example are shown in Fig. 1. There are also energy densities ($(W_\Psi(a,b)^2)$) and scalogramms $E_W(a) = \int W_\Psi(a,b)^2 db$, which are often used in practice.

The g_1 wavelet (see (2)) has a minimum at a negative value of its argument and maximum – at positive value. Positions of these extreme points at different scales can be seen quite well in the energy density spectra. The g_2 wavelet has 3 extreme points. All of them are presented in the energy spectra (see the region of the 1 particle). Scalogramms give generalized imagination of the extreme points.

As seen in the figure, different wavelets give different presentations of particles. The more "usual" ones are obtained at the application of even wavelets. Perhaps, odd wavelets can be useful at automatic data processing.

At the first glance, the g_1 wavelet allows one to locate the regions of unhomogeneouslity in the particle distribution. The positions of the local maxima of the energy spectra on the b-axis ($b = 2.5$ and $b = 3.5$) mark the group of the particles 2 and 3, and the positions on the a-axis show the group size. Though, the following local maxima are disposed at $a = 4$ and $b \sim 0$, $b \sim 9$. There is no selection of the group of the particles 4, 5, 6. At the same time, there are irregularities (extreme points and inflection points) in the corresponding scalogramm which are probably connected with characteristics of the particle group. 7 There are extreme points in the scalogramm obtained with help of the g_2 wavelet at $b \simeq 0.5$ and 1.2 associated with the group characteristics. So, we believe that scalogramms can be used for fast search of the particle group.

The g_4 wavelet has analogous properties. Though, the characteristics of the corresponding scalogramms are not so strongly correlated with the particle characteristics. Thus, below we will use mainly the g_2 wavelet.

We started our analysis with study of the particle distribution on the pseudorapidities in all interactions. The histogrammed distribution for $S + Em$ interactions at the energy of 200 GeV/nucleon is presented in Fig. 2. There are also g_2 and g_4 wavelet spectra at different scales. It should be noted that the wavelet transform was applied to raw experimental data, not to the histogrammed distribution. Thus, a fine structure of the spectra can be observed at small scales. The structure becomes more regular at large scales, and turns to the wavelet function in the limit of large a. At $a \sim 0.4$ one can see 3 maxima in the g_2 spectra at $\eta \sim 2$, 4 and 8. It seems that the maximum at $\eta \sim 2$ is connected with the particle production in the target fragmentation region; the maximum at $\eta \sim 4$ – with the particle production in the central region, and the maximum at $\eta \sim 8$ – with spectator fragments of the projectile nucleus. In reality, the three maxima only reflect what can be seen with the naked eye – the left wing of the distribution is different from the right one. One can clearly see a change of the slope on the right wing at $\eta \sim 6$. At smaller scales the structure is more rich and does not allow such simple interpretation. In order to find selected scales in the interactions and to analyze a fine structure of the events, we turned to a study of the energy density and scalogramm.

The spectrum of the energy density reflects peculiarities of $W_\Psi(a,b)$ function and can be used for searching the particle group. Though, definition of maxima and minima of the function is a quite complicated task. So, at the first stage we concentrated our attention on the energy distribution on scales, on scalogramm because it is a 1D-function.

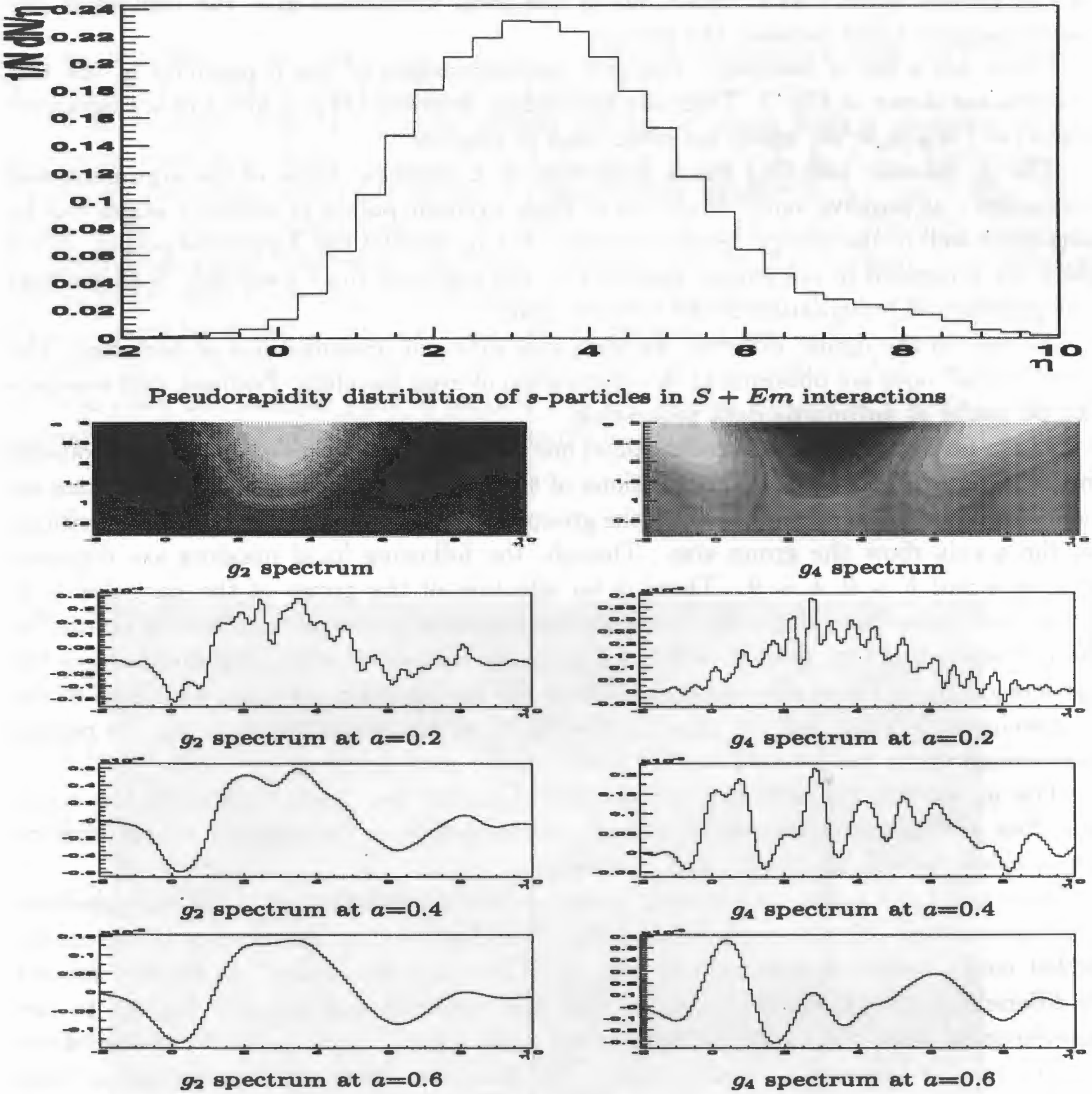

Figure 2: Wavelet analysis of s-particles pseudorapidity distribution in $S + Em$ interactions at the energy 200 GeV/nucleon

Scalogramms reflect characteristic features of events according to the test example. For example, the scalogramm of the g_2 spectrum has the minimum at $a \sim 1.1$ associated with an average distance between the groups of the particles 2, 3 and 4, 5, 6, and the maximum at $a \sim 0.5$, connected with the most compact group of particles 2, 3. It is possible to write out an analytical expression for the scalogramm using the g_2 wavelet and the distribution of the form (2).

$$S(a) = \frac{1}{32\sqrt{\pi}a^4} \sum_{i,j=1}^{N} \left[\Delta_{i,j}^4 - 12a^2\delta^2 - 12a^4\right] e^{-\frac{\Delta_{ij}^4}{4a^2}} \tag{4}$$

$$\Delta_{ij} = \eta_i - \eta_j$$

It is seen that the scalogramms is a statistical averaged squared distance between particles. Thus, we expected that an analysis of the scalogramms allowed us to find characteristic scales.

Distributions of local minimum and maximum positions in the scalogramms of the events of $S+Em$ interactions at the energy 200 GeV/nucleon are given in Fig. 3. Though there are some irregularities in the distributions, we can not say that they have a statistically guaranteed meaning. In addition, the analysis of connection between a_{min} and a_{max}, and characteristics of the real events did not show any regularity. However, we believe that the study of a larger volume of experimental data will produce interesting results.

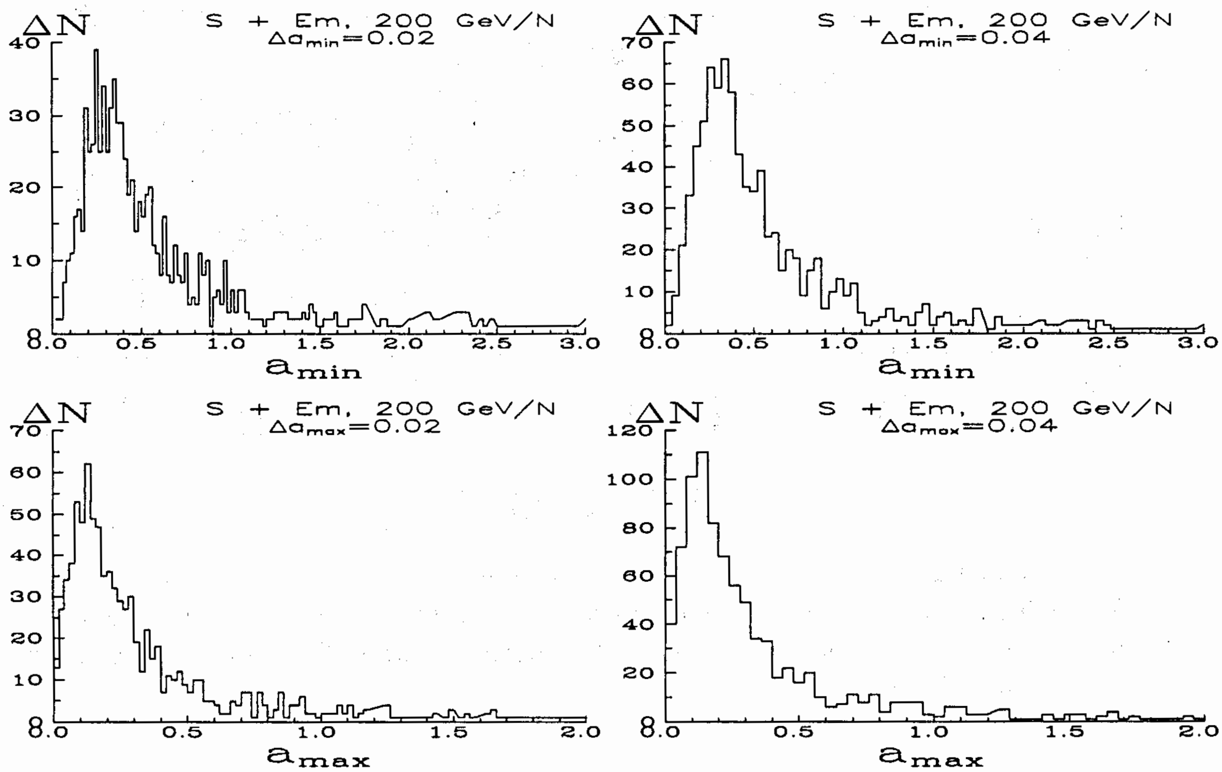

Figure 3: Distributions of the extreme points of the scalogramms of the $S + Em$ events

The next step of our study was search for extremum points of function $W_\Psi(a,b)$ of the real events. Distributions of points on the dilation scale in our interactions are presented in Fig. 4. At the first glance, the distributions have no any characteristic peculiarities – bumps or pits. We only can mark that the distributions can not be described by a simple exponential function. It is necessary to use at least 2 exponents at fitting the distributions. Simulation of pp-interactions with the help of the HIJING program [13] has shown that the appearance of the exponent with a larger slope is connected with production of jets of particles. So, we consider our distributions as a manifestation of jet existence in nucleus-nucleus interactions.

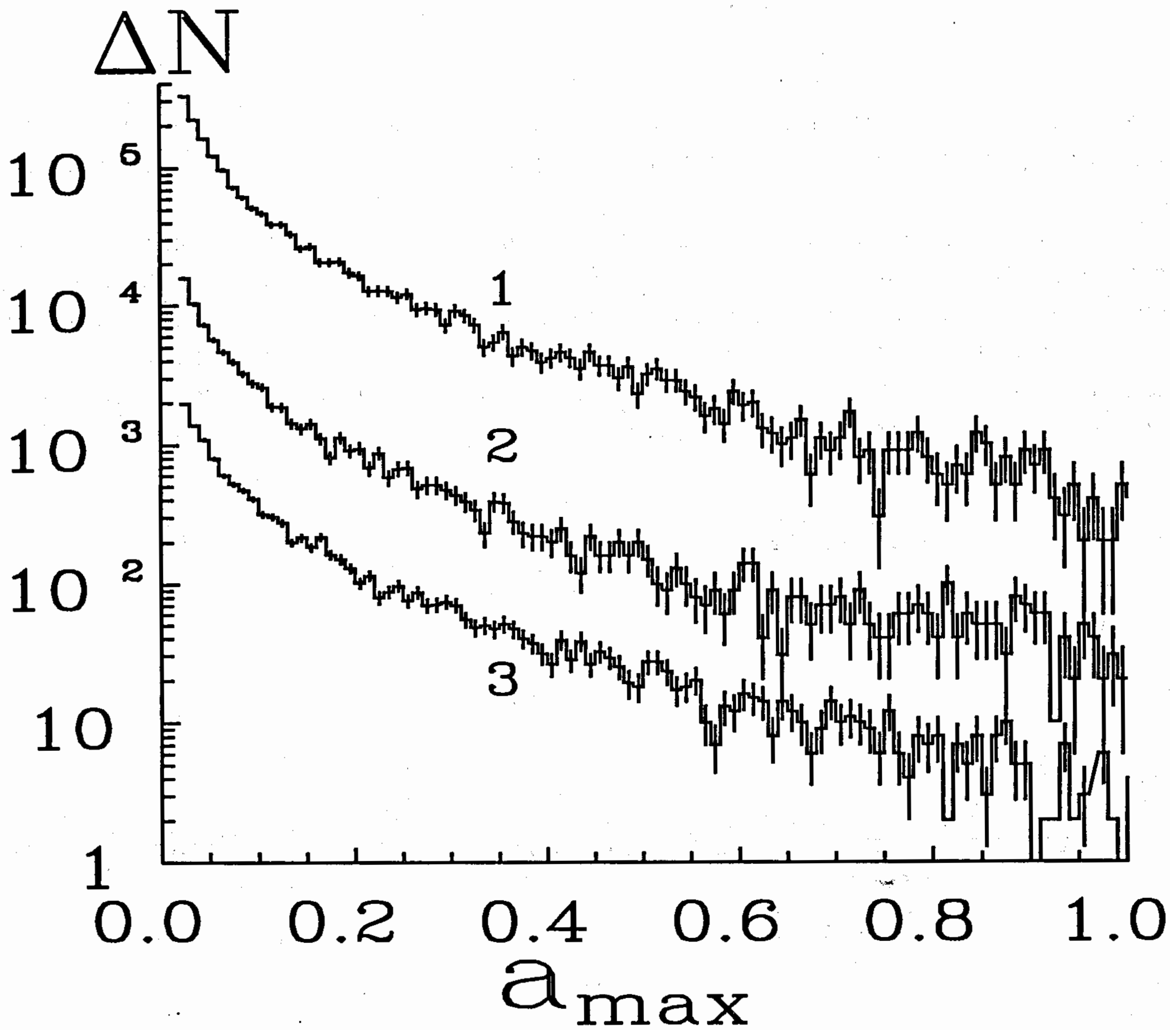

Figure 4: a_{max} distributions in the $S + Em$ and $O + Em$ interactions at the energy of 200 GeV/nucleon, and in the $O + Em$ interactions at the energy of 60 GeV/nucleon (histograms 1, 2 and 3, respectively). The distributions 1, 2, and 3 are multiplied by 10^2, 10^1 and 10^0, respectively.

Research in the distributions of local maximum of $W_\Psi(a, b)$ on b gives more interesting results. The Fig. 4 shows the distributions of all our interactions at $a_{max} > 0.05$ (1), $a_{max} > 0.1$ (2), $a_{max} > 0.2$ (3), and $a_{max} > 0.3$ (4). As seen, the peculiarities of the distributions at $\eta \sim 1.5$, $\eta \sim 2$, $\eta \sim 3$, $\eta \sim 3.5$, $\eta \sim 5$ are located at the same positions for different interactions. The peculiarities, as it can be seen, are connected with narrow groups, where $a_{max} < 0.05$. We interpret them as an existence of preference emission angles of the groups of the particles. Let us note that the positions of some irregularities found by us coincide with those observed early in Ref. [10] at the study of $Pb + Pb$ interactions at the energy of 158 GeV/nucleon. Unlike Ref. [10] where 5 mostly central events were analyzed, we present the results for more than 2000 events.

Research on narrow groups of the particles with help of traditional methods was the third step. Fig. 5 shows a distribution on a pseudorapidity interval between neighboring particles in an event. It was observed that there were pairs of the particles with close pseudorapidities, $\Delta < 10^{-5}$! Their number increases statistical fluctuations. The distribution of the centers of the pairs on η has two bumps at $\eta \sim 3$ and 4. So, we can conclude that the peculiarities of the wavelet spectra observed by us at small scales are connected with the narrow groups of the particles.

One can suppose that such pairs occur due to data input error when two or three entries in the event record are corresponded to the same particle. In this case, such ghost "particles" must have identical η and φ. The fraction of these pairs is lower than 20 % among all the observed narrow pairs. The other pairs have different values of azimuthal angles. The distribution of the particles of the narrow groups on φ (see Fig. 6) has no clear peculiarities and reflects the methodical drawback of the photoemulsion experiments – a poor identification of particles flying perpendicularly to the emulsion plate (at $\varphi \sim 0^\circ$ and 180°). The distribution of the azimuthal angle difference of the particles of the narrow group has no irregularities either. So, these pairs can not belong to a jet of particles. The nature of such pairs is not clear for us.

Summary

1. The continuous wavelet transform has been used for the analysis of more than 2000 events of nucleus-nucleus interactions at high energies ($S + Em$ and $O + Em$ interactions at the energies of 200 and 60 GeV/nucleon).

2. It is shown that the maxima of $W_\Psi(a, b)$ obtained with the help of the g_2 wavelet are associated with the groups of particles.

3. It has been found that the distribution of the group of particles on scales in the interactions under the study is geterogeneous what can be caused by jet production.

4. It is observed that the distributions of the groups on pseudorapidities have irregularities, there are preferences of emission angles of the groups.

5. The pairs of particles with close pseudorapidities, $\Delta < 10^{-5}$, are found for the first time.

The nature of the peculiarities observed by us is not clear yet.

The authors are grateful to the members of the EMU-01 collaboration for their kind permission to employ the experimental data analyzed in this paper. One of the authors (V.V.U.) thanks RFBR (grand N 00-01-00307) and INTAS (grand N 00-00366) for their financial support.

References

[1] H. Weng, K.-M. Lau// J. Atmos. Sci., 1994, **51**, p. 2523

[2] P. Kumar, E. Foufoula-Georgio// Rev. of Geophys., 1997, v. **235**, p. 385.

[3] N.M. Astafyeva, G.A. Bazilevskaya// Phys. and. Chem. of the Earth, 1999, v. **C25**, p. 129.

[4] K. Kudela et al.// Solar Phys., 2001, v. **199**, p. 200.

[5] .. // , 2000, . **170**, c. 1235.

[6] I. Daubechies – Ten Lectures on Wavelets// Soc. for Ind. and Appl. Math., Philadelphia, Pa., 1992, p. 357.

[7] N. Suzuki, M. Biyaima, A. Oksawa// Prog. Theor. Phys., 1995, v. **94**, p. 91.

[8] D. Huang// Phys. Rev., 1997, v. **D56**, p. 3961.

[9] Z. Huang, I. Sarcevic, R. Thews, X.-N. Wang// Phys. Rev., 1996, v. **D54**, p. 750.

[10] N.M. Astafyeva, I.M. Dremin, K.A. Kotelnikov// Mod. Phys. Lett., 1997, v. **A12**, p. 1185;
I.M. Dremin et al.// hep-ph/0007060, 2000;
I.M.Dremin et al.// Phys. Lett., 2001, v. **B499**, p. 97.

[11] M.L. Kopytine et al.// nucl-ex/0104002, 2001.

[12] C. Torrence, G.P. Compo// Bull. Amer. Meteorol. Society, 1998, v. **79**, p. 61.

[13] M. Gyulassy, M. Plumer// Phys. Lett. B, 1990, v. **243**, p. 432;
X.-N. Wang, M. Gyulassy// Phys. Rev. C, 1991, v. **44**, p. 3501.

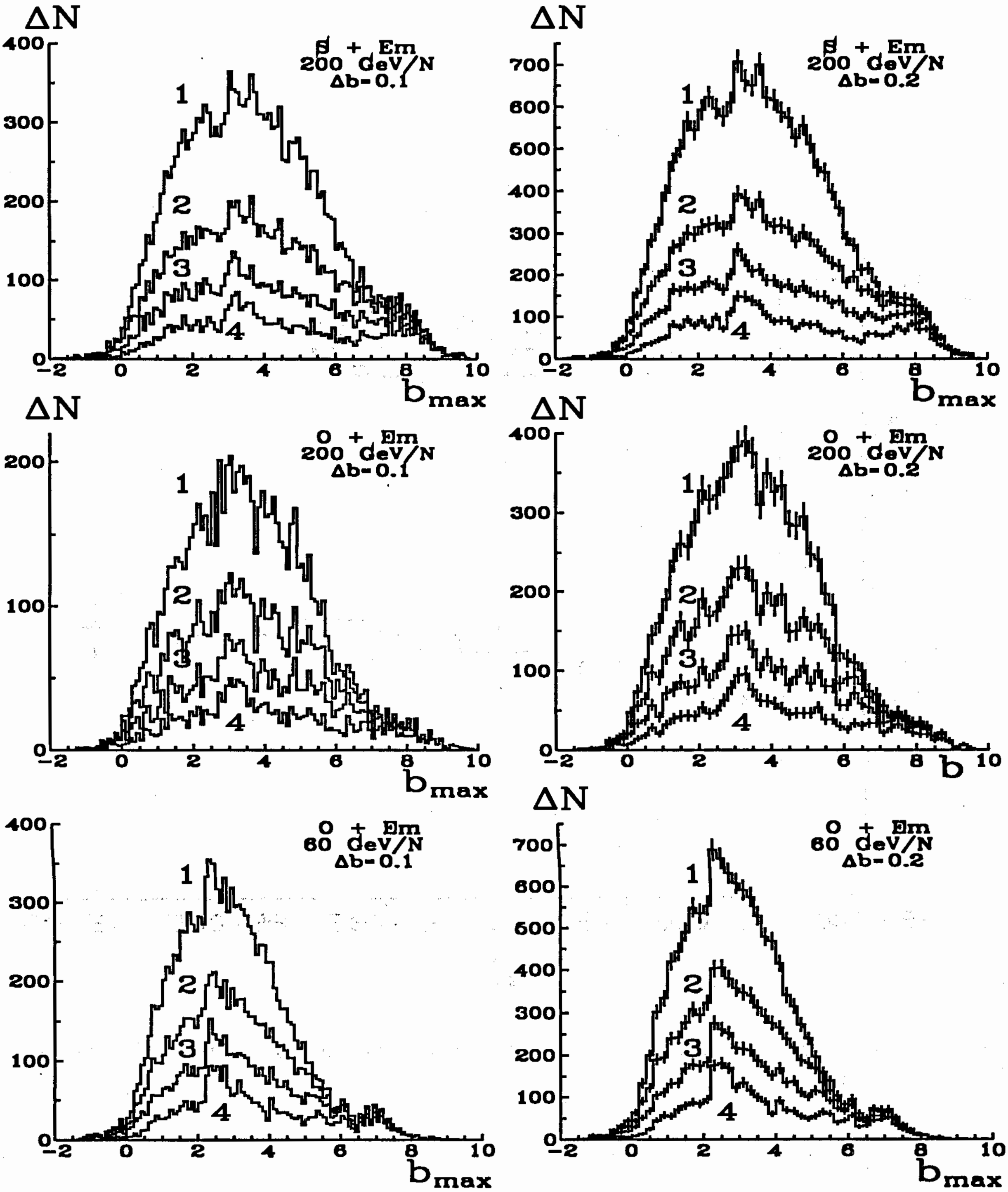

Figure 5: b_{max} distributions in the $S + Em$ and $O + Em$ interactions at the energy of 200 GeV/nucleon, and in the $O + Em$ interactions at the energy of 60 GeV/nucleon. Δb is step of the histogramming. The distributions 1 – 4 are obtained at $a_{max} \geq 0$, $a_{max} \geq 0.05$, $a_{max} \geq 0.1$ and $a_{max} \geq 0.2$, respectively.

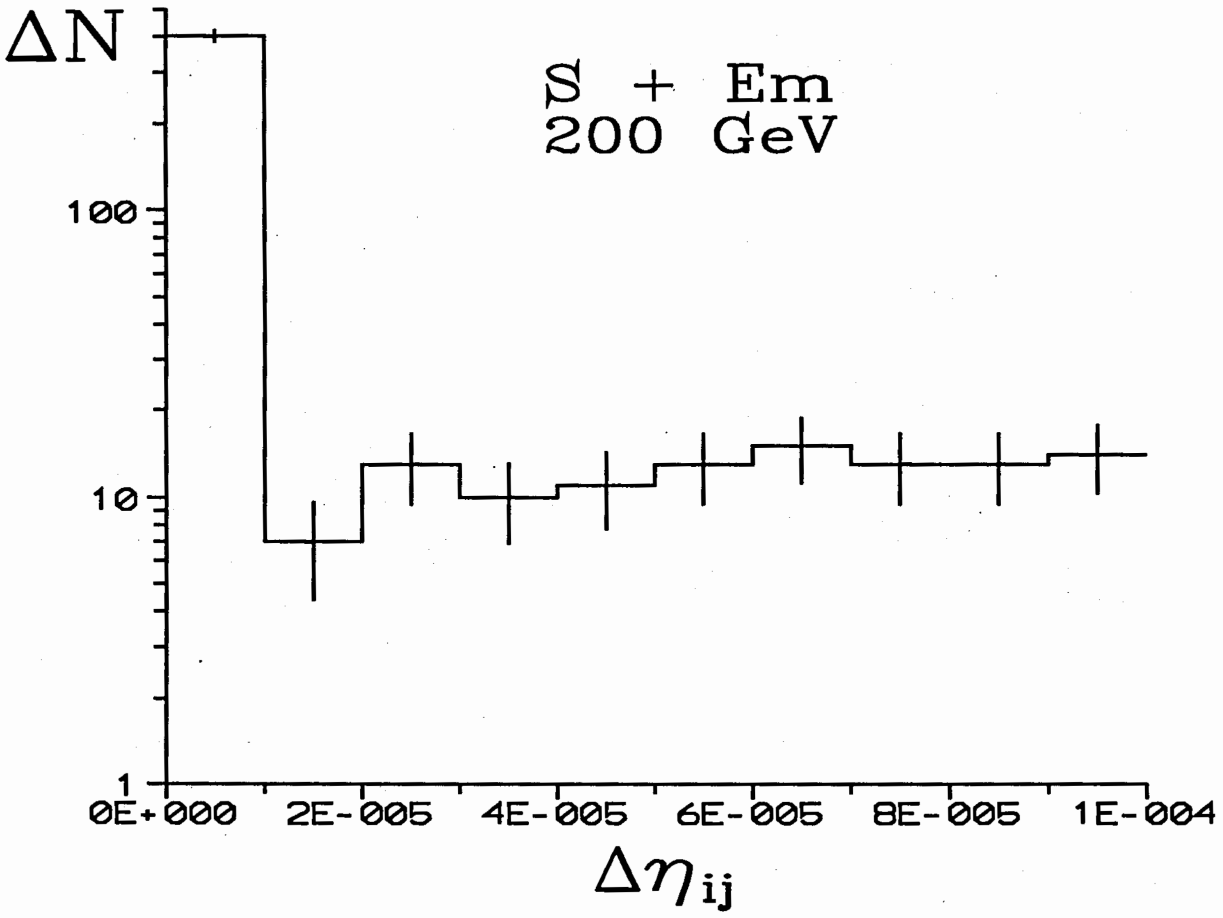

Figure 6: Distribution on the pseudorapidity interval between the neighbouring particles in all studied interactions.

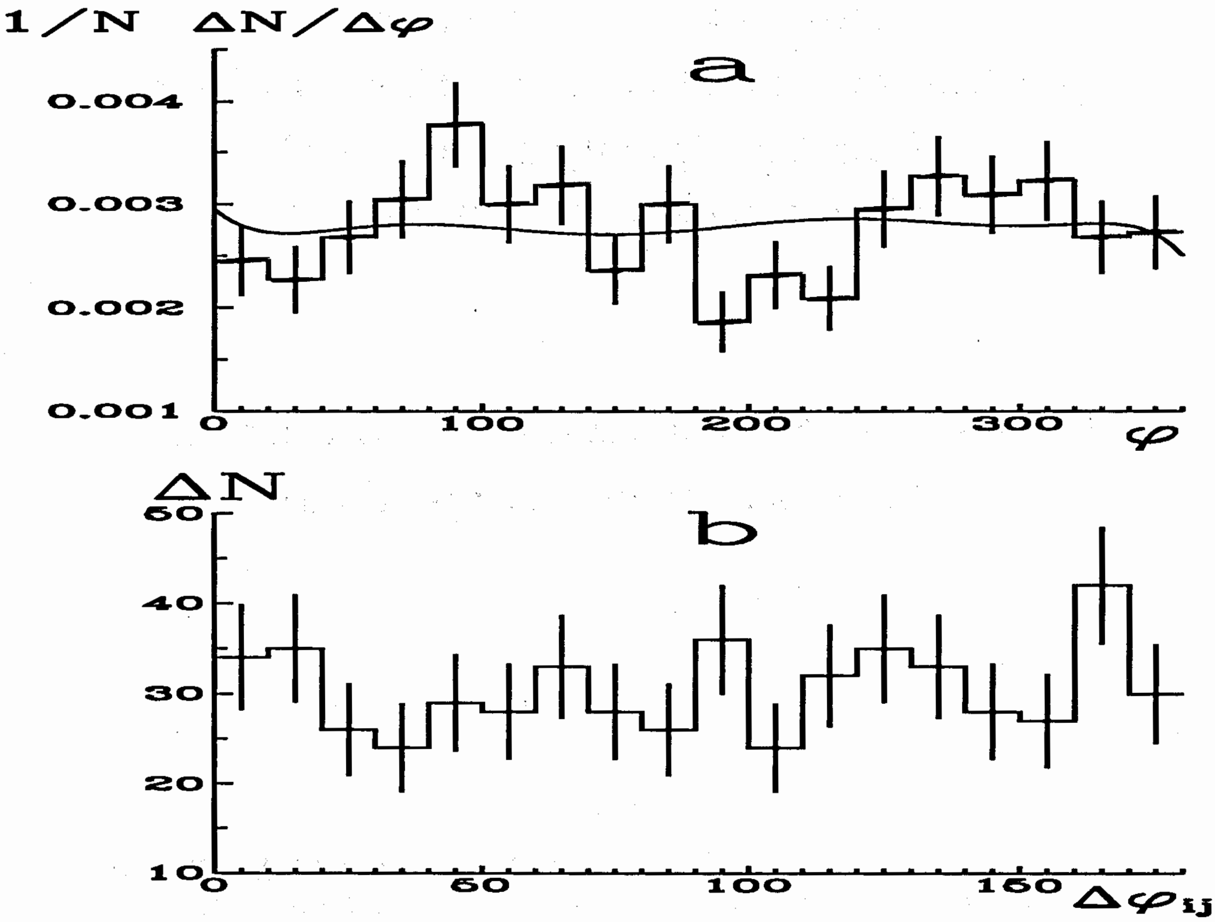

Figure 7: a) The azimuthal angle distribution of particles with close pseudorapidities. The distribution of all particles is presented by solid line. b) The distribution on the azimuthal angles difference of particles with close pseudorapidities.

Possibility to Investigate the Energy Correlators and their Ratio for High Multiplicity Events with pile-up background at 14 TeV

J. Budagov, Y. Kulchitsky[1], J. Manjavidze[2],
N. Russakovich, A. Sissakian

JINR, Dubna, Russia

Abstract

We present the results of the study of the energy correlators $K_2(n)$, $K_3(n)$ and their ratio $R_3(n)$ in dependence on the hadron multiplicity at the LHC. The PYTHIA generator has been used. The PYTHIA predicted that $R_3(n)$ does not depend on multiplicity. The $K_2(n)$, $K_3(n)$ and $R_3(n)$ ratio can be studied at ATLAS.

[1] also B.I. Stepanov Institute of Physics, National Academy of Sciences of Belarus, Minsk, Republic of Belarus

[2] also Institute of Physics, Tbilisi, Georgia

1 Introduction

The investigation of very high multiplicity (VHM) events is a very important task for high energy physics [1, 2]. The purpose of this study is to calculate the energy correlators $K_2(n,s)$, $K_3(n,s)$ and the ratio $R_3(n,s) = |K_3(n,s)|^{2/3}/|K_2(n,s)|$ as a function of the hadron multiplicity for the future ATLAS experiment at the LHC [3, 4]. The theory predicts that the $R_3(n,s)$ ratio has tendency to equilibrium for the VHM events [1].

2 Phenomenology of VHM events

We will call the very high multiplicity events the ones for which the condition $n(s) \gg \bar{n}(s)$ is fulfilled, where n is the number of hadrons in an event, $\bar{n}$ is the mean multiplicity of hadrons, and $\sqrt{s}$ is the c.m.s. energy.

Fig. 1 shows the distribution of $\langle n\rangle P(n)$, where $P(n) = \sigma_n/\sigma_{tot}$, as a function of the secondary particles multiplicity represented in the units of mean multiplicity. The points are the results of the E735 (FNAL) experiment at 1.8 TeV with $\langle n\rangle = 44$. The **A** region corresponds to the multi peripheral kinematics, where $n \sim \bar{n}(s)$. The **B** region is the thermodynamical region corresponding to the approximation of the non-interacting gas where $n \to n_{max}(s)$. The maximum possible number of hadrons is equal to $n_{\max}(s) = \sqrt{s}/m_\pi$, where m_π is a pion mass. The **C** region corresponds to the VHM events. The cross section of such a process is significantly smaller than $10^{-7}\sigma_{tot}$.

The thermodynamical description of the final state events in the high energy physics is possible at fulfillment of the condition of N.N. Bogolyubov's principle of the vanishing of the correlators [6]:

$$R_l(n,s) = |K_l(n,s)|^{2/l}/|K_2(n,s)| \ll 1,$$

where $l = 3,\ 4,\ \ldots$, $K_l(n,s)$ is the l-particle energy correlator for the n-particle event. Two and three particle correlators are defined as

$$K_2(n,s) = \langle([\varepsilon_1;n,s] - \langle\varepsilon;n,s\rangle)([\varepsilon_2;n,s] - \langle\varepsilon;n,s\rangle)\rangle,$$

$$K_3(n,s) = \langle([\varepsilon_1;n,s] - \langle\varepsilon;n,s\rangle)([\varepsilon_2;n,s] - \langle\varepsilon;n,s\rangle)([\varepsilon_3;n,s] - \langle\varepsilon;n,s\rangle)\rangle,$$

where ε_i is the energy of the i-particle and $\langle\varepsilon;n,s\rangle$ is the mean energy.

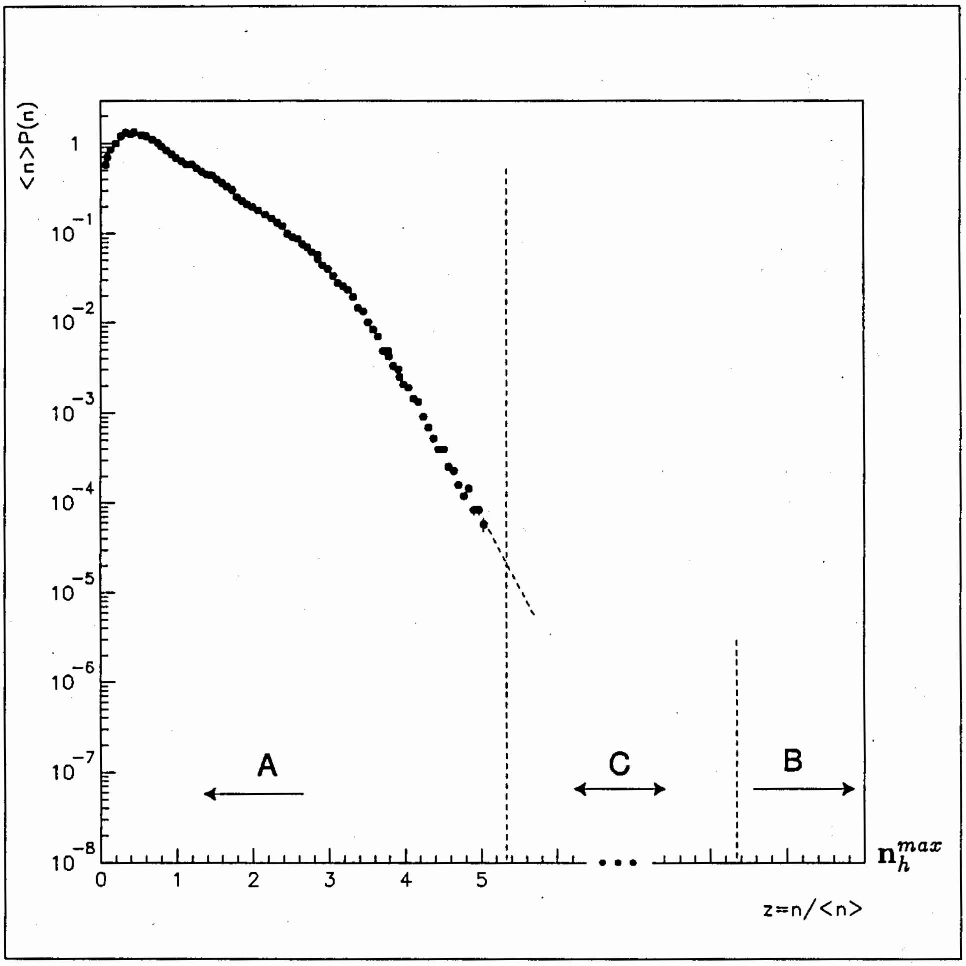

Figure 1: Multiplicity distribution $\langle n \rangle P(n)$ in the KNO scaling form at 1.8 TeV.

3 Energy correlators and their ratio

The PYTHIA has been used for this investigation [7]. The hard processes have been used for the simulation of the trigger events: $q_i\ q_j \rightarrow q_i\ q_j$, $q_i\ \bar{q}_i \rightarrow q_j\ \bar{q}_j$, $q_i\ \bar{q}_i \rightarrow g\ g$, $q_i\ g \rightarrow q_i\ g$, $g\ g \rightarrow q_i\ \bar{q}_i$, $g\ g \rightarrow g\ g$ where q are quarks and g are gluons.

The main background for the VHM events at the LHC will be soft processes. There will be ≈ 23 pp-interaction in the 25 ns of one interaction of bunches at the full LHC luminosity ($10^{34}\ cm^{-2}s^{-1}$). The time of data collection will be 125 ns, for example for the electromagnetic calorimeter. Therefore, there will be written about 115 soft background events, which

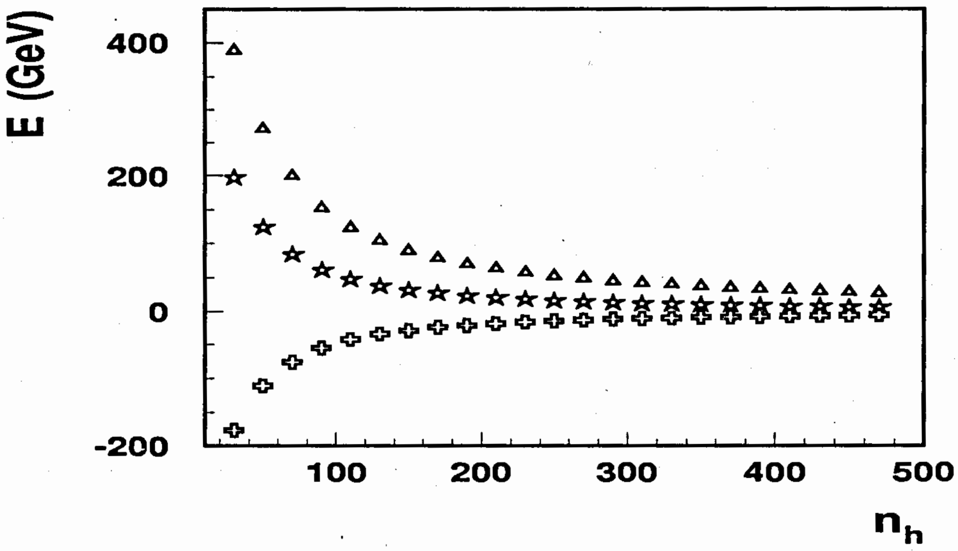

Figure 2: The average energy [$\triangle$], the correlators $\sqrt{K_2(n)}$ [✠], $\sqrt[3]{K_3(n)}$ [★] as a function of the multiplicity at 14 TeV.

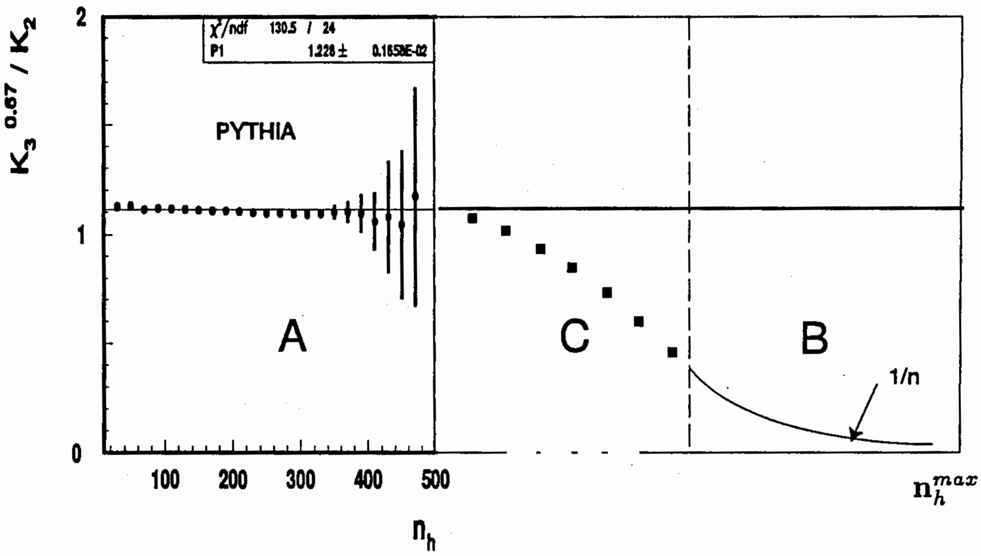

Figure 3: The $R_3(n)$ ratio [$\bullet$] as a function of the multiplicity at 14 TeV.

are called pile-up, simultaneously with the trigger event. The inelastic processes have been used for the simulation of the pile-up events.

Fig. 2 shows the results of calculations of the average energy and the correlators $\sqrt{K_2(n)}$, $\sqrt[3]{K_3(n)}$ in the GeV scale as a function of the hadrons multiplicity at 14 TeV. The values of $\sqrt{K_2(n)}$ have signs of $K_2(n)$. As can be seen the $K_2(n)$ and $K_3(n)$ trend to zero at $n_h \to 500$. The dependence of the $R_3(n)$ ratio on n_h is given in Fig. 3. The PYTHIA predictions are given for the **A** region shown in Fig. 1. The average value of the $R_3(n)$ ratio does not depend on the hadron multiplicity and equals to 1.23. There is no trend to equilibrium in this region. This can be understood as the PYTHIA is based on the multiperipheral model [1].

Taking into account the experimental trigger conditions harder events have been selected which increase the hadron multiplicity. The requirement on the transverse parton momentum $p_t^q \geq p_t^{q,\ min}$ has been used, where $p_t^{q,\ min} \geq 500$ GeV. This has led to multiplicity increasing to ≈ 800. However, the tendency to equilibrium is not observed although the $R_3(n)$ ratio decreases to 1.1 for $p_t^q \geq 2000$ GeV.

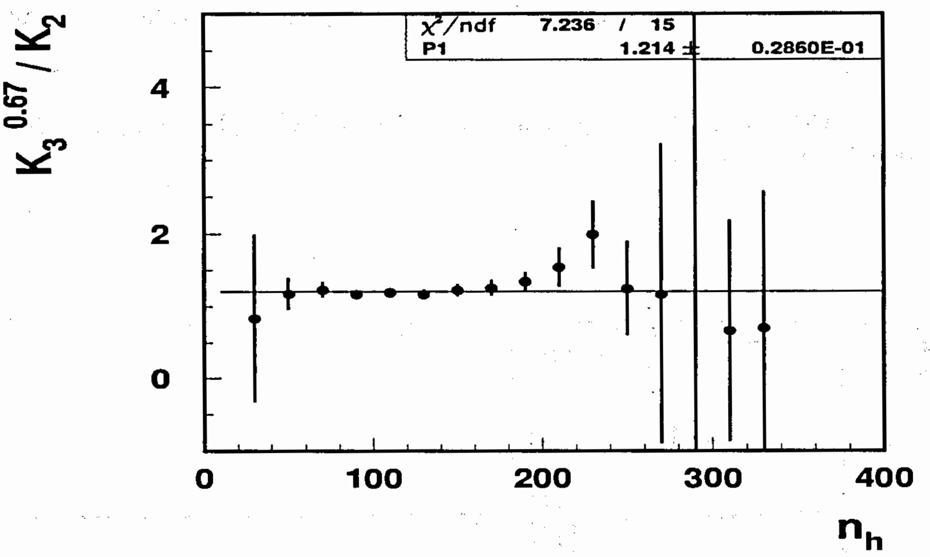

Figure 4: The $R_3(n)$ ratio [•] as a function of the multiplicity at 14 TeV taking into account the pile-up background.

The investigation of the behaviour of the VHM events is planned out at the ATLAS [3, 4] at $\sqrt{s} = 14$ TeV. Only charged particles with the transverse momentum more than ≈ 1.5 GeV reach the calorimeter because of the strong magnetic field (2 T) of the solenoïdal magnet. Therefore, only the hadrons with $p_t \geq 2$ in the central region $|\eta| \leq 2.5$ have been selected. The physics events satisfied the condition $p_t^q \geq p_t^{q,\ min}$ for partons which have been simulated for the decreasing of the background pile-up events.

The obtained distributions of the correlators $K_2(n)$ and $K_3(n)$ as a function of multiplicity taking into account the pile-up events are similar to the ones shown in Fig. 2. As a result of using the cuts $p_t \geq 2$ GeV and $|\eta| \leq 2.5$ the maximum multiplicity decreases to ≈ 300 hadrons per event. As before, there is no trend to equilibrium for the $R_3(n)$ ratio, $R_3(n) = 1.21$ for $p_t^q \geq 2000$ GeV (Fig. 4).

It is important to note, that it is not necessary to take into account the detector acceptance because the correlations are small and equal to all particles in the VHM region.

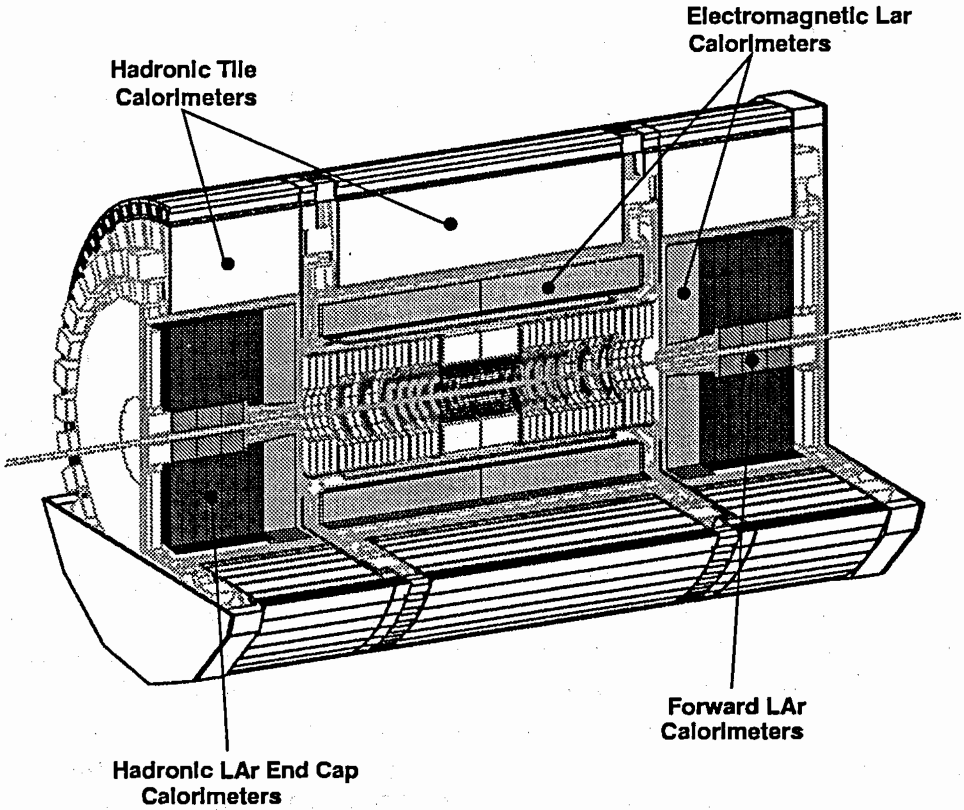

Figure 5: Three-dimensional view of the ATLAS calorimetry.

It is assumed to use the calorimetric [8, 9, 10] information for the determining of the energy correlators in the ATLAS experiment. This calorimeter (Fig. 5) has beautiful energy resolution $\sigma/E = (42\%/\sqrt{E} + 1.8\%) \oplus 1.8/E$ in the barrel region [11]. There is the projective geometry for ATLAS calorimeter towers. The initial transverse dimension of a hadronic calorimeter tower is equal to $\eta \times \phi = 0.1 \times 0.1$. The hadronic shower size is larger than one calorimeter tower size [12]. Signals from each tower have been used in the calculations separately. The ATLFAST [13] programme has been used for simulation.

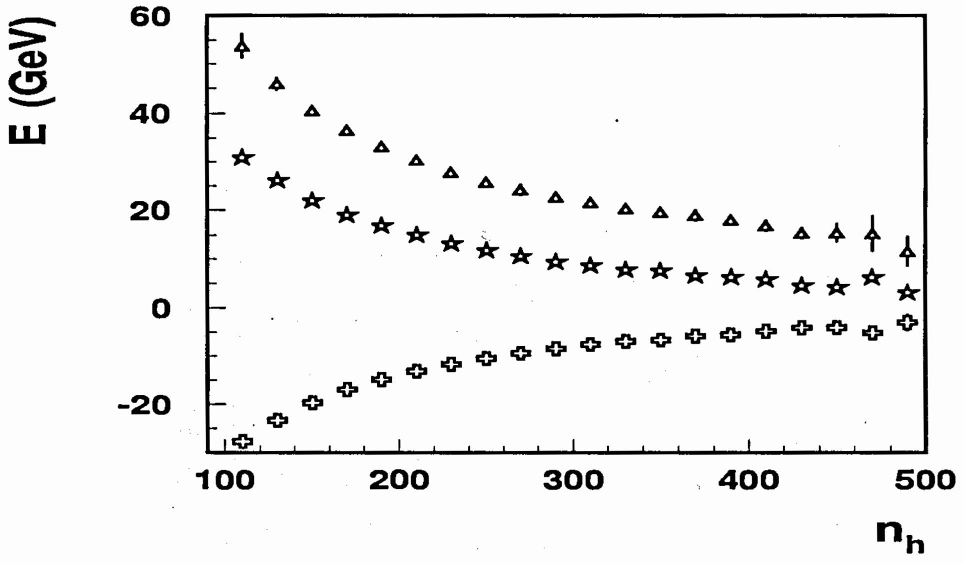

Figure 6: The average energy [Δ], the correlators $\sqrt{K_2(n)}$ [✣], $\sqrt[3]{K_3(n)}$ [★] for calorimeter towers as a function of the multiplicity at 14 TeV.

Fig. 6 shows the dependence of the average energy and the energy correlators $\sqrt{K_2(n)}$, $\sqrt[3]{K_3(n)}$ in calorimeter towers as a function of multiplicity of worked towers by using the cuts $p_t \geq 1.5$ GeV and $|\eta| \leq 3.5$. The values of the correlators lead to 5 GeV for $n_h \to 500$. The obtained distributions are also similar to the ones shown in Fig. 2. The dependence of the $R_3(n)$ ratio as a function of worked towers is shown in Fig. 7. There is no trend to decreasing the $R_3(n)$ ratio at n_h increasing. The value of this ratio is equal to 1.28 and coincides with the above obtained results (Fig. 3).

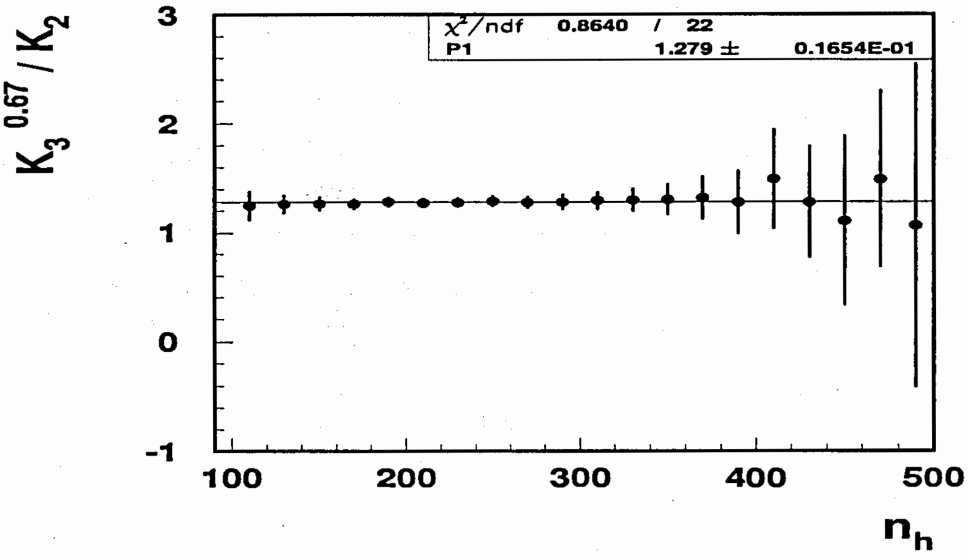

Figure 7: The $R_3(n)$ ratio [•] for calorimeter towers as a function of the multiplicity at 14 TeV.

4 Conclusion

The results of the study of the energy correlators $K_2(n)$, $K_3(n)$ and their ratio $R_3(n)$ as a function of hadron multiplicity at 14 TeV are represented. It is shown that the value of the ratio does not depend on multiplicity and is slightly more than unit. Thus, PYTHIA does not predict tendency to equilibrium, $R_3(n) \ll 1$, at high multiplicity. It is shown that the pile-up background and changing of the particle energy to the registered ones in the ATLAS calorimeter towers have a negligible effect on the $R_3(n)$.

5 Acknowledgement

Authors would like to take the opportunity to thank D. Froidevaux, R. Leitner, A. Olchevsky, S. Tapprogge, V. Vinogradov for valuable discussions and important comments. We acknowledged to the ATLAS experiment community for interest to this work and important discussions. Authors grateful to N. Dokalenko for help in preparation of this paper.

References

[1] J. Manjavidze, A. Sissakian, Phys. Rep. **346**, 1 (2001).

[2] J. Manjavidze, A. Sissakian, Bogolyubov Conf. "Problems of Theoretical and Mathematical Physics", Moscow-Dubna-Kiev, Ed. V.G. Kadyshevsky and A.N. Sissakian (1999); Part. & Nucl., 31 (2000) 104.

[3] ATLAS Collaboration, ATLAS Detector and Physics Performance Technical Design Report, v.1, CERN-LHCC-99-014, CERN, Geneva (1999).

[4] ATLAS Collaboration, ATLAS Detector and Physics Performance Technical Design Report, v.2, CERN-LHCC-99-015, CERN, Geneva (1999).

[5] T. Alexopoulos et al., Nucl. Phys. A544 (1992) 343.

[6] N.N. Bogolyubov, Studies in Statistical Mechanics, Amsterdam, 1962.

[7] T. Sjöstrand et al., Comp. Phys. Com., 135 (2001) 238.

[8] ATLAS Collaboration, ATLAS Calorimeter Performance, CERN-LHCC-96-040, CERN, Geneva (1996).

[9] ATLAS Collaboration, ATLAS Tile Calorimeter Technical Design Report, CERN-LHCC-96-042, CERN, Geneva (1996).

[10] ATLAS Collaboration, ATLAS Liquid Argon Calorimeter Technical Design Report, CERN-LHCC-96-041, CERN, Geneva (1996).

[11] S. Akhmadaliev et al., NIM A449 (2000) 461-477.

[12] P. Amaral et al., NIM A443 (2000) 51-70.

[13] E. Richter-Was et al., ATL-PHYS-98-131, CERN, Geneva, 1998.

On the Calculation of Phase Space Integral

J.Manjavidze, A.Sissakian, N.Shubitidze
JINR, DUBNA

We investigate the phase space integral. Such type integrals arrive when the topological cross-section is calculated.

$$Z_n = \int \left\{ \prod_{i=1}^{n} \frac{d^3\, k_i}{2\sqrt{k_i^2 + m^2}} \right\} \delta^4 \left(P - \sum k_i \right) f_n(k_1, \ldots, k_n)$$

We will consider the simplest case when the module square of amplitude f_n has the form:

$$f_n(k_1, \ldots, k_n) = \prod_{i=1}^{n} \exp\left(-r_0^2\, k_{t,i}^2 \right)$$

$P \equiv (E, 0, 0, 0)$; $k_{t,i} = \sqrt{k_{i,x}^2 + k_{i,y}^2}$ is the transverse momentum; r_0 is the cutting parameter - phenomenological constant.

Therefore, the aim of my talk is to formulate the effective method of calculation of the longitudinal phase space integral for the case when the number n is high enough.

The theory of calculation of integrals of this type have a long history. Note, that all these methods can't work for big (≥ 100) values of n. Considering the very high multiplicity, it is important to have an universal method of calculation of the phase space integrals. It can be useful in a wide range of multiplicity.

We neglect the momenta conservation low and leave only energy conservation low:

$$\int \ldots \delta^4\left(P - \sum_{i=1}^{n} k_i\right) \to \int \ldots \delta\left(E - \sum_{i=1}^{n}\sqrt{k_i^2 + m^2}\right)$$

After introducing spherical coordinates

$$k_{i,x} = k_{t,i}\cos(\phi_i)$$
$$k_{i,y} = k_{t,i}\sin(\phi_i)$$

and integration on ϕ_i we receive:

$$Z_n(E) = (\pi/2)^n \int \left\{ \prod_{i=1}^{n} \frac{d(k_{t,i}^2)dk_z}{\sqrt{k_{t,i}^2 + k_{z,i}^2 + m^2}} e^{-r_0^2 k_{t,i}^2} \right\} \times$$
$$\times\, \delta\left(E - \sum_{i=1}^{n}\sqrt{k_{t,i}^2 + k_{z,i}^2 + m^2}\right)$$

We may include to the previous the integral equality:

$$\int d\mathcal{E}_i \delta\left(\mathcal{E}_i - \sum_{i=1}^{n}\sqrt{k_{t,i}^2 + k_{z,i}^2 + m^2}\right) \equiv 1$$

and after some transformations receive:

$$Z_n(E) = (\pi/r_0)^n [m(n_{max} - n)]^{n-1} \times$$
$$\times \left\{ \prod_{i=1}^{n} \int_0^1 dy_i F(r_0 m \sqrt{(n_{max} - n)y_i((n_{max} - n)y_i + 2)} \right\} \delta\left(1 - \sum_{i=1}^{n} y_i\right)$$

where $n_{max} = E/m$, F(x) - is a Dawson's integral:

$$F(x) = e^{-x^2} \int_0^x e^{t^2} dt$$

Using Fourier representation of Dirac delta-function we receive final equation:

$$Z_n(E) = (\pi/r_0)^n[m(n_{max} - n)]^{n-1} \times$$
$$\times \int_0^\infty d\alpha \cos[-\alpha + n \arctan(\phi_s/\phi_c)][\phi_s^2 + \phi_c^2]^{n/2}$$

where

$$\phi_s = \frac{1}{\pi}\int_0^1 dy \sin(\alpha y) F\left(r_0 m\sqrt{(n_{max} - n)y((n_{max} - n)y + 2)}\right)$$
$$\phi_c = \frac{1}{\pi}\int_0^1 dy \cos(\alpha y) F\left(r_0 m\sqrt{(n_{max} - n)y((n_{max} - n)y + 2)}\right)$$

On the Figures 1,2 behavior of $\phi_c(\alpha, E)$ and $\phi_s(\alpha, E)$ are demonstrated.

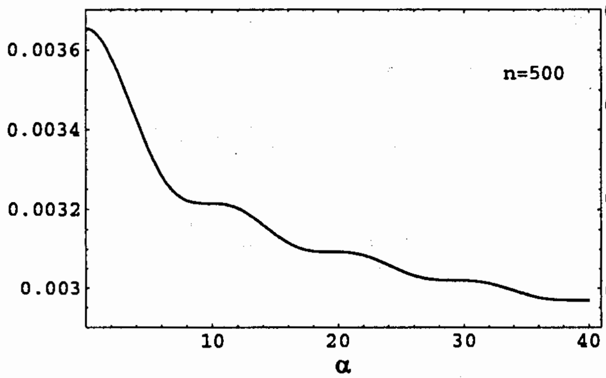

Figure 1:

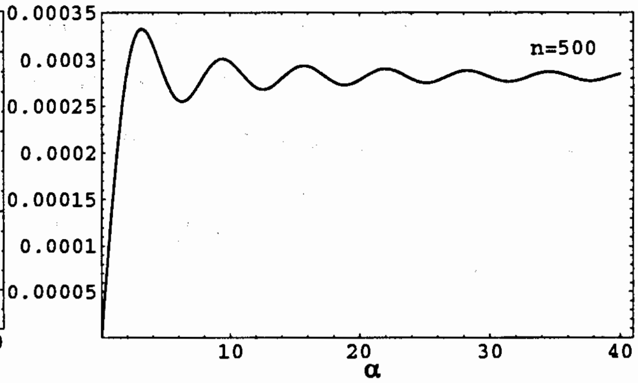

Figure 2:

Calculations are realized by the package "Mathematica" 4.1 with range of precision ~ 40. We meet with the serious difficulty when we execute numerical calculations. Integrand in (11) is a fast oscillatory function, see Figure 3 for normalized function.

For its precision computing we find roots of integrand and represent integral as a sum of small integrals between neighboring roots. We received unexpected result on this way - the sum of positive small integrals are equal sum of the negative small integrals with 34 number of mantissa digits. On the numerical analysis such result have the name "Roundoff Error".

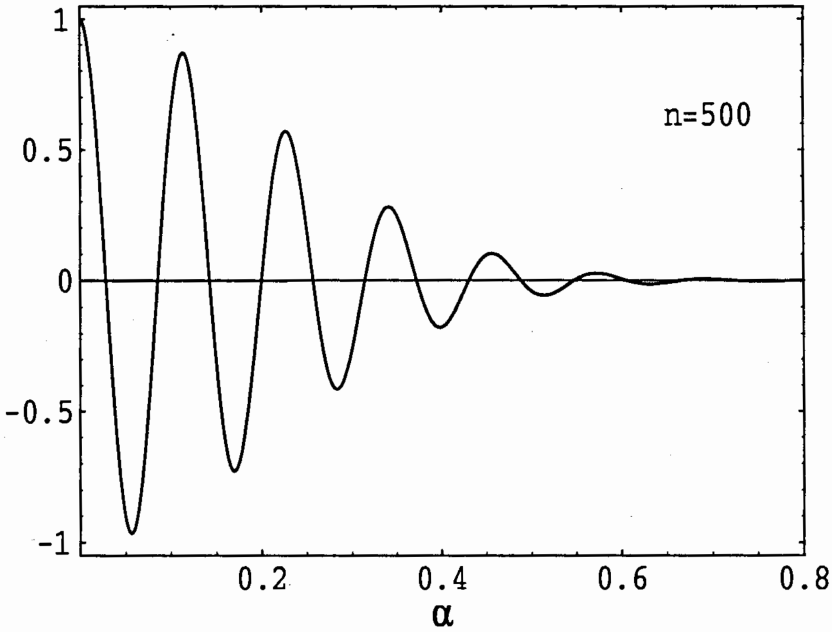

Figure 3: .

To find a way out of the impasse we use another method. After substitutions to the primordial integral Fourier representation of Dirac delta-function and replacement of variable we receive:

$$Z_n = -\frac{i}{2\pi}\int_{-i\infty}^{+i\infty} d\beta e^{\beta E + n\ln[K(\beta)]} = -\frac{i}{2\pi}\int_{-i\infty}^{+i\infty} d\beta e^{L(\beta)}$$

where

$$K(\beta) = \int \frac{d^3k}{2\sqrt{k^2+m^2}} e^{-\beta\sqrt{k^2+m^2} - r_0^2 k_t^2}$$

For last integral we use foregoing formalizm and receive:

$$K(\beta) = \frac{\pi}{r_0^3}\int_0^{u_{max}} e^{-\beta\sqrt{(u/r_0)^2+m^2}} \frac{uF(u)}{\sqrt{(u/r_0)^2+m^2}} du$$

where

$$u_{max} = r_0 m\sqrt{(n_{max}-n)(n_{max}-n+2)}$$

We estimate value of our integral by the method of pass:

M. V. Fedoryuk, Metod perevala."Nauka",1977,Moscow

Let β_0 is a root of equation:

$$\frac{\partial}{\partial\beta} L(\beta) = 0$$

Then we expand the range of exponent near point β_0 and write Z_n as:

$$Z_n = \frac{i}{2\pi}\int_{-i\infty}^{+i\infty} d\beta e^{L(\beta_0)+L''(\beta_0)/2(\beta-\beta_0)^2+L'''(\beta_0)/6(\beta-\beta_0)^3+\ldots}$$

If restrict oneself by the third part in exponent we receive:

$$Z_n = \frac{e^{L(\beta_0)}}{\sqrt{2\pi L''(\beta_0)}}\sum_{k=0}^{\infty}\frac{(6k-1)!!}{12^k(2k)!}R^{3k}$$

where

$$R = [L'''(\beta_0)]^{2/3}/L''(\beta_0)$$

Since series (19) is a Borel type, we may write condition of its semiconvergence:

$$R \ll 1$$

On the Figures 4,5 the behavior of R for $r_0 = 0.2$ and $r_0 = 1.0$ for various n are demonstrated.

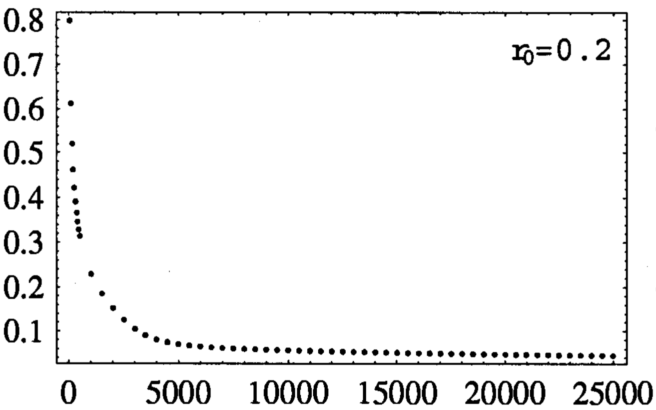

Figure 4:

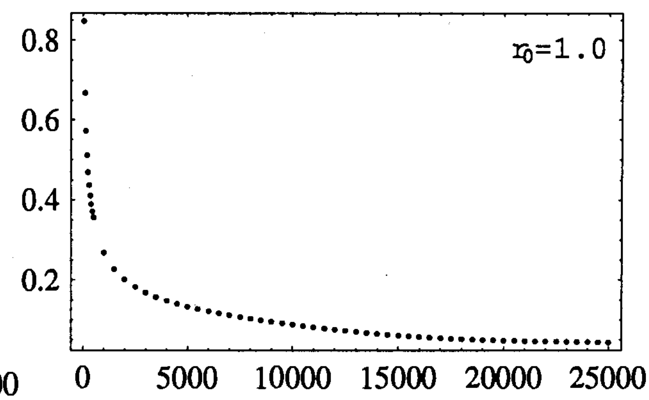

Figure 5:

On the figure 6 behavior of Z_n as function of n are demonstrated:

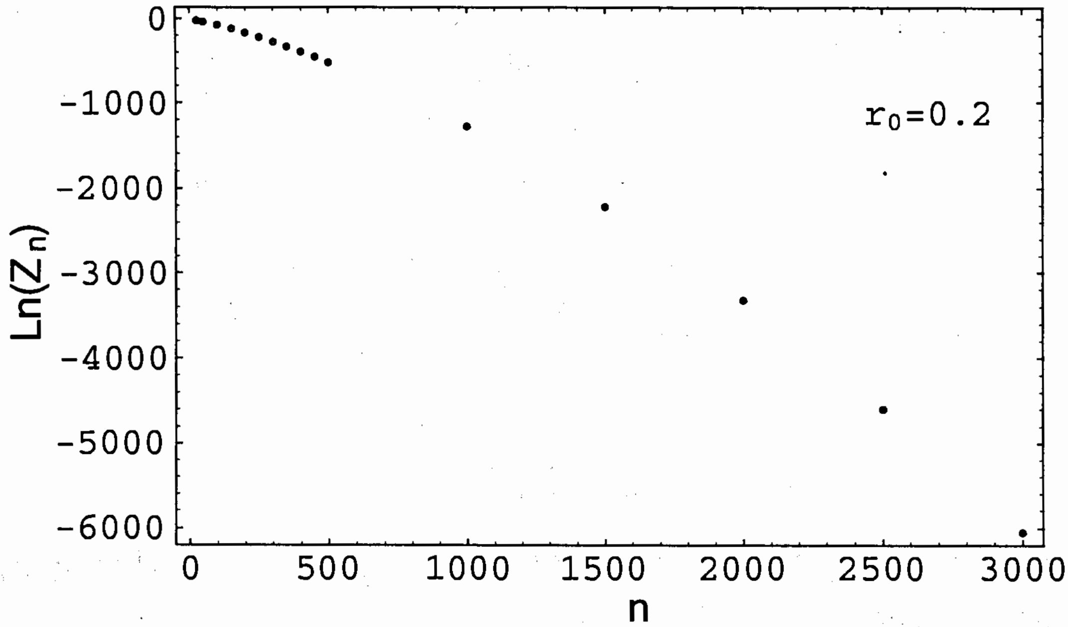

Figure 6: .

References

[1] F.Lurcat,P.Mazur, Nuovo Cim., **31**, (1964), 140

[2] A.Krzywicki, Nuovo Cim., **32**, (1964), 1067

[3] A.Krzywicki, J. Math. Phys., **6**, (1965), 485

[4] A.Bialas, T.Ruijgrok, Nuovo Cim., **39**, (1965), 1061

[5] E.H.de Groot, Nucl. Phys., **B48**, (1972), 295

[6] K.Kajantie, V.Karimaki, Computer Phys. Comm., **2**, (1971) 207

[7] P.Pirala, E.Byckling, Computer Phys. Comm., **4**, (1972), 117

[8] R.A.Morrow, Computer Phys. Comm., **13**, (1978), 399

[9] R.Kleiss, W.J.Stirling, Computer Phys. Comm., **40**, (1986), 359

[10] M.M.Block, Computer Phys. Comm., **69**, (1992), 459

Thermalization effect in high energy hadron collisions

J.Manjavidze[1] *and* *A.Sissakian*[2]

Abstract

We discuss the possibility to suppress the nonperturbative effects if the very high multiplicity hadron final states are chosen. We expect in result the effect of thermalization, when the energy is distributed over all degrees of freedom uniformly. The theoretical uncertainties and possible experimental measurements are described.

1. Very high multiplicity (VHM) events are expected to be produced at the future experiments at BNL (STAR), Fermilab (CDF), CERN (ATLAS). Then, it is natural to expect the VHM region to give new important information, which will be complementary to the ongoing investigations and/or unavailable in other than the VHM process. The studies of the VHM region have been proposed recently in [1] and attract an increasing interest in high energy physics [2, 3, 4, 5].

In this Letter, where we briefly consider the VHM topic in whole, we particularly emphasize the related physical quantities expected to be measured with forthcoming experiments. In this sense, it is crucial to understand experimental abilities of such measurements, since the topological cross section, σ_n, is extremely small (e.g., at TeV energies, $\sigma_n \ll 10^{-7}\sigma_{tot}$, compared to the total cross section σ_{tot}, Fig.1) and could lead to certain problems.

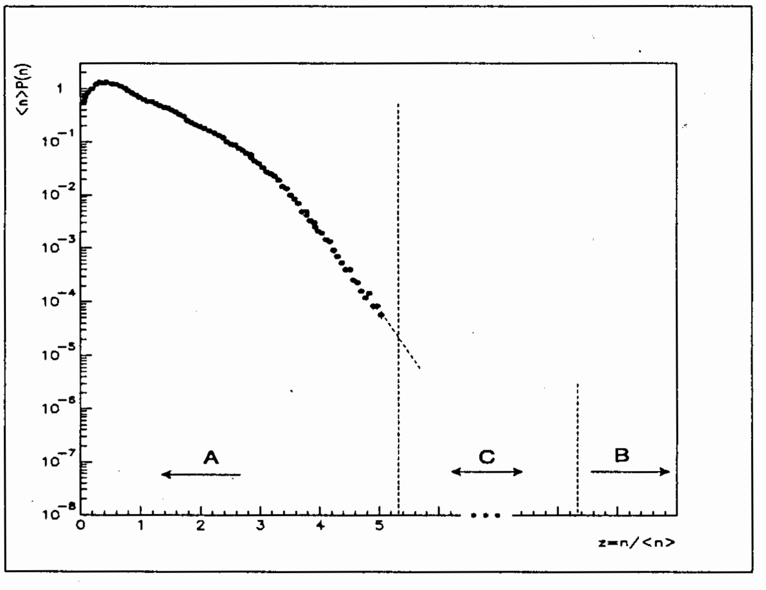

Figure 1: The KNO multiplicity distribution, $P(n) = \sigma_n/\sigma_{tot}$. The points are the E735 Tevatron data [6]. The range **A** corresponds to the multiperipheral kinematics. The range **B** corresponds to the non-interacting, ideal, gas approximation, $n \ll n_{max}$. **C** is the VHM region.

Started investigations of VHM processes, one has first of all ask a question: why the mean multiplicity in hadron processes being energy dependent as $\ln^2(s/m_\pi^2)$ is much *smaller* than the threshold multiplicity value $n_{max} = \sqrt{s}/m_\pi$ [7]? Here $\sqrt{s}$ is the c.m.s. energy and m_π is the pion mass.

[1]JINR,Dubna, Russia & Inst. of Phys., Tbilisi, Georgia. E-mail: joseph@nusun.jinr.ru
[2]JINR, Dubna, Russia. E-mail: sisakian@jinr.ru

In the present Letter, we follow the idea [1] that the multiple production process could be considered as a process of hot tea cooling in a cold environment. Then very hot tea cooling in very cold room is analogous to the VHM process. In that case, the cooling process proceeds "quickly", i.e. any process obstacled to the cooling fluctuations must be suppressed. The idea that the hadron multiple production process may consist of various mechanisms has been considered in [8].

In the QCD parton picture [9] the "fastness" of a process means that parton decay must prevail over its dissipation from an interaction zone. This is possible if the parton virtuality $|q|$ is high enough as far as the parton lifetime is $\sim 1/|q|$. As a result, the VHM process should be hard and, therefore, the forces preventing particle production (confinement) must be negligible.

Fig.2 shows the longitudinal-transverse momenta phase space domain of the VHM process. It is remarkable that the VHM domain occupies both regions, the "low-$p_{||}$" and the "low-$p_{\perp}$" ones. Therefore, despite the fact that the VHM process is hard one can not use the Leading Logarithm Approximation (LLA) [10] to describe it [1]. To stress is that, following the LLA formalism, there are the only two domains, namely the Regge and Deep inelastic Scattering (DIS) domains, as shown in Fig.2. The corresponding cross sections may be sufficiently large and the LLA is applicable.

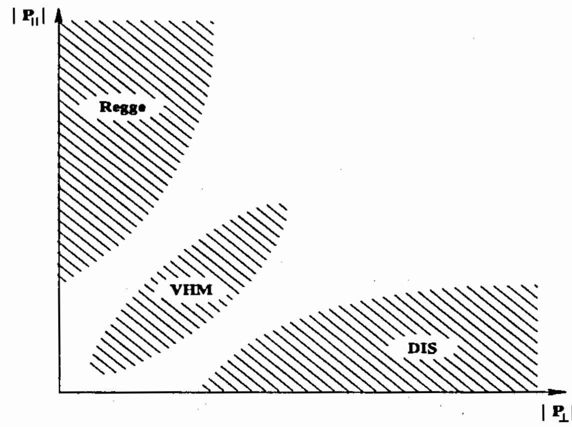

Figure 2: The longitudinal-transverse momentum phase space of inelastic hadron processes, see text.

The "low-$p_{||}$", or "low-x" [11] in DIS, also means that VHM particles have low energies. For that reason, the hadrons are mainly resulted from the "gluing" of coloured constituents created in the hard process. Therefore, *the (soft) process of coloured parton pair production from the vacuum is negligible in the VHM domain.* This distinguishes VHM processes from other hard processes (e.g., from hadron production in e^+e^--annihilations, or DIS processes). The VHM dynamics is free of the non-perturbative background.

Sec.2 argues the above conclusion, in Sec.3 the main properties of VHM dynamics are discussed and the concluding remarks are given in Sec.4.

2. The dominance of "Regge" processes stands for the "softness" of hadron dynamics [12]. This is based on the experimental observations: the mean transverse momentum of secondary particles, being energy and multiplicity independent, has a limited value, and the diffraction radius of hadron elastic scattering increases with increasing energy. Such "multiperipheral" kinematics is described by the Regge model with the *soft Pomeron* ansatz.

From the "microscopical" point of view, it means that the soft process can be roughly described by the very spatial class of the Feynman "ladder" diagrams of perturbative QCD (pQCD). This is the so-called "*BFKL Pomeron*" solution [13]. It is based on the LLA approach and assumes that the process described is sufficiently hard[3].

The both models are based on the assumption that the mean transverse momentum of produced hadrons is small. In the frame of the *soft Pomeron* approach, this constrain is hidden in the conservation laws, which are the consequence of the underlying non-Abelian gauge symmetry. In the *BFKL Pomeron* case, the LLA place a role of the constrain.

It is worse to note that the constrain restricts the production dynamics and, therefore, the produced states can not entirely cover the phase space with the same density, Fig.2. This requires the constrain to be suppressed in order to lead to the VHM final states. Remembering that the constrains are the consequence of the long-range connections among interacting degrees of freedom, this also points out that the VHM process must be the hard process.

The VHM scenario discussed realizes if (i) the hard processes has place in the VHM region and if (ii) the hard process ensures the "fast" hadron production.

The formal proof of the item (i) contains the following steps [1, 14]. First, it can be shown that if the final-state interactions are excluded, then the *soft* process only satisfies the following asymptotics:

$$\sigma_n^s < O(e^{-n}),$$

i.e. the "soft" topological cross section σ_n^s falls down faster than any power of $\exp\{-n\}$. The reason is just the softness of the process. On the other hand, the *hard* process leads to the following asymptotic estimate:

$$\sigma_n^h = O(e^{-n}).$$

Consequently, one always finds such energy $\sqrt{s}$ and multiplicity n that

$$\sigma_n^h \gg \sigma_n^s \text{ for } n \ll \sqrt{s}/m_\pi.$$

This proves the item (i).

The qualitative argument for the statement (ii) follows from the Ehrenfest-Kac model [15] of the irreversibility phenomenon[4]. It shows that if the initial state is far from the final one, then the system undergoes to equilibrium *in the fastest way* [5]. The result of the computer modelling of "particle production" within discussed model, Fig.3, confirms this. Indeed, as it is seen there are no fluctuations at early stage of the process: number of the "produced particles" is proportional to t, up to $t \simeq 1000$.

The formal proof of the statement (ii) can be obtained from the KNO-scaling of the multiplicity distribution in pQCD jets [1]. Introducing the quantity

$$\mu(n,s) = -\frac{1}{n}\ln\left\{\frac{\sigma_n(s)}{\sigma_{tot}(s)},\right\} \tag{1}$$

one finds at the mass M of a jet,

$$\mu_1(n,M) = \frac{a}{\bar{n}_j(M^2)} + O(1/n).$$

[3]The point is that this Regge-like theory depends on the phenomenological energy scale parameter s_0 and, therefore, its range of application may be chosen arbitrary.

[4]The Ehrenfest-Kac model considers two box a and b and $2N$ *numbered* balls. One may assume that the "far from the equilibrium" initial state presents the situation when all $2N$ balls are e.g., in the box a and in the equilibrium each box contains N balls. Then, choosing *randomly* the number of balls, one should take the corresponding ball from the box and put it into the other one. At the following step, the number of a ball will be again randomly chosen, and the corresponding ball should be put into the other box, and so on. One may measure the time t in the units of the ball shifting time. Then, the number of the "produced particles" in the box b measures the trend to equilibrium. In this equilibrium state, $N_a = N_b$ (Fig3).

[5]This phenomenon was not mentioned in the known publications concerning the Ehrenfest-Kac model.

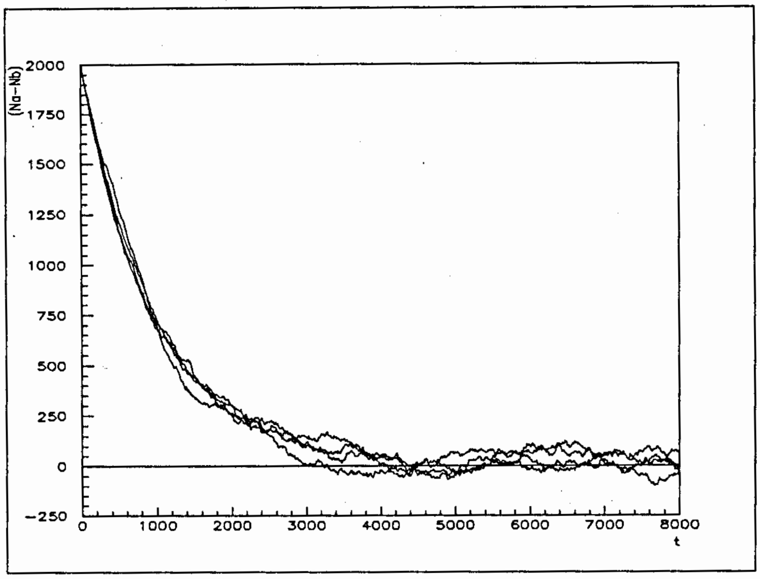

Figure 3: The Ehrenfest-Kac model simulation for random ball shifting from the a box to the b box. Initially the number of balls is N_a=2000 and N_b=0, while in the equilibrium, $N_a - N_b = 0$. Four simulations are displayed.

Here $a > 0$ and $\bar{n}_j(M^2)$ is the mean hadron multiplicity in a QCD jet, $\ln \bar{n}_j(M^2) \sim \{\ln(M^2/\Lambda^2)\}^{1/2}$. The two-jet contribution at the same energy M reads as

$$\mu_2(n, M) = \frac{a}{\bar{n}_j(s/4)} + O(1/n) > \mu_1(n, s),$$

where the energy conservation law is taken into account. Therefore, the asymptotics over n is defined by the events with the lowest numbers of pQCD jets.

This confirms the statement (ii) since just the jet mechanism of particle production is known to be the fastest one. Moreover, we conclude that the number of the jets decreases with increasing total multiplicity n and, thus, the heavier jets are produced in the VHM region. However, one has to note that this conclusion is based on the LLA and, therefore, we consider it just as a qualitative prediction.

3. From the above, one concludes that the VHM process is a hard process. In this case, the process of incident energy dissipation evolves *freely*, i.e. without the influence of the "hidden constrains". This is the important observation because it allows to assume that in such conditions the of final state distribution trends to the "equilibrium".

Let us remind some statistical properties of the maximally constrained systems, also called the "exactly integrable systems". It is known that if the system has $2N$ degrees of freedom and holds N constrains (first integrals in involution) then no thermalization occurs in such a system. The first observation of this phenomenon belongs to Fermi, Pasta and Ulam [1, 17]. On the other hand, it is evident that the system without any constrains should drift to the equilibrium.

The hadron dynamics hides definite number of constrains, which is not enough to completely suppress particle production, i.e. the thermalization process. This conclusion follows from the existence of large multiplicity fluctuations, see Fig.1. Nevertheless, the constrains occur and the mean multiplicity is reasonably small $\bar{n}(s) \ll n_{max}$.

To stress is that the term "equilibrium" is understood here as the absence of any macroscopic correlations among the extensive parameters of a system. For example, the absence of energy correlations implies the thermal equilibrium. Then, one can obtain the experimental condition, which reflects the "equilibrium phenomena" [1, 18]. It has been shown that the condition

$$R_l(n,s) = \frac{|K_l(n,s)|^{2/l}}{|K_2(n,s)|} < 1, \quad l = 3, 4, ..., \tag{2}$$

is the necessary and sufficient one to reach thermalization. Here $K_l(n,s)$ are the l-point energy correlators in the n-particle system, $l < n$. To note is that (2) reminds the "correlation relaxation condition" of Bogolyubov [19].

The tendency of the system to reach the equilibrium is considered as the dynamical effect, when the (symmetry) constrains are switched off, and for that reason the system may drift to the equilibrium state.

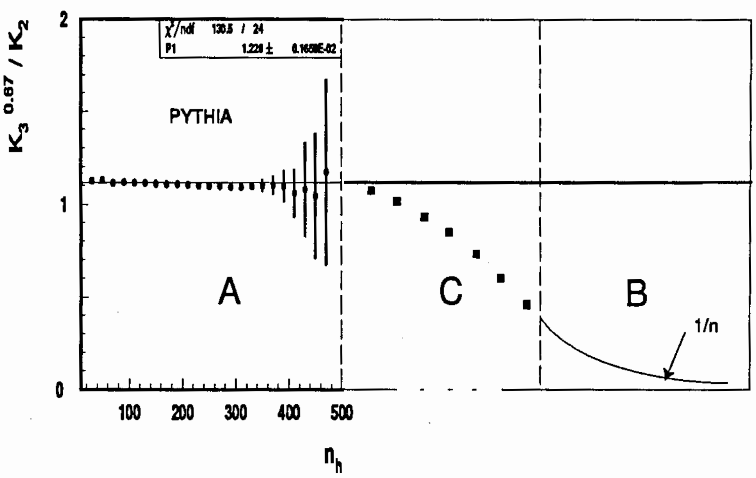

Figure 4: The ratio $R_3(n,s) = |K_3|^{2/3}(n,s)/|K_2(n,s)|$ of the energy correlators vs. multiplicity. The PYTHIA prediction is given for the **A** domain (see Fig.1). Domain **B** corresponds to the "non-interacting gas" approximation.

Fig.4 shows the result of Monte Carlo PYTHIA event generator [21] simulation of the ratio $R(n,s)$ for the domain **A** in Fig.1. The absence of the thermalization process is natural if one notes that PYTHIA resembles the Regge model. At the same time, it can be shown that in the region **B** the system without fail reaches the thermal equilibrium, $R(n) \sim 1/n$ in that domain.

4. We can conclude that:

(i) the VHM process allows us to investigate the hadron dynamics beyond the standard multiperipheral kinematics;

(ii) it is the hard process in sense that the influence of hidden constrains, connected with the high symmetries and the nontrivial vacuum of the Yang-Mills theory, is not important in the particle production dynamics;

(iii) the VHM process allows us to reach the thermal equilibrium, where the ordinary thermodynamical methods can be used. (This extends experimental possibilities and, therefore, is extremely important. For example, the μ-quantity introduced in (1) is the "chemical potential" if measured in the units of the mean energy of produced particles [1]);

(iv) the VHM domain seems to be one of the mostly interesting regions to investigate the collective phenomena, e.g. phase transitions. (To note is that the VHM final state is a "cold" one).

To note is that the production dynamics of VHM states might be well enough described by pQCD, but the logarithmic accuracy seems to be not enough. This is a main theoretical problem and to this end a more accurate perturbation theory, described in [20], has been formulated.

At the end, let us add that, as it follows from the above conclusion, the VHM process leads to the *dense*, *cold* and *equilibrium* locally-coloured state, e.g. "cold" plasma [22][6].

Acknowledgements

Authors would like to take the opportunity to thank Yu. Budagov, V.Kadyshevski, A.Korytov, E.Kuraev, L.Lipatov, V.Matveev, V.Nikitin and E.Sarkisyan for fruitful discussions and constructive comments. Special thanks to STAR (BNL) and CDF (FNAL) physics communities for continuous interest in the VHM problem.

References

[1] J.Manjavidze and A.Sissakian, Phys. Rep., 346 (2001) 1

[2] J.Manjavidze, Fields & Particles, 16 (1985) 101

[3] I.M.Dremin and V.A.Nechitailo, hep-ph/0207068

[4] J.Manjavidze and A.Sissakian, to appear in Proceedings of the Int. Conf. on High Energy Physics (Amsterdam, 24-31 July, 2002).

[5] S.Eliseev, L.Jenkovsky, G.Kozlov, B.Struminsky, talks at the VHM Workshops (Dubna, 2000-2002). See also contributions to the VHM Session of the XXXII Intern. Symp. for Multiparticle Dynamics (Alushta, Ukraine, 7-13 Sept., 2002)

[6] T.Alexopoulos et al., Phys. Rev, D48 (1993) 984

[7] Particle Data Group, K.Hagiwara et al., Phys. Rev., D66 (2002) 0001

[8] A.N.Sissakian and L.A.Slepchenko, Preprint JINR, P2-10651, 1977; A.N.Sissakian and L.A.Slepchenko, Fizika, 10 (1978) 21

[9] Yu.L.Dokshitser, D.I.Dyakonov and S.I.Troyan, Phys. Rep., 58 (1980) 211

[10] For a review, see V.A.Khose, W.Ochs, Int. J. Mod. Phys., A12 (1997) 2949

[11] L.V.Gribov, E.M.Levin and M.G.Ryskin, Phys. Rep., C100 (1983) 1

[12] P.V.Landshoff, Nucl. Phys.,B25 (1992) 129; M.Baker and K.Ter-Martirosyan, Phys.Rep., C28 (1976) 1

[13] E.Kuraev, L.Lipatov and V.Fadin, Sov. Phys. JETP, 44 (1976) 443; JETP, 71 (1976) 840; L.Lipatov, Sov.J. Nucl. Phys., 20 (1975) 94; V.Gribov and L.Lipatov, Sov.J. Nucl. Phys., 15 (1972) 438, 675; G.Altarelli and G.Parisi, Nucl. Phys., B126 (1977) 298;I.V.Andreev, Chromodynamics and Hard Processes at High Energies (Nauka, Moscow, 1981)

[14] J.Manjavidze, El. Part. At. Nucl., 16 (1985) 101

[15] M.Kac, *Probability and Related Topics* (Intersciens Publ., London, New York, 1957)

[16] J.Manjavidze and A.Sissakian, JINR Rap. Comm., 5/31 (1988) 5; *ibid.*, 2/288 (1988) 13

[17] A.F.Andreev, JETP, 45 (1963) 2064

[18] J.Manjavidze, El. Part. At. Nucl., 30 (1999) 124

[19] N.N.Bogolyubov, stadies in Statistical Mechanics (North-Holland, Amsterdam, 1962)

[20] J.Manjavidze, Journ. Math. Phys., 41 (2000) 5710; J.Manjavidze and A.Sissakian, Theor. Math. Phys., 123 (2000) 776; J.Manjavidze and A.Sissakian, J. Math. Phys., 42 (2001) 641; *ibid.*, 42 (2001) 4158; J.Manjavidze and A.Sissakian, Theor. Math. Phys., 130 (2002) #2

[21] T.Sjöstrand et al., Comp. Phys. Com., 135 (2001) 238

[22] L.Van Hove, Ann. Phys. (N.Y.) 192 (1989) 66

[6]It is hard to imagine the coloured state to form the QCD plasma one if the former is "hot". In this case the kinetic motion would rapidly separate the charges and this must lead to the strong polarization of the vacuum. This effect is absent in the QED plasma.

THE ATLAS HADRONIC TILE CALORIMETER

R. Leitner for the TILECAL Community

Appendix

Short status of the Tile Calorimeter project is given. Major achievements in the mechanical construction of the detector modules and their instrumentation as well as the principles of the detector front-end electronics are described. The ideas of Tile Calorimeter modules calibration are presented.

1 Introduction

The Tile Calorimeter is one of the sub-detectors of the ATLAS (see Fig. 1) general purpose pp detector [1] designed for the Large Hadron Collider (LHC) to be built at CERN. It is a large hadronic sampling calorimeter which makes use of steel as the absorber material and scintillating plates read out by wavelength shifting (WLS) fibres as the active medium. The new feature of its design is the orientation of the scintillating tiles which are placed in plane perpendicular to the colliding beams and are staggered in depth. A good sampling homogeneity is obtained when the calorimeter is placed behind an electromagnetic compartment and a coil equivalent to a total of about two nuclear interaction lengths of material. This has been verified with Monte Carlo simulation and has been proven by the test beam results.

The Tile Calorimeter [2] consists of a cylindrical structure with an inner radius of 2280 mm and an outer radius of 4230 mm. It is subdivided into a 5640 mm long central barrel and two 2910 mm extended barrels (see Fig. 2). The scintillating tiles lie in the $r - \phi$ (radius-azimuthal angle) plane and span the width of the module in the ϕ direction. WLS fibres running radially collect the light from the tiles along their two open edges. Readout cells are then defined by grouping together a set of fibres into a photomultiplier (PMT), to obtain a three dimensional segmentation. Radially, the calorimeter is segmented into three layers, approximately 1.4, 3.9 and 1.8 interaction lengths thick at pseudorapidity η=0; the $\Delta\eta$x $\Delta\phi$ segmentation is 0.1x0.1.

2 Mechanics

The Tile Calorimeter passive absorber is a laminated steel structure with pockets at periodic intervals to contain the scintillating tiles. The structure is built in a modular fashion to facilitate the construction. It is a self contained unit with the read-out electronics being fully contained within the calorimeter itself. In addition to its function as passive absorber, the Tile Calorimeter also provides the magnetic flux return for the ATLAS solenoid.

The Tile Calorimeter is built in three sections: a central barrel covering approximately from -1 to +1 in rapidity and two extended barrels extending the rapidity coverage to approximately ± 1.6. Each of the three calorimeter sections is constructed from 64 modules, each covering 5.6^{o} in azimuth. The barrel module is built out of 19 submodules mounted on a strong-back support girder which houses the read-out electronics. Its cross section is sufficient to form the primary magnetic flux return. Except for one "special" sub-module used to assure the final length of the module, all sub-modules are identical steel laminations approximately 300 mm long. The assembled calorimeter structure is self-supporting through a bearing connection between modules at the inner radius and aborted plate connection at the outer radius of the girder. The support saddles connect the calorimeter to rails which provide movement for installation and alignment. The TileCal also supports the Liquid Argon calorimeter and presents a great engineering challenge. Except for some details associated with integration with other ATLAS sub-systems, the design of an extended barrel module is identical to that of a barrel module although it involves nine rather than 19 sub-modules.

2.1 The Production

The mechanical design and the construction method for the barrel and for the extended barrel calorimeters have been worked out using a combined engineering effort from all the institutions involved. The concept of three regional centres came about naturally, each one with the task of constructing the modules of one entire cylinder. For the barrel section, the choice has been JINR in Dubna, where key equipment and facilities already existed to handle and store 20 tons objects. This laboratory also has all the necessary support in technical and engineering manpower to accomplish this task. For the extended barrels, one center will be in the USA, at Argonne National Laboratory, which allowed the effort of several universities to be focused effectively. As is the case for JINR Dubna, all necessary resources required for module handling and storage exist there. The second extended barrel regional center was in Spain (IFAE Barcelona), where a dedicated laboratory with all necessary infrastructure has been built. Around these three regional centres we had nine sub-module assembly plants, equipped with the necessary sub-module assembly tooling and ready to construct and providing about

350 sub-modules to the regional centres over a period of three years. In time being all modules are mechanically constructed.

2.2 The Assembly

The basic concept underlying the calorimeter assembly procedure is that the 64 modules, once assembled into the calorimeter form a cylinder which is a self-supporting structure. Each module rests on the module below and is supported on two well defined bearing surfaces at the innermost and at the outermost radii. The main structural elements in the assembly are the girders, which are coupled by connection plates fastened at the outer radius. These connecting plates will also be used for radial alignment of modules during the assembly process.

A second important concept is the assembly sequence. The cylinder will be built up, using an assembly fixture, starting from the lower modules and built up until the final few modules are inserted as a unit. The assembly must be stable in all intermediate configurations and special assembly cradle is used at its start. Shims, placed at the two bearing surfaces, ensure that the contact between modules is well controlled and occurs only at these two surfaces and allow individual adjustment of the position of each module within the design azimuthal gap. The shim sizes will also take account of overall structure deformation as measured during the assembly such that sufficient space is available for the installation of the final modules. The entire structure sits on dedicated supports (saddles) placed symmetrically on the left and on the right side, resting on the main rail system. The barrel and the two extended barrel calorimeters are mechanically independent and may move individually on the rail system to provide access to the inner part of the ATLAS detector.

As an additional complexity, the Tile Calorimeter must provide the support of the detectors placed inside, and in particular of the Liquid Argon cryostat. The weight of this is of the order of 300 tons for the barrel and 250 tons for each of the end-caps. Concerning the barrel, the base-line solution is to have the cryostat directly supported on four feet placed at the four extremes and resting directly on the saddle and the overall calorimeter support system. The four feet are placed at an angle of 45^o and are housed inside the gap region. For the extended barrels the situation is more complex because of the differences in the internal support of the mass of the Liquid Argon Calorimeter inside the cryostats and the need to minimize the amount of dead material in front of the calorimeter. In this case, the support is different for the front (the location closest to the interaction point) and back of the cryostat. In front, the cryostat will rest directly, through two dedicated feet, on the inner surface of the Tile Calorimeter. On the back, the two feet sit on heavy end-plates which transmit the weight directly to the support saddle. The particular position of the cryostat feet required an important modification of few modules in that region.

Current status of the preassembly is shown on Fig. 3.

3 Optics

The Tile Calorimeter is a sampling calorimeter using steel as the passive absorber and scintillating tiles as the active medium. Eleven sets of tiles of radial sizes from 97 mm to 187 mm form the longitudinal segmentation of the detector. A pair of wavelength shifting (WLS) fibres running radially collect light from the tiles at both of their edges. Readout cells are defined by grouping together a set of fibres onto a photomultiplier tube (PMT), to obtain three dimensional segmentation.

The principle of the Tilecal is illustrated on Fig. 4. Ionizing particles crossing the tiles induce the production of light in the base material of the tiles, with wavelengths in the UV range which subsequently is converted to visible light by scintillator dyes. This scintillation light propagates through the tile to its edges, where it is absorbed by the WLS fibres and shifted to a longer wavelength (chosen to match the sensitive region of the PMT photocathode). A fraction of the light re-emitted in the fibre is captured and propagated via total internal reflection to the PMT where it is detected. The ends of the fibres away from the PMTs are aluminized. The driving philosophy behind the optics is to achieve and maintain a uniform, minimum light yield so that the resolution of the detector is not compromised by a lack of photostatistics. A photoelectron yield of 0.5 photoelectron/mip at normal incidence/tile is enough to achieve the required energy resolution. However, to ensure that the muon signal is visible within each radial depth, this number is a lower limit and a safety factor should be added. Calculations show that with 1 pe/mip at normal incidence/tile the muon signal invisible within each cell, and that is confirmed by the test beam results. Nonuniformity throughout the detector should also be kept small so as not to impact the constant term oft he resolution. Our baseline goal is an rms nonuniformity within a cell up to 10%.

3.1 Scintillator tiles

The cost per scintillator tile and production rate are important parameters in the choice of the tile materials and production technology. These issues have led us to the choice of injection molding technology for tile production for the Tile Calorimeter. Having selected this technology, it is important to determine the performance factors. Light yield, uniformity of response within a tile and tile-to-tile uniformity are key performance issues. A total of approximately 460,000 scintillating tiles have been required for the Tile Calorimeter, half in the barrel, one quarter in each of the extended barrel sections. The barrel and extended barrels, are equipped with tiles of the same dimensions.

The Tile Calorimeter contains 11 different sizes of trapezoidal shaped tiles, ranging from about 200 mm to 400 mm in $R\phi$ length and 97 mm to 187 mm in radial width. The wavelength shifting fibres are placed in contact with the non parallel edges of the tiles. All tiles are 3 mm thick. Each tile has two holes, 9 mm in diameter, through the surface for the passage of the calibration source tubes.

Light yield Finite photostatistics gives a contribution to the calorimeter resolution, to be added in quadrature to the intrinsic sampling resolution. A requirement that we adopted was to be able to see the muon signal within each depth sampling. Furthermore, this detector is expected to operate a minimum of 10 years. To provide safety margin for ageing and other effects we set as requirement a minimum light yield 1.2 pe/mip/tile at production.

3.2 The WLS fibres

Four fibres are required to read out one side of each half-period. The total number of fibres required to build the 65 barrel and the 130 extended barrel modules is 640,000. In the barrel the length of the fibres ranges between 85 cm and 210 cm, depending on which cell is to be read and the location of the half-period. In the extended barrel the fibre length ranges from 90 cm to 230 cm. The total length of fibre required is 550 km for the barrel modules and 275 km for each extended barrel, which includes a 5% contingency, leading to 1120 km of fibre. WLS fibres, 1 mm in diameter, doped with a fast (< 10 ns decay time) shifter have been chosen as our baseline. Such fibres have been commercially available and produced by Kuraray, Japan.

Fig. 5 illustrates various steps during the optical instrumentation of the modules. The instrumentation of all TileCal modules is now completed.

4 Electronics

The overall design of the Tile Calorimeter read-out is simple and compact; all front-end and digitizing electronics are situated in the back-beam region of the calorimeters on a system of removable superdrawers (see Fig. 6) containing up to 45 PMTs. Phototube HVs are locally regulated. Pipelines and digitizers are located locally, and the digital information is transferred to the RODs in the counting room via optical fibres. Each cell of the Tile Calorimeter is read-out by two PMTs in order to provide redundancy in the light read-out and improve spatial uniformity. The total number of channels is approximately 10 000.

The design of the electronics read-out is constrained mainly by the available space, residual magnetic fields from the solenoid and toroids, and radiation. All of the Tile Calorimeter readout electronics are located inside the calorimeter modules, within the iron girders which also serve as the first level of magnetic shielding for the PMTs.

The remnant magnetic fields inside the drawers are not equal in every direction or location, butt hey are always below 20 Gauss. The most sensitive components, such as the PMTs and their individual HV regulation system, must be arranged or designed for these specific conditions in order to maintain a cell calibration accuracy of 1%.

Monte Carlo simulations of radiation levels show that the iron of the hadronic detector itself (and in addition the large amount of plastic tiles) considerably reduces radiation levels inside the girders. The maximum expected dose from 10 years operation at full luminosity is about 20 Gy.

The large iron mass of the Tile Calorimeter contributes also to the temperature stability inside the modules, but a dedicated cooling system must evacuate heat dissipated by the electronics, maintaining stable local temperatures to within 1°C.

Dynamic range From test beam results, we expect the photoelectron yield will be at least 50 pe/GeV. Detailed simulations have shown that at full luminosity, several events per year will deposit the equivalent of 1.5 TeV in a single cell, while energetic muons typically deposit 350 MeV in a single cell.This implies a 16 bit dynamic range for the Tile Calorimeter energy measurements. At the same time, the energy resolution of the Tile Calorimeter is such that an electronics precision of 10 bits is adequate to measure the largest signals.

4.1 PMT Blocks

The function of a PMT block is to convert light signals from the calorimeter cells into electronic signals. Each PMT block contains a photomultiplier tube, the light mixer which serves as the interface between the PMT and the fibre bundle, a high-voltage divider, and a 3-in-1 base which is the interface with the electronics read-out. The PMT block is installed in a dedicated hole inside a drawer.

The output of the PMT block is a shaped electronic signal which is subsequently digitized by electronics inside the superdrawer. The conversion of the light signal from the fibre bundles to electrical charge is done by the photomultipliers in the PMT blocks. Test beam studies indicate that a minimum gain of 10^5 is required to allow measurements of muons, which would deposit roughly 350 MeV in a single cell. At the same time, pulses coming from the highest energy particles must be measured without a saturation of the readout pipeline. Simulations have shown that, at full luminosity, several events per year are expected to deposit the equivalent of 1.5 TeV in a single cell. The commercially available PMT has been used as a baseline solution (Hamamatsu R5900).

4.2 Superdrawers

The superdrawer consists of two drawers. A drawer houses up to 24 PMT blocks, and supports electronics boards which are connected to each PMT block and provide the high voltage to the divider, the low voltages to the HV cards and the 3-in-1 card, and the control and calibration signals to the 3-in-1 card. They also contain electronics to process the signals coming from the shaper and the integrator. These electronics boards are arranged on the top and bottom sides of the drawers, with signal processing at the top and the HV distribution at the bottom.

4.3 Front-end electronics

The read-out electronics is divided into several parts. The front-end electronics is located on the 3-in-1 cards within the PMT Blocks described above. Here the current pulse from the PMT is shaped and converted to a voltage signal which is transmitted by short shielded cables to the fast digitizers located at one end of the Super Drawers. They receive services from the Mother Boards which run the length of the drawers. In order to meet the physics goals of ATLAS, it must be possible to measure particles which deposit a wide range of energies in the Tile Calorimeter. A dynamic range of 16 bits is needed to measure both minimum ionizing energy deposits from muons and deposits of up to 2 TeV in single cell from the highest energy jets. Since the intrinsic resolution of the calorimeter is less than 16 bits, it is desirable to compress the dynamic range and digitize the signals using ADCs with a resolution of 10 bits.

We use two linear outputs for each channel, differing in gain by a factor of 64. Each output covers a dynamic range of 10 bits and is linear in the charge of the input signal. In addition, provision has been made for an output for analog trigger summation.

The formation of analog sums for the LVL1 trigger towers is done on small printed circuit boards which form the third layer of the electronics drawer. Up to nine boards are needed in a Super Drawer. To reduce the amount of cabling, the boards are distributed over the length of the drawer close to the source of their five input signals. The output signal from each board is routed along this layer on a shielded twisted pair cable to the patch panel at the end of the drawer.

All integrators in a superdrawer are read-out sequentially by a single ADC. The ADC receives signals via an analog bus which runs along the entire length of the mother board, and each integrator is sequentially connected to the analog bus by closing a CMOS switch located on the 3-in-1 card. The analog bus consists of two lines (signal and ground) connected to an input differential amplifier on the ADC board in order to minimize common mode noise. Integrator digitization is performed on a separate board, which is mounted on the mother board.

4.4 Power supply and high voltage distribution

The Tile Calorimeter PMTs are supplied by a high voltage (HV) power supply system. The system reflects the division of the Tile Calorimeter into 256 submodules, which are electronically equivalent and independent. Each HV channel leads into the submodule drawer, where a special HV distributor supplies up to 48 PMTs. The HV distributor inside each submodule is able to set individual PMT voltages at up to 350 V below the supplied level. Only 2 HV power supply levels are needed to supply high voltages between 500V and 900V, including wide overlap regions. The source consists of two racks, each containing 8 crates. Each crate has 8 cards with 2 HV channels per card, and a communication and control unit.

The photomultipliers in each superdrawer are supplied by one channel of the high voltage main power source. To maintain all PMTs in the superdrawer at the same gain, each high voltage channel of the superdrawer must be individually controlled and regulated. This is done by the high voltage distributor in each superdrawer.

About 20 superdrawers have been produced up to now. Mass production will start in spring 2003.

5 Calibration and Performnance

The Tile Calorimeter Calibration consists of two main steps: PMT gain equalization using Cs radioactive source calibration system and setting the absolute electromagnetic scale for 1/8 of modules constructed.

5.1 Cs system

The Tile Calorimeter design includes the capability of running a 137Cs radioactive source along axial holes, through each scintillator tile, inside the rods compressing the calorimeter modules. This feature permits us to check the response of each scintillator tile. Furthermore, it is important to know how well the calorimeter tracks the source calibration. This is important in order to have confidence that the sample of production modules not exposed to beam will have performance characteristics as well known as those modules which were calibrated in a beam.

As the source is run through the holes, the average current produced by tile activation is integrated and recorded for the tile's respective PMT. The high voltage is then set such that the integrated current is the same for each group of scintillators coupled to a phototube.

The principle and results from the Cs runs are illustrated on Fig. 7.

5.2 Test beam program

The Tile Calorimeter test beam program was started in 1993. Since then it has evolved into a major collaborative ATLAS effort with not only the Tile Calorimeter group, but also in collaboration with the Liquid Argon (LAr) community. To this date, we can categorize the test beam setups as follows:

- Tile Calorimeter standalone measurements with a reduced scale prototype stack of five modules,
- Combined measurements with the LAr electromagnetic prototype and Tile Calorimeter prototype modules,

- Full scale barrel sector (Module 0) in standalone measurements.

- Final calibration of production modules.

The beam lines were instrumented in a standard fashion with one threshold Cherenkov counter used for p/e separation for GeV, a pair of wire chambers for both x and y coordinates, and scintillators to define a trigger. The scintillators defined a beam spot of around 2-3 cm, while the chambers allowed the reconstruction of the impact point on the calorimeter face to better than mm. Data were taken with muons, pions and electrons between 10 and 400 GeV. The momentum bite of the H8 beam,$\Delta p/p$, was always less than 0.5%. Recorded event rates evolved from about 150 per burst to todays value of 5000 per burst.

For the needs of the Tile Calorimeter a full simulation package has been developed based on the GEANT program which describes in full detail the detector prototypes that have been used for the test beam runs. A comparison between the test beam data of the Tile Calorimeter prototype modules and different hadronic shower simulation codes (FLUKA, GHEISHA, CALOR) in the framework of the GEANT program has been made.

An extensive program of beam tests has been carried out demonstrating the good performance of the calorimeter that fulfils the requirements for the ATLAS hadronic barrel calorimetry. Extensive tests with pions, electrons and muons have been undertaken with the prototype modules, from which we learned most of the features of the Tile Calorimeter described in the following sections. The performances of the first full-scale pre-series module for the barrel hadron calorimeter (Module 0) have also been investigated. Finally, we have shown that it is indeed possible to understand the response of an ATLAS wedge, taking data with the Liquid Argon test calorimeter upstream of the Tile Calorimeter in an almost projective geometry.

5.3 Modules calibration with particles

Since 2001 we are making calibartion of completed modules using electron beams of 10, 20, 100 and 180 GeV. Main aim of these tests is to set the absolute energy scale in the cells of the first and second longitudinal sampling of the calorimeter, where electrons deposit their energy. Calibration coefficients are then transported to other cells using Cs calibration results and special tests done with muons impinging the calorimeter modules at 90^o incident angle.

Many important results have been collected in past years. For illustration, the resolution of combined system of Liquid Argon and TileCal prototypes and module 0 are shown on Fig. 8. The energy resolution is compatible with a designed value of 50% for the stochastic term with relatively small constant term which is caused by the non-compensated nature of the Tile Calorimeter.

Other results have been published about development of hadronic showers and reconstruction of hadron energy [3], Tile Calorimeter response to muons [4], energy losses of high energy muons [5] and from the combined tests [6] and in many internal notes.

6 Conclusions

The Tile Calorimeter project is in an advanced stage. All modules have been produced and instrumented with the optical elements. The modules have been calibrated using particles beam at CERN. The preassembly of the first cylinder has started. Works now concentrate towards the mass production of electronics drawers and to the integration of the Tile Calorimeter into the ATLAS detector environment. The installation of the Tile Calorimeter in the ATLAS cavern will start in 2004.

References

[1] ATLAS Collaboration, ATLAS Technical Proposal, report CERN/LHCC/94–43.

[2] F. Ariztizabal et al., Nucl. Instrum. Methods A349 (1994) 384.
E. Berger et al., report CERN/LHCC 95–44.
Atlas Collaboration, Tile Calorimeter TDR, CERN/LHCC 96-42.

[3] P. Amaral et al., NIM A 443 (2000) 51-70.
S. Akhmadaliev et al., NIM A 480 (2002) 508-523.

[4] Z. Ajaltouni et al., NIM A 388 (1997) 64-78.

[5] E. Berger et al., Z. Phys. C 73 (1997) 455.
P. Amaral et al., Eur. Phys. J. C 20 (2001) 3, 487-495.

[6] Z. Ajaltouni et al., NIM A 387 (1997) 333-351
S. Akhmadaliev et al., NIM A 449 (2000) 461-477.

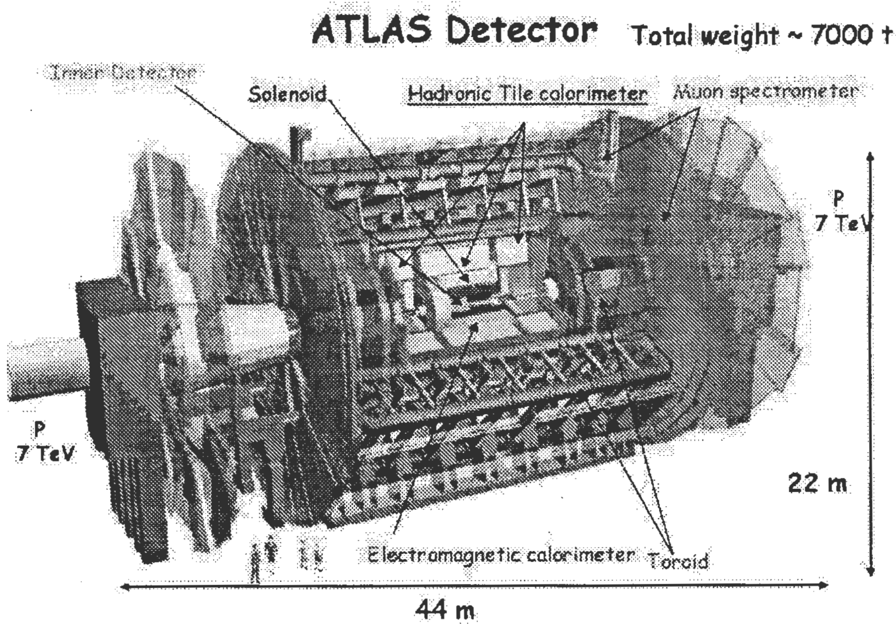

Fig. 1: The ATLAS detector.

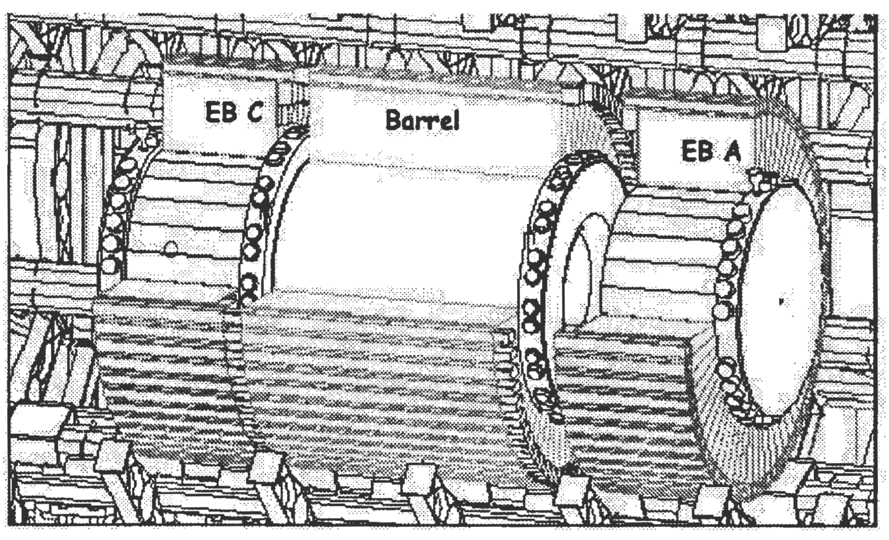

Fig. 2: The three cylindres of the TileCal subdetector.

Fig. 3: Therteen modules of the TileCal assembled.

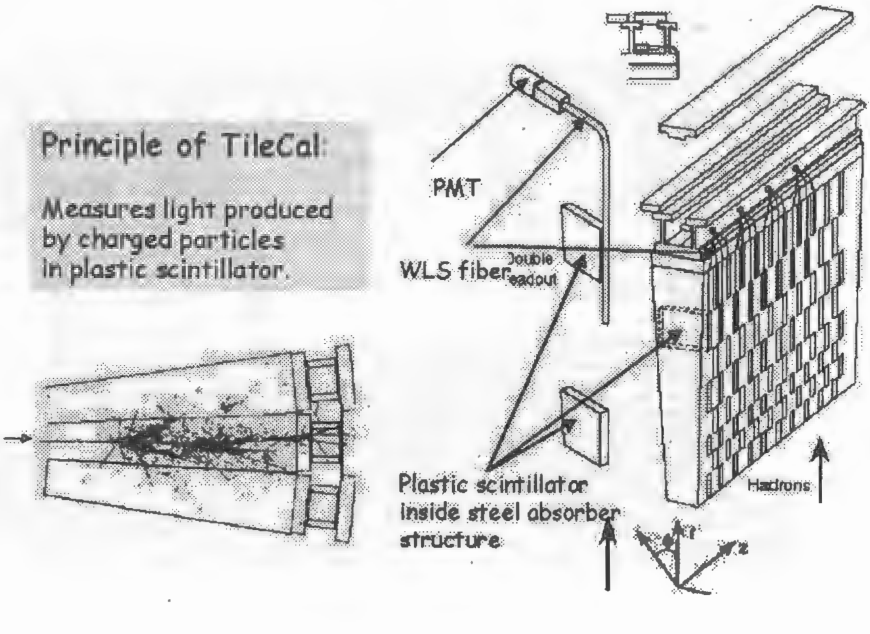

Fig. 4: The principle of the TileCal.

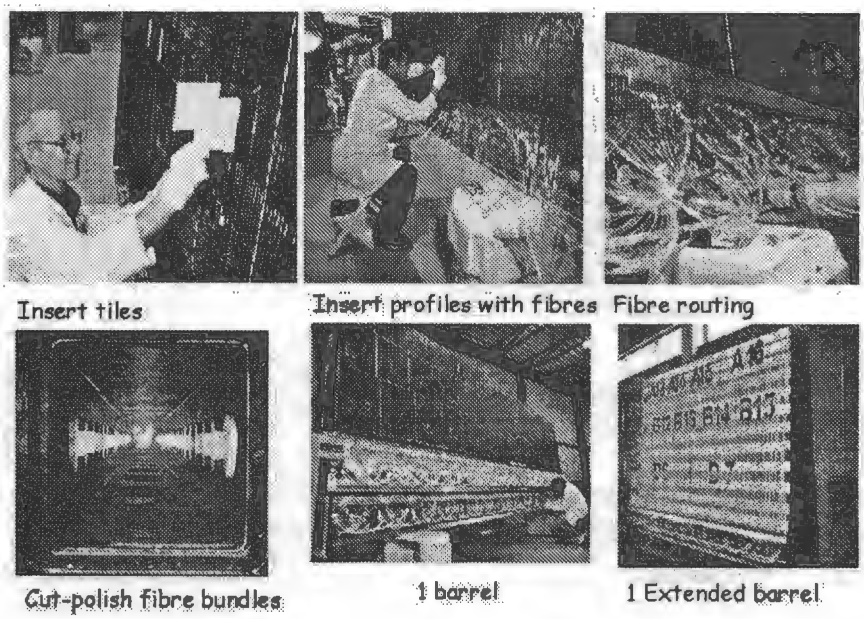

Fig. 5: Various steps of the TileCal instrumentation.

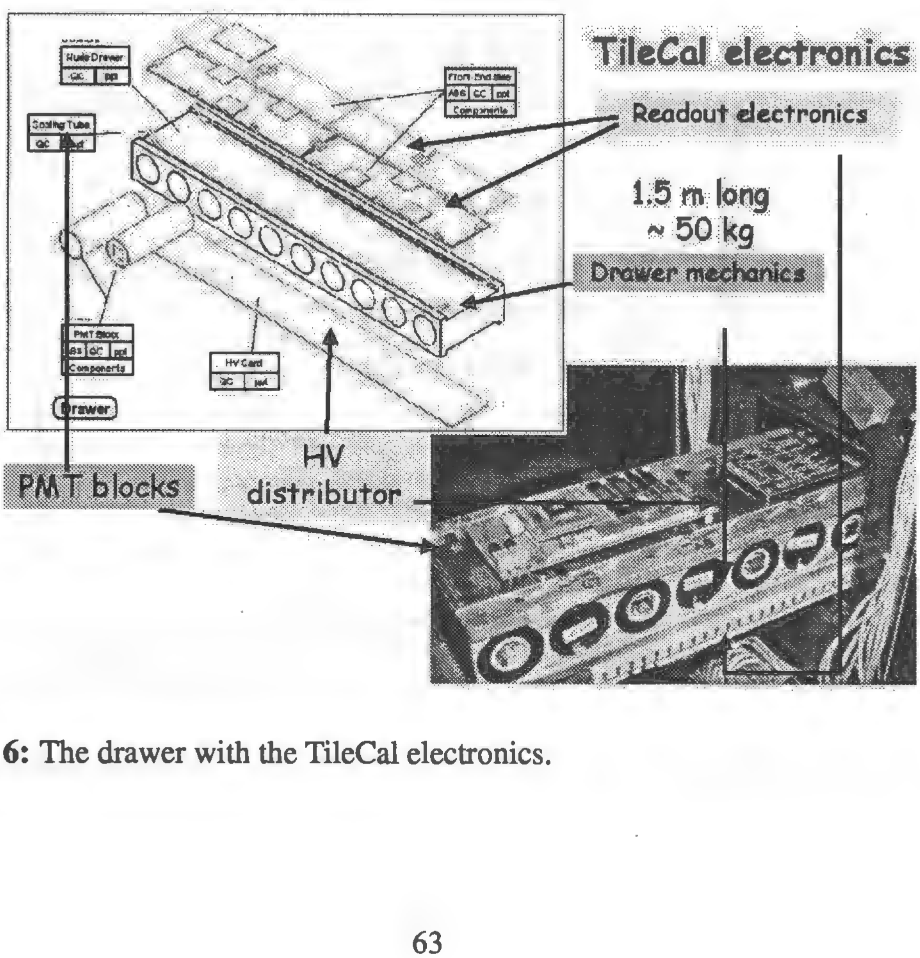

Fig. 6: The drawer with the TileCal electronics.

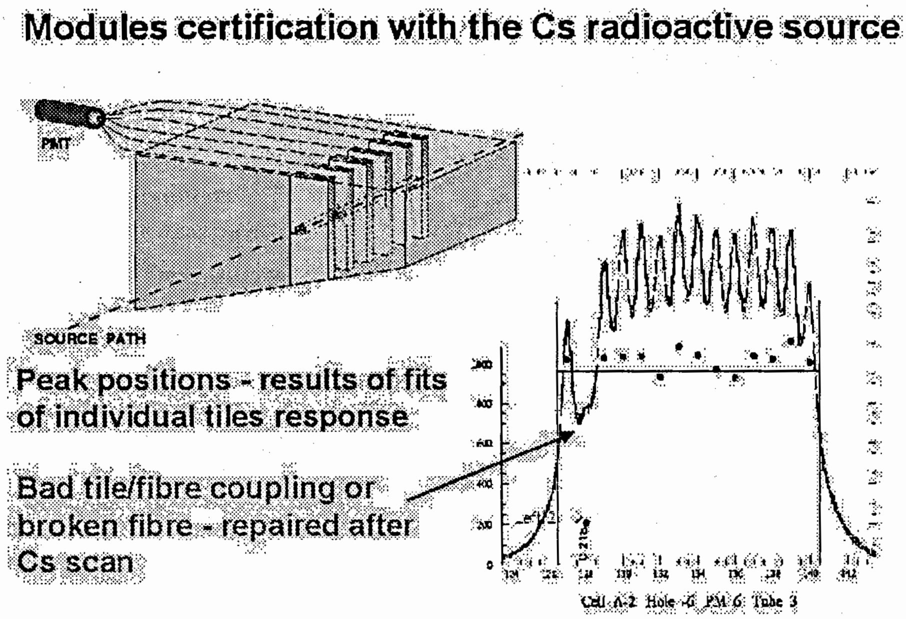

Fig. 7: Certification of modules using Cs radioactive source.

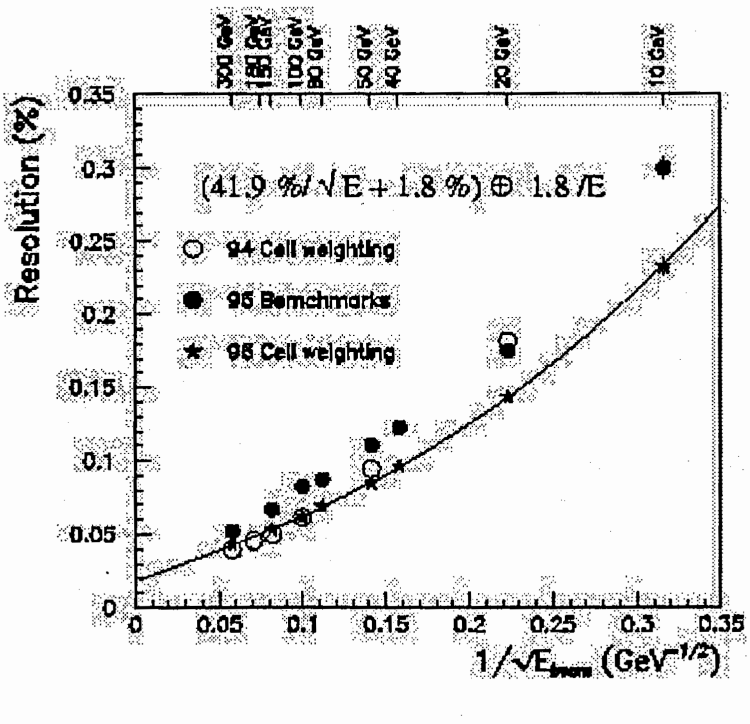

Fig. 8: Hadron energy resolution from the LAr and TileCal combined tests.

Soft and Hard Interactions in $p\bar{p}$ Collisions at $\sqrt{s} = 1800$ and 630 GeV

Presented by
F. Rimondi
for the CDF Collaboration

Abstract

We present a study of $p\bar{p}$ collisions at $\sqrt{s} = 1800$ and 630 GeV collected using a minimum bias trigger by the CDF experiment in which the data set is divided into two classes corresponding to "soft" and "hard" interactions. For each sub-sample, the analysis includes measurements of the multiplicity, transverse momentum (p_T) spectrum, and the average p_T and event-by-event p_T dispersion as a function of multiplicity. A comparison of results shows distinct differences in the behavior of the two samples as a function of the center of mass (CM) energy. We find evidence that the properties of the *soft* sample are invariant as a function of CM energy.

I. INTRODUCTION

Hadron interactions are often classified as either "hard" or "soft" [1, 2]. Although there is no formal definition for either, the term "hard interactions" is typically understood to mean high transverse energy (E_t) parton-parton interactions associated with such phenomena as high E_t jets, while the soft component consists of everything else. Whereas perturbative QCD provides a reasonable description of high E_t jet production, there is no equivalent theory for the low E_t multi-particle production processes that dominate the inelastic cross section. Some QCD inspired models [2] attempt to describe these processes by the superposition of many parton interactions extrapolated to very low momentum transfers. It is not known, however, if these or other collective multi-parton process is at work.

The study of low-E_t interactions usually involves collecting data using minimum bias (MB) triggers, which, ideally, sample events in fixed proportion to the production rate — in other words, in their "natural" distribution. Lacking a comprehensive description of the microscopic processes [3] involved in low-E_t interactions, our knowledge of the details of low transverse momentum (p_T) particle production rests largely upon empirical connections between phenomenological models and data collected with MB triggers at many center-of-mass (CM) energies. Such comparisons are further complicated by the difficulty in isolating events of a purely "soft" or purely "hard" nature.

This paper adopts a novel approach in addressing this issue using samples of $p\bar{p}$ collisions at $\sqrt{s} = 1800$ and 630 GeV collected with a MB trigger. The analysis first divides the full minumum bias samples into two sub-samples, one highly enriched in soft interactions, the other relatively depleted of soft interactions. We then compare inclusive distributions and final state correlations between the sub-samples and as a function of CM energy in order to gain insights into the mechanisms of particle production in soft interactions. The results in the isolated soft sample exhibit some interesting properties, in particular an unpredicted invariance with CM energy. The results presented in this talk are published in [4].

II. DATA SET AND EVENT SELECTION

Data samples have been collected with the CDF detector at the Fermilab Tevatron Collider. The CDF apparatus has been described elsewhere [5]; here only the parts of the detector utilized for the present analysis are discussed.

Data at 1800 GeV were collected with a minimum bias trigger during Run 1A and 1B, and at 1800 and 630 GeV during Run 1C. This trigger requires coincident hits in scintillator counters located at 5.8 m on either side of the nominal interaction point and covering the pseudo-rapidity ($\eta = -\log(\tan(\theta/2))$ where θ = angle with respect to the proton direction) interval $3.2 < |\eta| < 5.9$, in coincidence with a beam-crossing signal.

The analysis uses charged tracks reconstructed within the Central Tracking Chamber (CTC). The CTC is a cylindrical drift chamber covering a η interval of about three units with full efficiency for $|\eta| \leq 1$ and $p_T \geq 0.4$ GeV/c.

Inside the CTC inner radius, a set of time projection chambers (VTX) [6] provides r-z tracking information out to a radius of 22 cm for $|\eta| < 3.25$. The VTX is used in this analysis to find the z position of event vertices, defined as a set of tracks converging to the same point along the z-axis. Reconstructed vertices are classified as either "primary" or "secondary" based upon a combination of the number of tracks pointing to the vertex and the forward-backward symmetry of these tracks. High multiplicity vertices with highly symmetric topologies are considered to be primaries; low multiplicity, highly asymmetric vertices are classified as secondaries.

The transverse energy flux was measured by a calorimeter system [7] covering from -4.2 to 4.2 in η.

The 1800 GeV data sample consists of sub-samples collected during three different time periods. Approximately 1,700,000 events were collected in run 1A at an average luminosity of 3.3×10^{30} s^{-1}cm^{-2}, 1,500,000 in run 1B at an average luminosity of 9.1×10^{30} s^{-1}cm^{-2} and 106,000 in run 1C at an average luminosity of 9.0×10^{30} s^{-1}cm^{-2}. The 630 GeV data set consists of about 2,600,000 events recorded during run 1C at an average luminosity of 1.3×10^{30} s^{-1}cm^{-2}.

Additional event selection conducted offline removed the following events: (i) events identified as containing cosmic-ray particles as determined by time-of-flight measurements using scintillator counters in the central calorimeter; (ii) events with no reconstructed tracks; (iii) events exhibiting symptoms of known calorimeter problems; (iv) events with at least one charged particle reconstructed in the CTC to have $p_T > 400$ MeV/c, but no central calorimeter tower with energy deposition above 100 MeV; (v) events with more than one primary vertex; (vi) events with a primary vertex more than 60 cm away from the center of the detector (in order to keep full tracking efficiency in the CTC and avoid energy leakage through exposed cracks in the calorimeter); (vii) events with no primary vertices.

After all event selection cuts, 2,079,558 events remain in the full minimum bias sample at $\sqrt{s} = 1800$ GeV (runs 1A + 1B + 1C), and 1,963,157 in that at $\sqrt{s} = 630$ GeV (run 1C).

The vast majority of rejected events failed the vertex selection. About 0.01% of selected events contain background tracks from cosmic rays that are coincident in time with the beam crossing and pass near the event vertex. The residual beam gas contamination is about 0.02%.

Section VI. discusses the systematic uncertainties that arise from the event selection criteria and other sources.

III. TRACK SELECTION

Reconstructed tracks within each event must pass selection criteria designed to remove the main sources of background. Tracks must pass through a miniumum number of layers in the CTC, and have a minimum number of hits in each superlayer in order to reduce the number of tracks with reconstruction errors. Fake and secondary particle tracks are removed by requiring that tracks pass within 0.5 cm of the beam axis, and within 5 cm along the z-axis of the primary event vertex. Accepting only tracks with $p_T \geq 0.4$ GeV/c and within $|\eta| \leq 1.0$ ensures full efficiency and acceptance.

We define the charged track multiplicity in an event, $N^{\star}_{ch}$, as the number of selected CTC tracks in the event. The mean p_T of the event is defined as:

$$\bar{p}_T = \frac{1}{N^{\star}_{ch}} \sum_{i}^{N^{\star}_{ch}} p_{T_i} \qquad (1)$$

unless stated otherwise.

IV. SELECTION OF *SOFT* AND *HARD* INTERACTIONS

The identification of "soft" and "hard" interactions is largely a matter of definition [8]. In this analysis we use a jet reconstruction algorithm to distinguish between the two classes. The algorithm employs a cone with radius $R = (\Delta\eta^2 + \Delta\phi^2)^{1/2} = 0.7$ to define "clusters" of calorimeter towers belonging to the jet. To be considered, a cluster must have a transverse energy (E_T) of at least 1 GeV in a seed tower, plus at least 0.1 GeV in an adjacent tower.

In the regions $|\eta| < 0.02$ and $1.1 < |\eta| < 1.2$, a track clustering algorithm is used instead of the calorimeter algorithm in order to compensate for energy lost in calorimeter cracks. A track cluster is defined as one track with $p_T > 0.7$ GeV/c and at least one other track with $p_T \geq 0.4$ GeV/c in a cone of radius $R = 0.7$.

We define a *soft* event as one that contains no cluster with $E_T > 1.1$ GeV. All other events are classified as *hard.*

V. EFFICIENCY CORRECTIONS

The track reconstruction efficiency for the CTC has been investigated for several different analyses and under various conditions at CDF [9, 10, 11]. For this analysis, we have calculated a full-event track reconstruction efficiency using a parametric MC sample. Version 5_7 of the Pythia generator was used with the minimum bias configuration tuned to match the inclusive multiplicity and p_T distributions of the 1800 GeV sample. For each inclusive distribution, a track finding efficiency correction was computed by taking the ratio of the Pythia generated distribution to the corresponding distribution from tracks traced through the apparatus. The efficiency for reconstructing the correct event charged multiplicity is about 95% up to a multiplicity of about 20, falling to about 85% at multiplicities above about 20.

The same Pythia MC sample was used to evaluate the background from gamma ray conversions, charged and neutral particle decays. Correction factors due to these effects have been computed as a function of track p_T and the event multiplicity.

There exists a small contamination from diffractive events even in the restricted region of phase space examined in this study. We have evaluated this contamination with a special Pythia MC run in which only the diffractive generation algorithm was switched on. The data were then subjected to the full event and track selection procedure. The correction for this effect is estimated to be about 5% in the zero multiplicity bin, decreasing rapidly to zero for $N^{\star}_{ch} \sim 4$. In the p_T distribution, the correction is between zero and 1% up to about 1 GeV/c.

VI. SYSTEMATIC UNCERTAINTIES

Several sources of systematic errors have been investigated. The effect of each on the final distributions is discussed below.

- Vertex selection. As discussed in Section II., the vertex selection classifies vertices as either "primary" or "secondary". The standard selection demands that primary vertices be highly isolated. Mis-classification or identification of vertices can strongly influence the p_T and multiplicity distributions, particularly the latter. We set conservative bounds on the magnitude of this effect in the following way. Two samples of events are selected. In one, all vertices except the highest quality one are classified as secondaries. In the other sample, all vertices are classified as primary. Compared to results obtained using the standard vertex selection, the ratio of the multiplicity distribution at $\sqrt{s} = 630$ to that at 1800 GeV varies by about 5% in the region between a multiplicity of two and 11, and reaches 40% for multiplicities in excess of 22. The deviation in the ratio of p_T distributions at the two energies is almost constant at about 10% up to a p_T around 11 GeV/c, increasing to 15% as p_T increases.

- Vertices in some multiple interaction events remain unresolved and introduce a residual luminosity-dependent contamination. We estimate the systematic uncertainty from this source by comparing the results of the complete analysis on two sub-samples of data, one at low luminosity ($< 1.5 \times 10^{30} cm^{-2}s^{-1}$) and the other at high luminosity ($> 7 \times 10^{30} cm^{-2}s^{-1}$). Differences range between 2% and 6% for multiplicities less than 20, increasing to about 16% for multiplicities in the range $20 < N^{\star}_{ch} < 30$, and to 45% for multiplicities greater than 30. The effect on the ratios of the various distributions is negligible.

- The selection of events identified with known calorimeter problems depends upon thresholds applied to classify the anomalous behavior. This selection removes $\lesssim$1% of the total sample. Changing the rejection factor causes no appreciable change in the distribution ratios.

- Tracking efficiencies evaluated at CDF under various conditions and using different techniques obtain results that differ by as much as 8–10% in the low p_T (below 1 GeV/c), high p_T (above 2 GeV/c) or high multiplicity regions. The impact of using widely different efficiency corrections on the multiplicity and p_T distributions is – at most – as large as the statistical uncertainty. The effect on the distribution ratios is negligible.

- The systematic uncertainty due to the correction for gamma conversions, secondary particle interactions and particle decays is estimated to be about 1%, almost independent of multiplicity and p_T . The effect on the ratios of distributions is negligible.

- The systematic uncertainty in the correction to the multiplicity distribution due to contamination from diffractive production is on the order of 1%, and limited to the very low multiplicities

($0 \leq N^*_{ch} \leq 3$). No correction was applied to the p_T distribution, where the magnitude of the effect was less than 1% for all p_T . The effect is neglibible on the distribution ratios.

The systematic uncertainty from the vertex selection dominates all other sources. The curves on the final inclusive distribution ratios are obtained as the ratios of the distributions originated by the extreme selections outlined above. They are not intended as point-to-point systematic uncertainties, but are included in the figures to show the approximate range over which the shape of the final distribution may be changed by altering the vertex selection.

Systematic effects cancel in the ratios of final state correlations (see Section B. and C.).

VII. DATA ANALYSIS

A. Inclusive Distributions

We first examine the inclusive multiplicity and transverse momentum distributions. Fig. 1a shows the multiplicity distributions for the full MB samples at 1800 and 630 GeV, plotted in KNO variables [12]. The distributions at the two energies show a weak violation of KNO scaling, as it is expected in a

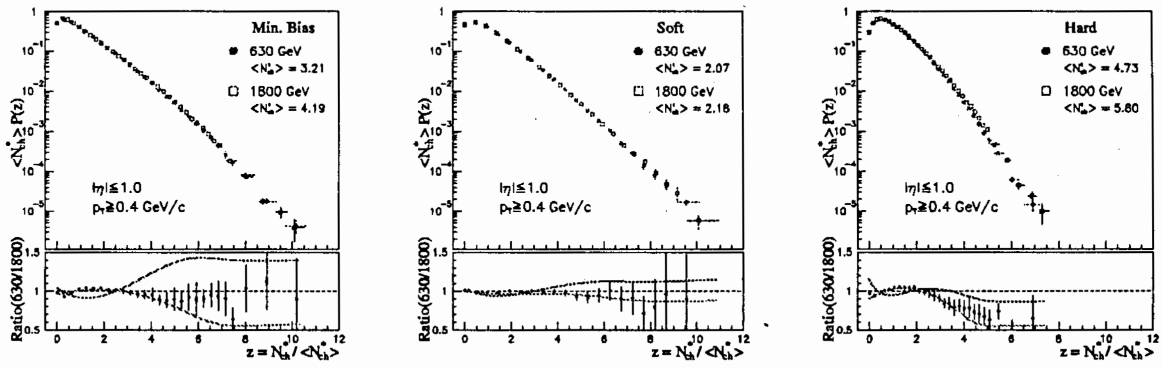

Figure 1: Multiplicity distributions at 1800 and 630 GeV for a) the full MB samples (left), b) the soft samples (center) and c) the hard samples (right); data are plotted in KNO variables. In the bottom panel the ratio of the two above distributions is shown. The two continuous lines delimit the band of all systematic uncertainties (see section II. of text).

limited phase space region [13]. The same comparison is made in Figs. 1b and 1c for the soft and hard samples separately. The ratio of the multiplicity distributions at the two energies are plotted at the bottom of Fig. 1.

Transverse momentum distributions at the two energies are shown in Fig. 2a for the full MB sample. Fig. 2b and Fig. 2c show the same distributions for the "soft" and "hard" sample, respectively. As for the multiplicity distributions, the ratios of the distributions at the two energies are shown in the bottom of these figures. The p_T spectrum in the soft sample falls more rapidly with increasing p_T than that of the hard sample. This difference is expected and reflects the absence of events with high p_T jets in the soft sample.

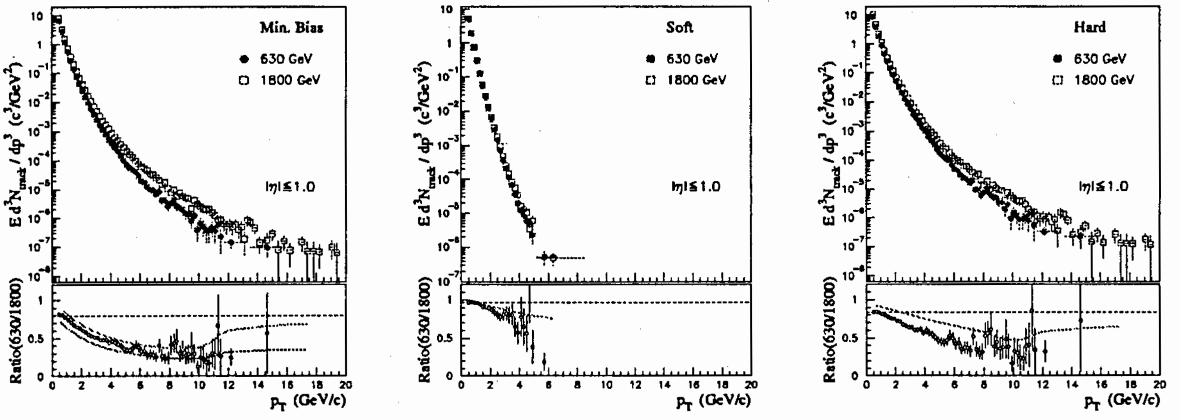

Figure 2: Transverse momentum distributions at 1800 and 630 GeV for a) the full MB samples (left), b) the soft samples (center) and c) the hard samples (right). In the bottom panel the ratio of the two distributions is shown. The two continuous lines delimit the band of all systematic uncertainties (see section II. of text). N_{track} refers to the number of charged tracks in a unit η interval.

A deeper insight into the dynamics of the interactions can be gained by comparing the p_T distributions for *fixed* charged multiplicity as a function of $\sqrt{s}$. Fig. 3 shows fixed-multiplicity p_T distributions for the full MB sample at the two energies superimposed.

The same distributions are plotted in Figs. 4 and 5 for the soft and hard sub-samples, respectively. For brevity, only multiplicities of 1, 5, 10 and 15 are shown.

We observe that, within uncertainties, the p_T distributions for a given multiplicity are the same at $\sqrt{s}$ equal to 1800 and 630 GeV — they are CM energy invariant. None of the current models predict or suggest such an invariance. The result suggests that in purely soft interactions the number of produced (charged) particles is the only global event variable changing with $\sqrt{s}$. The particle multiplicity may also fix other event properties independently of the energy of the reaction.

A further observation is worth noting. It is known that for minimum bias samples, the slope of the inclusive p_T distribution increases steadily by some power of $\log s$ up to Tevatron energies [9, 14]. Such an increase is also visible for p_T distributions at fixed multiplicity for the full MB sample shown in Fig. 3. The result of the present analysis implies that the $\sqrt{s}$ dependence in the slope of the p_T distribution of the soft sample is due entirely to the change in the mean multiplicity. In contrast, the more pronounced change in the shape of the full MB and the hard samples as a function of $\sqrt{s}$ must be caused in part by the increasing cross section of hard parton interactions.

B. Dependence of Mean Track p_T on Charged multiplicity

The correlation between mean p_T and charged multiplicity was first observed by UA1 [15], and then investigated at ISR [16] and Tevatron Collider energies [14, 17]. Although several different theoretical explanations have been proposed, such as geometrical models [18], thermodynamical models [19] and contributions from semihard parton scattering (*minijets*) [20], none provide satisfactory predictions for existing experimental results, leaving the real origin of the effect unexplained. Simulations performed

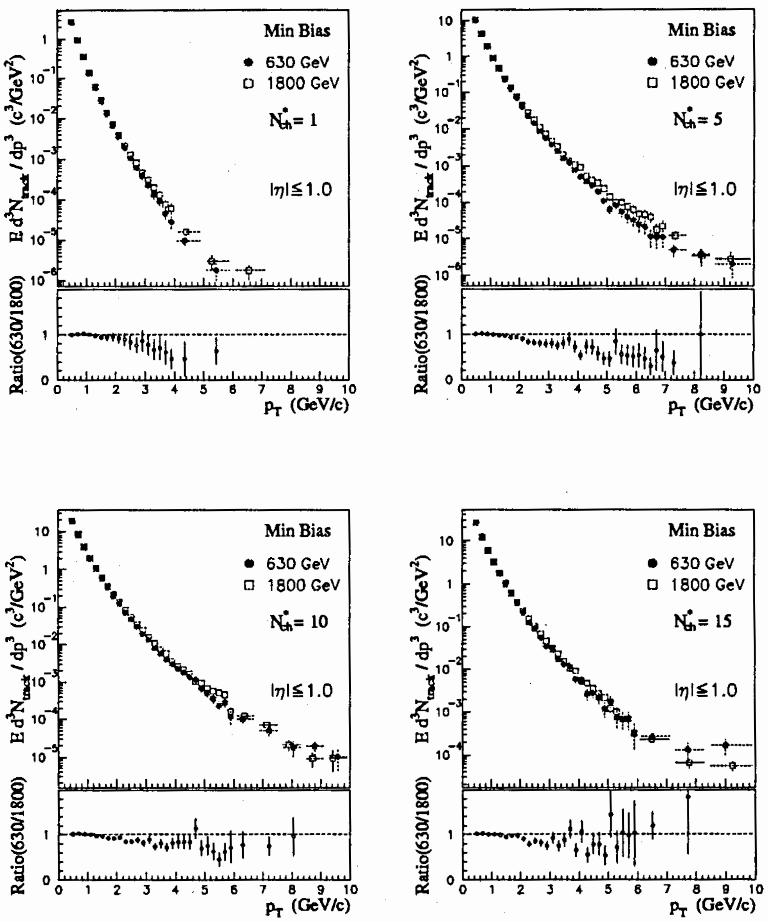

Figure 3: Transverse momentum distributions at fixed multiplicity (multiplicity = 1, 5, 10, 15) for the full MB samples at 1800 and 630 GeV. At the bottom of each plot the ratio of the two above distributions is shown. Error bars represent statistical error only. Systematic error was found to be negligible and is not included.

with Pythia and Herwig generators do not show better agreement with data (see Fig. 6) [21]. In this analysis the mean p_T (to be distinguished from the mean event p_T) is obtained by summing the p_T of all reconstructed charged tracks in all events with a given charged multiplicity, then dividing by the number of such tracks. The results are shown in Fig. 7a for the full minimum bias sample at the two analysed energies, and in Figs. 7b and 7c for the *soft* and for the *hard* samples, respectively.

The event multiplicity is smeared by track finding inefficiency. We correct the data points for the average track finding efficiency at each multiplicity.

The mean p_T as a function of multiplicity for the soft sample (Fig. 7b) is nearly identical at the two energies. This invariance is a direct consequence and a confirmation of the invariance of the soft p_T spectra at fixed multiplicities noted in the previous section.

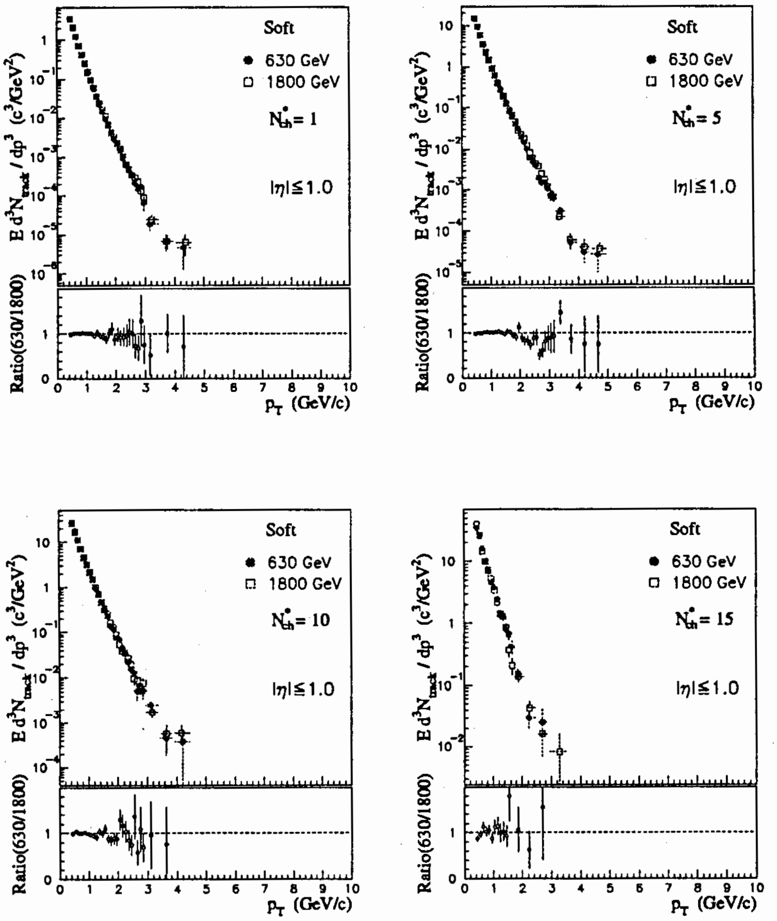

Figure 4: Same as Fig. 3 for the *soft* samples.

Comparing Figs. 7b and 7c , we note a clear difference in the mean p_T correlation of the *soft* and *hard* samples. Interestingly, the mean p_T increases at low multiplicity even in the soft sample, which should be highly depleted in high E_t events. This observation suggests that an increasing contribution from hard gluon production, as proposed in Ref. [20], is at least not the only mechanism responsible for the correlation at low multiplicity.

C. $\langle p_T \rangle_{ev}$ Dispersion versus multiplicity

Event-by-event fluctuations of the mean event p_T have been shown to be a useful tool to investigate the collective behavior of soft multi-body production, and has been used to analyze experimental data in various different ways[22, 23, 24]. Following the approach of [22], the dispersion, D_m, of the mean event p_T for events with multiplicity m is defined as:

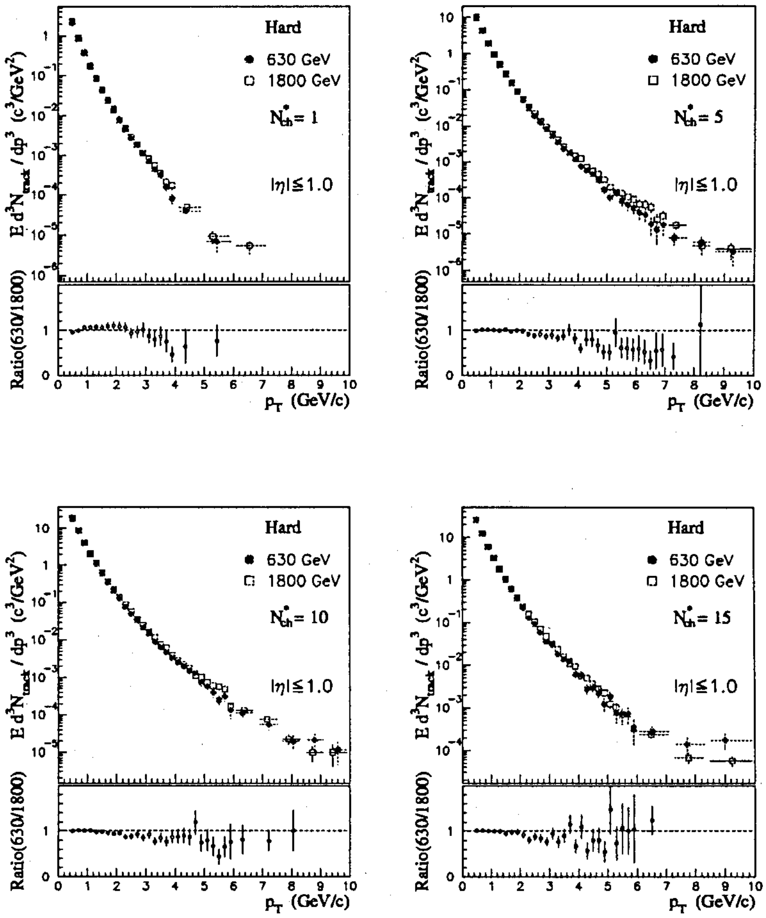

Figure 5: Same as Fig. 3 for the *hard* samples.

$$D_m\left(\bar{p}_T\right) = \frac{\langle \bar{p}_T^2 \rangle_m - \langle \bar{p}_T \rangle_m^2}{\langle p_T \rangle_{sample}} \tag{2}$$

Brackets $\langle\rangle$ indicate an average over all events with the given multiplicity m, while $\bar{p}_T$ is the mean event p_T from Eq. 1.

The dispersion is expected to decrease with increasing multiplicity and to converge to zero when $m \to \infty$ if only statistical fluctuations are present. Conversely, an extrapolation to a non-zero value would indicate the presence of non-statistical fluctuations in $\bar{p}_T$ from event to event. This indeed is what was found in [22] and, in different ways, in Refs. [23] and [24]. Large non-statistical fluctuations of the mean event p_T are a consequence of particle correlations in the multi-body final state [25]. Fig. 8a shows the present measurement of the dispersion as a function of the inverse multiplicity for the full minimum bias samples.

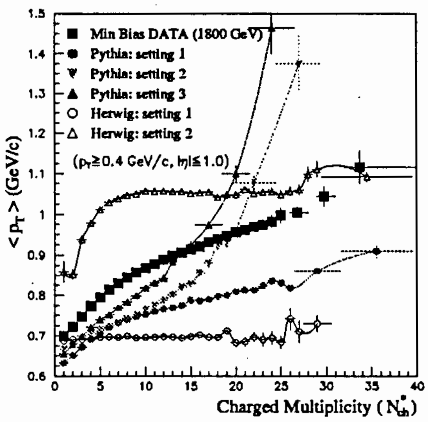

Figure 6: Mean transverse momentum vs multiplicity from MonteCarlo. The different parameter settings for each MC generator are given in the appendix.

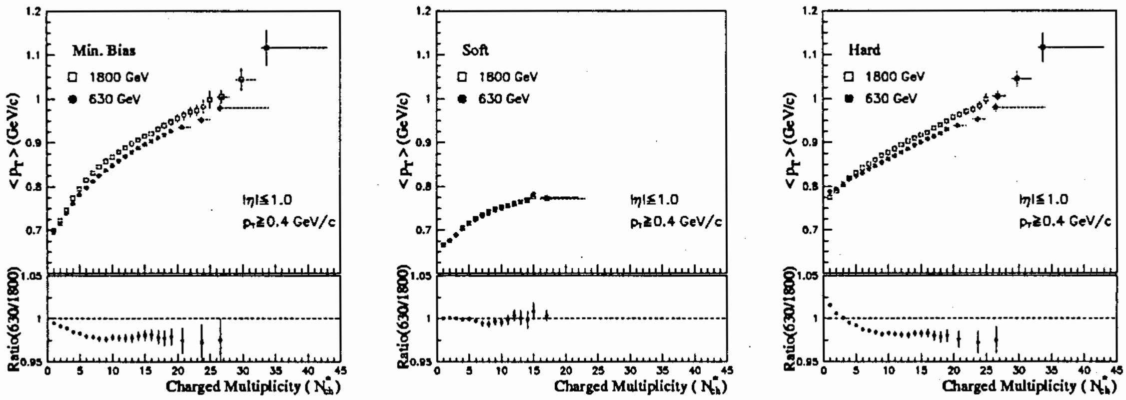

Figure 7: Mean transverse momentum vs multiplicity at 1800 and 630 GeV for a) the full MB samples (left), b) the soft samples (center) and c) the hard samples (right). On the bottom the ratio of the two curves is shown.

The correlation curve has a slope that varies across multiplicities, particularly at $\sqrt{s} = 1800$ GeV. The dispersion versus inverse multiplicity for the soft and hard samples, shown in Figs. 8b and 8c, confirms that this effect is related to the contribution of jet production which, as discussed in [26], increases event-by-event fluctuations. The plots show only statistical uncertainties.

Comparing our soft sample results with the full MB results of Ref. [22], where hard jet production has a much lower cross section than at Tevatron energies, we note that our points, unlike those in Ref. [22], drop at high multiplicity (multiplicity $\gtrsim 7$). Since statistical fluctuations vary linearly with the multiplicity, the drop we observe indicates that final state particle correlations change with multiplicity. Moreover the results plotted in Fig. 8b are consistent with an extrapolation to zero at infinite multiplicity. These observations support the idea that asymptotically the event mean p_T has

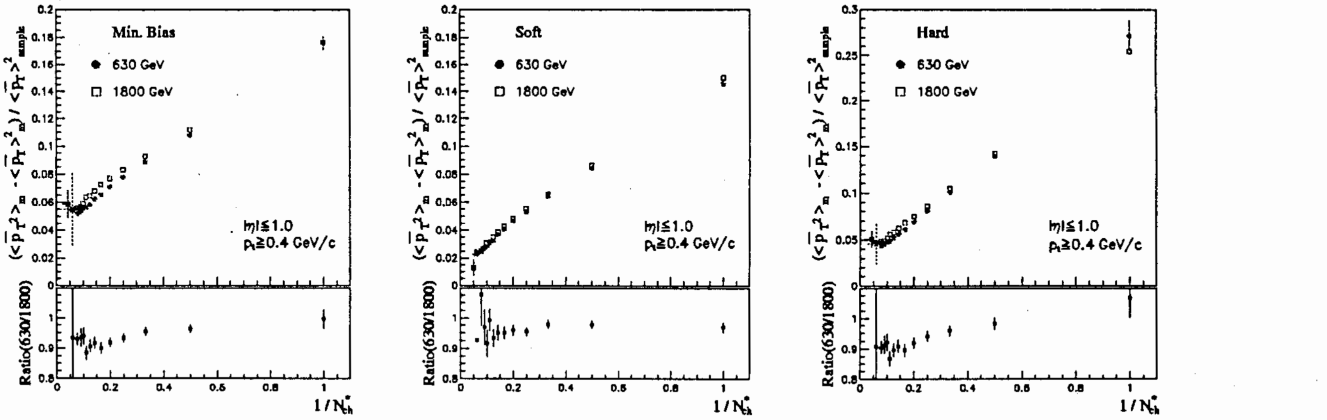

Figure 8: Dispersion of the mean event p_t as a function of the inverse multiplicity at 1800 and 630 GeV for a) the full MB samples (left), b) the soft samples (center) and c) the hard samples (right). At the bottom the ratio of the two curves is shown.

no dynamical fluctuations [1].

Finally, the dispersion as a function of the inverse multiplicity for the soft samples has a constant ratio at the two energies, a fact which is not true for the hard samples.

VIII. CONCLUSIONS

Assuming that hard parton interactions in $\bar{p}p$ scattering eventually develop into final state particles observable as clustered within jet cones, and pushing the cluster identification threshold as low as possible, we separate minimum bias events into sub-samples enriched in soft or hard collisions. Comparing the behavior of the two samples at two energies, we obtain the following results.

- The multiplicity distributions of "soft" interactions follow KNO scaling going from $\sqrt{s} = 630$ to 1800 GeV. This is not true for those of the "hard" sub-sample. The p_T distribution at fixed multiplicity in the "soft" sample is also energy invariant, a property which was unexpected. By this, we mean that the momentum distribution in the soft sample is determined only by the number of charged particles in the final state, independently of the center of mass energy.

- The mean p_T as a function of the charged multiplicity in the soft samples scales remarkably well with energy. In addition, the mean p_T increases with multiplicity even in the soft sample where hard parton interactions are at most strongly suppressed. Neither feature is predicted by current theoretical or phenomenological models.

- The dispersion of the $\langle p_T \rangle_{ev}$ shows a non-linear dependence on the inverse multiplicity, an observation not previously reported. The rise at multiplicity greater than ~10 is essentially due to the presence of hard parton interactions.

[1] It has been observed [27] that this method cannot exclude the possibility of opposite sign correlations that perfectly cancel each other.

In the same multiplicity region, the slope of the dispersion in the soft sample extrapolates to zero at infinite multiplicity. This means that asymptotically there are no dynamical correlations in the event mean p_t. The ratio of the dispersion in the soft sample at the two energies is flat as a function of multiplicity, a feature not exhibited by the hard sample.

All the distributions and correlations studied using the soft sub-sample are compatible with the hypothesis of invariance with the center of mass energy, which is a new result. We conclude that the dynamical mechanism of inelastic multiparticle production in soft interactions, at least in this energy interval, is invariant with center of mass energy, and that the properties of the final state are determined only by the number of (charged) particles.

References

[1] R. Ansari *et al.*, Z. Phys. **C36** 175 (1987); X. Wang and R. C. Hwa, Phys. Rev. **D39** 187 (1989); UA1 Collaboration, F. Ceradini, Bari Europhys. High Energy 1985:0363.

[2] T. Sjöstrand and M. van Zijl, Phys. Rev. **D36** 2019 (1987), and references therein.

[3] A summary of the references to these models can be found in [2].

[4] D. Acosta *et al.* Phys. Rev. **D65**, 072005 (2002).

[5] F. Abe *et al.*, Nucl. Instrum. Methods **A271** 387 (1988), and references therein.

[6] F. Snider *et al.*, Nucl. Instrum. Methods **A268** 75 (1988).

[7] F. Balka *et al.*, Nucl. Instrum. Methods **A267** 272 (1988); S. R. Hahn *et al.*, *ibid.* **A267** 351 (1988); K. Yasuoka *et al.*, *ibid.* **A267** 315 (1988); R. G. Wagner *et al.*, *ibid.* **A267** 330 (1988); T. Devlin *et al.*, *ibid.* **A267** 24 (1988); S. Bertolucci *et al.*, *ibid.* **A267** 301 (1988); Y. Fukui *et al.*, *ibid.* **A267** 280 (1988); S. Cihangir *et al.*, *ibid.* **A267** 249 (1988); G. Brandenburg *et al.*, *ibid.* **A267** 257 (1988).

[8] F. Abe *et al.*, Phys. Rev. **D56** 3811 (1997); Phys. Rev. Lett. **79** 584 (1997);
X.Wang, Phys. Rev. **D46** 1900 (1992);
UA1 Collaboration, C.Albajar *et al*, Nucl. Phys. **B309** 405 (1988).

[9] F. Abe *et al.*, Phys. Rev. Lett. **61** 1819 (1988).

[10] F. Abe *et al.*, Phys. Rev. Lett. **76** 2015 (1996).

[11] F. Abe *et al.*, Phys. Rev. **D58** 072001 (1998).

[12] Z.Koba, H.B.Nielsen and P.Oleson, Nucl. Phys. **B40** 317(1972).

[13] UA5 Collaboration, R.E. Ansorge *et al.*, Z.Phys. **C43** 357 (1989); K. Alpgard *et al.*, Phys. Lett. **B121** 209 (1983).

[14] E735 Collaboration, T.Alexopoulos *et al.*, Phys. Lett **B336** 599 (1994); Phys. Rev. Lett. **60** 1622 (1988);
N.Moggi, Nucl. Phys. Proc. Suppl. **B71** 221 (1999).

[15] UA1 Collaboration, G. Arnison *et al.*, Phys. Lett. **B118** 167 (1982).

[16] A.Breakstone *et al.*, Phys. Lett. **B132** 463 (1983); Phys. Lett. **B183** 227 (1987); Z.Phys.Phys. **C33** 333 (1987).

[17] E735 Collaboration, T. Alexopoulus, Phys. Rev. **D48** 984 (1993);
S.H. Oh, Nucl. Phys. Proc. Suppl. **B25** 40 (1992).

[18] S. Barshay, Phys.Lett. **B127** 129 (1983).

[19] L.Van Hove, Phys. Lett. **B127** 138 (1982); R. Hagedorn, Rev Nuovo Cim. **6** 10 (1983); J.D.Bjorken, Phys. Rev. **D27** 140 (1983).

[20] C. Hwa and X. Wang, Phys. Rev. **D39** 187 (1989); M. Jacob, CERN preprint CERN/TH. 3515 (1983); F.W. Bopp, Phys. Rev. **D33** 1867 (1986).

[21] T. Sjöstrand, Computer Phys. Commun **82** (1994) 74; G.Marchesini, B.R.Webber, G.Abbiendi, I.G.Knowles, M.H.Seymour, and L.Stanco, Computer Phys. Commun. **67** (1992) 465.

[22] K. Braune *et al.*, Phys.Lett. **B123** 467 (1983).

[23] H.Appelshäuser, Phys. Lett. **B459** 679 (1999).

[24] M.L. Cherry *et al*, Acta Phys. Pol. **B29** 2129 (1998).

[25] M. Gaździcki, Eur. Phys. J. **C6** 365 (1999) and references therein.

[26] F. Liu, Eur. Phys. J. **C8** 649 (1999).

[27] T.A.Trainor, Nucl. Phys. Proc. Suppl. **B92** 16 (2001); H.C. Eggers, K. Fialkowski, Proceedings of the ISMD 2000, Tihany (Ungary), October 2000, World Scientific.

Particle Correlations in $e^+e^- \longrightarrow W^+W^-$ Events

N.Pukhaeva
University of Antwerpen, Antwerpen, Belgium
Joint Institute for Nuclear Research, Dubna, Russian Republic

Abstract

Preliminary results are reported on the two-particle correlation function $R(Q)$ in hadronic Z decays, fully hadronic WW decays and mixed hadronic-leptonic WW decays using data collected by the DELPHI detector at LEP at energies between 189 and 206 GeV. Evidence for Bose-Einstein correlations was observed in all three cases.

The event mixing technique was used to determine correlations between particles arising from *different* Ws in fully hadronic WW decays. An excess of like-sign particle pairs with low four-momentum difference in fully hadronic WW events is observed, consistent with the effect expected from correlations between identical particles from different Ws.

1 Introduction

The possible presence of colour reconnection effects and Bose-Einstein correlations in hadronic decays of WW pairs has been discussed on a theoretical basis, in relation to the measurement of the W mass (see for example [1, 2] and references therein). These effects can induce a systematic uncertainty on the W mass measurement in the fully hadronic channel [1] comparable with the expected accuracy of the measurement.

Bose-Einstein correlations (BEC) originate from the symmetrization of the production amplitude for identical bosons. The effects of BEC between identical bosons have been studied extensively in different types of reactions and for different boson species. Although many studies exist, there is still no complete understanding of the influence of this quantum mechanical effect on a multiparticle system generated in a high energy collision. The description of a given multiparticle system itself is complicated by needing to know the amplitude for the system and symmetrize it.

The observable most often used for the investigation of BEC in multiparticle final states is the two-particle correlation function. It was also demonstrated that BEC considerably affect other observables in high energy reactions [3]. A strong distortion of the $\rho^0(770)$ line shape due to BEC was observed in experimental data at LEP1 [4].

The $e^+e^- \rightarrow$ WW events allow a comparison of the characteristics of the W hadronic decays when both Ws decay hadronically in the reaction $e^+e^- \rightarrow W^+W^- \rightarrow q_1\overline{q}_2q_3\overline{q}_4$ (in the following we shall often refer to this as the $(4q)$ mode) with the case in which one of the Ws decays leptonically in the reaction $e^+e^- \rightarrow W^+W^- \rightarrow q_1\overline{q}_2\ell\nu$ (denoted $(2q)$ mode for brevity). Since the distance between the W^+ and W^- decay vertices is considerably smaller than the typical hadronisation distance, their decay products are expected to overlap in space and time and identical bosons from *different* Ws can be subject to Bose-Einstein correlations. In the framework of LUBOEI, the Bose-Einstein algorithm embedded in JETSET [5], the authors of [2] concluded that BEC between identical bosons from the decays of different Ws could strongly influence the measured mass of the W. On the other hand some authors (see e.g. [6]) argue that such inter-W correlations should not exist. It is therefore important to establish whether such correlations exist.

A rigorous mathematical treatment of correlations between pions from different Ws is given in [7]. Bose-Einstein correlations are incorporated in a space-time parton-shower model for e^+e^- annihilation into hadrons in [8]. In the present paper, Bose-Einstein correlations are studied for Ws in $(4q)$ and in $(2q)$ events. Such a combined study allows us to extract information on BEC between decay products of the two hadronically decaying Ws. The data used for the analysis related to Ws were collected with the DELPHI detector [9, 10] at LEP in 1998, 1999 and 2000 at centre-of-mass energies of 189–206 GeV with integrated luminosities of 155 pb^{-1}, 228 pb^{-1} and 164 pb^{-1}, respectively, with total statistics of 547 pb^{-1}.

The layout of the paper is the following. Section 2 summarizes the general properties of BEC. Section 3 describes the particle and event selection criteria. Section 4 presents the measurements of correlation functions in Z, fully hadronic and mixed hadronic-leptonic WW events. Section 5 describes measurements of correlations between particles from different Ws in fully hadronic WW events. A summary is given in Section 6.

2 Bose-Einstein Effects

BEC manifest themselves as an enhancement in the production of pairs of identical bosons close in phase space. To study the enhanced probability for emission of two identical bosons, the correlation function R is used. For pairs of particles, it is defined as

$$R(p_1,p_2) = \frac{P(p_1,p_2)}{P_0(p_1,p_2)}, \tag{1}$$

where $P(p_1,p_2)$ is the two-particle probability density, subject to Bose-Einstein symmetrization, p_i is the four-momentum of particle i, and $P_0(p_1,p_2)$ is a reference two-particle distribution which, ideally, resembles $P(p_1,p_2)$ in all respects, apart from the lack of Bose-Einstein symmetrization.

If $f(x)$ is the space-time distribution of the source, $R(p_1,p_2)$ takes the form

$$R(p_1,p_2) = 1 + |G[f(x)]|^2,$$

where $G[f(x)] = \int f(x)e^{-i(p_1-p_2)\cdot x}\,dx$ is the Fourier transform of $f(x)$. Thus, by studying the correlations between the momenta of pion pairs, one can study the distribution of the points of origin of the pions. Experimentally, the effect is often described in terms of the variable Q, defined by $Q^2 = -(p_1-p_2)^2 = M_{\pi\pi}^2 - 4m_\pi^2$, where $M_{\pi\pi}$ is the invariant mass of the two pions. The correlation function can then be written as

$$R(Q) = \frac{P(Q)}{P_0(Q)}, \tag{2}$$

which is frequently parametrized by the function

$$R(Q) = \gamma(1+\delta Q)\left(1+\lambda e^{-rQ}\right). \tag{3}$$

In the above equation, in the hypothesis of a spherically homogeneous pion source, the parameter r gives the radius of the source and λ is the strength of the correlation between the pions.

Bose-Einstein correlations can be included in PYTHIA/JETSET [5] by using the LUBOEI code, where they are introduced as a final state interaction [2, 5]. After the generation of the pion momenta, the values generated for all identical pions are modified by an algorithm that reduces their momentum vector differences according to equation 3. For the present analysis, the BE_{32} version of the LUBOEI code was used. For the comparison with the data, BEC were switched on in LUBOEI with a Gaussian parametrization for pions that are produced either promptly or as decay products of short-lived resonances (resonances with decay width less than 45 MeV were considered long-lived), with parameters set to λ=PARJ(92)=1.35 and $r = 0.58$ fm, which corresponds to model parameter R=PARJ(93)=0.34 GeV. It should be noted that the measured values for λ and r, corresponding to all particles, do not reproduce the above LUBOEI input values which correspond to primary particles or particles from short lived resonance decays only.

Two scenarios were considered for the study of BEC in W pairs.

(a) BEC were included for particles from the same and from different Ws (hereafter called *full* BE). In this case, BEC between particles from different Ws are treated in the same way as BEC between particles from the same W.

(b) BEC were included only for particles from the same Ws (hereafter called *inside* BE).

The correlation function was also studied in Z decays. Since the fraction of heavy quark pairs initiating the hadronic final state differs in Z and in W events, and especially b quarks are practically absent in W decays, a Z sample depleted in $b\bar{b}$ pairs has also been studied.

3 Particle and Event Selections

The present analysis relies on the information provided by the tracking detectors: the micro-Vertex Detector, the Inner Detector, the Time Projection Chamber as main tracking detector, the Outer Detector, the Forward Chambers and the Muon Chambers. The calorimeters were used for lepton identification and to detect neutral particles. All charged particles except those tagged as hard leptons in semileptonic events were taken to be pions and assigned the pion mass. Events were selected using a run quality flag, requiring all detectors essential for the analysis of the different decay channels of the W's to be fully operational and efficient.

In the event selection, charged particles were selected if they had a polar angle between 10° and 170°, momentum between 0.2 GeV/c and the beam momentum, and good quality, i.e. track length greater than 15 cm, transverse and longitudinal impact parameters less than 4 cm (as measured from the nominal interaction point with respect to the beam direction) and error on the momentum measurement less than 100%. Neutral particles were considered if they were associated to an electromagnetic or hadron shower with energy greater than 0.5 GeV and had a relative error on the energy measurement less than 100%.

Electron identification in the polar angle range between 20° and 160° used the characteristic energy deposition in the central and forward/backward electromagnetic calorimeters and demanded a nominal energy-to-momentum ratio consistent with unity. For this polar angle range the identification efficiency for high momentum electrons was determined from simulation to be $(77 \pm 2)\%$, in good agreement with the efficiency determined using Bhabha events measured in the detector.

Tracks were identified as muons if they had at least one associated hit in the muon chambers, or an energy deposition in the hadronic calorimeter consistent with a minimum ionizing particle. Muon identification was performed in the polar angle range between 10° and 170°. Within this acceptance, the identification efficiency was determined from simulation to be $(92 \pm 1)\%$. Good agreement was found between data and simulation for high momentum muons in $Z \rightarrow \mu^+\mu^-$ decays, and for lower momentum muons produced in $\gamma\gamma$ reactions.

In the subsequent more restrictive cuts were used. The information from the Time Projection Chamber of DELPHI was used to reconstruct the track, which gavean implicit track length cut of 25 cm. Only tracks with polar angle θ between 30° and 150° were accepted. The impact parameters in the transverse and longitudinal plane were required to be smaller than 0.4 cm and 1 cm/sin θ. The energetic isolated charged particle of the mixed decay channel was not included in the analysis.

year	$\sqrt{s}$	Number of events	Purity(%)	Efficiency(%)
1998	189 GeV	855	89.1	60.0
1999	192 –200 GeV	1181	89.8	53.2
2000	202 –206 GeV	771	90.5	49.6

Table 1: The year of the run, the numbers of events selected, the purity of the samples and the efficiency at different energies for WW ($4q$).

3.1 Fully Hadronic Channel (WW$\rightarrow 4q$)

The event selection criteria were optimised in order to ensure that the final state was purely hadronic and in order to reduce the residual background, for which the dominant contribution is radiative $q\bar{q}$ production, $e^+e^- \rightarrow q\bar{q}(\gamma)$, especially the radiative return to the Z peak, $e^+e^- \rightarrow Z\gamma \rightarrow q\bar{q}\gamma$.

For each event passing the above criteria, all particles were clustered into jets using the LUCLUS algorithm [5] with the resolution parameter $\mathrm{d_{join}} = 8$ GeV/c. At least four jets were required, with at least three particles in each jet.

Events from the radiative return to the Z peak were rejected by requiring the effective centre-of-mass energy of the e^+e^- annihilation to be larger than $E_{cm}\times 0.79$. The effective energy was estimated using either the recoil mass calculated from one or two isolated photons measured in the detector or, in the absence of such a photon, by forcing a 2-jet interpretation of the event and assuming that a photon had been emitted colinear to the beam line.

The remaining events were then forced into a four-jet ($4j$) configuration. The four-vectors of the jets were used in a kinematic fit, which imposed conservation of energy and momentum. The variable D was defined as [11]

$$D = \frac{E_{min}}{E_{max}} . \frac{\theta_{min}}{(E_{max} - E_{min})}, \tag{4}$$

where E_{min}, E_{max} are the minimum and maximum jet energies and θ_{min} is the smallest interjet angle after the constrained fit. Events were used only if the variable D was larger than 0.006 rad.GeV^{-1}.

A total of 2807 events were selected.

The detector effects on the analysis were estimated using samples of WW events generated with EXCALIBUR [12] for all four-fermion final states.Background events were generated with PYTHIA 5.7 [5] with the fragmentation tuned to the DELPHI data at LEP1 [13]. The generated events were passed through the full detector simulation program DELSIM [10]. The purity and efficiency of the selection of WW$\rightarrow q\bar{q}q\bar{q}$, estimated using simulated events, were about 90% and 54%, respectively (see table 1).

3.2 Mixed Hadronic-Leptonic Channel (WW$\rightarrow 2q.l\nu$)

Events in which one W decays into a lepton plus neutrino ($l\nu$) and the other one into quarks are characterized by two hadronic jets, one energetic isolated charged lepton, and missing momentum resulting from the neutrino. The main backgrounds to these events are radiative $q\bar{q}$ production and four-fermion final states containing two quarks and two charged leptons of the same flavour.

Events were selected by requiring six or more charged particles and a missing momentum of more than 5% of the nominal total centre-of-mass energy. Electron and muon tags were applied to the events. In $q\bar{q}(\gamma)$ events, the selected lepton candidates are either leptons produced in heavy quark decays or misidentified hadrons, which generally have rather low momenta and small angles with respect to the corresponding quark jet. The momentum of the selected muon, or the energy deposited in the electromagnetic calorimeters by the selected electron, was required to be greater than 17 GeV/c. The energy not associated to the lepton, but assigned instead to other charged or neutral particles in a cone of 10° around the lepton, is a useful measure of the isolation of the lepton; this energy was required to be less than 5 GeV for both muons and electrons. In addition, the isolation angle between the lepton and the nearest charged particle with a momentum greater than 1 GeV/c was required to be larger than 10°. If more than one identified lepton passed these cuts, the one with highest momentum was considered to be the lepton candidate from the W decay. The angle between the lepton and the missing momentum vector was required to be greater than 70°. All the other particles were forced into two jets using the LUCLUS algorithm [5]. Both jets had to contain at least one charged particle.

The radiative $q\bar{q}$ background was suppressed by looking for evidence of an Initial State Radiation (ISR) photon. Events were removed if there was a cluster with energy deposition greater than 20 GeV in the electromagnetic calorimeters, and it could not be attributed to a charged particle. Events with ISR photons at small polar angles, where they would be lost inside the beam pipe, were suppressed by requiring the polar angle of the missing momentum vector to satisfy $|\cos\theta_{\mathrm{miss}}| < 0.96$.

The four-fermion neutral current background was reduced by applying additional cuts to events in which a second lepton of the same flavour as the first was detected. Such events were rejected if the energy in a cone of 10° around the second lepton direction was greater than 5 GeV.

If no lepton was identified, the most energetic particle which formed an angle greater than 25° with all other charged particles was considered as a lepton candidate. In this case tighter cuts were applied. The lepton momentum had to be greater than 20 GeV/c, the amount of missing momentum greater than 20 GeV/c and its polar angle $|\cos\theta_{\mathrm{miss}}| < 0.85$.

A kinematical fit was performed on the selected events. The four-vectors of the two jets, of the lepton and of the missing momentum were used in the fit, which imposed conservation of energy and momentum and equality of the masses of the two-jet system and the lepton-neutrino system, attributing the missing momentum of the event to the undetected neutrino. Events were used only if the fit probability was larger than 0.1%. In total, 2233 events were selected. The purity and efficiency of the selection, estimated using simulated events, were about 96% and 50%, respectively (see table 2).

4 Correlation Functions for Z, WW$\rightarrow$ $4q$, and WW$\rightarrow$ $2q.l\nu$ Events

To compute the correlation function $R(Q)$ (equation 2), the two-particle probability density $P(Q)$ was calculated; the reference $P_0(Q)$ came from EXCALIBUR without BEC after full simulation of the DELPHI detector and after the same selection criteria as for

year	$\sqrt{s}$	Number of events	Purity(%)	Efficiency(%)
1998	189 GeV	630	95.2	51.8
1999	192 – 200 GeV	960	96.6	51.1
2000	202 – 206 GeV	643	97.2	48.0

Table 2: The year of the run, the numbers of events selected, the purity of the samples and the efficiency at the different energies for WW ($2q$).

real data. The $P_0(Q)$ reference distribution was normalised to the number of pairs in the $P(Q)$ distribution.

The presence of bin-to-bin and inside-bin correlations influences the errors on the $R(Q)$ distribution [14]. If there are N particles of given charge in an event, each one has (N-1) entries in the two-particle density $P(Q)$, mostly contributing to different bins of the histogram. But due to the finite size of the bins, the same track can also contribute several times to the same bin, which is a source of inside bin correlations. The covariance matrix technique was used to measure the parameters. The covariance matrix was calculated from the data themselves. The method is based on classical statistics (see for details [15]). Let us consider the i-th event from the set of n events and to two-particle probability density P which is presented in the histogram h^i with N_p bins.

The histogram $H = \sum_{i=1}^{n} h^i$ and the values

$$c_{jk} = \sum_{i=1}^{n}(h^i_j - H_j/n)(h^i_k - H_k/n)(1 + 1/n)$$

were calculated event by event. Here j and k are the bin numbers for the histograms. The correlations and errors for one event are not known but the different events are uncorrelated. Considering bin values of the histogram made for one event as a random vector with unknown distribution, one has an uncorrelated ensemble of these vectors and hence the covariance matrix can be estimated statistically.

For all events the resulting histogram H for the two-particle probability density the covariance matrix $P(Q)$ and $V_{jk} = c_{jk} \cdot n/(n-1)$ for this histogram were calculated. The fits below were performed using the inverted V_{jk} matrix.

4.1 Correlation Between Particles in Z events

Correlations between particles in Z events produced during the calibration runs were investigated. The track selection for the analysis was the same as above. The event selection was similar to the one in [16]. The number of selected events amounted to 24681.

The $R(Q)$ distribution for like-sign combinations is shown in figure 1a. The fit using the expression (3) yielded:

$$\lambda_Z = 0.712 \pm 0.021(stat) \tag{5}$$
$$r_Z = 0.888 \pm 0.040(stat)\ \text{fm}. \tag{6}$$

Since the fraction of heavy quark pairs that initiated the hadron cascade is different in Z and in W decays, a light flavour enriched Z sample has been used for comparison.

The $b\bar{b}$ fraction has been reduced from the original 22% to about 2% by removing a large fraction of $b\bar{b}$ events using a b-event tagging procedure (see [10] for details). The correlation functions for this sample are shown in figure 1b for like-sign combinations. The fit results were:

$$\lambda_{Z-no\ b\bar{b}} = 0.913 \pm 0.027(stat) \quad (7)$$
$$r_{Z-no\ b\bar{b}} = 0.893 \pm 0.047(stat)\ \mathrm{fm}. \quad (8)$$

The λ and r parameters in the LUBOEI BE_{32} code were tuned to the correlation function measured at the Z for like-sign pairs. The tuned parameters $\lambda = 1.35$ and $r = 0.58$ fm were obtained (PARJ(92)=1.35 and PARJ(93)=0.34). The $R(Q)$ distributions for the data for Z events are compared with the LUBOEI predictions in figure 1a–1b. Good agreements between data and model were found.

4.2 Correlation Between Particles from any Ws in WW→ $4q$ and WW→ $2q.l\nu$ Events

The $R_{2q}(Q)$ and $R_{4q}(Q)$ distributions for the data are shown in figure 2. A fit to the correlation functions $R(Q)$ using equation (3) yielded the values:

$$\lambda_{2q} = 0.791 \pm 0.096(stat) \quad (9)$$
$$r_{2q} = 1.177 \pm 0.121(stat)\ \mathrm{fm} \quad (10)$$

for the mixed hadronic-leptonic channel and

$$\lambda_{4q} = 0.725 \pm 0.053(stat) \quad (11)$$
$$r_{4q} = 1.117 \pm 0.070(stat)\ \mathrm{fm} \quad (12)$$

for the fully hadronic decay channel.

4.2.1 Background Subtraction in WW→ $4q$ Events

Averaged over all energies, the selected WW fully hadronic events contained 10% of $q\bar{q}$ events (Table 1). The correction for these background contributions to the fully hadronic sample was done in following way.

A sample of $q\bar{q}$ events was generated with BEC included according to LUBOEI BE_{32} with parameters λ=1.35 and r=0.58 fm as was tuned at Z-peak. These events were subjected to the same event and track selection criteria as the fully hadronic sample and the Q-distribution of the background was calculated from the events passing the selection.

The agreement between data and simulated events at Z-peak for 4 jet samples selected using the d_{join} requirement was then checked.

The comparison of Q-distributions for data and simulated Z events are shown in Fig. 3 for all events (Fig. 3a) and for 4 jet events (Fig. 3b, 3c and 3d for $d_{join} > 4\ GeV/c$, $d_{join} > 5\ GeV/c$ and $d_{join} > 6.5\ GeV/c$, respectively). The agreement for all events is satisfactory (as was shown also in section 4.1), while the model strongly overestimates the correlations at low-Q for selected 4 jet samples.

We then used an alternative simulated sample at Z-peak with reduced parameter of λ=0.90 (instead of λ=1.35). All other model parameters were the same. The comparison of Q-distributions for data and these simulated Z events are shown in Fig. 4.

The Q plot for simulated background $q\bar{q}$ events was corrected for the discrepancy between the data and the simulated sample at Z-peak shown in figure 3c. This distribution, properly weighted by the percentage of the background, was subtracted from the experimental WW (4q) distribution. Alternatively, the contribution of background $q\bar{q}$ events were subtracted using the simulated sample with parameter λ=0.90 (without corrections). These two procedures yielded practically the same background subtracted distributions.

The Q-distributions for real WW fully hadronic events and for background events, calculated as described above, are shown in figure 5a. Figure 5b presents the $R(Q)$ distributions for WW (4q) events without (closed circles) and with background subtraction (triangles).

It can be seen that the background contribution practicaly does not change the Q-distribution for (4q) events (Fig. 5b).

We note also that for WW BEC analysis at LEP the background contribution in the WW fully hadronic channel was usually estimated using the LUBOEI model tuned at the Z-peak. As shown in this section, this can overestimate the correlations at low-Q for 4 jet samples. This problem is most important for selections with high background contribution (which is up to 20% for some selections used at LEP).

A fit to the $R(Q)$ after the background subtraction with equation (3) yielded the values:

$$\lambda_{4q} = 0.741 \pm 0.065(stat) \tag{13}$$
$$r_{4q} = 1.199 \pm 0.088(stat) \text{ fm} \tag{14}$$

In the subsequent analyses the $R(Q)$ distributions after the background subtraction were used.

5 Correlations Between Particles from Different Ws

To perform a direct measurement sensitive to BEC between particles from different Ws, the analysis used a comparison sample which contained only BEC for particle pairs coming from a single W boson, but not for particle pairs from different Ws. This comparison sample of (4q)-like events was constructed by mixing of two hadronic Ws from the different (2q) events in the following way.

The pairs of Ws were accepted for mixing if they had momentum imbalance $|\vec{P}_1 + \vec{P}_2| < 25$ GeV. From each selected semileptonic event, the hadronic part was boosted to the rest frame of the W candidate. The rest frames of the W candidates were determined using the energy and momenta of the Ws obtained from the kinematical fits. The mixed event was then constructed from two W candidates by boosting the particles of the individual Ws in opposite directions. The boost vectors were determined taking into account energy-momentum conservation and the fitted mass of W candidate.

The fully hadronic event selections were applied to mixed events. Some event shape variables, multiplicities and single particle distributions for fully hadronic and mixed events for data and MC are shown in Figs. 6–10. In general good agreement was found.

The expected R_{4q} when there are no correlations between Ws, constructed from the experimental values of P_{2q} (for pairs from same W) and from the mixed sample P_{mix} (for pairs from different Ws), can be written as

$$R_{4q}(Q)(mixing) = \frac{[P_{2q}(Q) + P_{mix}(Q)]_{data}}{[P_{2q}(Q) + P_{mix}(Q)]_{DELSIM\ no\ BE}}, \tag{15}$$

where $P_{mix}(Q)$ was obtained using the mixing of two ($2q$) events as described above. The measured $R_{4q}(Q)$ and $R_{4q}(Q)(mixing)$ are shown in figure 11 for like-sign pairs, indicating the correlations between particles from different Ws.

To perform model independent measurements of correlations between particles from different Ws, the ratio which is independent of any Monte-Carlo model:

$$D(Q) \equiv \frac{P_{4q}(Q)}{P_{2q}(Q) + P_{mix}(Q)}, \tag{16}$$

was used. This was fitted by the expression:

$$D(Q) = N\,(1 + \delta Q)\left(1 + \Lambda e^{-RQ}\right). \tag{17}$$

The resulting plots are shown in Fig. 12.

The fit for model with full BEC gave:

$$\Lambda(full\ BE) = 0.227 \pm 0.026(stat) \tag{18}$$

$$R(full\ BE) = 0.895 \pm 0.100(stat)\ \text{fm} \tag{19}$$

$$\delta(full\ BE) = 0.000 \pm 0.002(stat) \tag{20}$$

$$N(full\ BE) = 0.998 \pm 0.004(stat) \tag{21}$$

Fixing the parameter R to the value obtained above (R=0.895 fm) and repeating the fit for the model with inside BEC and for the data, yielded

$$\Lambda(inside\ BE) = -0.002 \pm 0.016(stat) \tag{22}$$

$$\delta(inside\ BE) = 0.001 \pm 0.001(stat) \tag{23}$$

for model with inside Ws BEC, and

$$\Lambda(data) = 0.149 \pm 0.045(stat)^{+0.025}_{-0.020}(syst) \tag{24}$$

$$\delta(data) = -0.003 \pm 0.004(stat) \tag{25}$$

for data.

The systematic error quoted on the measured value of $\Lambda(data)$ in (24) is the sum in quadrature of the following contributions.

- Due to the event mixing technique. Two estimated were made.

  The model with BEC only inside Ws should give Λ=0.0. The magnitude of the value $\Lambda(inside\ BE)$ plus one sigma(equation 22) is 0.018.

  The effects of discrepancies between fully hadronic and mixed events were studied. Weights were assigned to the mixed events which were equal to the ratio of the event shape and single particle distribution variables shown in figures 6–10. The maximum deviation obtained from the value (24) was 0.020.

  The value $\pm$0.020, i.e. larger of these two estimates, was used as a conservative systematic error due to the mixing technique.

- Due to background events. The value of parameter $\Lambda(data)$ without background subtraction was

$$\Lambda(data) = 0.164 \pm 0.043(stat)\,. \tag{26}$$

  The difference between the values of (24) and (26), i.e. +0.015, was used as estimation of the systematic error.

- The contribution due to other sourcies were found negligible.

The analysis were repeated using the requirement $\alpha > 3°$, where α is the angle between pairs of particles. The corresponding $D(Q)$ plots are shown in Fig. 13. The fit for the prediction of the model with full BEC gave:

$$\Lambda(full\ BE, \alpha\ cut) = 0.292 \pm 0.037(stat) \tag{27}$$

Note that the $\alpha > 3°$ requirement increases the sensitivity to inter-Ws correlations (values (18) and (27)).

The fit values for the prediction of the model with inside BEC and for the data were

$$\Lambda(inside\ BE, \alpha\ cut) = -0.002 \pm 0.021(stat)\,, \tag{28}$$

$$\Lambda(data, \alpha\ cut) = 0.177 \pm 0.055(stat)^{+0.033}_{-0.023}(syst)\,. \tag{29}$$

The value of Λ without background subtraction was $\Lambda(data, \alpha\ cut)$=0.201$\pm$0.052.

6 Summary

The correlation functions for like-sign particles were measured in hadronic Z decays, in semileptonic and in fully hadronic WW channels using data collected with the DELPHI detector during the 1998, 1999 and 2000 runs with integrated luminosity of 547 pb^{-1} at centre-of-mass energies of 189–206 GeV.

Measurements were performed to extract correlations between pions from different Ws. The event mixing technique was used to construct a comparison sample which contained only BEC for particle pairs coming from a single W boson.

The value of parameter $\Lambda(data)$ characterizing the correlations between particles from different Ws was found to be

$$\Lambda(data) = 0.149 \pm 0.045(stat)^{+0.025}_{-0.020}(syst) \tag{30}$$

The value using the $\alpha > 3^\circ$ requirement, where α is the angle between pairs of particles, was found to be

$$\Lambda(data, \alpha\ cut) = 0.177 \pm 0.055(stat)^{+0.033}_{-0.023}(syst)\,. \tag{31}$$

Our overall conclusion is that our data support the hypothesis of correlations between like-sign pions coming from different Ws.

Acknowledgments

I thank T. Sjöstrand for very useful discussions. I am greatly indebted to our technical collaborators and to the funding agencies for their support in building and operating the DELPHI detector, and to the members of the CERN-SL Division for the excellent performance of the LEP collider. I also with thank to Organizing committee of the VHMP Workshop.

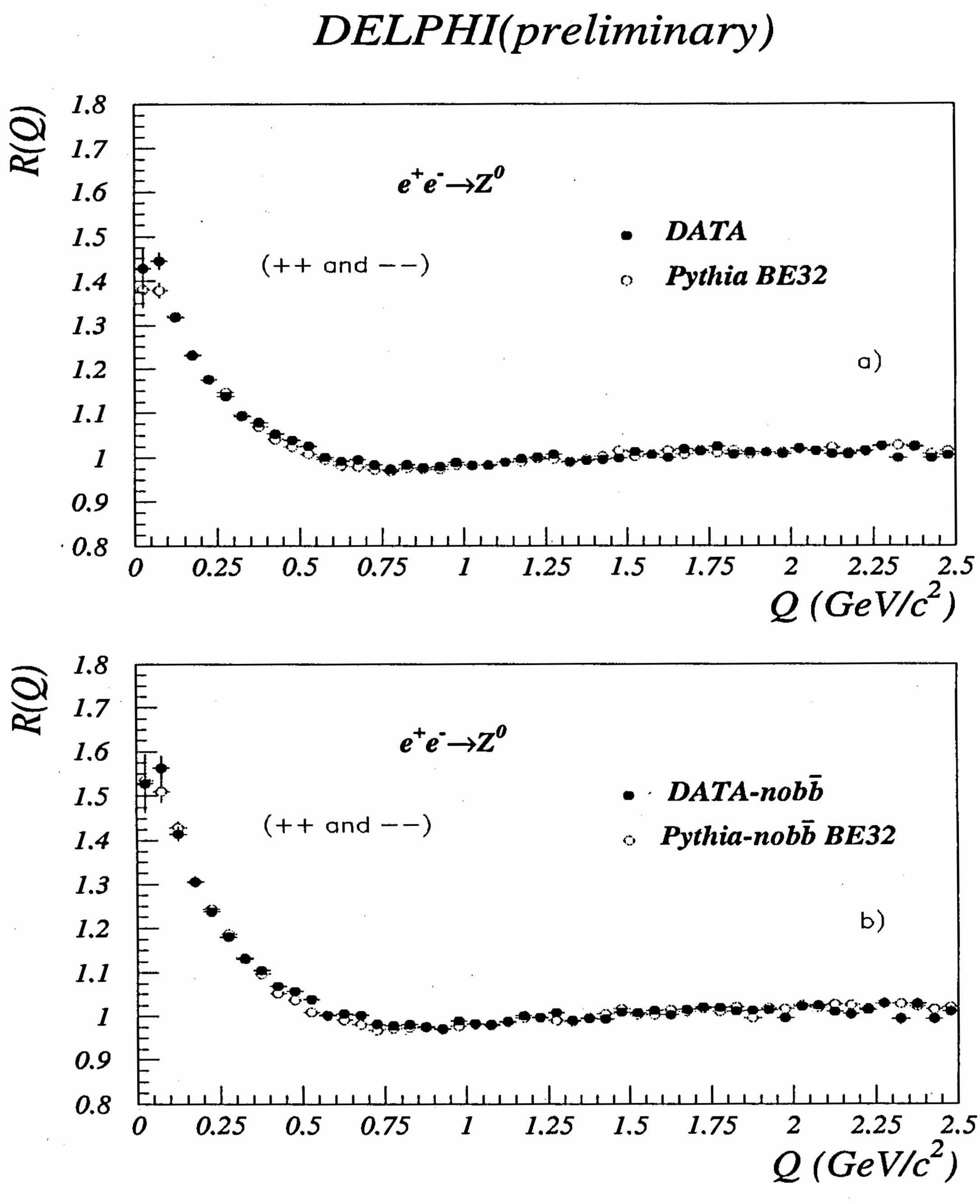

Figure 1: (a) Measured correlation functions $R(Q)$ for like-sign pairs in Z decays for data (closed circles) and the PYTHIA Monte Carlo model tuned at the Z peak (open circles). (b) Same as in (a), but for Z events depleted in $b\bar{b}$ production.

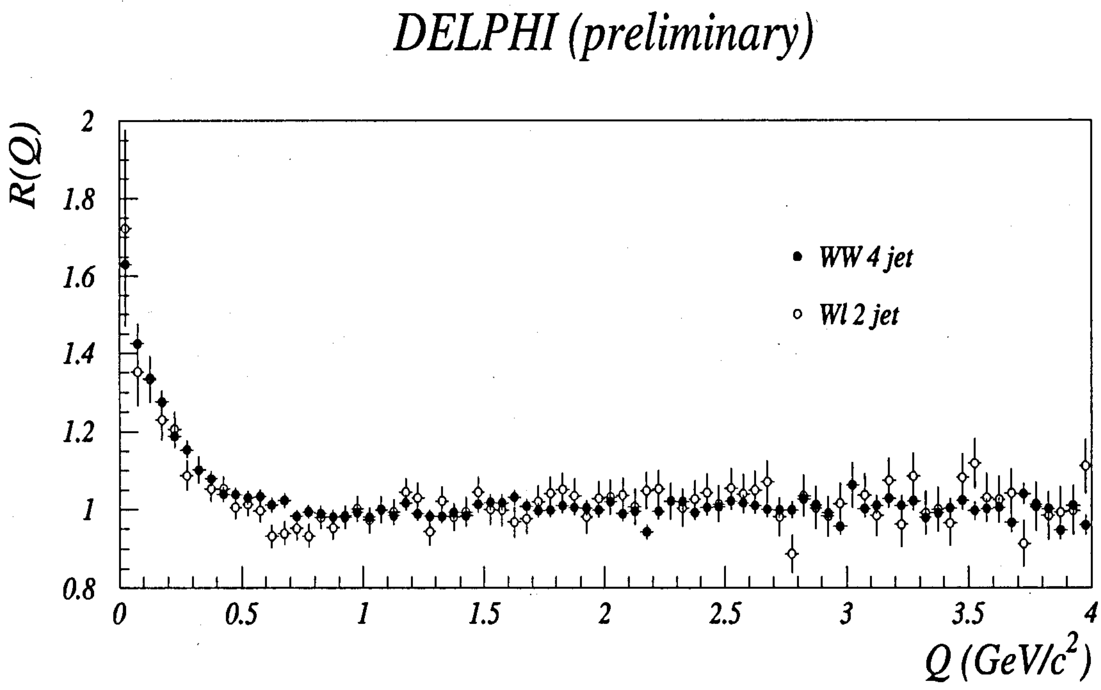

Figure 2: Measured correlation functions $R_{2q}(Q)$ (open circles) and $R_{4q}(Q)$ (closed circles) for like-sign pairs.

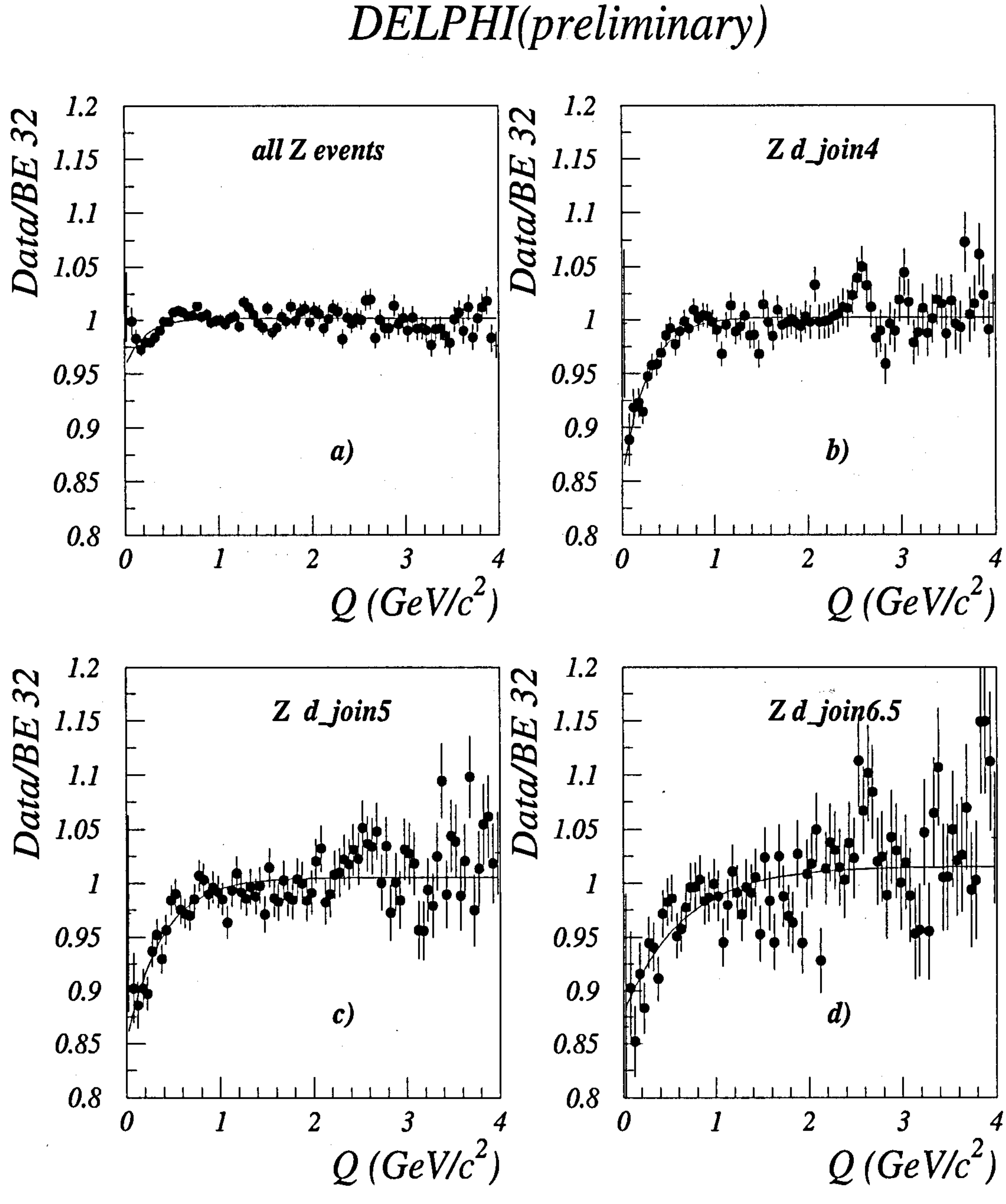

Figure 3: The ratio of Q-plots for real and simulated events in Z decays data (a) for all Z events and for selected Z 4 jet events with (b) $\mathrm{d_{join}} > 4\ GeV/c$, (c) $\mathrm{d_{join}} > 5\ GeV/c$, (d) $\mathrm{d_{join}} > 6.5\ GeV/c$. The model parameters were $\lambda = 1.35$ and $r = 0.58$ fm.

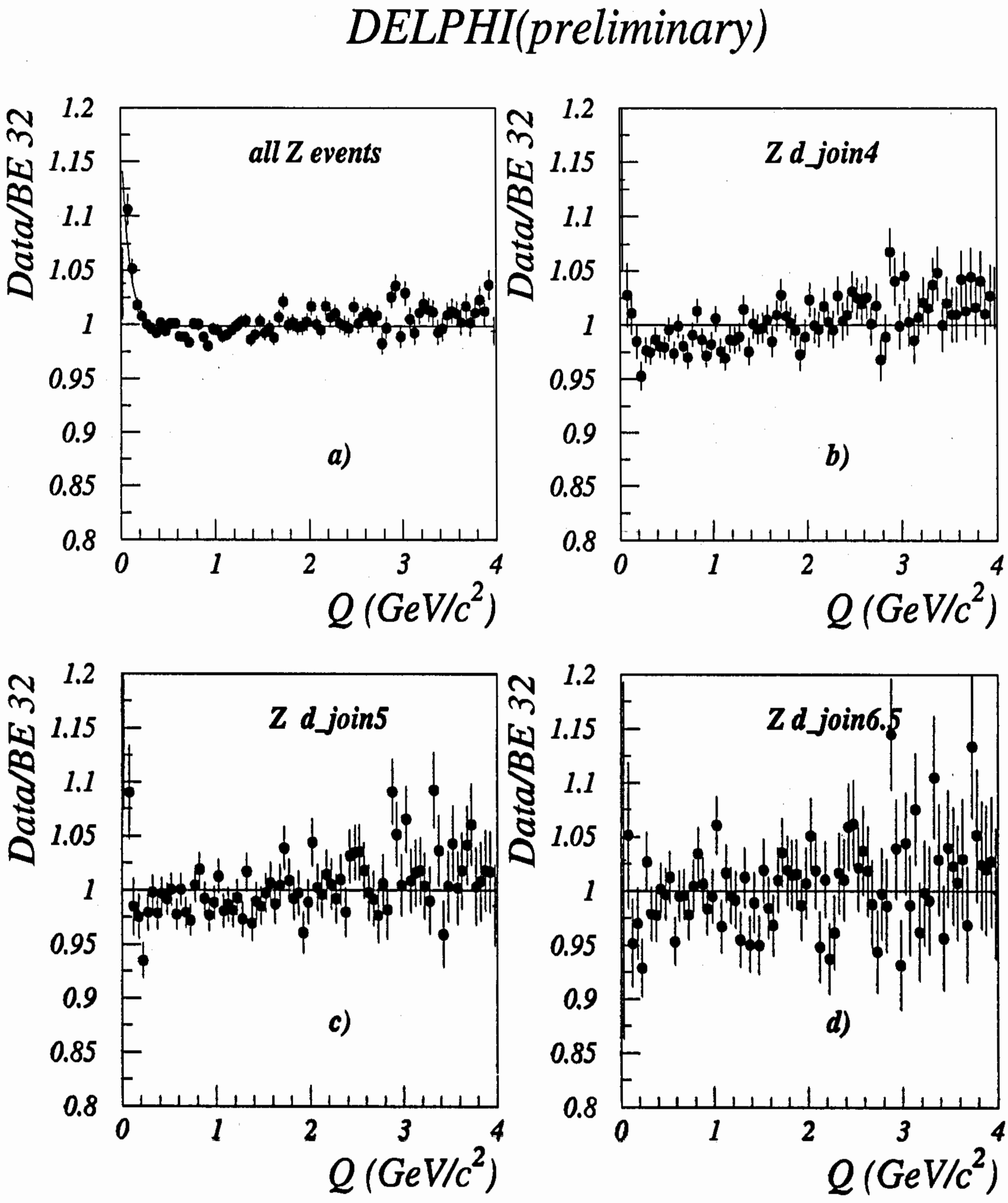

Figure 4: Same as in figure 3 but for simulated events with parameters of $\lambda = 0.90$ instead of $\lambda = 1.35$.

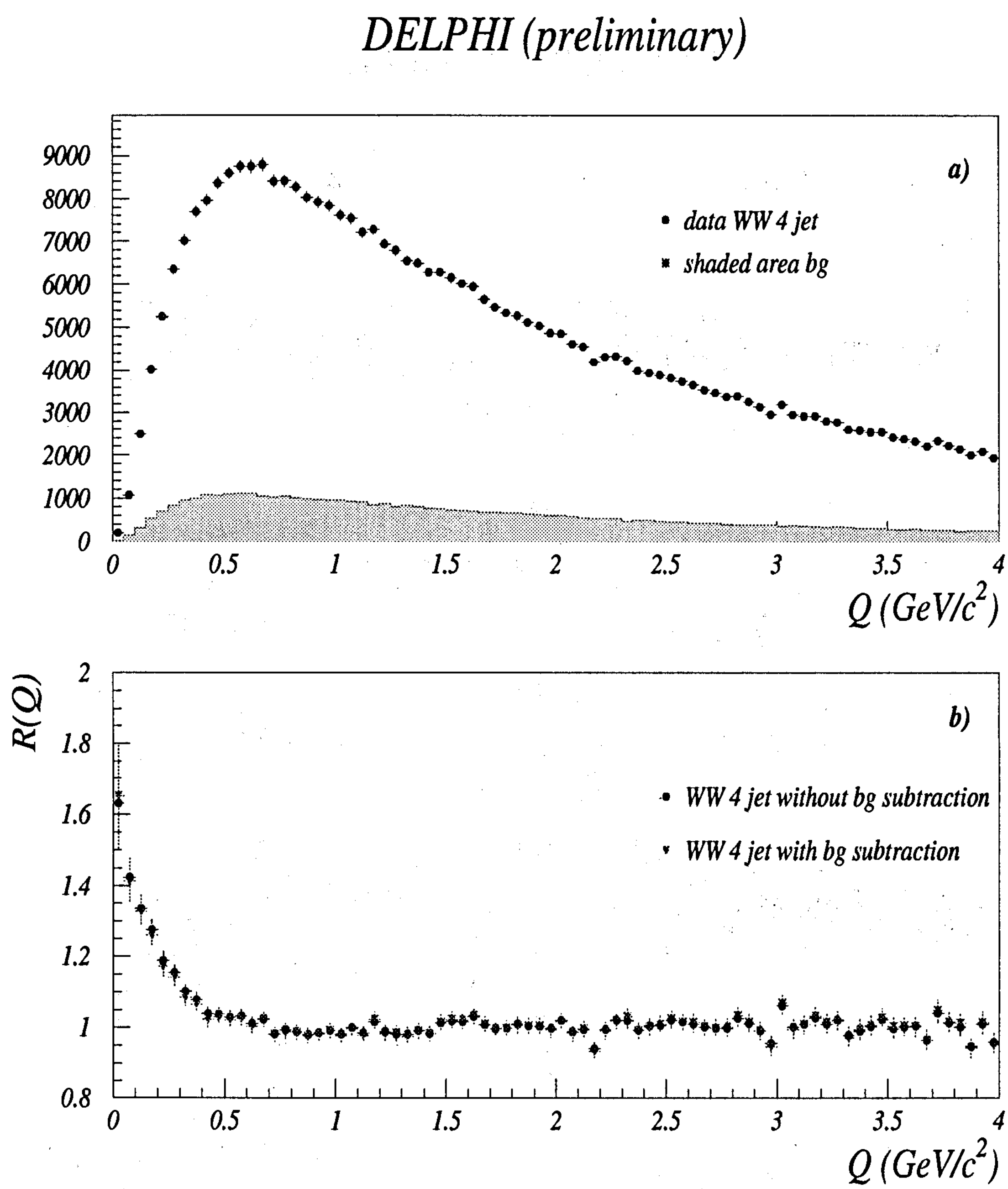

Figure 5: (a) Q-distributions for real (4q) events and for simulated (4q) background events for like-sign pairs. (b) measured $R_{4q}(Q)$ distributions for (4q) before and after background subtraction (closed circles and triangles, respectively).

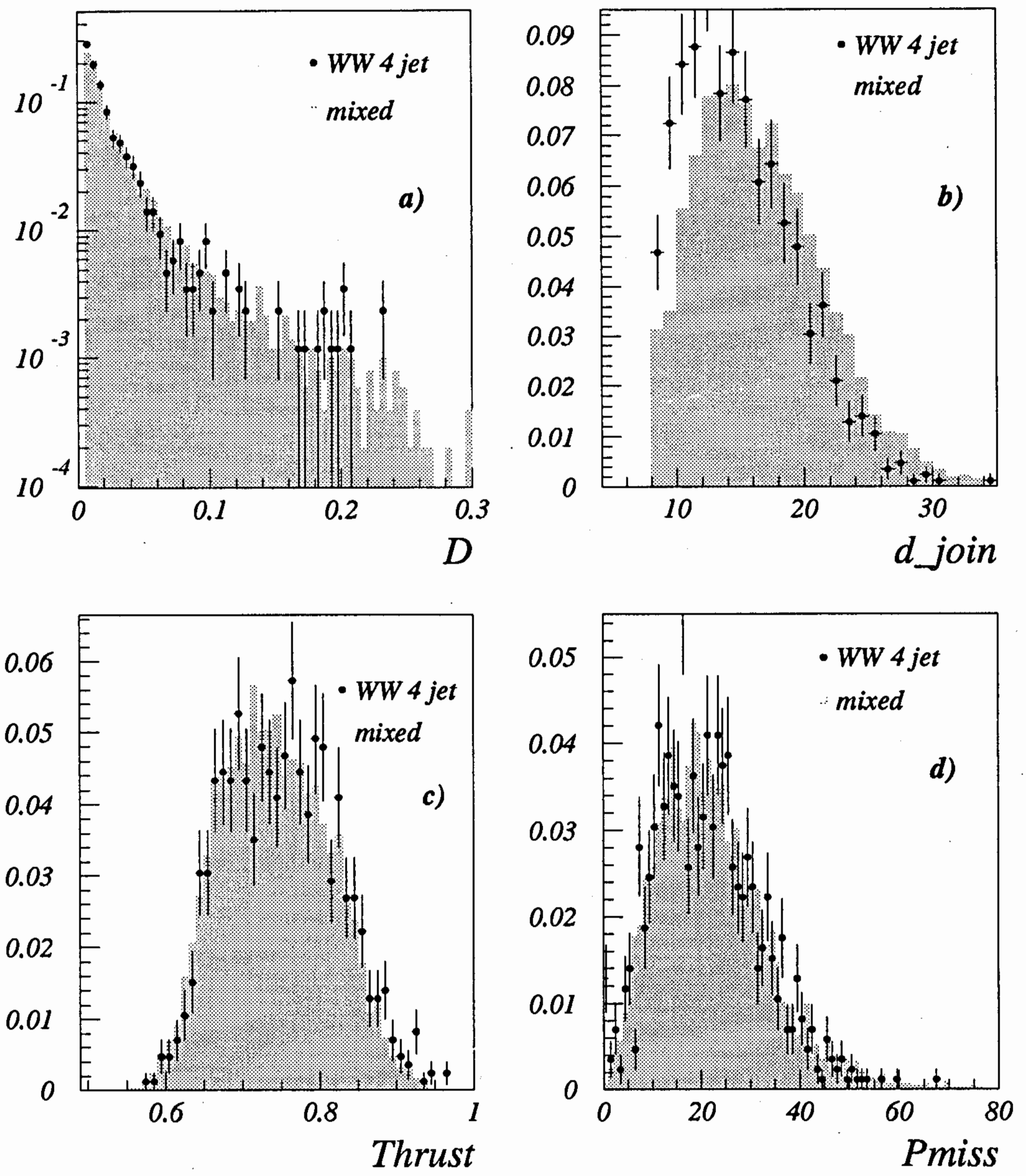

Figure 6: Comparison of events shape variables for (4q) and mixed events for real 1998 data.

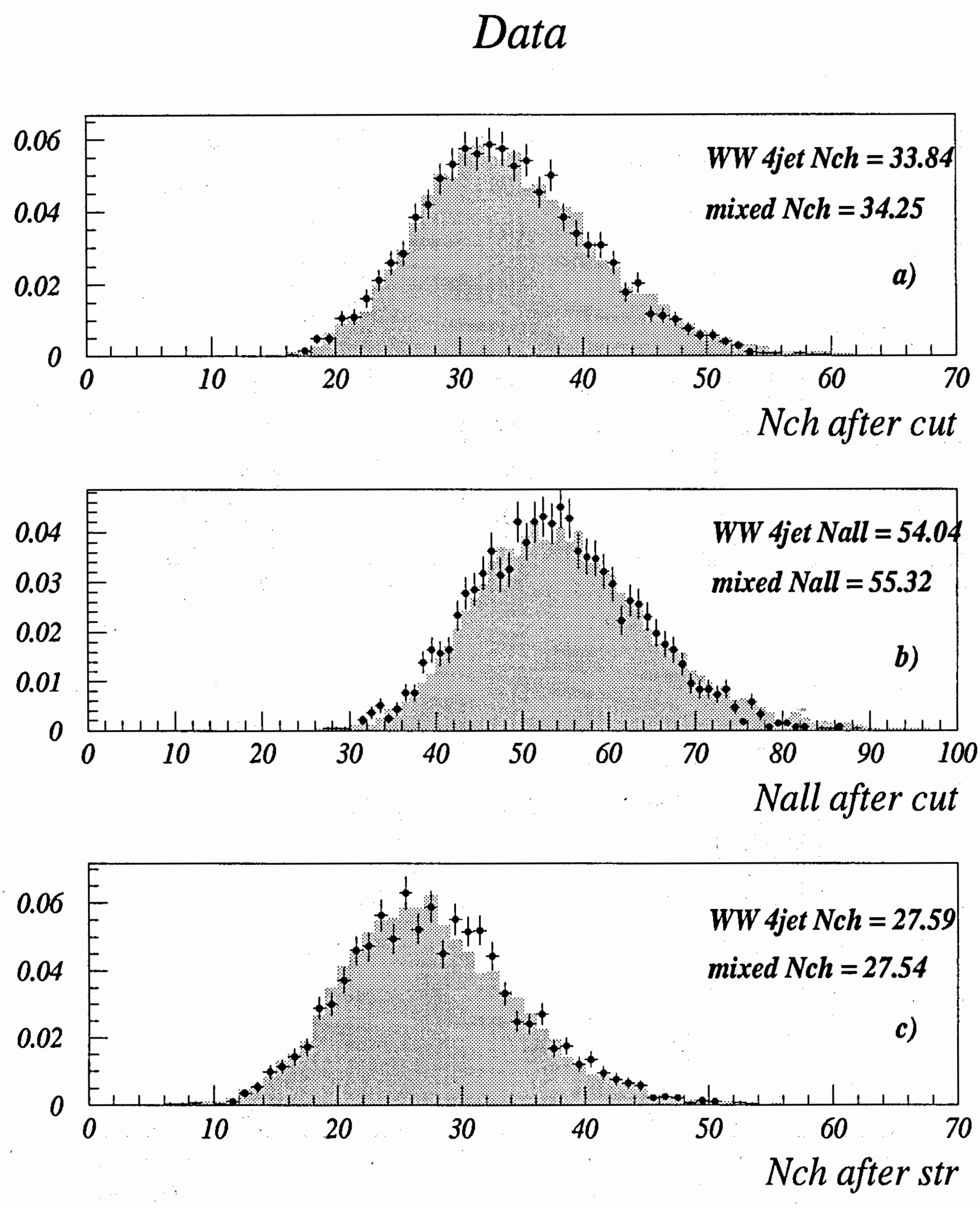

Figure 7: Comparison of multiplicity distributions for (4q) and mixed events for real 1998 data for a) all charged particles used for event selections, b) all particles including neutrals, c) charged particles used for analysis of Q-distributions.

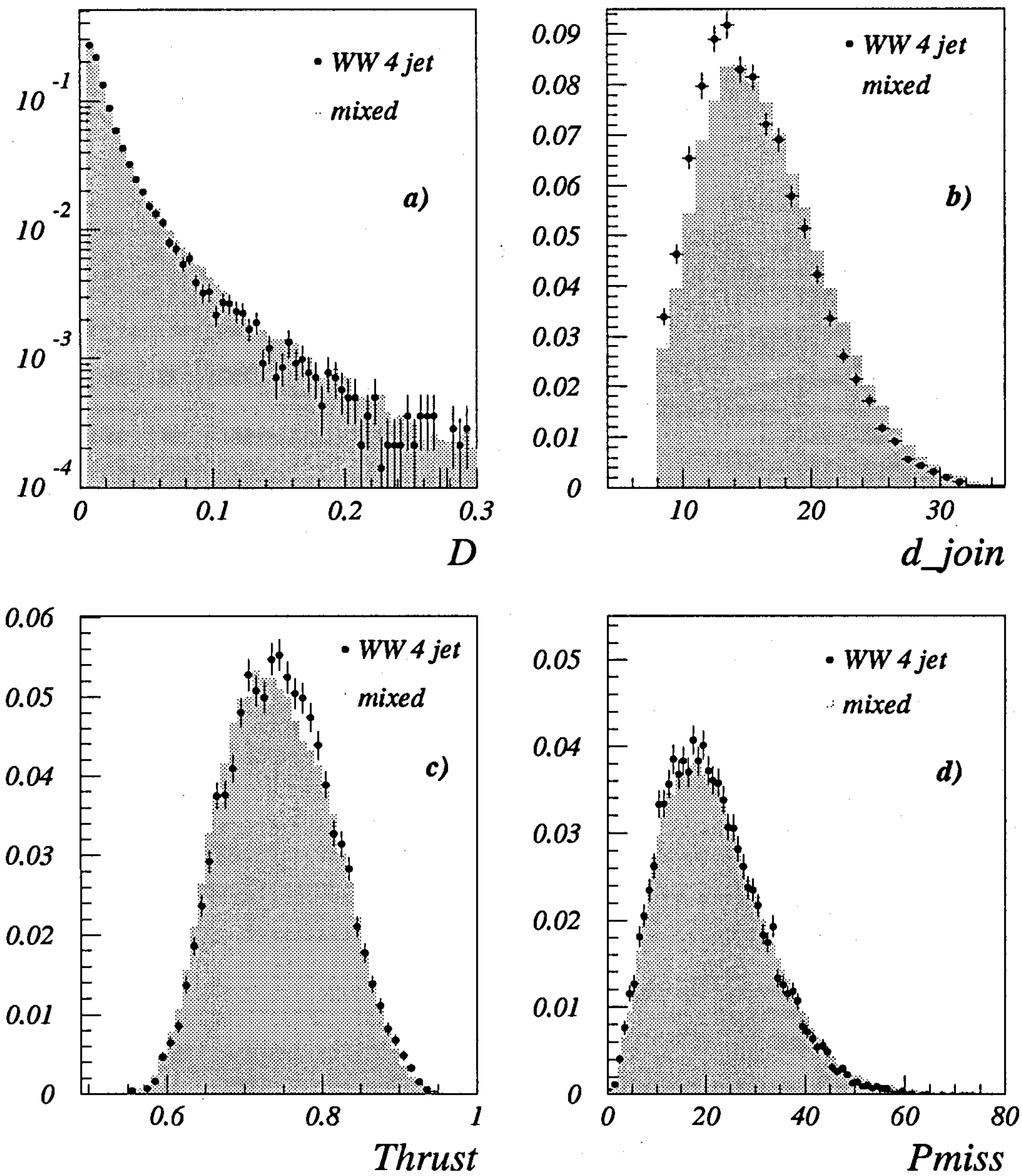

Figure 8: Comparison of events shape variables for (4q) and mixed events for simulated data.

single particle distributions for Data

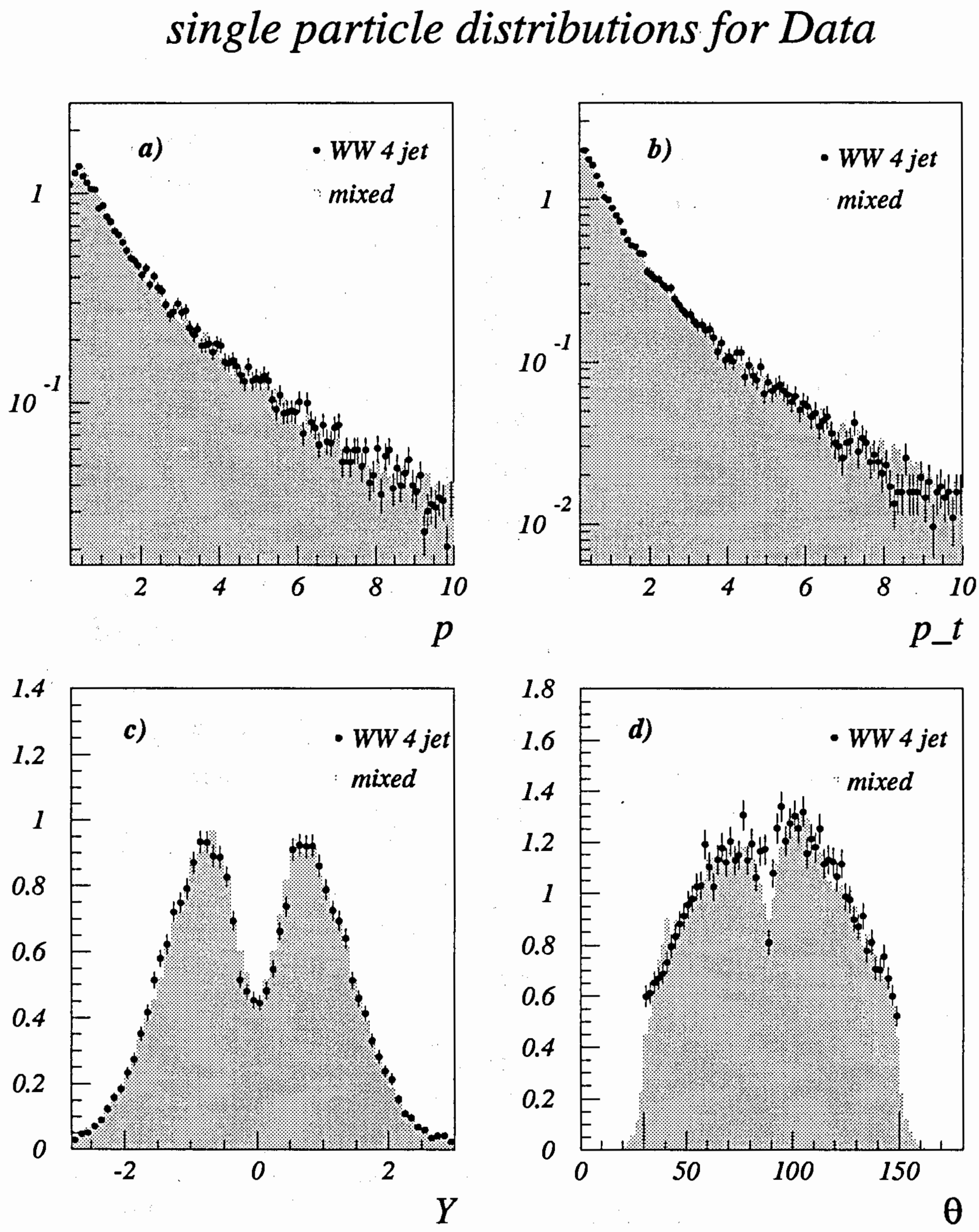

Figure 9: Comparison of single particle distributions for (4q) and mixed events for real 1998 data.

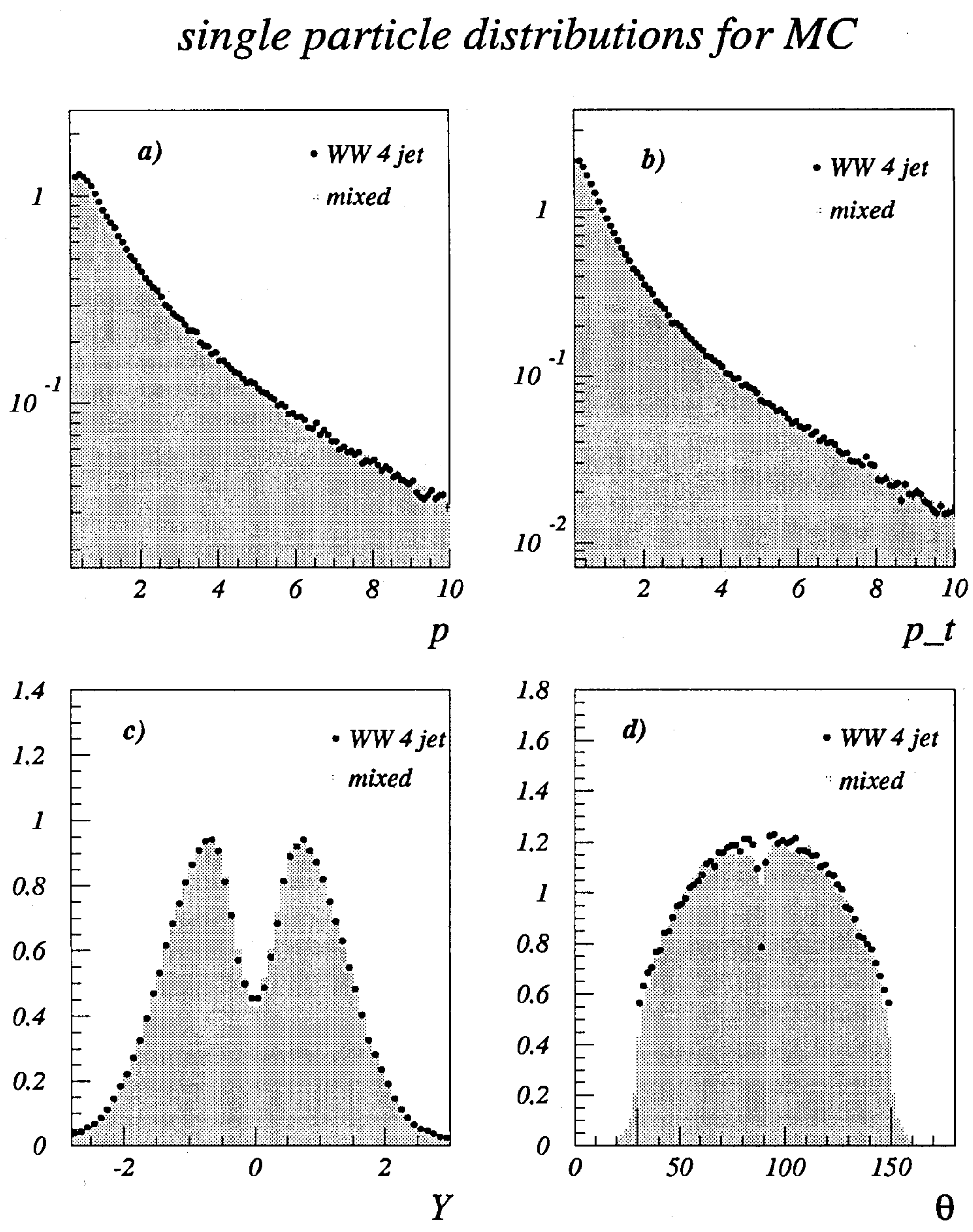

Figure 10: Comparison of single particle distributions for (4q) and mixed events for simulated data.

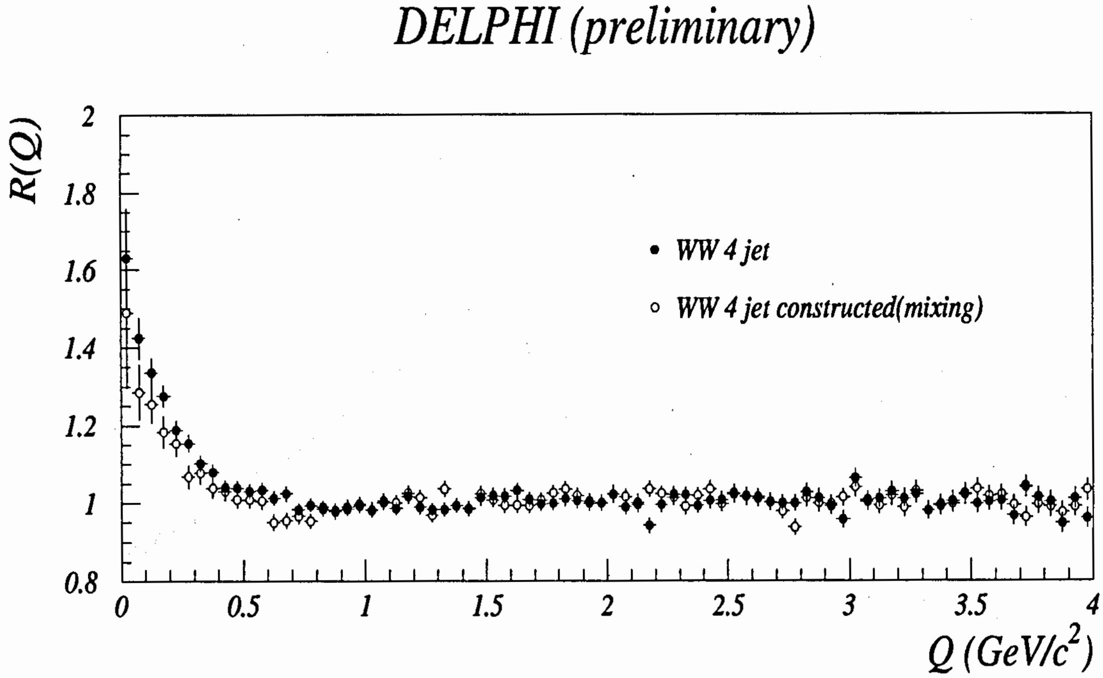

Figure 11: Measured correlation functions $R_{4q}(Q)$ (closed circles) and $R_{4q}(Q)(constructed)$ (open circles) computed from (2q) events using the mixing technique.

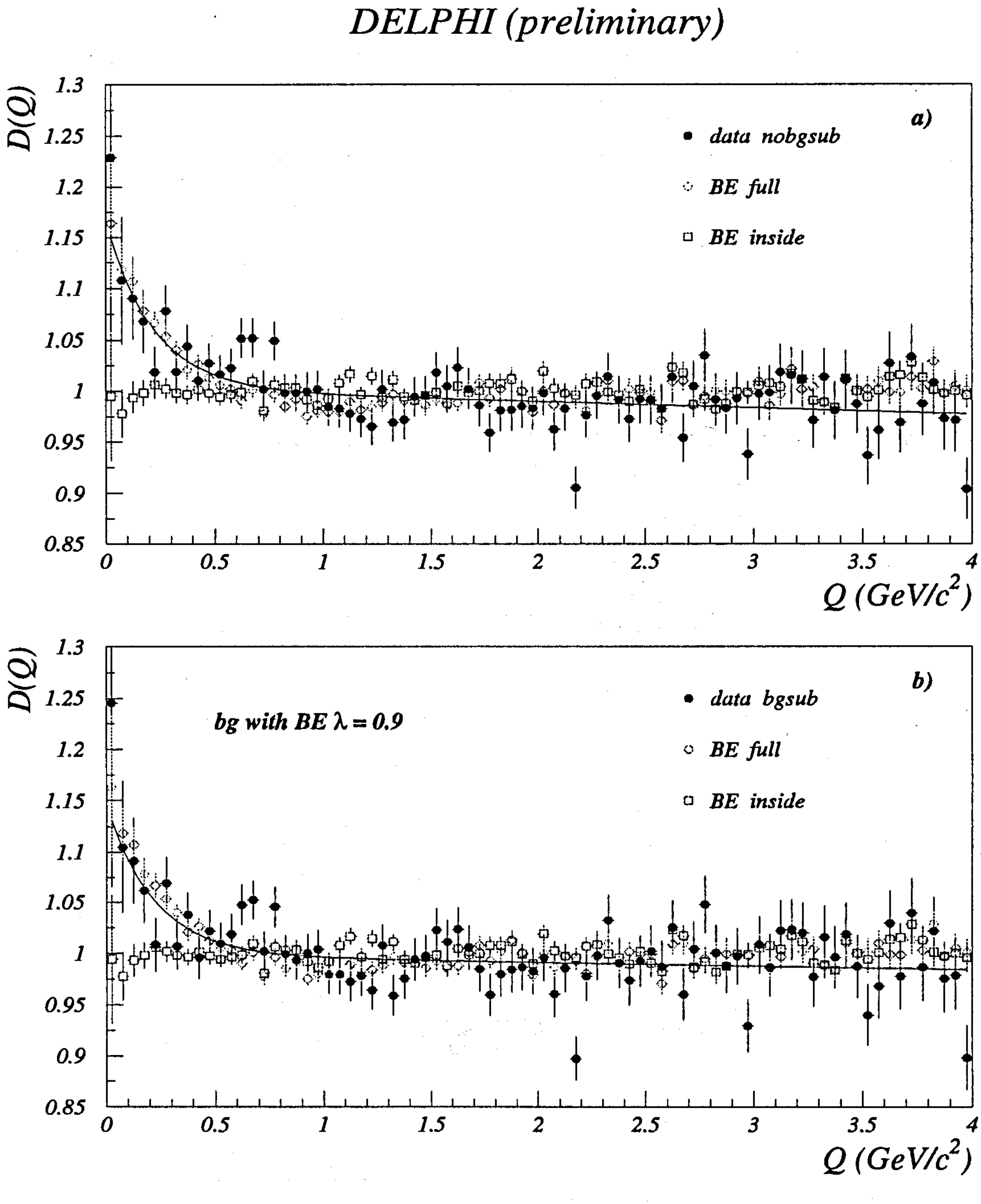

Figure 12: (a) The ratio $D(Q)$ of full hadronic to mixed events for data, for *full* BEC and for *inside* BEC. (b) same as (a) but after background subtraction from the data. The curves in figures show the best fit to expression (17) for data. The errors shown are propagation of sqrt(entries), but the fit results quoted in the text were obtained using the full covariance matrix.

DELPHI (preliminary)

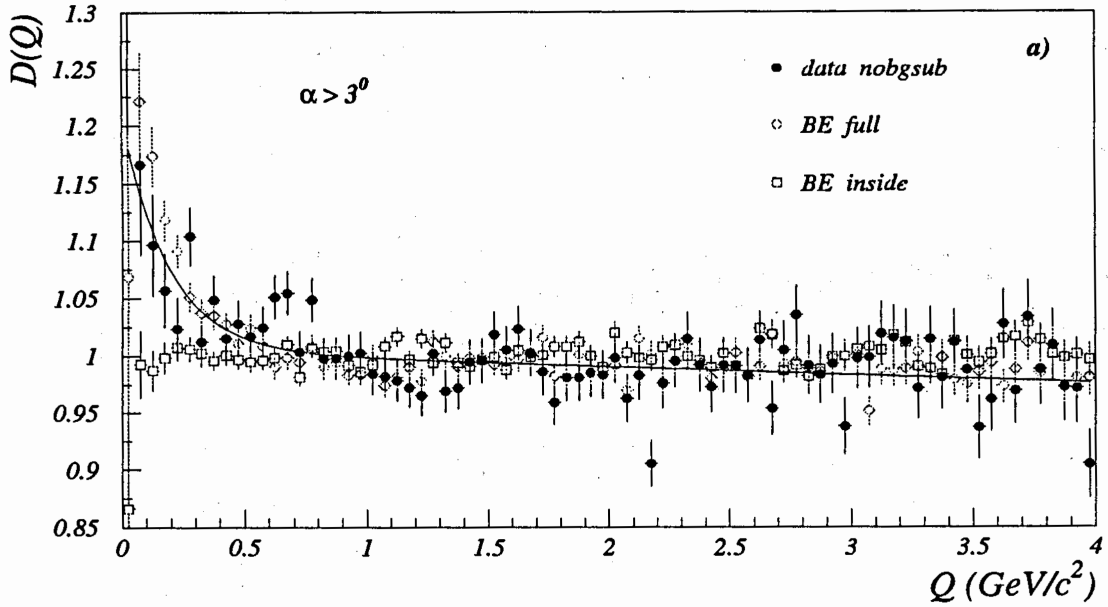

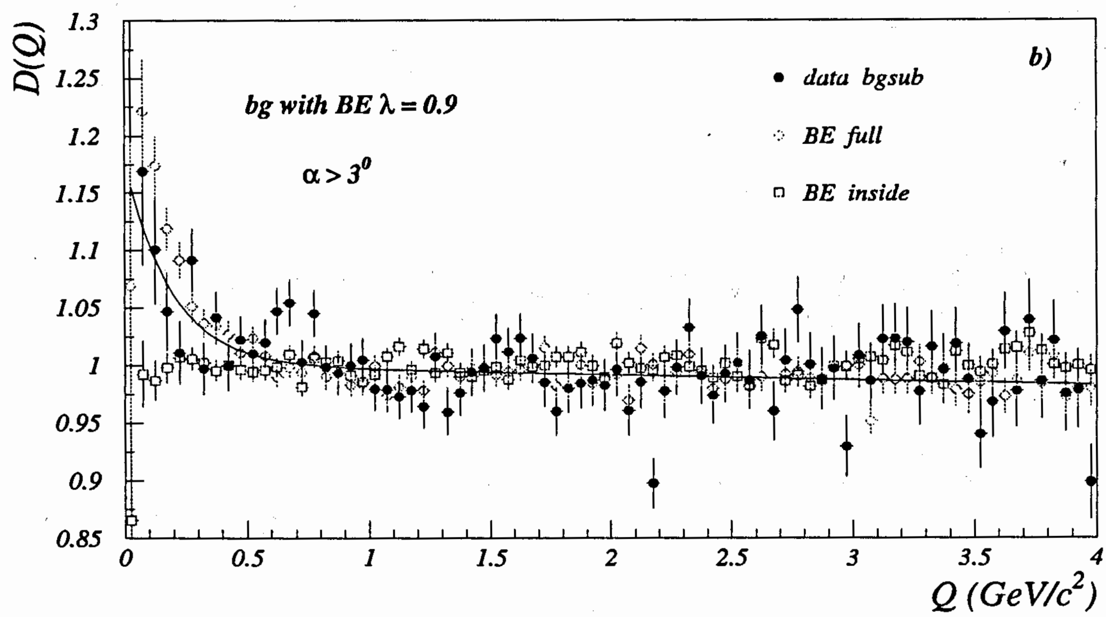

Figure 13: Same as in figure 12 but for $\alpha > 3°$ cut.

References

[1] *Physics at LEP2,* eds. G. Altarelli, T. Sjöstrand and F. Zwirner, CERN 96-01 (1996) Vol 1.

[2] L. Lönnblad and T. Sjöstrand, Eur. Phys. J. **C2** (1998) 165.
L. Lönnblad and T. Sjöstrand, Phys. Lett. **B351** (1995) 293.

[3] G. Lafferty, Z. Phys. **C60** (1993) 659;

[4] P.D. Acton et al., (OPAL Coll.), Z. Phys. **C56** (1992) 521.
P. Abreu et al., (DELPHI Coll.), Z. Phys. **C63** (1994) 17.
P. Abreu et al., (DELPHI Coll.), Z. Phys. **C65** (1995) 587.
D. Buskulic et al., (ALEPH Coll.), Z. Phys. **C69** (1996) 379.

[5] T. Sjöstrand, Comp. Phys. Comm. **82** (1994) 74;
T. Sjöstrand et al., Comp. Phys. Comm. 135 (2001) 238;
for more details see T. Sjöstrand, L. Lönnblad and S. Mrenna, *PYTHIA 6.2 Physics and Manual,* hep-ph/0108264.

[6] J. Hakkinen and M. Ringner, Eur. Phys. J. **C5** (1998) 275

[7] S.V. Chekanov, E.A. De Wolf, W. Kittel, Eur. Phys. J. **C6** (1999) 403.

[8] K. Geiger, J. Ellis, U. Heinz and U.A. Wiedemann, Phys. Rev. **D61** (2000) 054002.

[9] P. Aarnio et al. (DELPHI Coll.), Nucl. Instr. Methods **A303** (1991) 233.

[10] P. Abreu et al. (DELPHI Coll), Nucl. Instr. Methods **A378** (1996) 57.

[11] P. Abreu et al. (DELPHI Coll.), Phys. Lett. **B456** (1999) 310.

[12] F.A.Berends, R.Kleiss and R.Pittau, Nucl. Phys. **B424** (1994) 308.

[13] P. Abreu et al. (DELPHI Coll.), Z. Phys. **C73** (1996) 11.

[14] A. De Angelis and L. Vitale, Nucl. Instr. Methods **A423** (1999) 446.

[15] V. Perevoztchikov, M Tabidze and A. Tomaradze, *Influence of the bin-to-bin and inside-bin correlations on measured quantities*, DELPHI 2000 – 027 CONF 346

[16] P. Abreu et al. (DELPHI Coll.), Z. Phys. **C63** (1994) 17.

Jet reconstruction at CMS

Olga Kodolova, SINP MSU

✓ ***Jet reconstruction and jet energy correction in pp collisions***

Effect of jet finder cone size on energy/space resolution of jet

Including tracker information to jet energy measurement

✓ ***Jet reconstruction and jet energy correction in AA collisions***

✓ ***γ+jet and dijet in AA collisions***

Iterative cone algorithm (Snowmass convention) with calorimeter towers as an input is mostly used in CMS

Sampling and/or global jet energy corrections on the MC jet in the same cone is applied

---

We start to use tracks to improve jet energy resolution

We start to use algorithm with pile–up subtraction being developped for AA collisions (slides below) for high luminosity pile–up.

Factors influent on jet energy resolution (1:2)

From jet physics (from parton to jet on particle level):

- Fragmentation
- ISR and FSR
- Underlying event
- Minimum bias

From detector performance:

- Magnetic field
- Electronic noise
- Dead materials and cracks
- Longatudinal leakage for high−Pt jets
- Shower size, out of cone loss, jet separations

Factors influent on jet energy resolution (2:2)

- ➢ **Calorimeter (central region |η|<3) consists of two compartments: Crystal ECAL and Brass/Scintillator with WLS fibre readout, granularity $\Delta\eta \times \Delta\phi = 0.087 \times 0.087$**

and both has different response to electrons and hadrons

Non−linearity 15%

- ➢ **Jets have both hadronic (charged and neutrals) and e/γ components.**

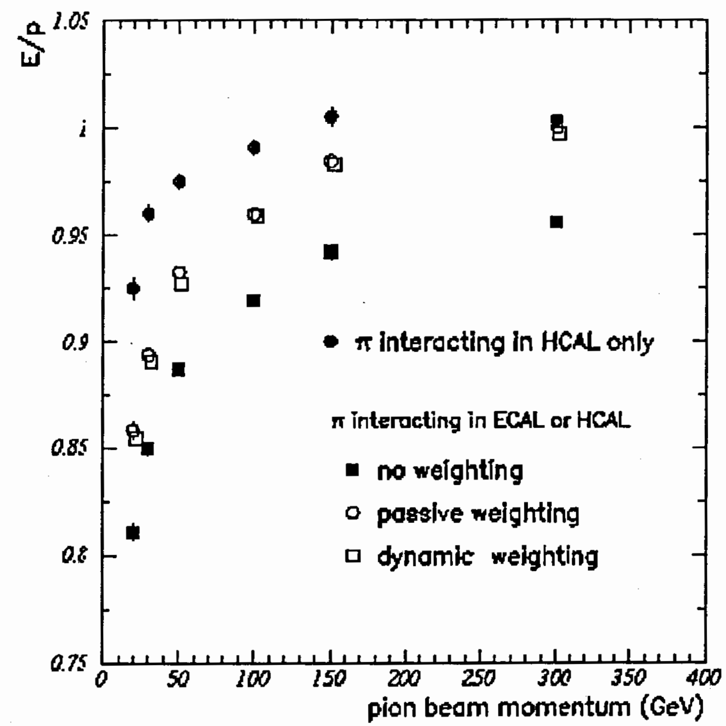

E/π for HCAL (1996 beam test)

Jet energy resolution in cone 0.5 for |eta|<0.7

$$\frac{sigma}{E} = \frac{119}{\sqrt{E}} \circ 7$$

Forward region (3</η/<5): Fe/Quartz fibre, cherenkov light, segmentation $\Delta\eta x \Delta\phi = 0.175x0.175$

Single pion resolution.

|η|<3

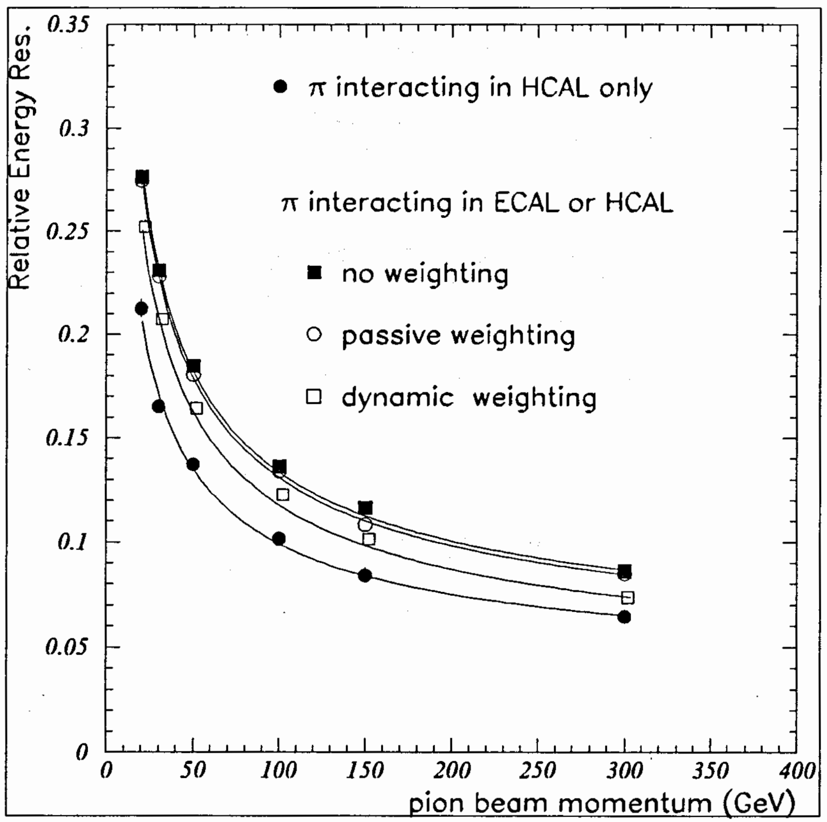

3<|η|<5 **E, GeV**

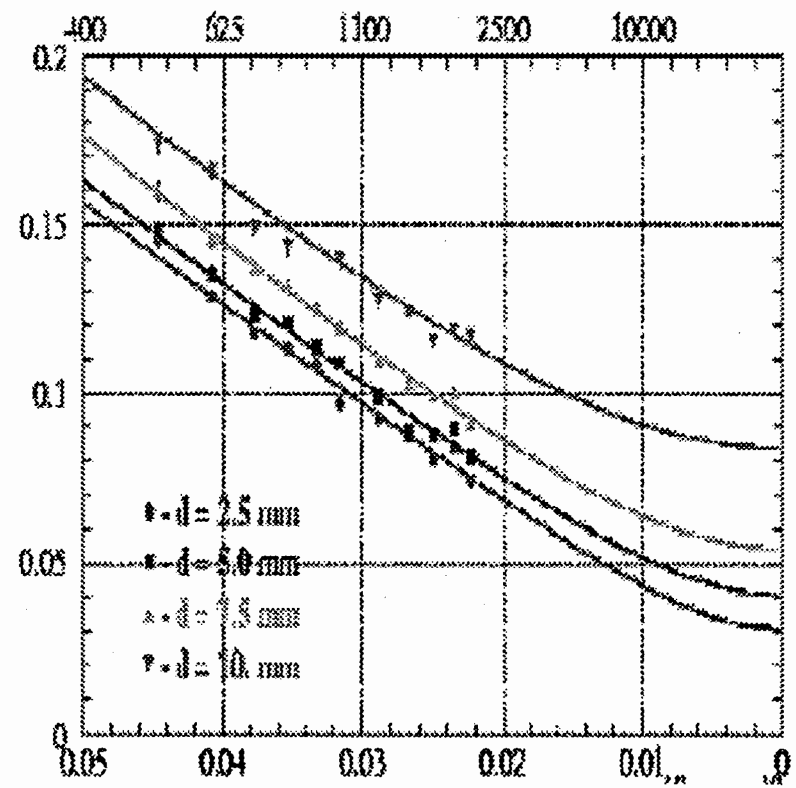

$E^{-1/2}$, GeV $^{-1/2}$

Jet correction with Erec(Egen) parametrisation: $E_{jet}^{rec} = A x E_{gen}^{2} + B x E_{gen} + C$

A.Krokhotine

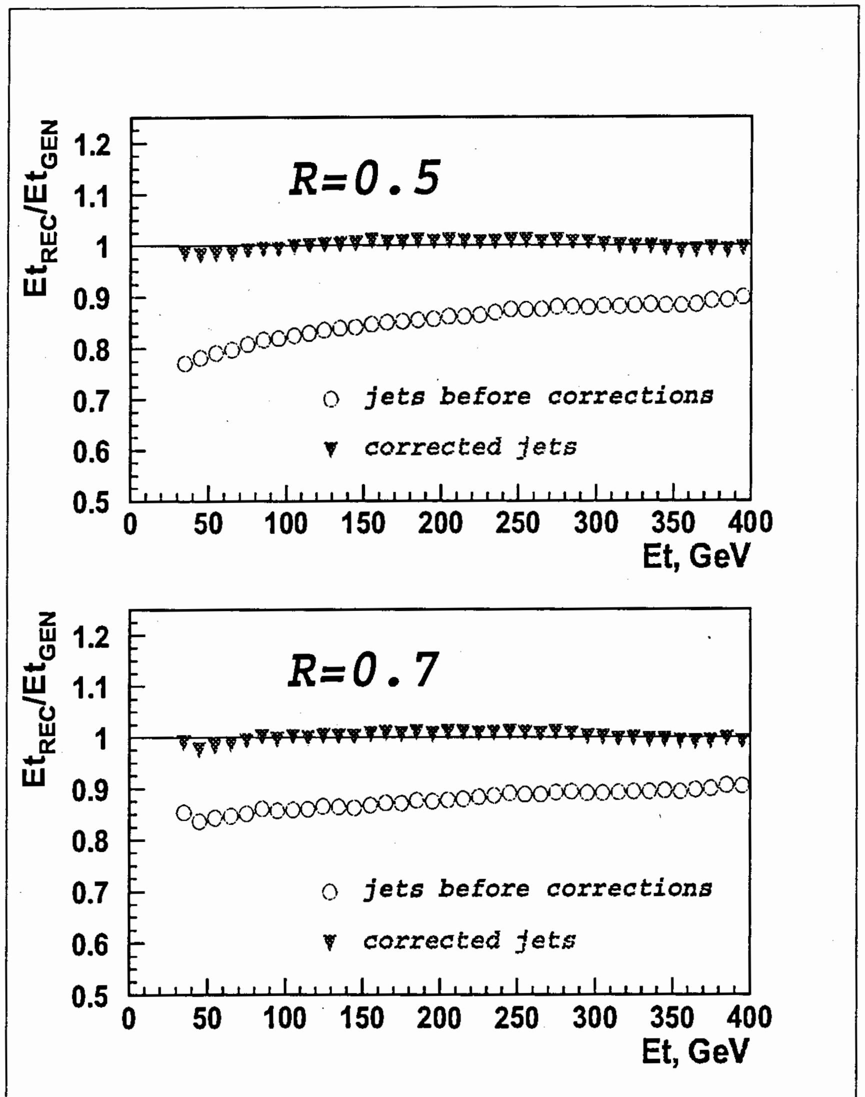

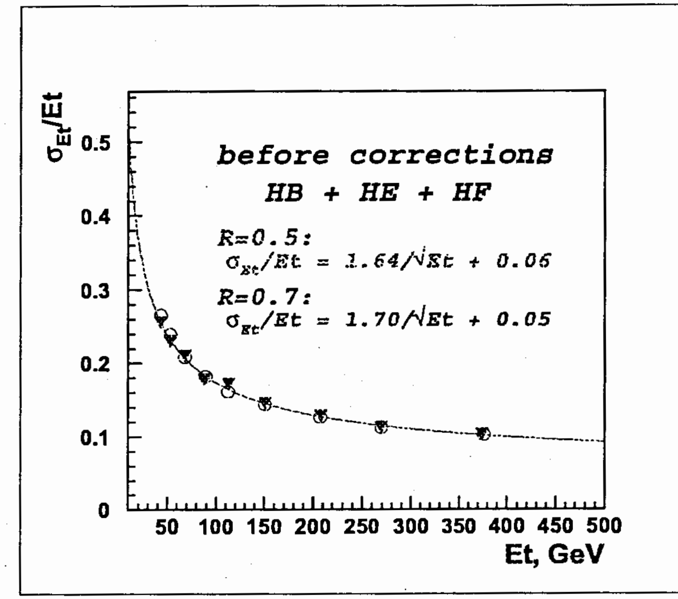

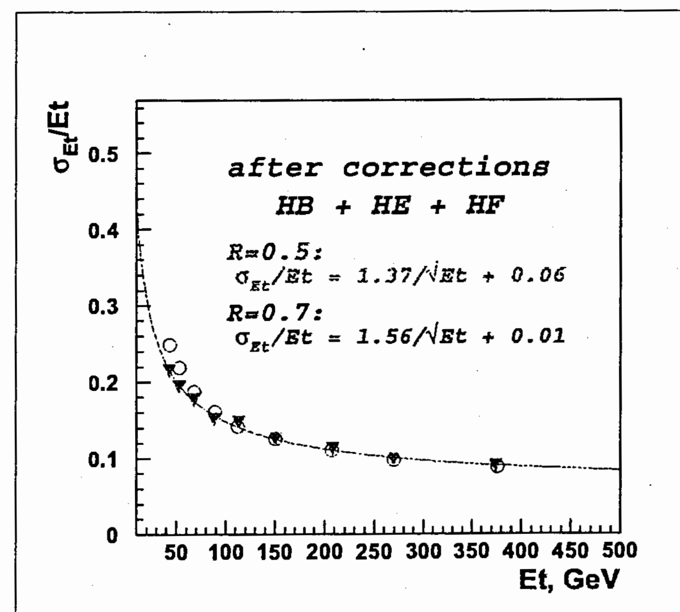

Using tracker information for jet energy corrections.

✔ *Example (A.Nikitenko): Jet with Et = 45 GeV.*

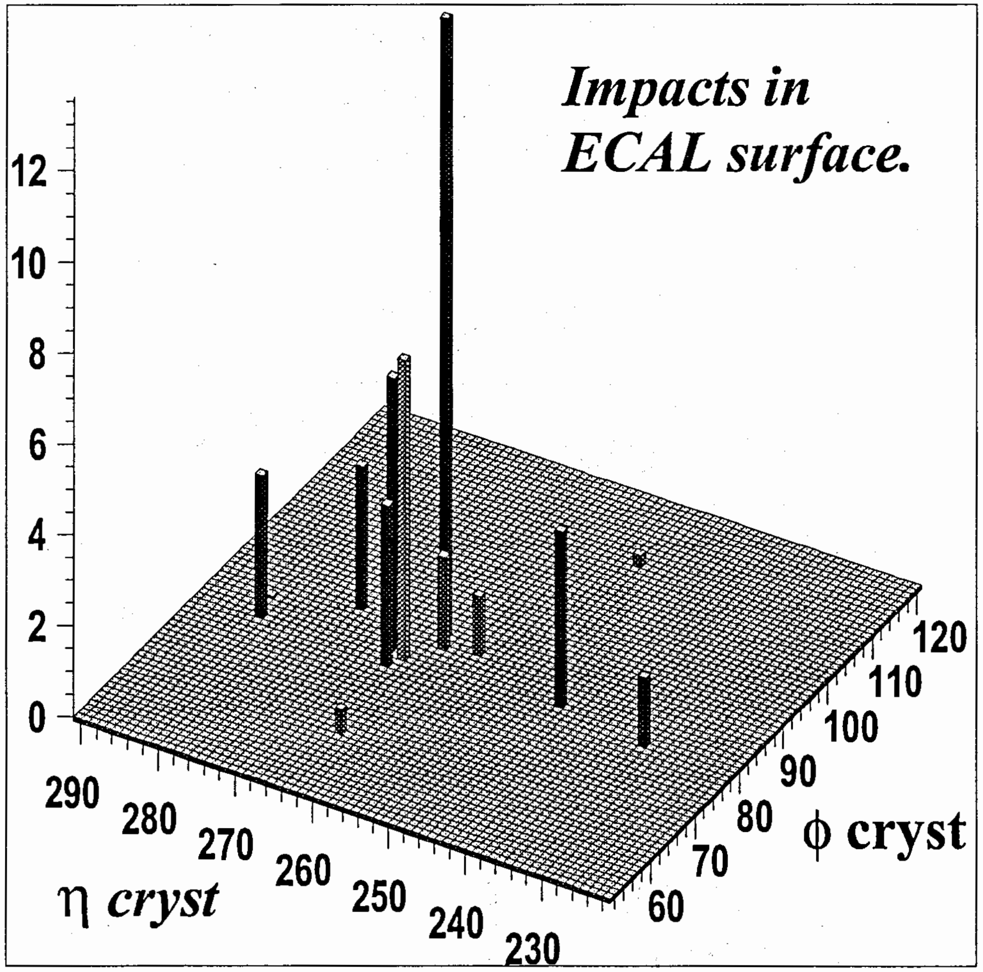

red – photons
blue – charged hadrons
green – neutral hadrons

✔ *Example (A.Nikitenko): Jet with Et = 45 GeV. (contin.)*

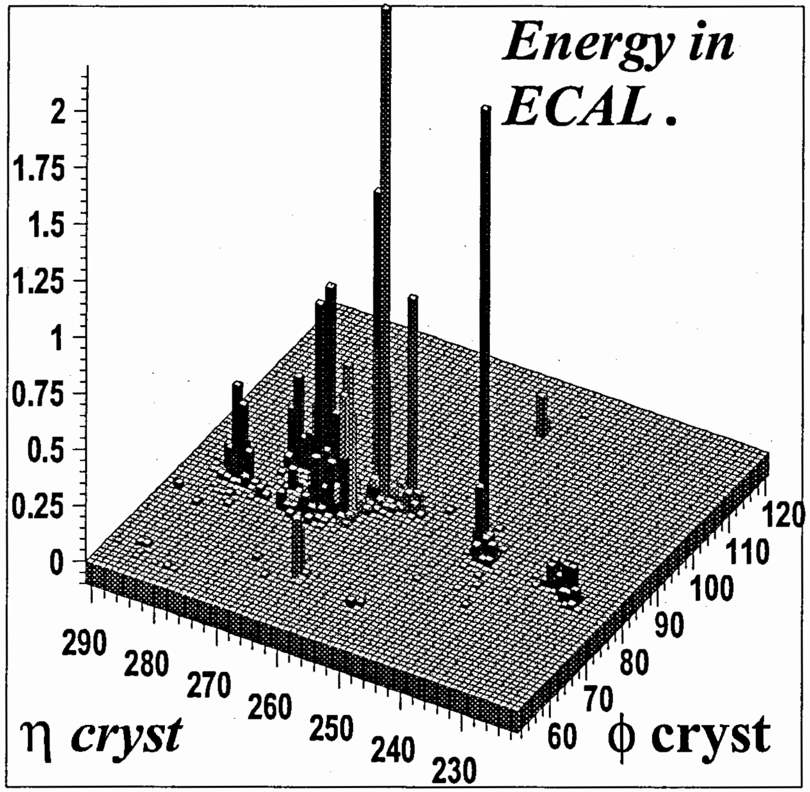

red – photons
blue – charged hadrons
green – neutral hadrons

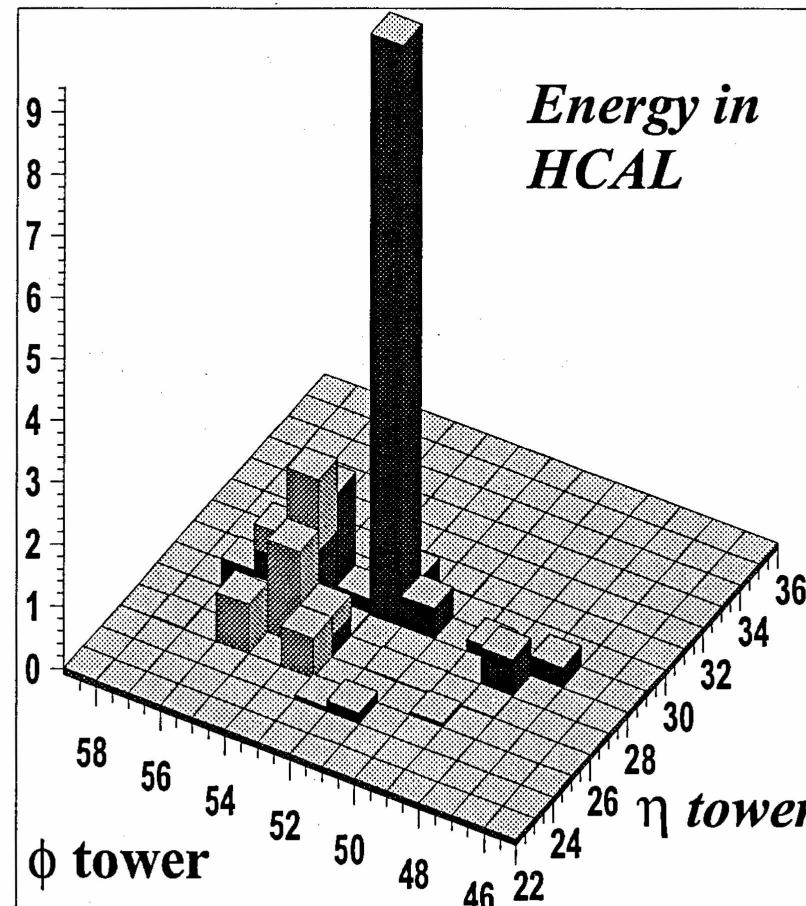

Part of clusters are isolated both in ECAL and HCAL and can be associated with charged tracks

Example (A. Nikitenko) Barrel jet of $E_T = 100$ GeV

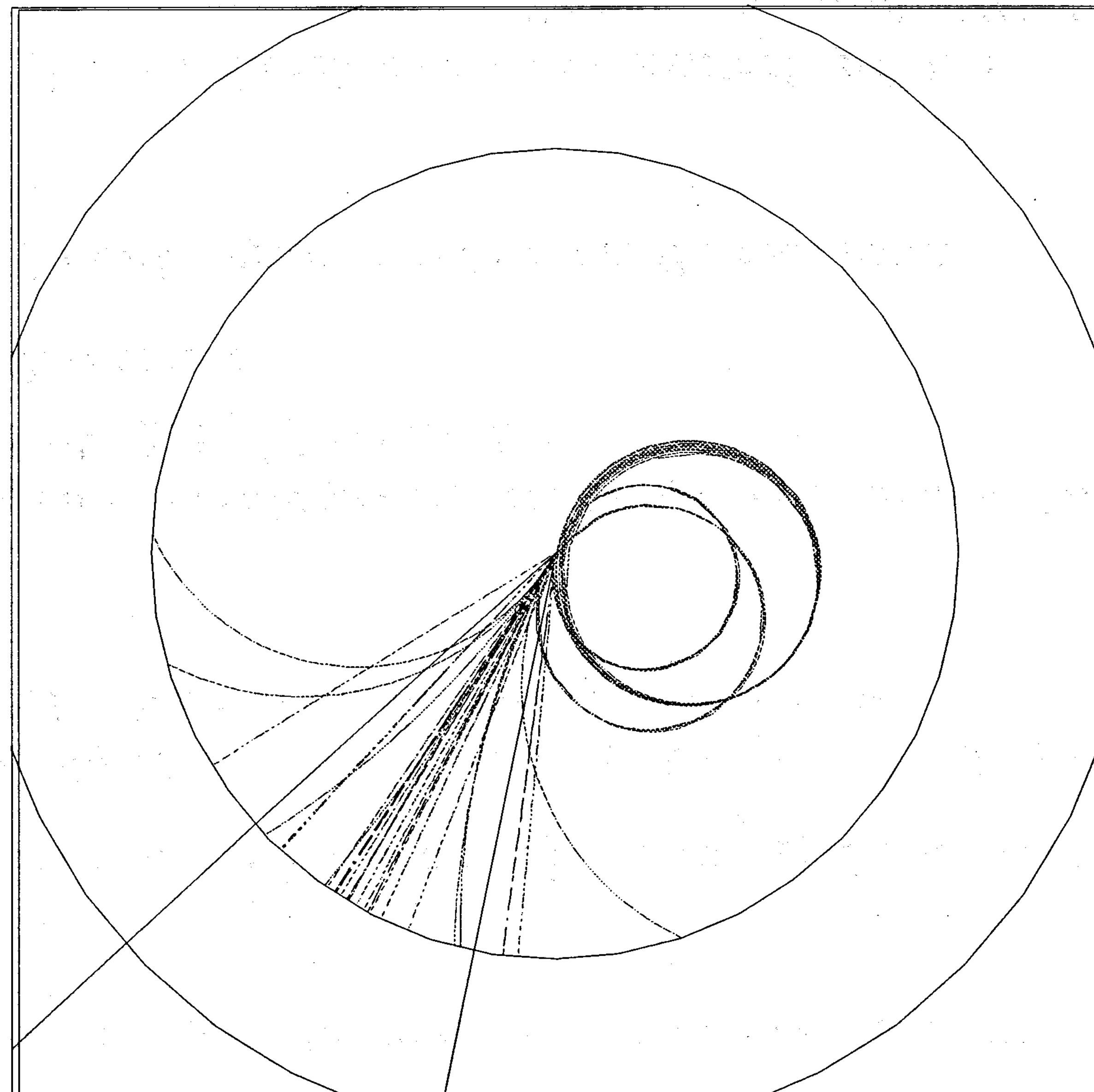

Part of charged tracks go out of the cone deflecting in magnetic field.

$$E_{Tjet}=E_{Tjet}^{in\ cone}+P_T^{trks}$$

Jet energy=Response_charged+Response (e/γ)+Response (neutral)

- **Change response of charged hadron of jet to energy from Tracker**

Use energy flow objects inside reco cone (exchange isolated clusters associated with charged track to an energy from tracker)
D.Green.

For overlapping clusters subtract expected responce of matched tracks within cone and add $\sum P_T^{trk}$ from tracker.
I.Vardanyan, O.Kodolova

- *Use tracks of the jet with impact in calo out of the reco cone.*

A.Nikitenko

Result: Jet energy=E_TRACKER+Response (e/γ+neutral)_ECAL+ Response (neutral)_HCAL

Procedure 1 (A.Nikitenko): add out of reco cone charged track.

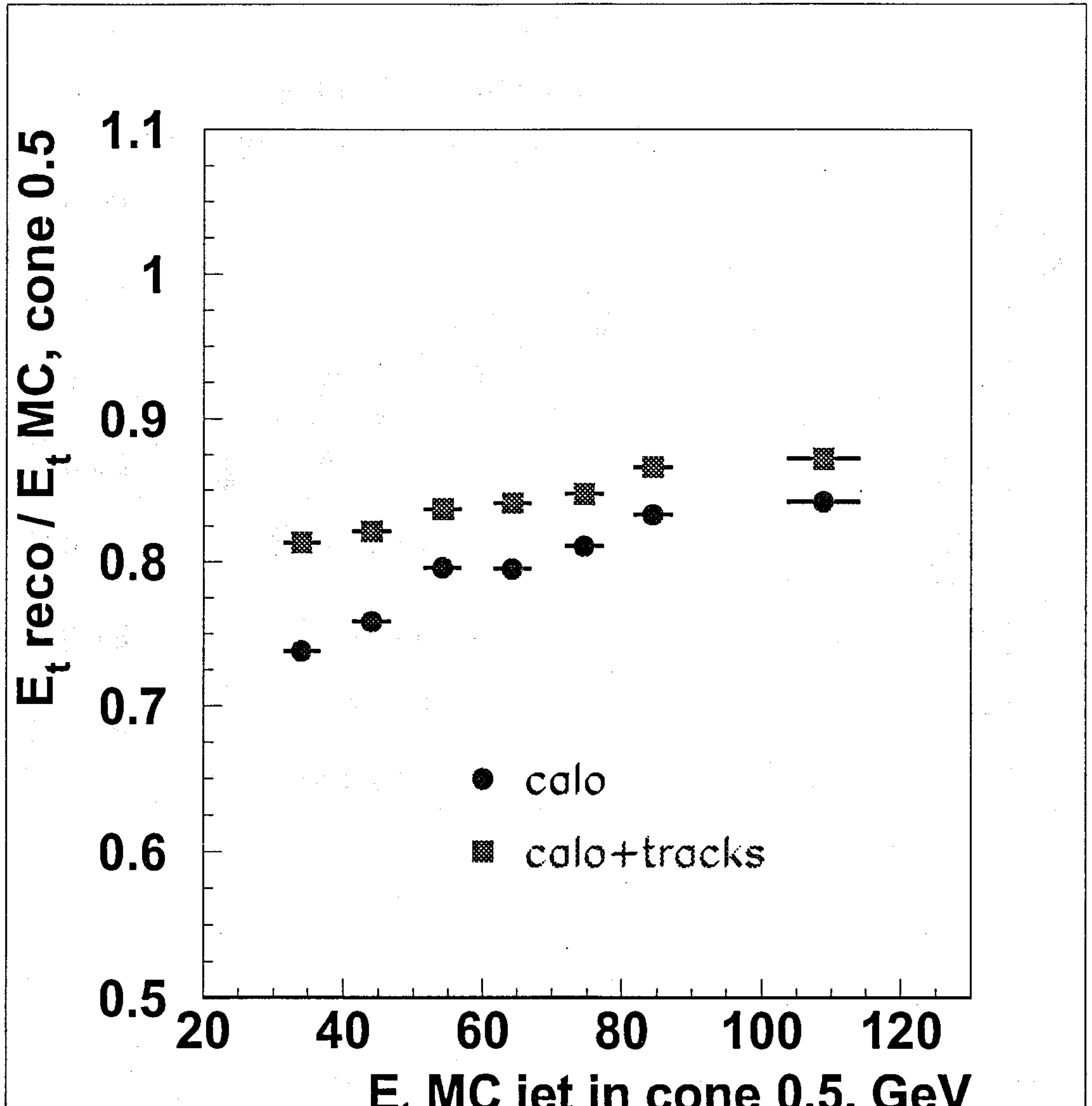

Calorimeter simulation with cmsim122 MC track used.

Jet was selected on the particle level and only particles in R=0.5 were propagated.

Jet energy is calculated:

$E_T^{jet} = E_T^{calo} + P_T^{out}$

P_T^{out} *–tracks out of cone*

Jet energy scale improved.

Improvement in resolution is the same order as in CDF for the low E_T jets.

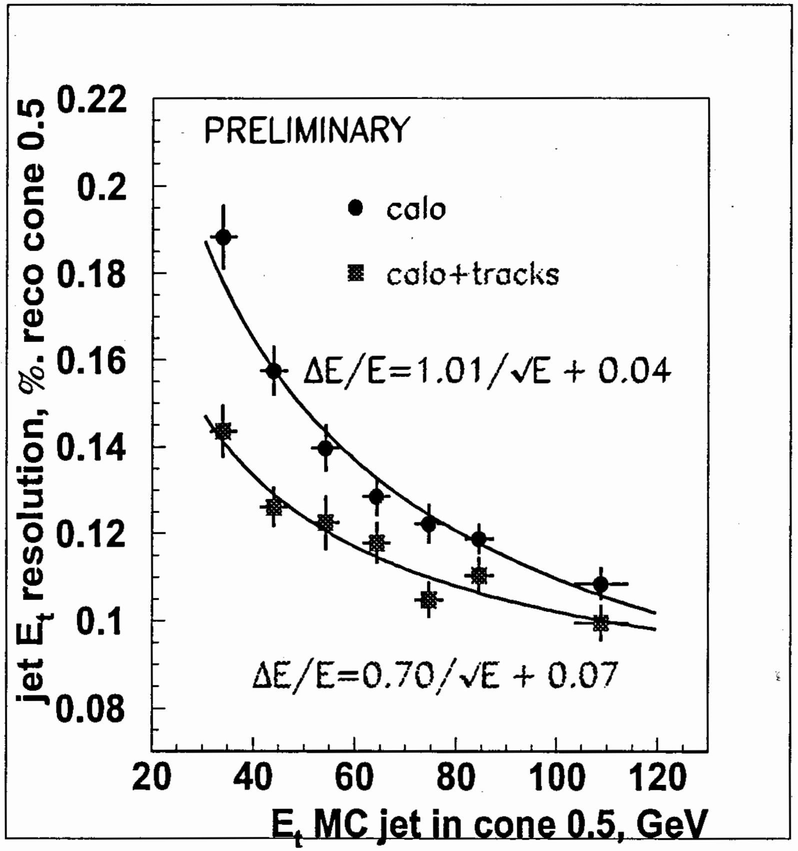

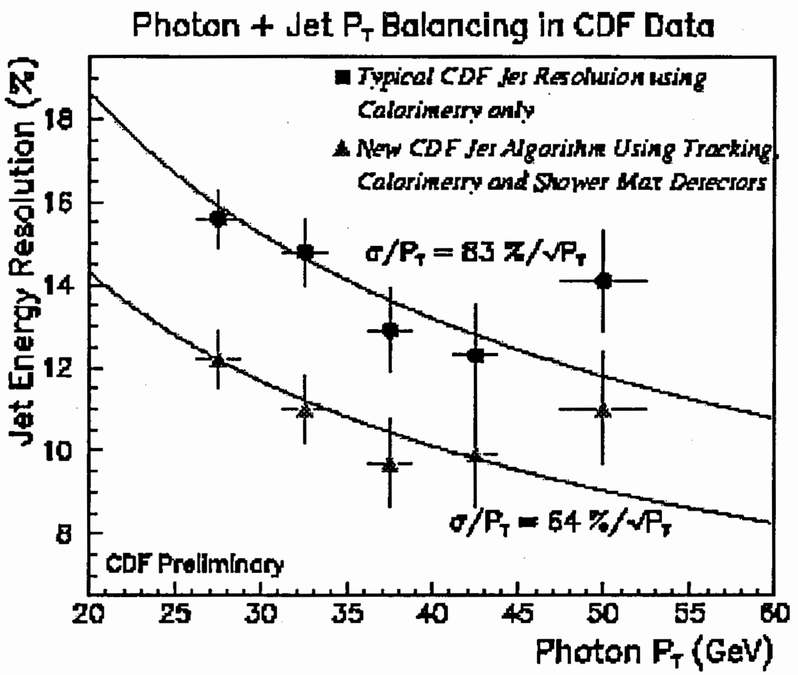

Procedure 2 (Dan Green) : energy flow objects.

Z(120) events were used. ISR and FSR were switched on.

Isolated clusters in ECAL (3x3) crystals and HCAL (3x3 towers) were found.

Cluster classification:

photon — *Cluster in ECAL has not associated hadronic energy.*

hadron — *Cluster in ECAL has associated hadronic energy of at least 30%.*

charged hadron interacted in ECAL — *If matched with tracker*

hadron interacted in HCAL — *Cluster in HCAL without sufficient ECAL energy*

All clusters within cone matched with tracks were extracted from E_{jet}^{calo} and P_T^{trk} was added instead.

$$E_{jet} = E_{jet}^{calo} - E_{clus}^{in\ cone} + P_T^{trks\ in\ cone}$$

Dijet mass

Calo clusters only

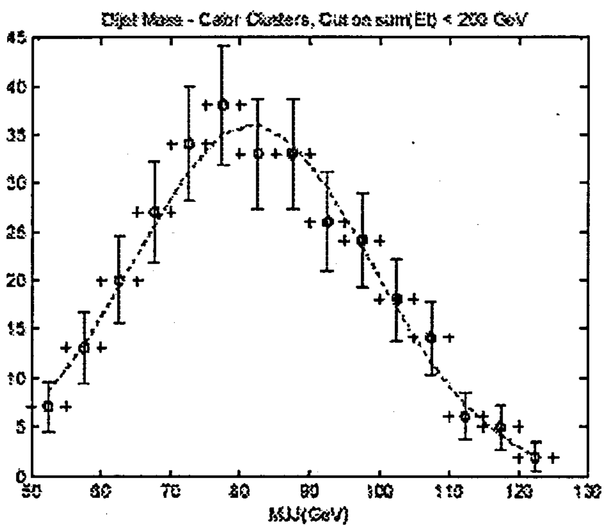

Mean=81.7+−1.1 GeV
Sigma=17.1+−1 GeV

Calo clusters+tracker

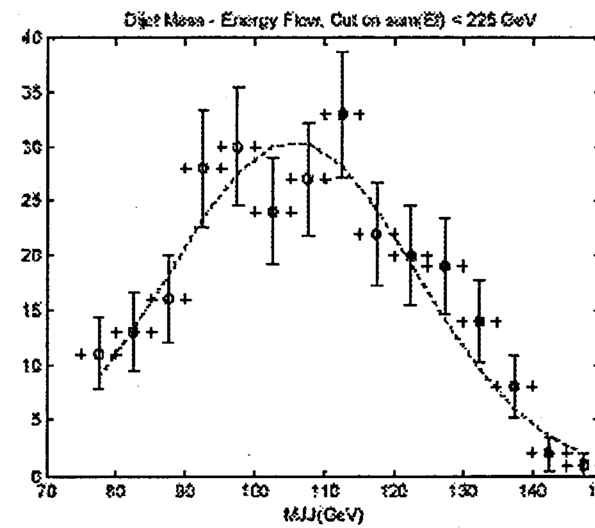

Mean=105.5+−1.1 GeV
Sigma=17.1+−1 GeV

Procedure 3 (O.Kodolova, I.Vardanyan): response subtracting

- ✔ **Energy (R(ECAL), R(HCAL) is calculated in cone around jet axis using standard procedure and with default coeffients.**
- ✔ **Summarized averaged response from charged particles with entry point inside a cone is subtracted from R(ECAL), R(HCAL).**
- ✔ **Expected response was calculated in different ways:**

  e/π technique (1), library of responses(2), matched cluster(3)

e/π technique, energy flow objects = matched cluster (D. Green, CMS NOTE's in draft).

$$E_{EM+neutral}(ECAL)=R(ECAL)-sum(R\_ECAL\_i)$$
$$E_{neutral}(HCAL)=R(HCAL)-sum(R\_HCAL\_i)$$

$$Etracker=sum(Etracker\_i)$$

$$Ejet=E_{EM+neutral}(ECAL)+E_{neutral}(HCAL)+Etracker$$

- ✔ **Tracks out of cone were added (A.Nikitenko)**

e/π technique (Version 1)

- For each interacted charged particle Dan Green's procedure to find response of this particle in ECAL and HCAL is used to calculate mean response in calorimeters.

For each charged the ratio of responses to electrons and pions is calculated:

$$e/\pi(ECAL)=e/h(ECAL)/(1+(e/h(ECAL)-1)*F0\_ECAL$$

$$e/\pi(HCAL)=e/h(HCAL)/(1+(e/h(HCAL)-1)*F0\_HCAL$$

$$F0\_ECAL=0.11*\log(E\_ECAL)$$

$$F0\_HCAL=0.11*\log(E\_HCAL)$$

F0_ECAL,HCAL−electromagnetic fraction of hadronic shower.
E_ECAL, E_HCAL − energy deposited in ECAL,HCAL e/h is obtained by fitting test−beam data.

- For each charged particle E3x3 around entry point is used to determine if particle interacts in ECAL or not. If E3x3>0.5 GeV charged particle is considered to be interacted in ECAL.

How deposited energy E_ECAL, E_HCAL are evaluated:

Particle interacted in ECAL

E_ECAL=0.4*Etracker (test beam, talk of J.Freeman)

E_HCAL=0.6*Etracker

Particle does not interact in ECAL

E_ECAL=E_MIP (energy from EM cluster)

E_HCAL=Etracker−E_MIP

Response from charged particles is calculated.

Particle interacted in ECAL

R_ECAL=E_ECAL/(e/π)(ECAL)

R_HCAL=E_HCAL/(e/π)(HCAL)

e/h(ECAL)=1.6

e/h(HCAL)=1.39

Particle does not interact in ECAL

R_ECAL=E_MIP

R_HCAL=E_HCAL/(e/π)(HCAL)

Library of responses (Version 2)

Mean responses were calculated using pion samples of different energies for the cases when pion is interacted in ECAL or not

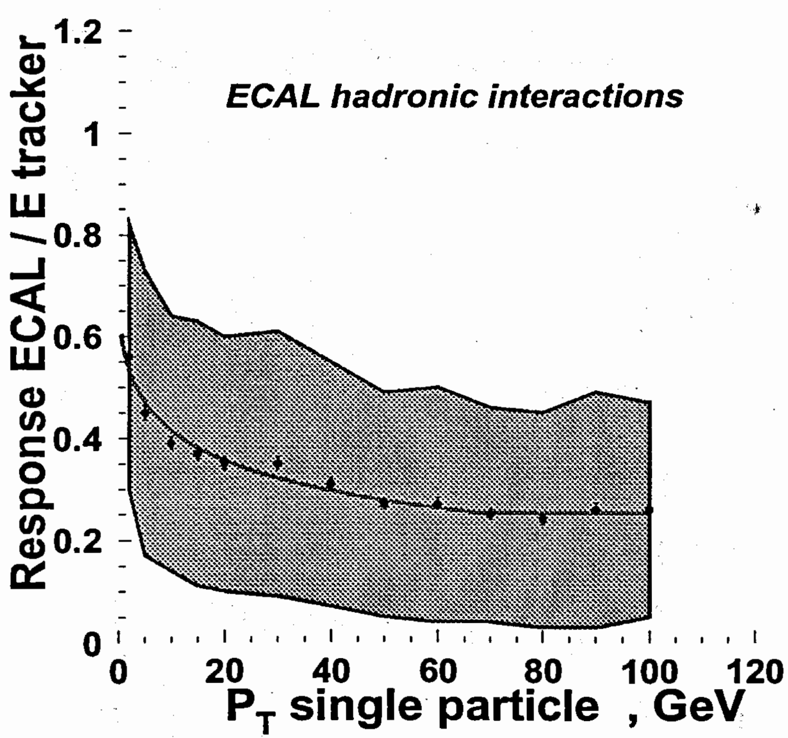

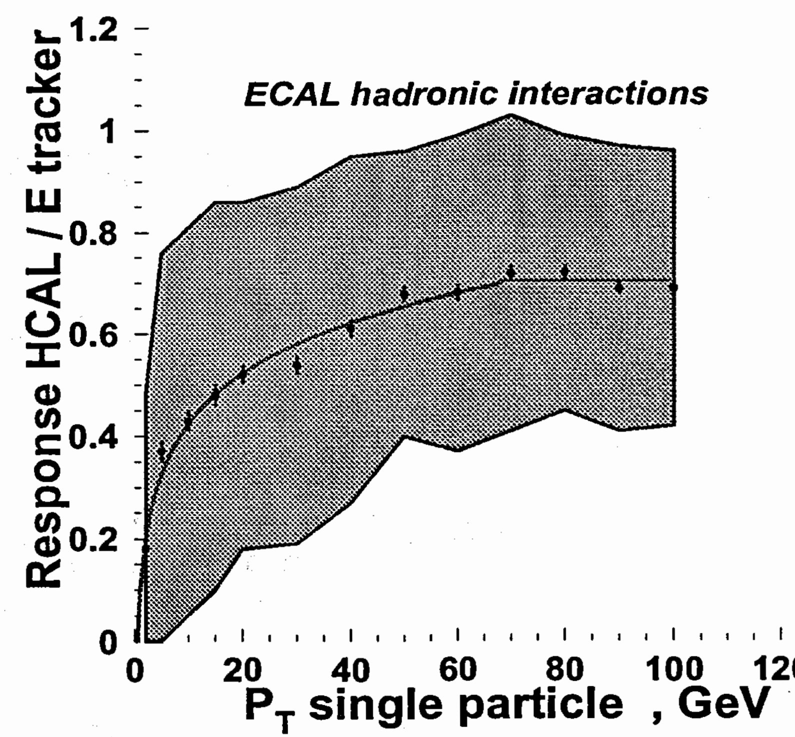

Matched cluster+library of responses (Version3)

- For each charhed particle (in reco cone) 3x3 ECAL crystal matrix was constructed around entry point. Cluster building starts from maximal track.
- For each charged particle (in reco cone) 3x3 HCAL tower matrix was constructed around entry point.
- Energy response in ECAL+HCAL cluster (3x3 crystal+ 3x3 tower) was compared with Etracker for this particle
- Energy of cluster matched with track was changed to the energy of particle in tracker.

Cluster is matched with track if: $-\sigma < (E_{tracker} - E_{cluster})/E_{tracker} < 2\sigma$

$$\sigma / E = 100\%/sqrt(E) \oplus 5\%$$

- For tracks non–matched cluster expected response subtraction procedure was applied (1,2).
- Charged particles out of reco cone were added

Mean number of all charged particles with hit within reco cone and mean number of particles matched with clusters for different jet energy (left figure). Distribution the number of all charged and charged matched with clusters for jet energy 100 GeV (right figure).

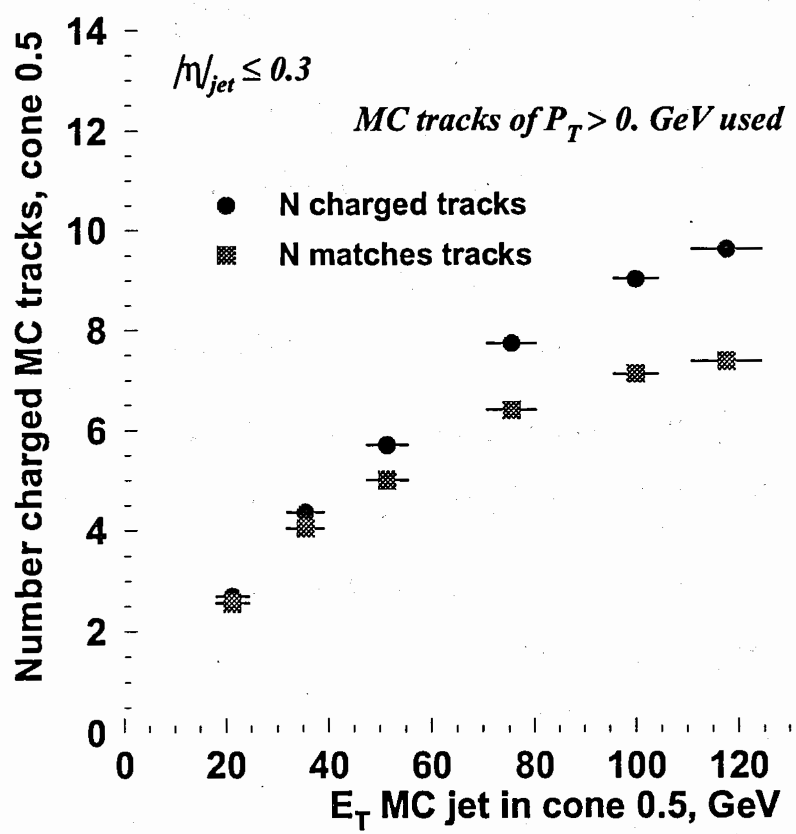

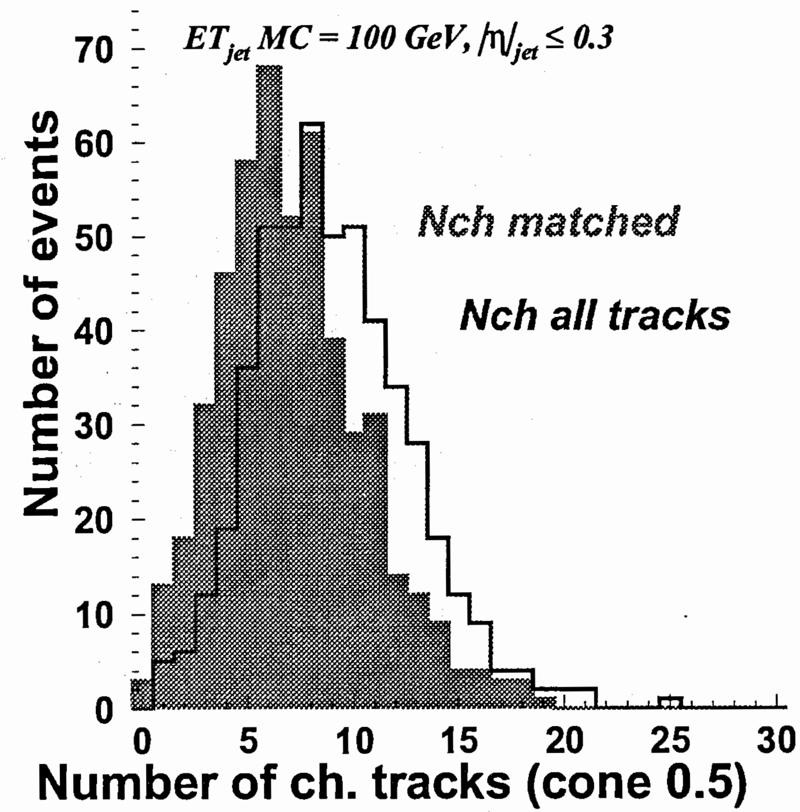

Resolution and mean ETrec/ETgen for different MC jet energy.

Three options are used for calculating expected response: e/π technique (calo+tracks(1)), library of responses (calo+tracks (2)), matched clusters+library of responses (calo+tracks(3))

for 20 GeV: from 24% to 14%

for 100 GeV: from 12% to 8%

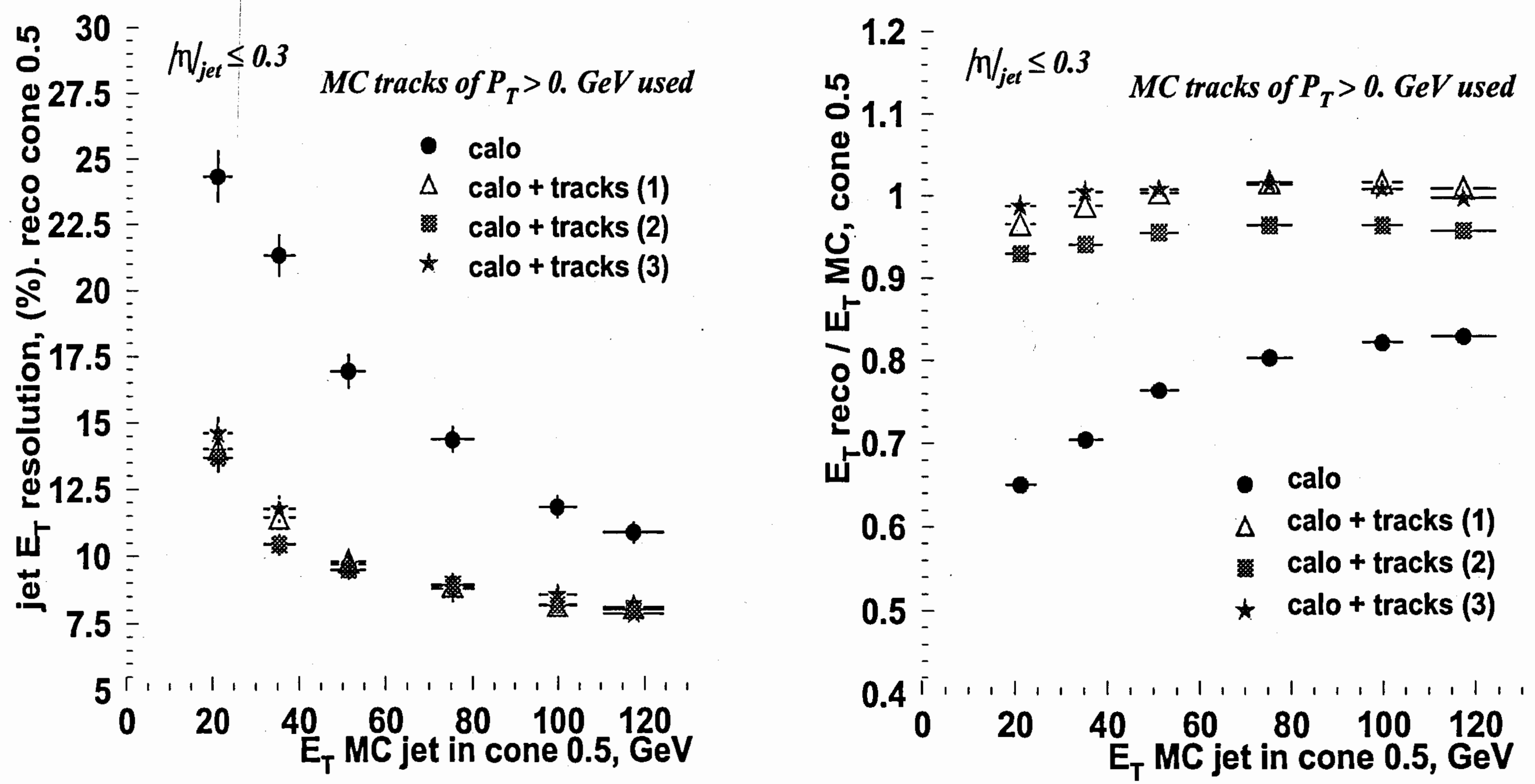

Why for expected response subtraction $D(E_{jet}^{rec}/E_{jet}^{gen})/\langle E_{jet}^{rec}/E_{jet}^{gen}\rangle$ should be better:

Only calorimeter information:

$$E_{jet}^{calo}=\sum \mathrm{Response}\,(e/\gamma)+\sum \mathrm{Response}(\mathrm{neutral})+\sum \mathrm{Response}(\mathrm{charged})$$

$$D(E_{jet}^{calo})=\sum D(\mathrm{Response}(e/\gamma))+\sum D(\mathrm{Response}(\mathrm{neutr}))+\sum D(\mathrm{Response}(\mathrm{char}))$$

Include Tracker information:

$$E_{jet}^{tracker}=\sum \mathrm{Response}\,(e/\gamma)+\sum \mathrm{Response}(\mathrm{neutral})+\sum \mathrm{Response}(\mathrm{charged})-\sum \mathrm{Response}(\mathrm{charged})\_\mathrm{teor}+\sum E\mathrm{tracker}=$$

$$=E_{jet}^{calo}+\sum E\mathrm{tracker}-\sum \mathrm{Response}(\mathrm{charged})\_\mathrm{teor}$$

$$D(E_{jet}^{tracker})=D(E_{jet}^{calo})+\sum D\left(E\mathrm{tracker}\right)+\sum D(\mathrm{Response}(\mathrm{charged})\_\mathrm{teor})=$$

$$=D(E_{jet}^{calo})$$

Statistical error is kept unchanged but mean energy become closer to it's value on generator level. But there is a systematical error connected with expected response calculations.

Minimization of systematical error can be made with Z–>jj for example.

Jet reconstruction in heavy ion collisions (I.Vardanyan)

Pb–Pb, $dN^{ch}/dy=8000$

Barrel:
$\langle E_T^{tower}\rangle = 4.7 \pm 1.4$ *GeV*

Endcap:
$\langle E_t^{tower}\rangle = 11.8 \pm 5.3$ *GeV*

Most of the energy is deposited in ECAL

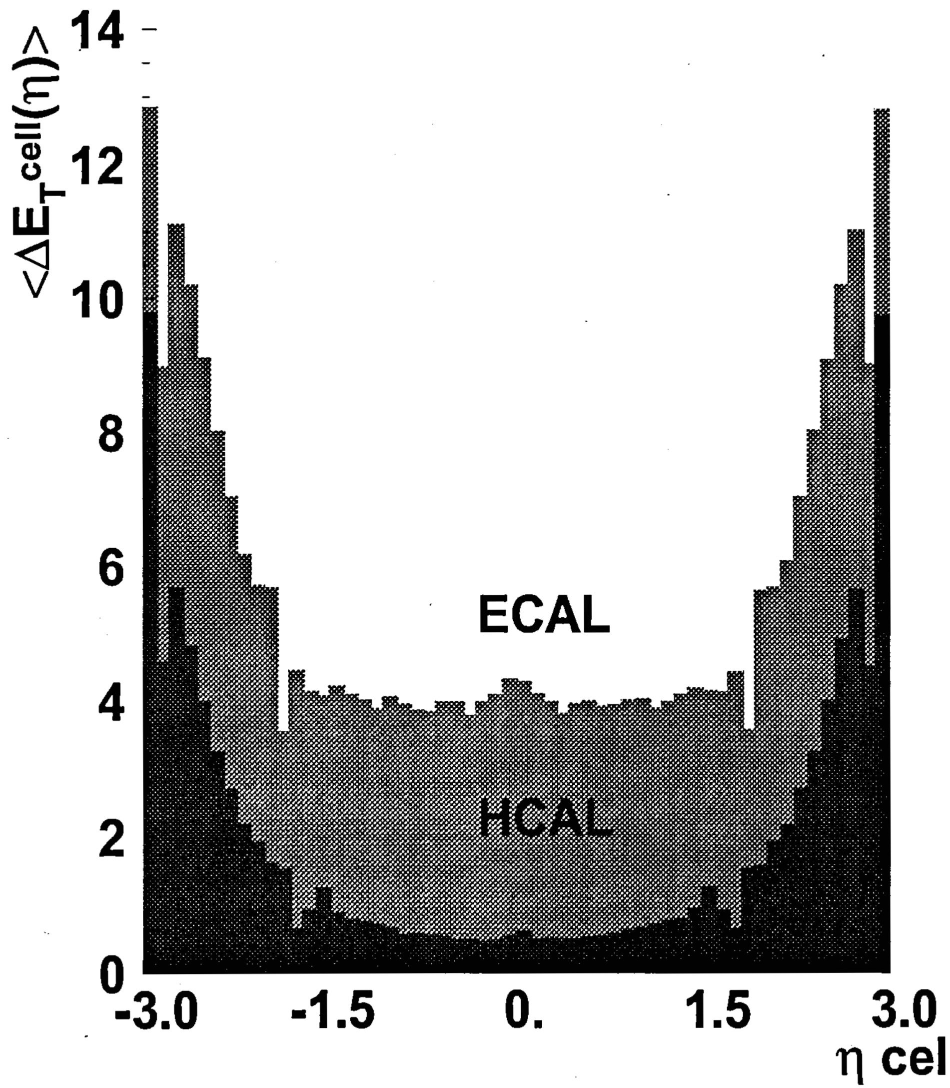

Jet reconstruction algorithm in AA

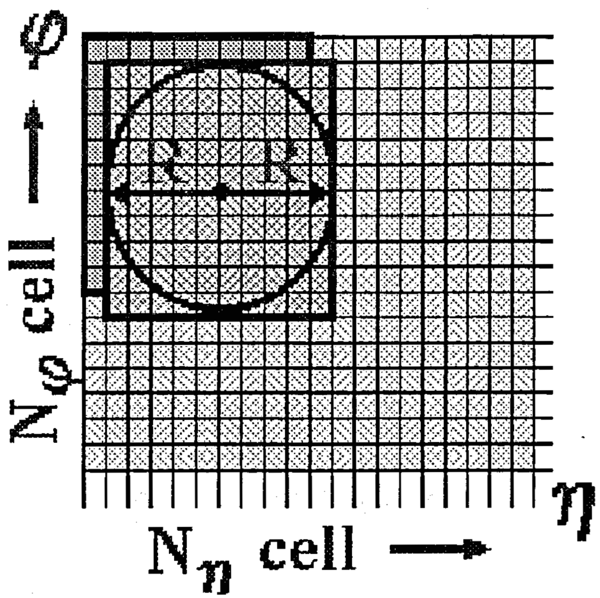

- ***Calculate*** $<E_t^{tower}(\eta)>$ ***and*** $D^{tower}(\eta)$ ***at each*** η ***ring of towers for GIVEN event***

- ***Sliding window runs with step one tower in*** η,ϕ

- $E_t^{candidate} = E_T^{window} - E_T^{pile-up}$

  $E_t^{pile-up} = sum(<E_t^{tower}(\eta)> + D^{tower}(\eta))$

- ***Non−overlaping windows of*** $E_T^{window} > E_t^{cut}$ ***are considred as candidates***

- ***Build cone (radius=R) around max*** E_t^{tower} ***of the candidate***

- ***Recalculate pile up with towers outside of the jet cones and calculate jet energy again as*** $E_t^{jet} = E_t^{cone} - E_t^{pile-upnew}$

Jet of ET=40 GeV in HF (K.Teplov)

No heavy ion collisions

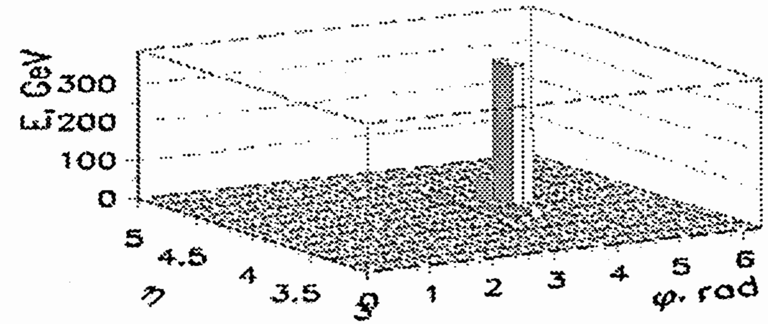

With Ar−Ar central collision
dN^{ch}/dy=800

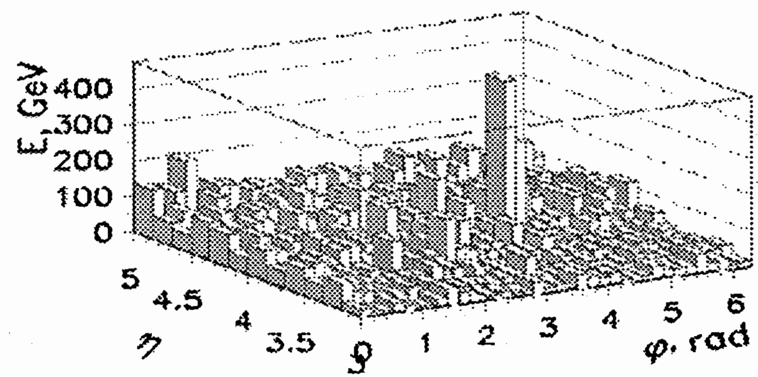

With Ar−Ar central collision
and pile−up subtraction

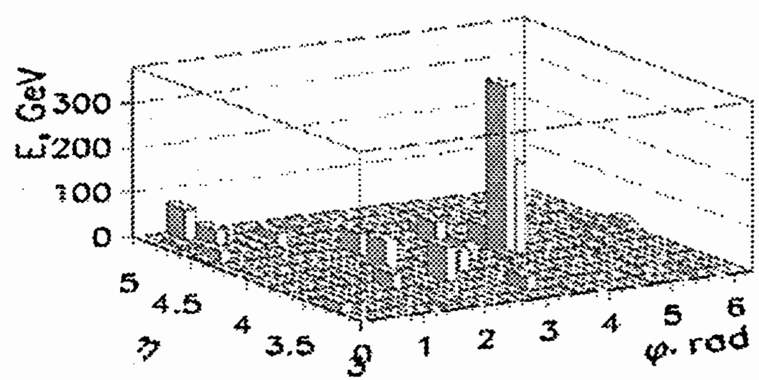

We include "purity" for the reconstructed jet sample.

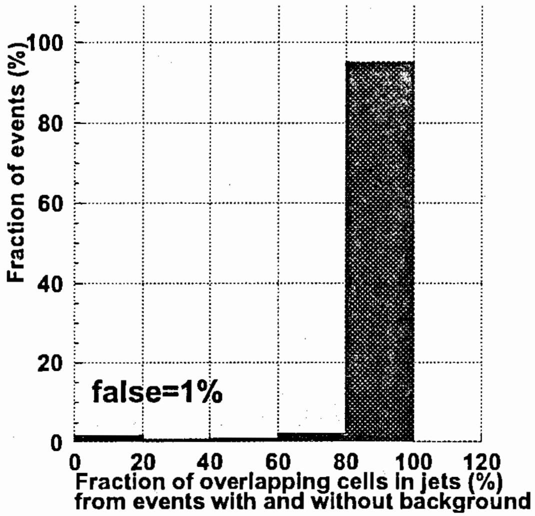

✔ **Find jet without soft AA background**

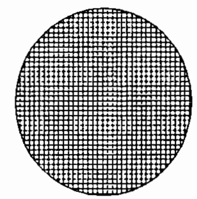

✔ **Find the same jet with AA background and calculate the number of common cells**

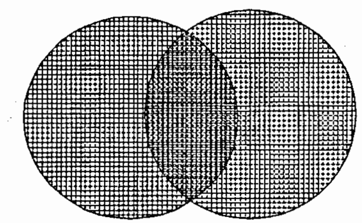

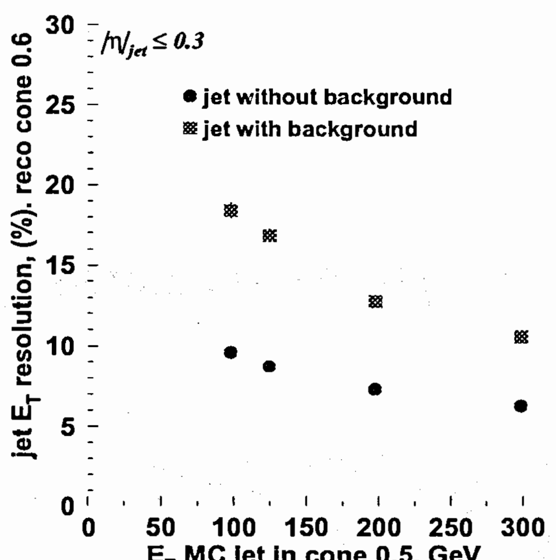

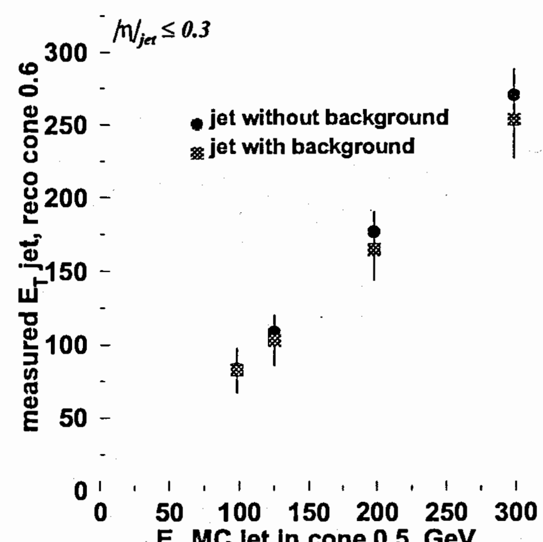

Efficiency to find the true jet.

Barrel	*HF*

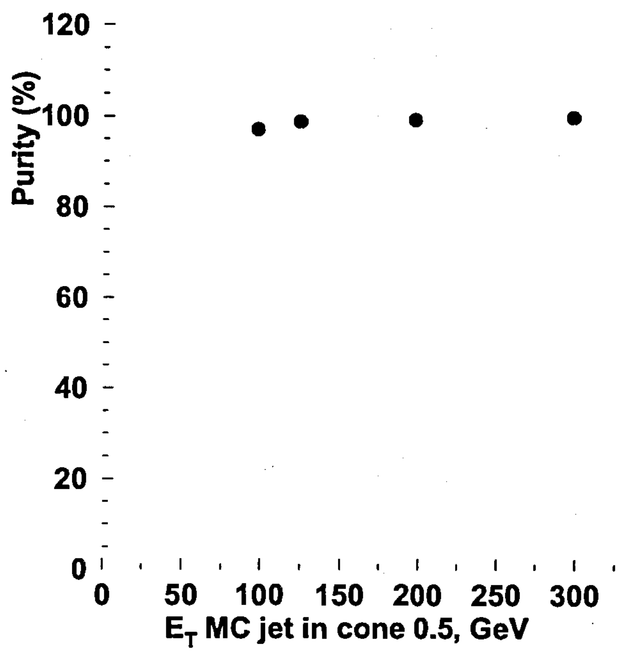

Purity vs ET of MC jet

Central Pb−Pb, dN^{ch}/dy=8000

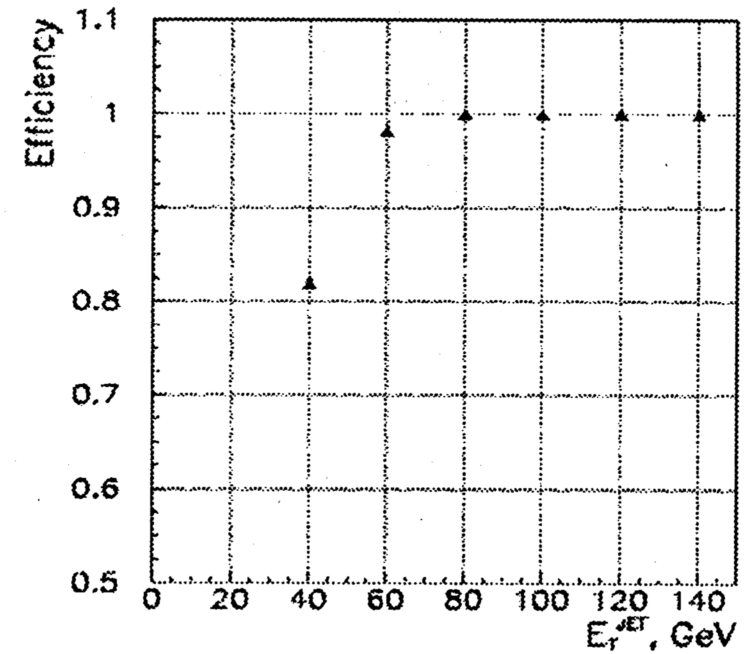

Purity vs ET of MC jet

Central Ar−Ar, dN^{ch}/dy=800

Degradation of ϕ resolution of jets of Et=100 GeV in Pb−Pb central collision (dNch/dy=8000)

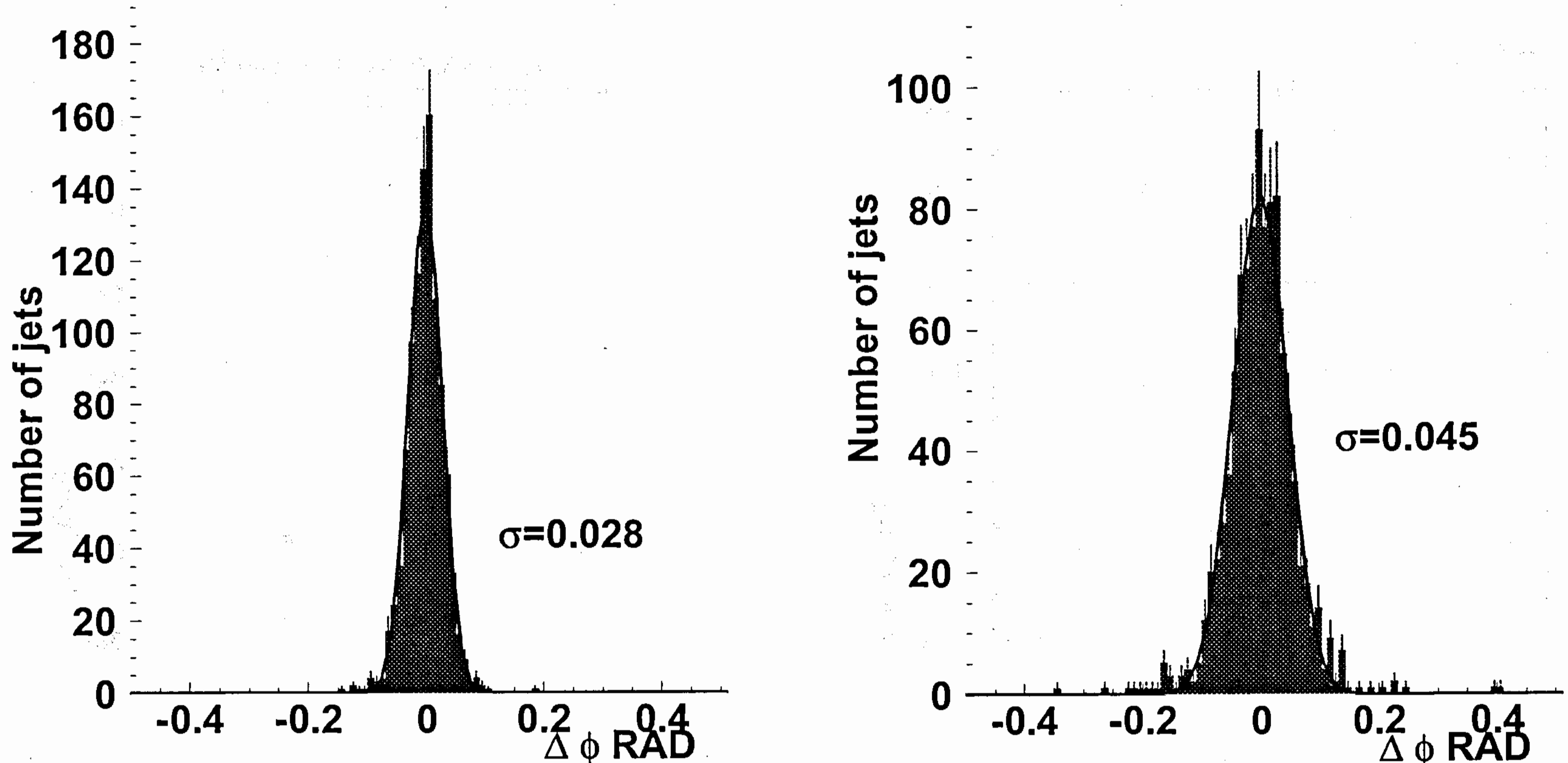

Still better than ϕ size of calorimater tower − 0.087

Summary

✓ *Jet reconstruction in pp is performed with iterative cone algorithm for the low and high luminosity cases. However, the observed effect of cone size so as the number of false jets with Et~20 GeV shows the nessecity to apply background subtraction procedure already in pp collisions at the case of High Luminosity.*

✓ *Including tracker information to jet energy measurement gives essential improvement of the jet energy resolution:*

for 20 GeV: from 24% to 14%

for 100 GeV: from 12% to 8%

so as jet energy linearity

The next step is to include full reconstruction in tracker.

✓ *Jet reconstruction algorithm based on background subtraction procedure was developped for AA collisions. The same algorithm can be useful for the High Luminosity pile−up events in pp collisions.*

✓ *γ+jet and dijet events can be used in CMS to investigate additional parton energy losses in AA collisions.*

Russian Regional Center for LHC Data Analysis

by O.Kodolova

On the base of the Conception approved on 24 August 2001
by Scientific Coordination Board
of Russian Regional Center for LHC Computing

Russia will participate in LHC computing through creating

Russian Regional Center for LHC (RRC–LHC)

RRC–LHC should be a functional part of the world–wide distributed LHC computing GRID infrastructure, and it is created in the framework of a common project for the all four LHC experiments:

ALICE, ATLAS, CMS, LHCb.

All institutes will participate:

Moscow – INR RAS, ITEP, KI, LPI, MEPhI, MSU …
Dubna – JINR
Protvino – IHEP
St–Petersburg – PNPI RAS, StP U., …
Novosibirsk – INP SD RAS
…

Goals

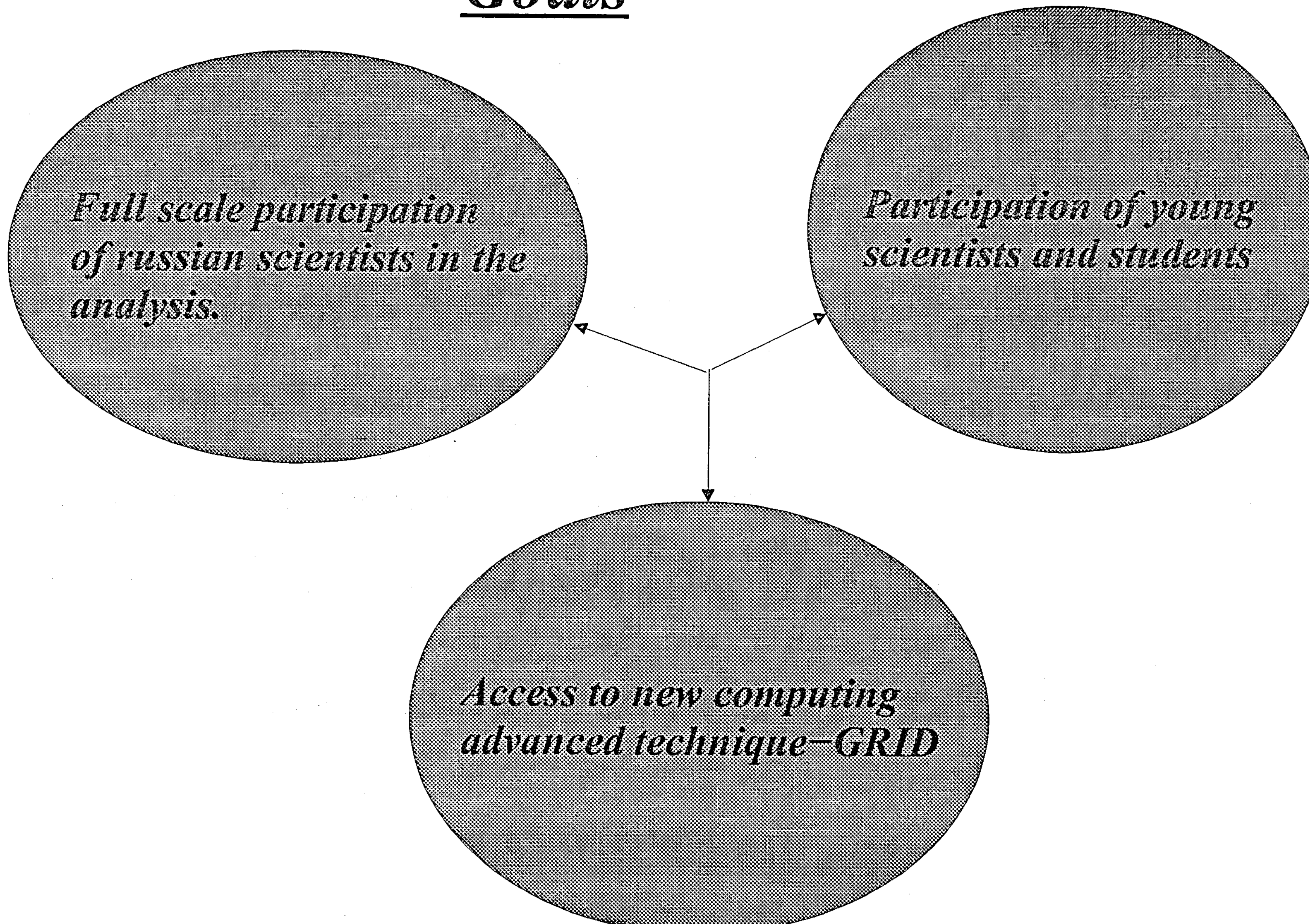
Full scale participation of russian scientists in the analysis.
Participation of young scientists and students
Access to new computing advanced technique–GRID

Functions

- Physical analysis of AOD (Analysis Object Data);
- access to (external) ESD/RAW and SIM data bases
    - ❑ for preparing necessary (local) AOD sets;
- replication of AOD sets from the other centers;
- event simulation
    - ❑ at the level of 5–10% of the whole SIM data bases for each experiment;
- replication and store of 5–10% of ESD
    - ❑ required for testing the procedures of the AOD creation;
- storage of data produced by users.

The opportunity of Grid technology

LHC Computing Model
2001 – evolving

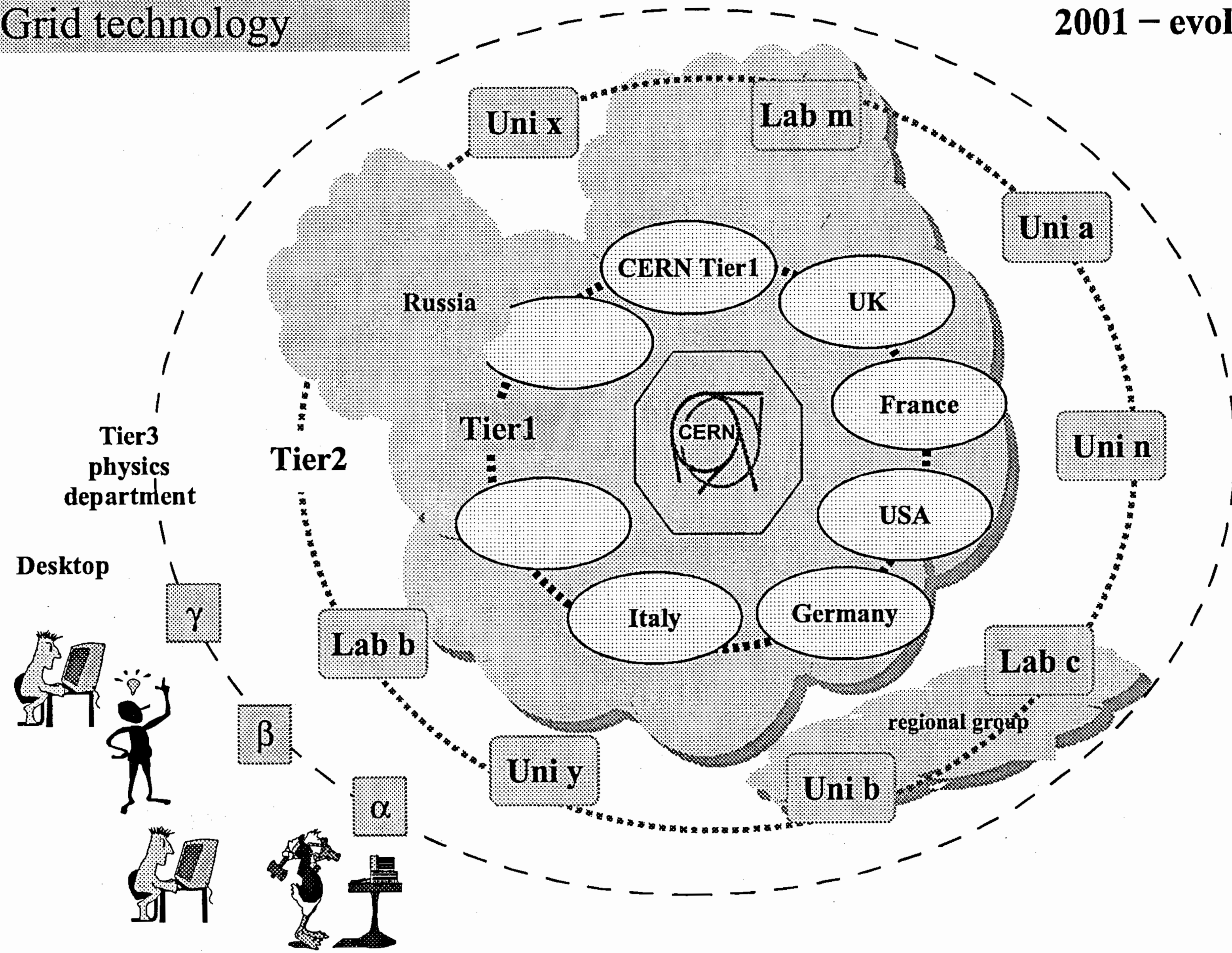

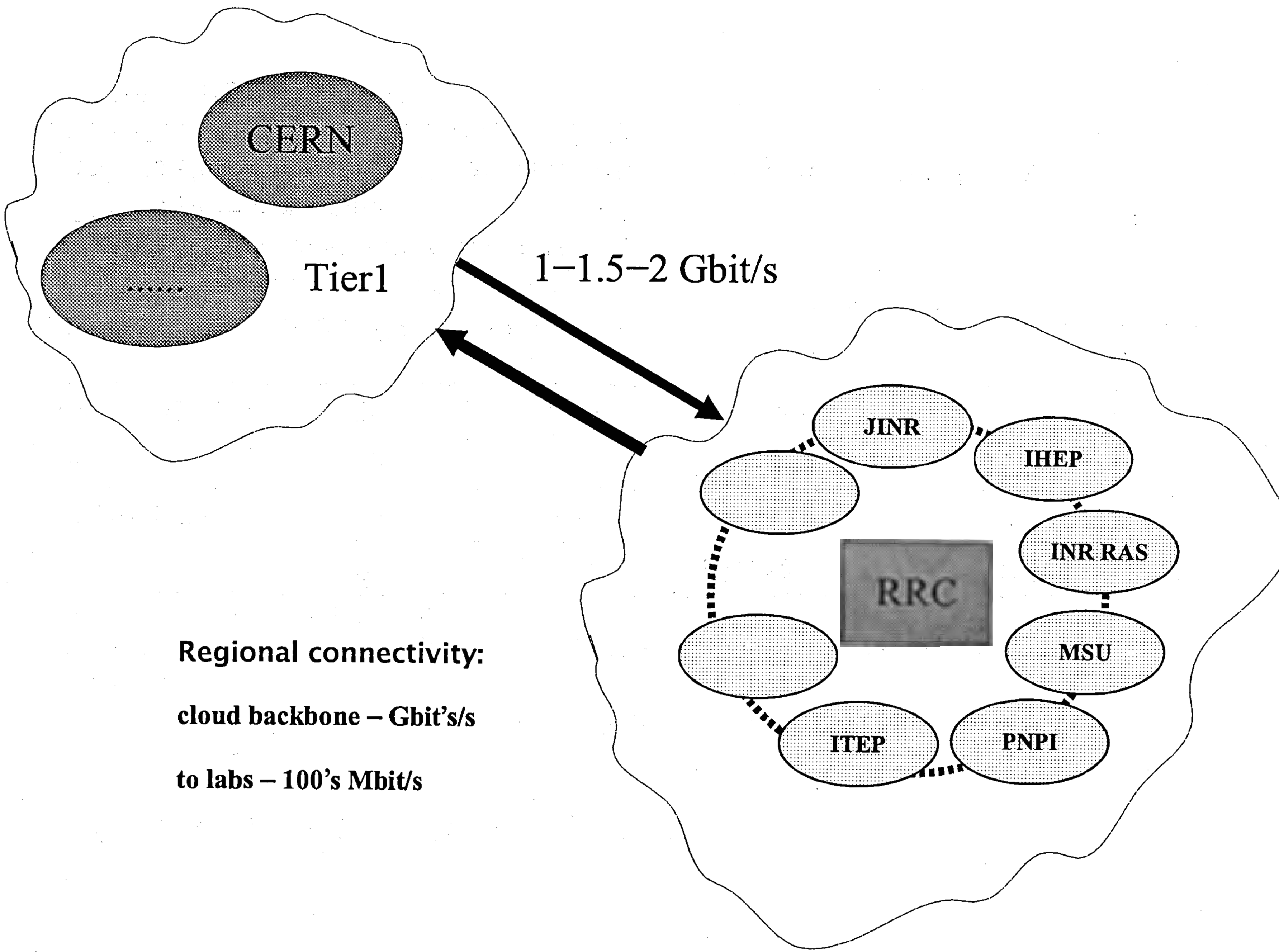

Regional connectivity:

cloud backbone – Gbit's/s

to labs – 100's Mbit/s

Resources required by the 2007

We suppose:

•each active user will create local AOD sets ~10 times per year, and keep these sets on the disks during the year

•the general AOD sets will be replicated from the Tier1 cloud ~10 times per year, storing previous sets on the tapes.

	ALICE	ATLAS	**RDMS CMS**	LHCb
CPU(KSI95)	100	120	**120**	70
Disk (TB)	200	250	**250**	150
Tape (TB)	300	400	**400**	150

The disk space usage will be partitioned as

- 15% to store general AOD+TAG sets;
- 15% to store local sets of AOD+TAG;
- 15% to store users data;
- 15% to store current sets of sim.data (SIM–AOD, partially SIM–ESD);
- 30–35% to store the 10% portion of ESD;
- 5–10% cache.

~4000 2 CPU boxes of 1GHz

Construction timeline

Timeline for the RRC–LHC resources at the construction phase:

2005	2006	2007
15%	30%	55%

After 2007 investments will be necessary for supporting the computing and storage facilities and increasing the CPU power and storage space.

In 2008 about 30% of the expenses in 2007.

Every next year: renewing of 1/3 of CPU, increase the disk space for 50%, and increase the tape storage space for 100%.

Prototyping (Phase1) & DataChallenges

2004: minimal acceptable level of complexity – 10% of 2007

summary (of 4 Collab.) resources:

CPU (KSI95)	20
Disk (TB)	50
Tape (TB)	50

The time profile for the prototype:

2001	2002	2003	2004
1.5%	10%	30%	55%

should allow the participation of Russian institutes in the CMS Data Challenge program at the level of 5–10%. **(talk by E.Tikhonenko)**

✓ *the budget is received (Rus.Min.Ind.Sci.&Tech. + Institutes)*

EU-DataGrid

RRC–LHC participates in the EU–DataGrid activity

- WP6 (Testbed and Demonstration) *collaboration with CERN IT*
- WP8 (HEP Application) *through Collaborations*

In 2001 the DataGrid information service (GRIS–GIIS) has been created in Moscow region, as well the DataGrid Certificate Authority and user Registration services.

WP6 Testbed0 (Spring–Summer 2001) – 4 sites, 8 FTE.

Testbed1 – 4 sites (MSU, ITEP, JINR, IHEP), 12 FTE, significant resources (160 CPUs, 7.5 TB disk), active sites in CMS Testbed1.

(talk by L. Shamardin)

CERN–INTAS grant 00–0440 (2001–2002) : CERN IT, CNRS, MSU, ITEP, JINR, IHEP

Collaboration with
- SCC MSU
- Keldysh Inst. for Appl. Math. RAS (metacomputing, GRID)
- Telecommunication Center " Sci & Society " (GigaEthernet)

Networking

In 2002–2004 data exchange with CERN:

50–120–250 TByte in 2002–2003–2004

2002	2003	2004
30 Mbit/sec	70 Mbit/sec	150 Mbit/sec

For 2005–2007 (construction phase and 1st physics run):

2005	2006	2007
0.3 Gbit/sec	0.6 Gbit/sec	1.5 Gbit/sec

Regional links between basic RRC–LHC institutes should be comparable (or even better) than the link to CERN.

CMS Production
ATLAS Data Challenge
ALICE
LHCb

CMS production began in spring 2000 year.

The main goals are:

-- to generate large samples of events for Physics, Trigger and DAQ investigations.

-- to install full data processing software chain from DAQ to Physics

-- to create protypes of computing and storage facilities.

Participation of Russian institute (5% of all CMS simulations):

Spring 2000 year – SINP MSU+ITEP– 50000 events,
25 GB transferred to CERN

Autumn 2000 year – SINP MSU+ITEP+JINR – 110000 events,
180 GB transferred to CERN

Autumn 2001 year – (SINP+RRC)+ITEP+JINR+FIAN – 270000 events,
OO Database distributed between SINP and ITEP
~200 GB transferred to CERN

Spring 2002 year –(SINP+RRC)+ITEP+JINR+IHEP – 430000 events,
180 GB transferred to FNAL (2–3 days), ~200 GB transferred to CERN (10 days), 90 GB transferred (10 days) from CERN to Moscow, Two OO Database
We need Mass Storage – will begin to use JINR DLT.

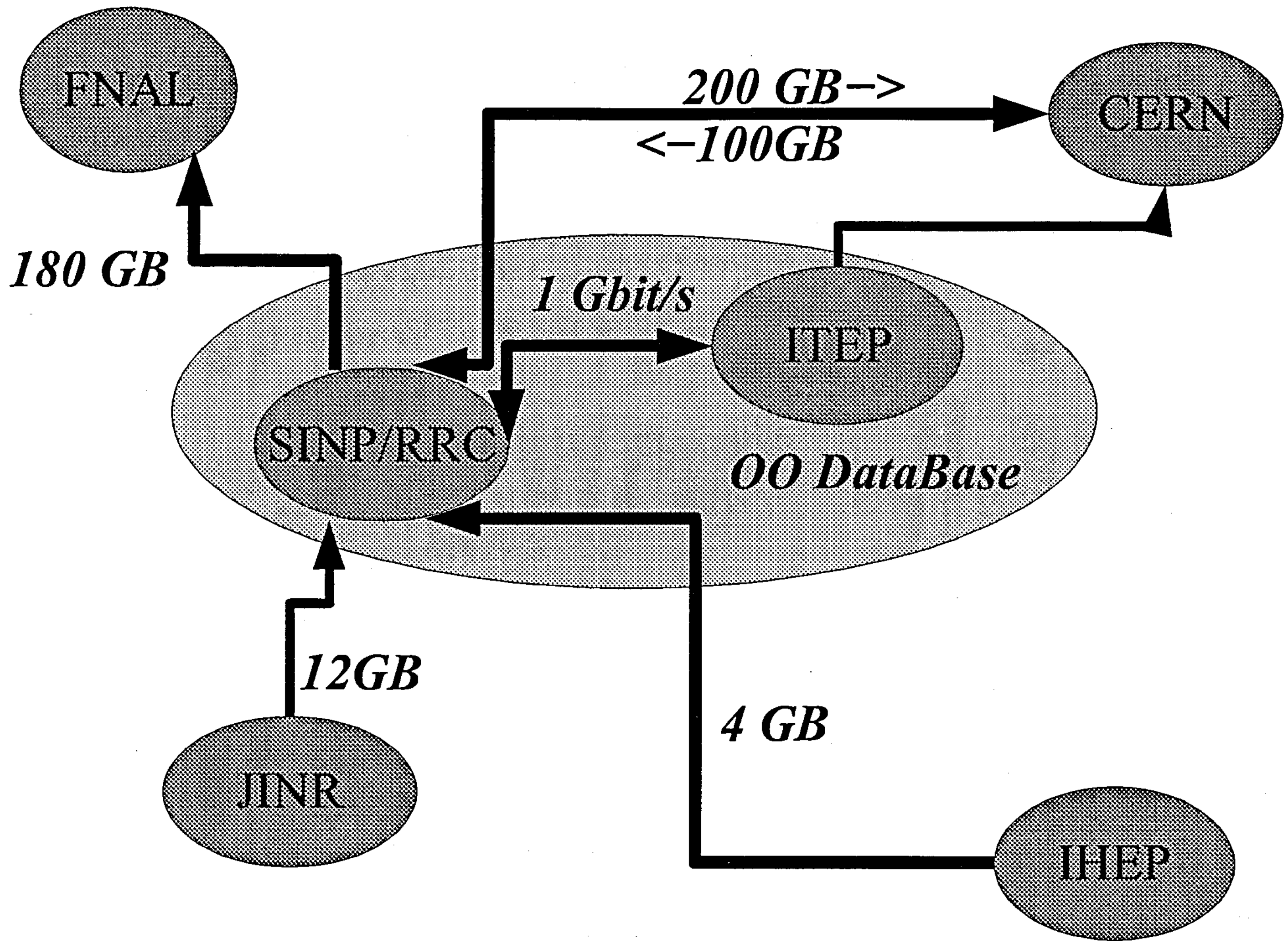

Dataflow in the last production

ATLAS Data Challenge

DC 0: ~15 countries are generating 12000 events. The goal is to have identical results.

DC1: Mass production will run in the second half of June for 2−3 weeks. The full number of events to generate − 10 000 000 events in ~15 sites

Russia participation: 4 sites
JINR with a new farm
ITEP
IHEP
SINP

Services Supported at JINR by LIT Computing Centre

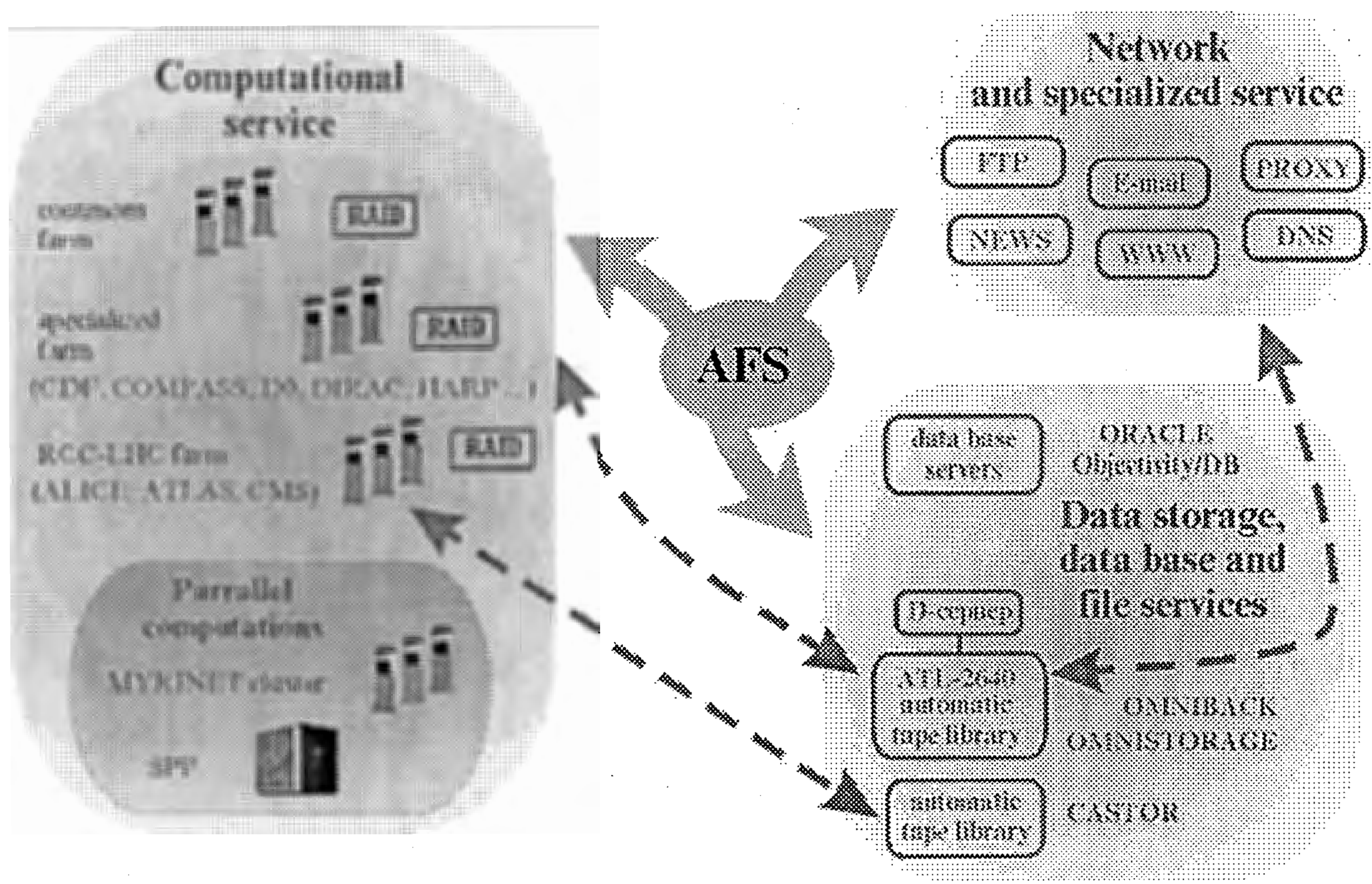

Hardware & Software Resources at JINR High Performance Computer Centre for LHC Computing Support

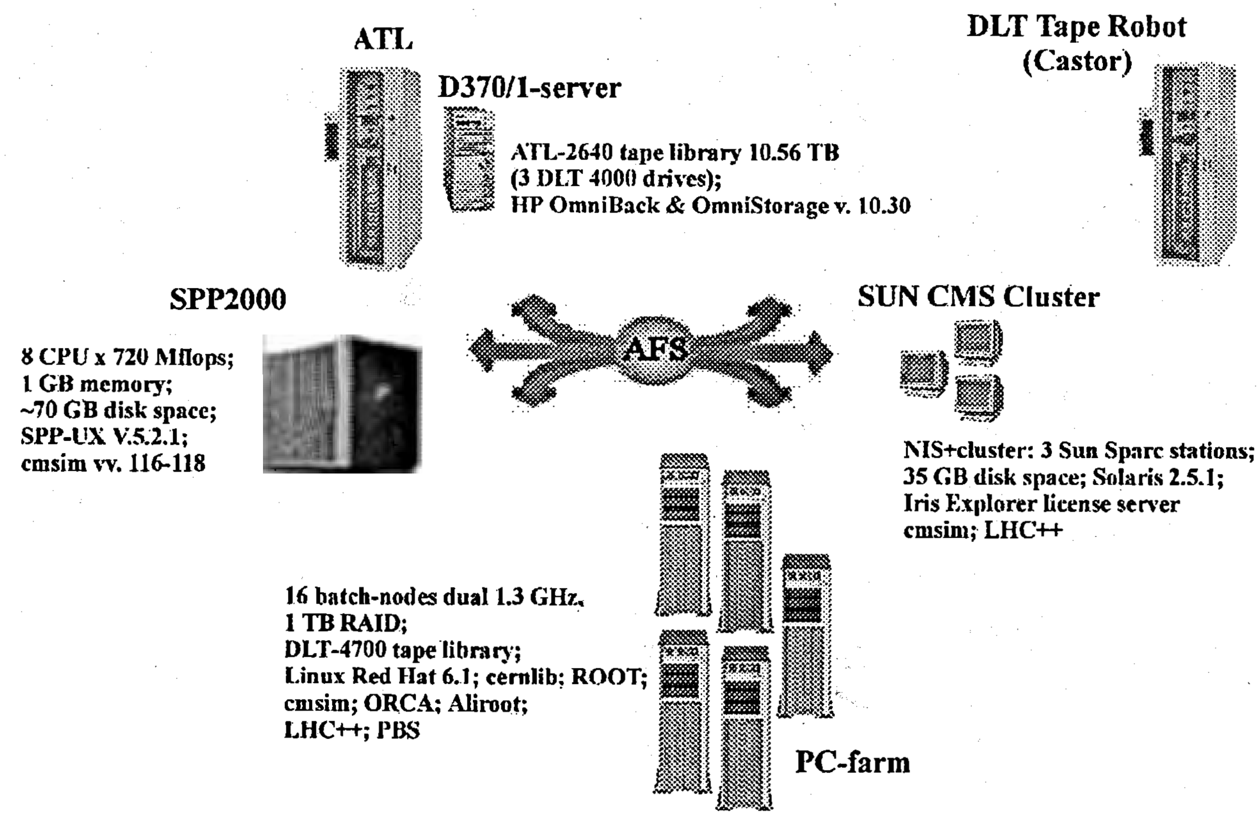

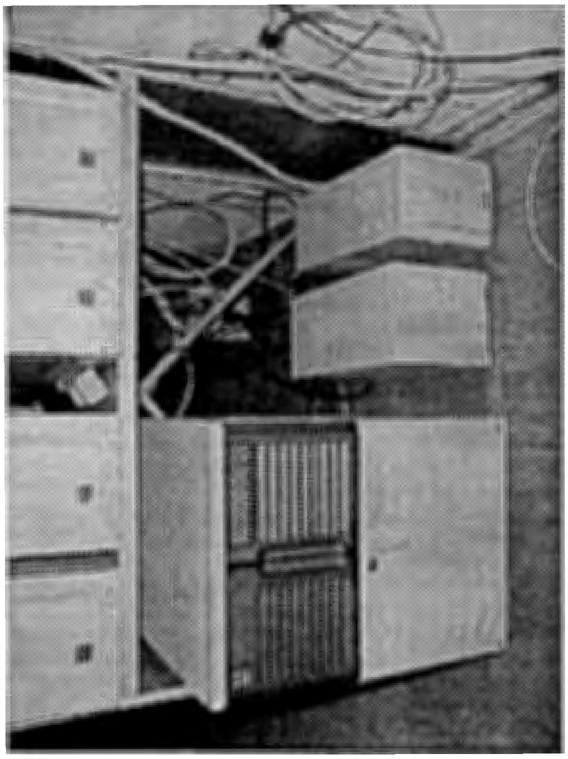

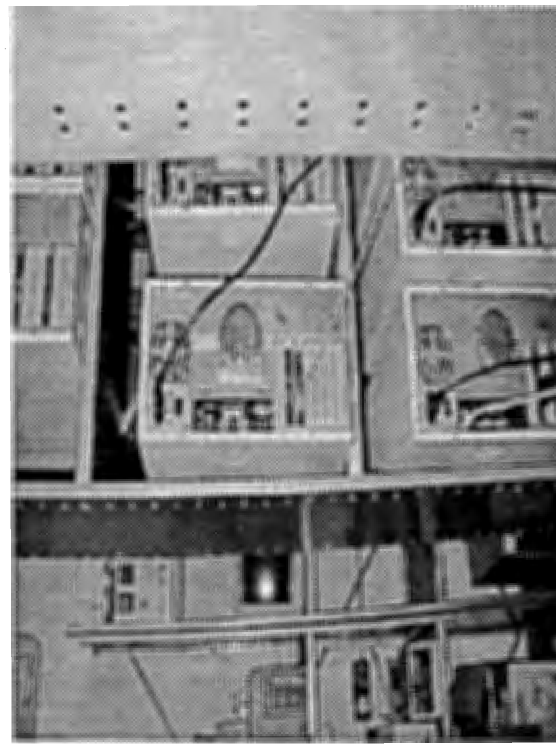

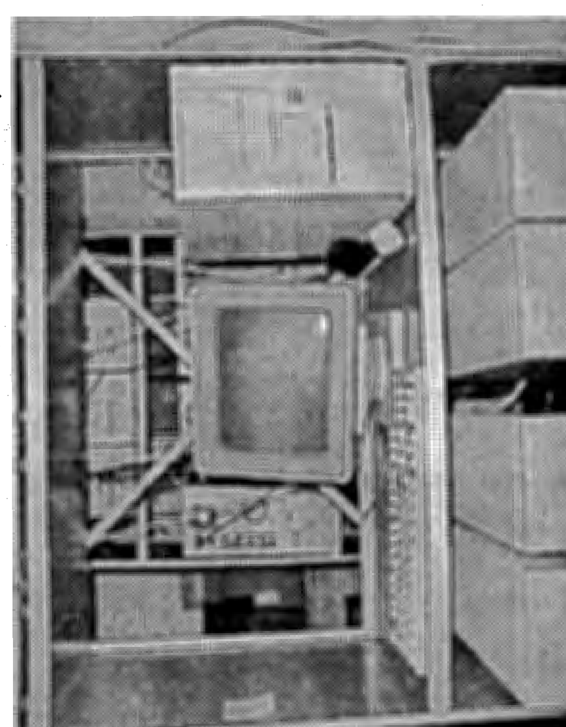

Total Cross Section, Inelasticity and Multiplicity Distributions in Proton – Proton Collisions.

Genis Musulmanbekov[1,*]

[1] *Joint Institute for Nuclear Research, RU–141980 Dubna, Russia*

Multiparticle production in high energy proton – proton collisions has been analysed in the frame of Strongly Correlated Quark Model (SCQM) of hadron structure, elaborated by author. It is shown that inelasticity decreases at high energies and violation of KNO – scaling is a consequence of total cross section growth and of increasing with collision energy masses of intermediate clusters.

1. INTRODUCTION

In inelastic hadronic interactions with multiparticle production only the fraction of collision energy is converted into the production of secondaries. For quantitative estimation of this fraction one can use for a given interaction a characteristic, originating from cosmic ray physics, inelasticity, which can be defined as

$$k_1(s) = \frac{M}{\sqrt{s}}, \tag{1}$$

where s – is square of c.m. energy and M is the mass of intermediate system which decays into final produced particles. The remaining part of incident energy is carried away by participant's remnants – so called, leading particles. From experimental point of view more suitable is another definition of inelasticity

$$k_2(s) = \frac{1}{\sqrt{s}} \sum_i \int dy \mu_i \frac{dn_i}{dy} \cosh y, \tag{2}$$

where $\mu_i = \sqrt{p_{T_i}^2 + m_i^2}$ is transverse mass of produced particle of type i and dn_i/dy is its measured rapidity distribution. Fluctuation of inelasticity from event to event leads to the distribution $P(k)$ with mean inelasticity $< k(s) >$. The energy dependence of inelasticity is

---

* genis@jinr.ru; This research was partly supported by the Russian Foundation of Basics Research, grant 01–07–90144.

a problem of great interest both from theoretical and experimental points of view. There is no consensus in physical community on the energy dependence of $< k(s) >$. The decrease of inelasticity with energy is advocated by some authors [1–4], while others believe that inelasticity is increasing function of energy [5–8]. The question can not be answered by collider experiments. At ISR energies ($23 \div 60$ GeV) where leading particle spectrum could be measured the inelasticity defined to be about 0.5. In collider experiments at higher energies (SPS and Tevatron) leading particles are emitted in an extremely forward cone and could not be measured due to the presence of the beam pipe. Obviously, multiplicity distributions are connected with inelasticity distributions, and so one can study features of multiplicity distributions deriving the information on inelasticity or fraction of the initial energy converted into particle production. As we know, scaled multiplicity distributions exhibit KNO [9] scaling up to ISR energies which is violated for higher energy data (SPS) where they can be described approximately by negative binomial distribution (NBD). And again at the most high SPS energy, 900 GeV, there is an evident deviation of multiplicity distributions from NBD. In this paper we demonstrate that there is a connection between the energetic behavior of the shape of scaled multiplicity distribution and of inelasticity distribution which, in turn, relates to the effect of total cross section growth. For this purpose we use geometrical considerations which are justified by the following arguments. First, hadrons are extended objects with the size about 1 fm and ,second, at high energies de–Bloglie wave–length becomes small.

Our analysis is based on the model of hadron structure , so called, Strongly Correlated Quark Model (SCQM) [10] which is described in Section 2. In Section 3 the model is applied for calculation of proton – proton total cross sections and simulation of inelastic events.

2. STRONGLY CORRELATED QUARK MODEL

The ingredients of the model are the following. Single quark of definite color embedded in vacuum starts to polarize its surrounding that results in formation of quark and gluon condensate. At the same time it experiences the pressure of the vacuum because of zero point radiation field or vacuum fluctuations which act the quark tending to destroy the ordering of the condensate. Suppose that we place the corresponding antiquark in the vicinity of the first one. Owing to their opposite signs color polarization fields of quark and antiquark interfere destructively in the overlapped space regions eliminating each other at most in the middle–point between the quarks. This effect leads to decreasing of condensates density in the same space region and overbalancing of the vacuum pressure acting on quark and antiquark from outer space regions. As a result the attractive force between quark and antiquark emerges and quark and antiquark start to move towards each other. The density of the remaining condensate around quark (antiquark) is identified with hadronic matter distribution. At maximum displacement in $\overline{q}q-$ system, that corresponds to small overlapping of polarization fields, hadronic matter distributions have maximum extent and magnitude. The closer they to each other, the larger is the effect of mutual destruction and the smaller hadronic matter distributions are around quarks and the larger their kinetic energies. In that way quark and antiquark start to oscillate around their middle–point. For such interacting $\overline{q}q-$ pair located on X axis at the distance $2x$ from each other the total Hamiltonian is

$$H = \frac{m_{\overline{q}}}{(1-\beta^2)^{1/2}} + \frac{m_q}{(1-\beta^2)^{1/2}} + V_{\overline{q}q}(2x), \tag{3}$$

were $m_{\overline{q}}$, m_q – current masses of valence antiquark and quark, $\beta = \beta(x)$ – their velocity depending on displacement x and $V_{\overline{q}q}$ – quark–antiquark potential energy with separation $2x$. It can be rewritten as

$$H = \left[\frac{m_{\overline{q}}}{(1-\beta^2)^{1/2}} + U(x)\right] + \left[\frac{m_q}{(1-\beta^2)^{1/2}} + U(x)\right] = H_{\overline{q}} + H_q, \tag{4}$$

were $U(x) = \frac{1}{2}V_{\overline{q}q}(2x)$ is potential energy of quark or antiquark. Quark (antiquark) with the surrounding cloud (condensate) of quark – antiquark pairs and gluons, or hadronic matter distribution, forms the constituent quark. It is natural to assume that the potential energy of quark (antiquark), $U(x)$, corresponds to the mass M_Q of constituent quark:

$$2U(x) = C_1 \int_{-\infty}^{\infty} dz' \int_{-\infty}^{\infty} dy' \int_{-\infty}^{\infty} dx' \rho(x, \mathbf{r}') \approx 2M_Q(x) \tag{5}$$

where C_1 is dimensional constant and hadronic matter density distribution, $\rho(x, \mathbf{r}')$, is defined as

$$\rho(x, \mathbf{r}') = C_2 \left|\varphi(x, \mathbf{r}')\right| = C_2 \left|\varphi_Q(x'+x, y', z') - \varphi_{\overline{Q}}(x'-x, y', z')\right|. \tag{6}$$

Here C_2 is a constant, φ_Q and $\varphi_{\overline{Q}}$ are density profiles of the condensates around quark and antiquark located at distance $2x$ from each other. Here we consider that the condensates around quark and antiquark have opposite color charges. They look like compressive stress and tensile stress (around defects) in solids. Generalization to three–quark system in baryons is performed according to $SU(3)_{color}$ symmetry: in general, pair of quarks have coupled representations

$$3 \otimes 3 = 6 \oplus \overline{3} \tag{7}$$

in $SU(3)_{color}$ and for quarks within the same baryon only the $\overline{3}$ (antisymmetric) representation occurs. Hence, an antiquark can be replaced by two correspondingly colored quarks to get color singlet baryon and destructive interference takes place between color fields of three valence quarks (VQs). Putting aside the mass and charge differences and spins of valence quarks we may say that inside baryon three quarks oscillate along the bisectors of equilateral triangle. Therefore, keeping in mind that quark and antiquark in mesons and three quarks in baryons are strongly correlated, we can consider each of them separately as undergoing oscillatory motion under the potential (5) in 1 | 1 dimension. Hereinafter we consider VQ oscillating along $X-$ axis, and $Z-$ axis is perpendicular to the plane of oscillation XY. Density profiles of condensates around VQs are taken in gaussian form. It has been shown in papers [11] that the wave packet solutions of time dependent Schrodinger equation for harmonic oscillator move in exactly the same way as corresponding classical oscillators. These solutions are called „coherent states". This relationship justifies our semiclassical treatment of quark dynamics.

We specify the mass of constituent quark at maximum displacement as

$$M_{Q(\overline{Q})}(x_{\max}) = \frac{1}{3}\left(\frac{m_\Delta + m_N}{2}\right) \approx 360\ MeV,$$

where m_Δ and m_N are masses delta–isobar and nucleon correspondingly. The parameters of the model, namely, maximum displacement, $x_{\max}$, and parameters of gaussian function, $\sigma_{x,y,z}$, for hadronic matter distribution around VQ are chosen inside the following corridors:

$$x_{\max} = 0.64 \div 0.66\ fm,\ \sigma_{x,y} = 0.24 \div 0.28\ fm,\ \sigma_z = 0.12 \div 0.20\ fm. \tag{8}$$

They are estimated by comparison of calculated and experimental values of inelastic cross sections, $\sigma_{in}(s)$, and inelastic overlap function $G_{in}(s,b)$ for $pp-$ and $\overline{p}p-$ collisions (see the next Sect.). The current mass of valence quark is taken to be 5 MeV. The behavior of potential (5) evidently demonstrates the relationship between constituent and current quark states inside a hadron (Fig. 1). At maximum displacement quark is nonrelativistic, constituent one (VQ surrounded by condensate), since the influence of polarization fields of other quarks becomes minimal and the VQ possesses the maximal potential energy corresponding to the mass of constituent quark. At the origin of oscillation, $x = 0$, antiquark and quark in mesons and three quarks in baryons, being close to each other, have maximum kinetic energy and correspondingly minimum potential energy and mass: they are relativistic, current quarks (bare VQs). This configuration corresponds to so called „asymptotic freedom“. In the intermediate region there is increasing (decreasing) of constituent quark mass by dressing (undressing) of VQs due to decreasing (increasing) of the destructive interference effect. Evolution of color charge density profiles of quark – antiquark pair during half–period of oscillation are shown in Fig. 2. Here we supposed that quark color charge is positive and antiquark color charge is negative.

The proposed dynamical picture meets local gauge invariance principle. Indeed, destructive interference of color fields of quark and antiquark in mesons and three quarks in baryons depending on their displacements can be treated as phase rotation of wave function of single VQ in color space ψ_c on angle θ depending on displacement x of the VQ in coordinate space

$$\psi_c(x) \rightarrow e^{ig\theta(x)}\psi_c(x). \tag{9}$$

Color phase rotation,in turn, leads VQ dressing (undressing) by quark and gluon condensate that corresponds to the transformation of gauge field

$$A_\mu(x) \rightarrow A_\mu(x) + \partial_\mu\theta(x). \tag{10}$$

Here we drop color indices of $A_\mu(x)$ and consider each quark of specific color separately as changing its effective color charge, $g\theta(x)$, in color fields of other quarks (antiquark) due to destructive interference. Thus gauge transformations (9, 10) map internal (isotopic) space of colored quark onto coordinate space. On the other hand this dynamical picture of VQ dressing (undressing) corresponds to chiral symmetry breaking (restoration). Due to this mechanism of VQs oscillations nucleon runs over the states corresponding to the certain terms of the infinite series of Fock space

$$\mid B\rangle = c_1 \mid q_1q_2q_3\rangle + c_2 \mid q_1q_2q_3\bar{q}q\rangle + c_3 \mid q_1q_2q_3g\rangle ... \tag{11}$$

The proposed model has some important consequences. Inside hadrons valence quarks and accompanying them gluons and quark–antiquark pairs, as well, are strongly correlated. Nucleons are nonspherical object: they are flattened along the axis perpendicular to the plane of quarks oscillations.

From the form of the quark potential (Fig. 1) one can conclude that dynamics of VQ corresponds to nonlinear oscillator and VQ with its surrounding can be treated as nonlinear wave packet. Moreover, our quark – antiquark system turned out to be identical to, so called, „breather"solution of (nonlinear) sine–Gordon (SG) equation[12]. SG equation in $(1 \mid 1)$ dimension in reduced form for scalar function $\phi(x,t)$ is given by

$$\Box\phi(x,t) + \sin\phi(x,t) = 0, \tag{12}$$

where x, $t-$ dimensionless. Breather is a periodic solution representing bound state of soliton–antisoliton pair which oscillate around their center of mass:

$$\phi_{br}(x,t) = 4\tan^{-1}\left[\frac{\sinh\left[ut/\sqrt{(1-u^2)}\right]}{u\cosh\left[x/\sqrt{(1-u^2)}\right]}\right], \tag{13}$$

where u is 4–velocity. During the oscillations of soliton–antisoliton pair their density profile

$$\varphi_{br}(x,t) = \frac{d\phi_{br}(x,t)}{dx} \tag{14}$$

evolves like our quark–antiquark system, i.e. at maximal displacement soliton and antisoliton are maximal and at minimum displacement they „annihilate"(Fig. 3).This similarity is not surprising because our quark–antiquark system was formulated in close analogy with the model of dislocation–antidislocation, which in continuous limit is described by breather solution of SG equation [13]. It can be shown that soliton, antisoliton and breather obey relativistic kinematics, i.e. their energies, momenta and shapes are transformed according to Lorentz transformations. Since the above consideration of quarks as solitons is purely classical the important problem is to construct quantum states around them. Although soliton solution of SG equation looks like extended (quantum) particle the relation of classical solitons to quantum particles is not so trivial. Technique of quantization of classical solitons with usage of various methods has been developed by many authors. The most known of them is semiclassical method of quantization (WKB) which allows one to relate classical periodic orbits (breather solution of SG) with the quantum energy levels [14].

Hereinafter we adhere to our semiclassical model (SCQM) applying it for analysis of cross sections and multiparticle production in hadron–hadron collisions.

3. HADRON – HADRON COLLISIONS

Different configurations of quark content inside a hadron realized at the instant of collision result in different types of reactions. The probability of finding any quark configuration inside a hadron is defined by the probability of VQ's displacement in proper frame of a hadron:

$$P(x)dx = \frac{Adx}{\sqrt{1 - m_q^2/\left[E_q - U(x)\right]^2}}, \tag{15}$$

where E_q is total energy of valence quark (antiquark) and constant A can be derived from normalization condition

$$\int_{-\infty}^{\infty} P(x)dx = 1. \tag{16}$$

Configurations with nonrelativistic constituent quarks ($x \simeq x_{max}$) in both colliding hadrons lead to soft interactions with nondiffractive multiparticle production in central and fragmentation regions (Fig. 4a). Hard scattering with jet production and large angle elastic scattering takes place when configurations with current VQs ($x \simeq 0$) in both colliding hadrons are realized (Fig. 4b). Near current quark configuration inside one of the hadrons and constituent quark configuration inside the second one results in single diffraction scattering (Fig. 4c). And, at last, intermediate configurations inside one or both hadrons are responsible for semihard and double diffractive scattering (Fig. 4d). The same geometrical consideration can be applied to deep inelastic scattering processes if one assumes that real or virtual photon converts into the vector meson, according to vector dominance model.

First, we apply our model for calculation of proton–proton and antiproton–proton cross sections at high energies and demonstrate that the growth of cross section with energy is caused by predominantly increasing contribution of peripheral interactions that, in turn, leads to decreasing of inelasticity of collisions. Then we will show that the energetic behavior of inelasticity distributions governs the energetic behavior of scaled multiplicity distributions.

3.1. Cross Sections

To calculate cross sections we used impact parameter representation, namely Inelastic Overlap Function (IOF), which can be specified via the unitarity equation

$$2Imf(s,b) = |f(s,b)|^2 + G_{in}(s,b), \tag{17}$$

where $f(s,b)$—elastic scattering amplitude and $G_{in}(s,b)$ is IOF. IOF is connected with inelastic differential cross sections in impact parameter space:

$$\frac{1}{\pi}(d\sigma_{in}/db^2) = G_{in}(s,b). \tag{18}$$

Then inelastic, elastic and total cross sections can be expressed via IOF as

$$\sigma_{in}(s) = \int G_{in}(s,\mathbf{b})d^2\mathbf{b}, \tag{19}$$

$$\sigma_{el}(s) = \int \left[1 - \sqrt{1 - G_{in}(s,\mathbf{b})}\right]^2 d^2\mathbf{b}, \tag{20}$$

$$\sigma_{tot}(s) = 2\int \left[1 - \sqrt{1 - G_{in}(s,\mathbf{b})}\right] d^2\mathbf{b}. \tag{21}$$

Since IOF relates to the probability of inelastic interaction at given impact parameter, we carried out Monte Carlo simulation of inelastic nucleon–nucleon interactions. Inelastic interaction takes place at definite impact parameter b if the mass produced in the region where hadronic matter distributions of colliding hadrons overlap meets the following requirement:

$$M^2_{CF} = 4M_P\gamma_P M_T\gamma_T \int \rho_P(\mathbf{r})\rho_T(\mathbf{r}-\mathbf{b})\; d^3\mathbf{r} \geq (M^2_{CF})_{\min}, \tag{22}$$

where M_{CF} is the mass of fireball produced at that region, ρ_P and ρ_T are hadronic matter density distributions in projectile and target hadrons, M_P, M_T – masses, γ_P, γ_T – gamma–factors of colliding hadrons and $(M^2_{CF})_{\min}$ – minimal mass of fireball that results in inelastic event. This expression is the modification of assumption of Heisenberg [15] on interaction of extended particles: we replaced in his original formula pion mass squared (on right hand side) by $(M^2_{CF})_{\min}$. In our previous papers this quantity corresponded to the transverse mass of pion: $m^2_{\pi\perp} = p^2_\perp + m^2_\pi$. Taking into account energy dependence of the average momentum of produced particles and increasing yield of minijets (as treated in what follows) we parametrize the minimal fireball mass as

$$(M_{CF})_{\min} = 0.3 + 0.03s^{1/4}. \tag{23}$$

Specifying the quark configurations in each colliding hadrons according to (15) we calculated $G_{in}(s,b)$ for particular values of impact parameter b and then according to (21) – total cross sections, σ_{tot}. Fig. 5 shows the results of calculation for total cross sections for proton – proton and antiproton – proton collisions in a wide range of collision energies. One can see that the model with fixed parameters characterizing the geometrical size of hadrons describes the energetic behavior of σ_{tot} rather well. The growth of total cross section with energy coming from the growth of inelastic cross section is due to the continuous tails of condensates (hadronic matter distributions) around VQs not compensated by destructive interference effect inside each interacting particle. With rising collision energy the overlap of more peripheral parts of these tails make it possible to meet requirement (22) and consequently results in the increasing effective size of hadronic matter distribution inside nucleons and correspondingly the increasing radius of interactions. It can be seen from the comparison of IOFs for ISR and SPS energies which is given in Fig. 6. According to Eq. (18) the difference $G_{in}^{SPS} - G_{in}^{ISR}$ exhibits the predominantly peripheral increase of the inelastic cross section (and thus of the total cross section, since $\sigma_{el}/\ \sigma_{tot}$ is only about 20%) which is centered around 1 fm (Fig. 6b). As noted by the authors of paper [17] at high energies colliding nucleons become blacker, edger and larger („BEL–effect"). The model gives linear logarithmic energy dependence for total cross sections. At energies $\sqrt{s} < 30\ GeV$ calculated cross sections were corrected on contributions of Regge poles exchange by using Donnachie and Landshoff parametrization[18]. An oscillatory motion of VQs appearing as interplay between constituent and bare (current) quark configurations results in fluctuations of hadronic matter distribution inside colliding nucleons. The manifestation of these fluctuations is a variety of scattering processes, hard and soft, in particular, the process of single diffraction (SD). SD–events correspond to constituent quark configuration inside one colliding hadron and (semi)bare quark configuration inside another one. Our unified geometrical explanation of diffractive, nondiffractive and DIS processes could give an answer on long standing question: what is pomeron? Historically the concept of „pomeron", starting from simple Regge pole with intercept $a_0 = 1$, transformed to a rather complicated object with relatively arbitrary features and smooth meaning. To produce rising cross sections it must have intercept such that $a_0 = 1 + \varepsilon$. The fact that the parameter ε is universal, independent of particles being scattered in hadronic and DIS interactions, could say us that the nature of the cross section growth is the same for all processes. Our interpretation of pomeron is geometrical one. Both diffractive and nondiffractive particle production emerge from disturbance (excitation) of overlapped continuous vacuum polarization fields (gluon and $\overline{q}q$ condensate) around valence quarks of colliding hadrons followed by fragmentation process. The type of interaction depends on quark configurations inside colliding hadron occurring at the instant of interaction and the value of impact parameter. So, what we used to call „Pomeron"in $t-$

channel is solely continuum states in $s-$ channel and we claim that Pomeron is unique in elastic, inelastic (diffractive and nondiffractive) and DIS.

3.2. Multiparticle Production in Hadronic Collisions

According to our model the configurations with nonrelativistic constituent quarks ($x \simeq x_{max}$) inside two colliding hadrons lead to soft interactions with multiparticle production in central and fragmentation regions. Additional restriction by small impact parameters selects central collisions when hadronic matter distributions of colliding hadrons (quarks) overlap totally. In this case kinetic energies of colliding hadrons dissipate totally converting to production of secondary particles that corresponds to collision inelasticity close to 1 and very high multiplicity in comparison with the mean one. We will consider soft interaction and nondiffractive multiparticle production in particular. According to KNO hypothesis scaled multiplicity distributions $\langle n \rangle P_n(s)$ depends on the ratio of the number of particles to the average multiplicity $z = n/\langle n \rangle$ and is energy independent. From our geometrical point of view such behavior could be explained as superposition of relatively narrow distributions corresponding particular impact parameters of the collisions. Indeed, multiplicity distribution can be defined as

$$P_n(s) = \int_0^1 P(n \mid k)\; P[k(s)]dk, \tag{24}$$

where $P[k(s)]$ is inelasticity distribution and $P(n \mid k)$ is the probability of production of n particles at given inelasticity, k. So if conditional probability $P(n \mid k)$ is sufficiently narrow then the shape of the distribution P_n is defined by the shape of inelasticity distribution $P[k(s)]$. Inelasticity distributions are strictly connected to impact parameter distributions. KNO scaling holds (at least, approximately) if impact parameter distributions and consequently inelasticity distributions are energy independent. As shown in the previous subsection the growth with energy of inelastic and total cross sections in hadronic collisions is due to increasing of effective sizes of interacting hadrons. To make a quantitative analysis of energetic dependence of multiplicity distributions we performed, in the frame of SCQM, Monte Carlo simulation of inelastic proton – proton interactions, selecting nondiffractive events. The process of simulation includes the following steps.

1. Applying Heisenberg prescription (22) we define the mass of central "fireball" (CF)

(Fig. 7) produced in proton–proton collision at particular impact parameter. Quark configurations inside each proton at the instant of collision is specified randomly according to probability (15) that allows one to fix energies and momenta of quarks inside both protons. Since the mass of CF is formed by overlap of hadronic densities of individual constituent quarks (CQ) of colliding protons we know the energies and momenta of quarks in both remnants which we call, by convention, forward and backward „fireballs"(FF and BF). The notion „fireball"is applied by convention only because all fireballs, CF, FF and BF, can decay string – like manner and there is no sharp boundary between secondaries emitted from fireballs in rapidity space for nondiffractive events. Then we calculate effective masses of FF and BF (Fig. 7):

$$M_{FF} = \sqrt{\left(\sum_{i=1}^{3} E_i'\right)^2 - \left(\sum_{i=1}^{3} \mathbf{k}_i\right)^2}, \tag{25}$$

$$M_{BF} = \sqrt{\left(\sum_{i=4}^{6} E_i'\right)^2 - \left(\sum_{i=4}^{6} \mathbf{k}_i\right)^2}, \tag{26}$$

where E_i' and $\mathbf{k}_i$ are energies and momenta of constituent quarks after collision.

2. We assume that each fireball breaks up, in general, into clusters. Here the bremsstrahlung ananogy is used, namely, at the instant of collision proton (electron) loses its energy dumping fraction of its hadronic(electromagnetic) field by means of emission of clusters (photons). To simulate the masses of clusters we apply the result of paper [19] for cluster mass spectrum

$$P(m_{cl}) = (m_{cl}/m_0)\exp(-m_{cl}/m_0), \tag{27}$$

following from statistical nature of cluster emission. Our next assumption is that masses of clusters increase with the collision energy. This is dictated by necessity to take into account such peculiarities of multiparticle production as growth of rapidity distribution plateau and of transverse momenta of secondaries and increasing yield of minijets. We parametrize energy dependence of the average mass of clusters as

$$\langle m_{cl}\rangle = 0.3 + 0.09 s^{1/4}. \tag{28}$$

Notice that we have chosen the same energetic dependence for the minimal fireball mass in Heisenberg prescription (23) except for the value of slope parameter.

3. Given the position of centers of masses of each fireball in rapidity space and kinematically allowed rapidity (sub)spaces for breaking up of each fireball into clusters we simulate momenta for each generated cluster in proper frame of corresponding fireball. Bremsstrahlung mechanism of fireball fragmentation corresponds to statistically independent emission of clusters with limited transverse momenta. Therefore, we apply the cylindrical phase space model according to which the rapidity of i–th cluster is defined as

$$y_i = \xi Y_i, \tag{29}$$

where ξ is random number uniformly distributed in the interval [0,1]. Allowed rapidity interval, Y_i, is given by

$$Y_i = \ln(M_F^2/(\mu_{cl})_i^2,$$

where $(\mu_{cl})_i^2 = (m_{cl})_i^2 + p_{\perp i}^2$, transverse mass of cluster i. Moreover, rapidity interval for fragmentation of central fireball, Y_i^{CF}, is restricted by requirement

$$Y_i^{CF} \leq Y^{FF} - Y^{BF}, \tag{30}$$

where Y^{FF} and Y^{BF} are rapidities of forward and backward fireball respectively. Transverse momenta of clusters are generated according to distribution

$$f(p_\perp^2) \propto \exp(-bp_\perp^2). \tag{31}$$

The energy of remnant baryon in proper frame of FF (BF) is defined by the summary energy of two quarks closest each other in rapidity space, i.e. kinematic characteristics of baryon are connected to those of „diquark". Physical picture of multiparticle production that corresponds to the cylindrical phase space model

4. Since our clusters are identified with minijets they should decay in jet–like manner. One could assume that these minijets are formed by fragmentation of excited sea quark–antiquark pair. Hence we can approximate the spectrum of cluster decay using data on electron–positron annihilation provided that cluster mass is identified with the center of mass energy of electron and positron: $m_{cl} = \sqrt{s}_{e^+e^-}$. One can apply for this purpose any of appropriate Monte – Carlo generators. The axis of decaying jet is generated to be directed isotropically. And, at last, the model meets energy – momentum conservation requirements for all products of a reaction.

Calculated such a manner multiplicity distributions in KNO form and energetic dependence of mean multiplicity for charged particles are shown in Figures 8 and 9. Given all characteristics of produced particles in the event we can calculate inelasticity k_2 (Eq. 2). Its distributions for $pp-$ interactions at different collision energies are shown in Fig. 10. The inelasticity distribution evolves with energy in such a way that its maximum position shifts to lower values of inelasticity at higher collision energies. It means that the higher is the collision energy the lower is the average inelasticity (Fig. 11). Analyzing multiplicity distribution at different energies one can see that its maximum position shifts to lower values of scaled multiplicities and contribution of high multiplicities increases while the collision energy increases. According to Eq. (24) multiplicity distribution can be expressed via conditional multiplicity distribution at particular inelasticity and inelasticity distribution. Conditional multiplicity distribution at particular inelasticity, in turn, is built from multiplicities of clusters emitted from forward, backward and central fireballs and multiplicities going from clusters fragmentation. If inelasticity distribution and (average) mass of clusters would not depend on collision energy then scaled multiplicity distributions do not depend on energy,as well, and KNO – scaling takes place. The shift of the position of maximum of inelasticity distribution with energy growth shifts the position of scaled multiplicity distribution. On the other hand, growing with collision energy masses of clusters lead to narrowing of available rapidity space and, consequently, to violation of Feynman scaling. This effect most obviously exhibiting at inelasticities approaching to 1 cause the lift of multiplicity distribution tail at high multiplicities. To summarize we claim that mean inelasticity decreases with energy and violation of KNO – scaling is a consequence of growth of inelastic and total cross sections and of masses of emitted clusters with energy.

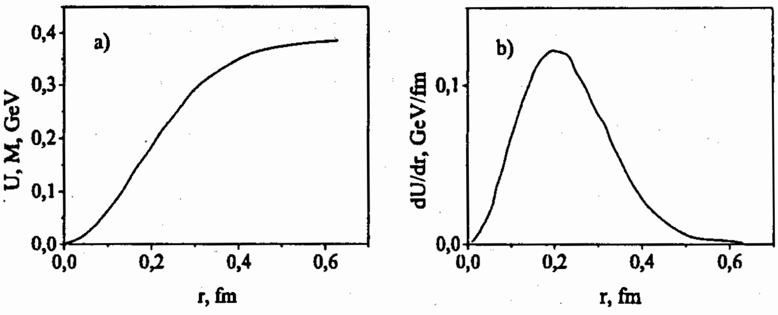

Figure 1. a) Potential energy of valence quark and mass of constituent quark; b) "Confinement" force.

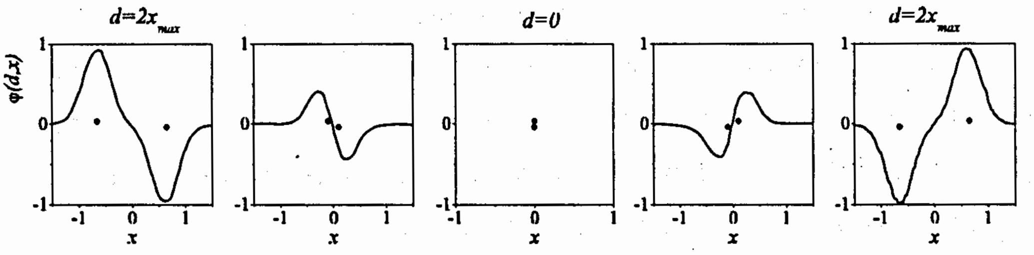

Figure 2. Evolution of color charge density profile, φ, in quark–antiquark system during half–period of oscillations; $d = 2x$ – distance in *fermi* between quark and antiquark depicted as dots.

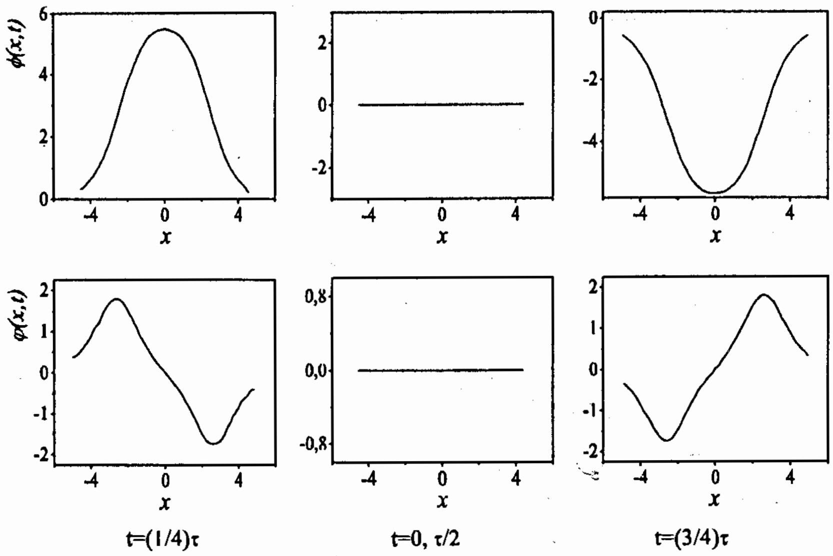

Figure 3. Evolution of breather, ϕ, and its energy density profile, φ, during a half-period of oscillation. Scales are abitrary.

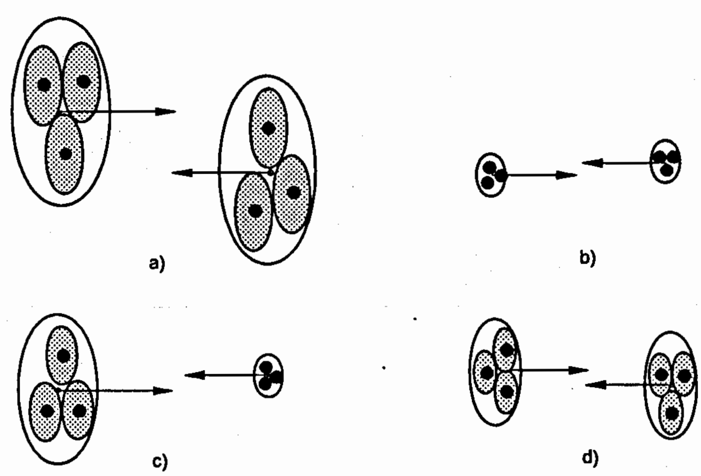

Figure 4. Different quark configurations realized inside colliding nucleons at the instant of collision.

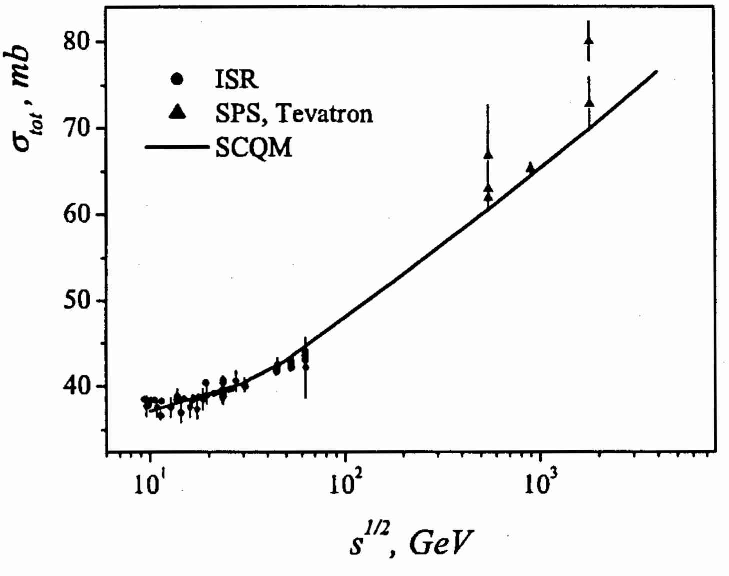

Figure 5. Total cross section for pp and $\bar{p}p$. Data are taken from electronic data base HEPDATA [16].

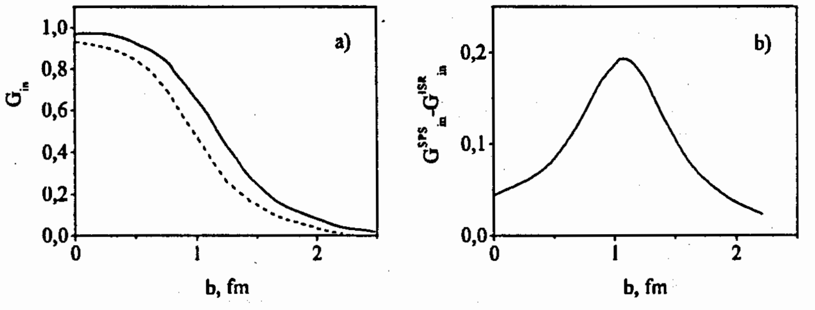

Figure 6. Plot of overlap functions at ISR and SPS energies, (a), and the difference of overlap functions $G_{in}^{SPS} - G_{in}^{ISR}$, (b), as a function of impact parameter b.

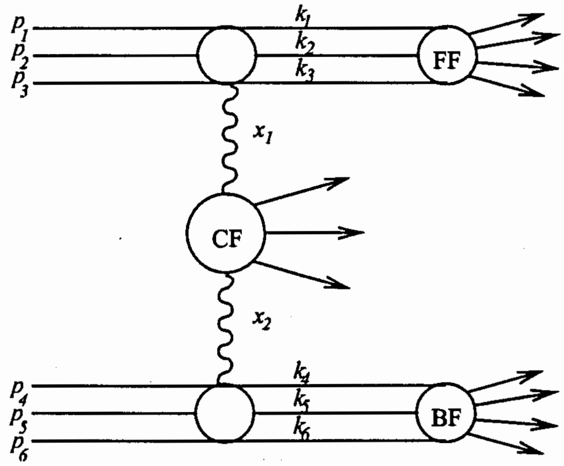

Figure 7. Fireball picture of multiparticle production in proton – proton collision. p_i and k_i are momenta of constituent quarks before and after collision, respectively; x_1 and x_2 – fractions of protons momenta forming the central fireball.

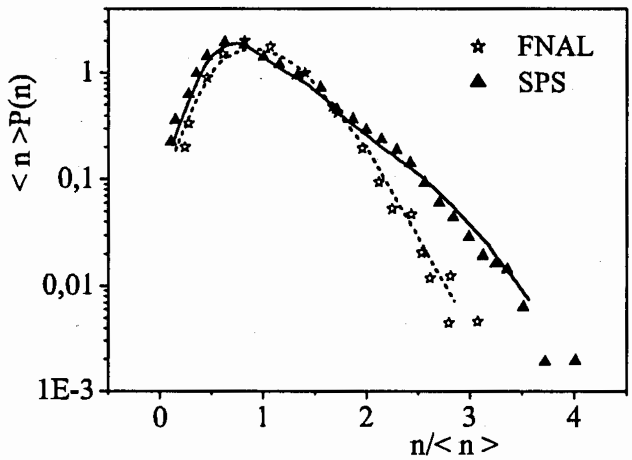

Figure 8. The multiplicity distributions of charged particles in $pp-$ and $\bar{p}p-$ collisions. Data are taken from electronic data base HEPDATA [16].

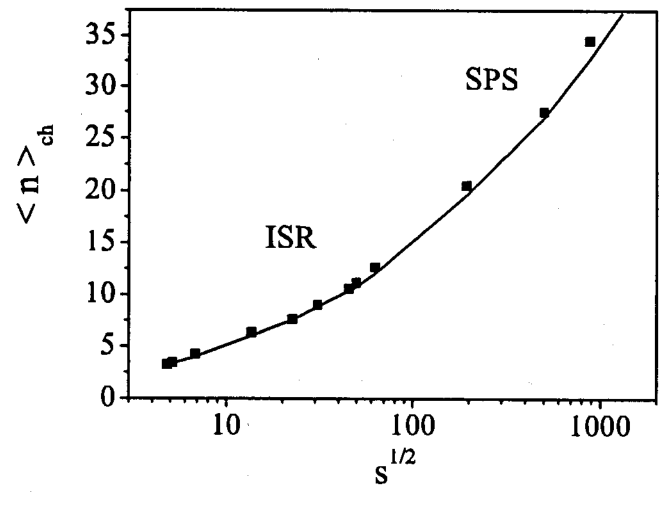

Figure 9. The energetic dependence of the average multiplicity of charged particles in $pp-$ and $\bar{p}p-$ collisions. Data are taken from electronic data base HEPDATA [16].

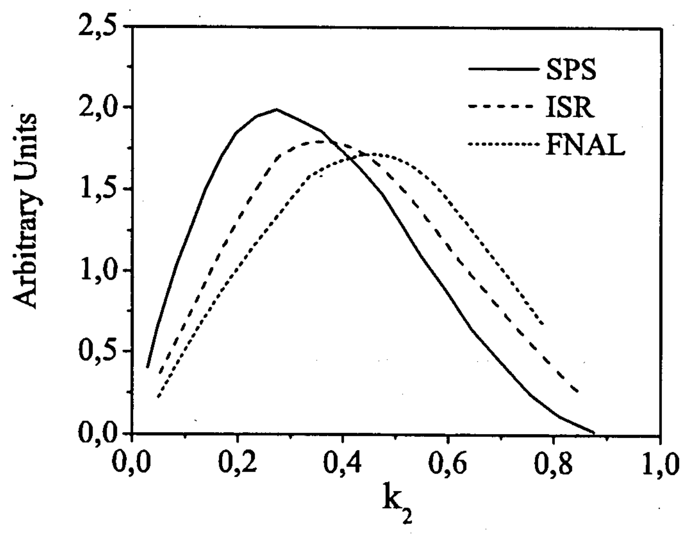

Figure 10. Inelasticity distributions for $pp-$ and $\bar{p}p-$ collisions calculated according to Eq. (2).

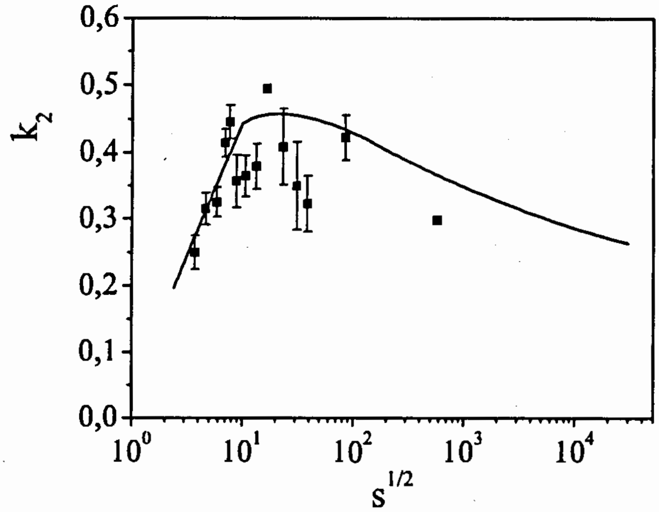

Figure 11. The average inelasiticity plotted as a function of the energy for $pp-$ and $\bar{p}p-$ collisions. Boxes are compilation of data given in paper [20].

1. G. Fowler, R. M. Weiner, G. Wilk, Phys. Rev. Lett., **55**, 177 (1985).
2. Z. Wlodarczyk, J. Phys. G: Nucl. Part. Phys., **19**, L128 (1993).
3. Yu. A. Shabelski *et al.*, J. Phys. G: Nucl. Part. Phys., **18**, 1281 (1992).
4. Y. D. He, J. Phys. G: Nucl. Part. Phys., **19**, 1953 (1993).
5. J. Dias de Deus, Phys. Rev. **D32**, 334 (1985).
6. Gaisser T. K. and Stanev T., Phys. Lett., **B219**, 375 (1989).
7. Kopeliovich B. Z., Nikolaev N. N. and Potashikova I. K., Phys. Rev. **D39**, 769 (1989).
8. F. S. Duraes, F. O. Navarra and G. Wilk, Phys. Rev., **D47**, 3049 (1993).
9. Z. Koba, N. B. Nielsen and P. Olesen, Nucl. Phys., **B40**, 317 (1972).
10. G. Musulmanbekov, *Proc. VIIIth Blois Workshop,* Ed. V. A. Petrov, World Scientific, 2000, p. 341–350, and references therein.
11. E. Schrodinger, Naturwissenschaften **14**, 664 (1926).
12. G. Musulmanbekov in *Frontiers of Fundamental Physics 4*, Ed. B. G. Sidharth, Klewver Acad. Press, 2001, p. 109–120.
13. R. Rajaraman, Phys. Rep. **21C**, 229 (1975).
14. R. Dashen, B.Hasslacher and a. Neveu, Phys. Rev. **D10** , 4114 (1974).
15. W. Heisenberg, Zeit. Phys., Bd. **133**, 65 (1952).
16. `http://durpdg.durham.ac.uk/HEPDATA`.
17. R. Henzi and P. Valin, Phys. Lett. **132B** (1983) 443; R. Henzi, *Proc. of the 4th Topical Workshop on $\bar{p}p$ Collider Physics*, Bern, 1984.
18. A.Donnachie and P.V. Landshoff, CERN–TH 6635/92.
19. Chou Kuang–chao, Liu Lian–son, Meng Ta–chung, Phys. Rev., **D28**, 1080 (1983).
20. V. S. Barashenkov, N. B. Slavin, Acta Phys. Pol., **B12**, 563 (1981).

Very high energy multiplicity distributions

L.L. Jenkovszky* and B.V. Struminsky

Bogolyubov Institute for Theoretical Physics
Academy of Sciences of Ukraine
UA-03143 Kiev, Ukraine

Abstract

A regularity connecting the geometrical properties in high-energy dynamics (GS and KNO scaling) with the dynamics of the high-multiplicity processes is found. We show, in particular, that exact geometrical, or KNO scaling results in a cut-off at large z of the distribution function $\Psi(z)$. Any departure from scaling shifts the point z_m according to eq. (15). It varies within the present accelerator energy domain (ISR, SPS, Tevatron) reaching the critical value at LHC, where we predict a change of the regime: $z_{max}(s)$ will start decreasing and the black disc limit will be exceeded, which corresponds to the transition from shadowing to antishadowing.

* *e-mail address:* JENK@GLUK.ORG

As pointed out in a series of recent papers [1], the dynamics of rare processes with Very High Multiplicities (VHM) may be quite different from the rest of events. In this talk we present our predictions concerning the behaviour of the multiplicity distributions $\Psi(z)$ near their high-z border. Our model, in principle, is applicable to any z, but here we ignore the shape of the small- and moderate z, concentrating on the righmost edge of $\Psi(z)$.

Our knowledge about high-energy multiplicity distributions comes from the data collected at the *ISR*, $Sp\bar{p}S$ collider (UA1, UA2 and UA5 experiments) and the Tevatron collider (CDF and E735 experiments). In should be noticed that the recent results from the E335 Collaboration taken at the Tevatron [2] do not completely agree with those obtained by the UA5 Collaboration at comparable energies at the $Sp\bar{p}S$ collider [3].

Notice that the delicate features of $\Psi(z)$ at very large multiplicities, near the large-z edge can be better seen if the variable z is used instead of n.

On the theoretical side, it became common [4], [5], [6], [7] to approximate the observed distributions by the convolution of two binomial distributions, accounting for the general "bell-like" shape of $P(n)$ with the observed structures ("knee" and possible oscillations) superimposed.

One of the hottest issues in this field is the dynamics of very high multiplicities (VHM) [8], close to the kinematical limit imposed by the phase space. The VHM events are very rare, making up only about 10^{-7} of the total cross-sections at the LHC energy, which makes their experimental identification very difficult. An intriguing question is the possible existence of a cut-of in the VHM region, beyond $z = n/ < n > \approx 5$, where $< n >$ is the mean multiplicity. In our opinion, a better understanding of the underlying physics can be inferred only in a model involving both elastic and inelastic scattering, related by unitarity. Such an approach has been advocated in a series of papers [9], [10], [11], summarized in ref. [12].

After a brief summary of the main ideas behind this approach, we analyze the relation of the distribution of secondaries and the behavior of the elastic and total cross sections with the possible transition from shadowing to antishadowing [13].

We show that the existence of a cut-off at high multiplicities in the distribution $\Psi(z)$ is related to the validity of GS and KNO scaling.

The basic idea of the geometrical approach to multiple production, used in the present paper, is that the number of the secondaries at a given impact parameter ρ, $n(\rho, s)$ is proportional to the amount of the hadronic matter in the collision or the the overlap function $G(\rho, s)$

$$< n(\rho.s) >= N(s)G(\rho, s), \tag{1}$$

where $N(s)$ is related to mean multiplicity, not specified in this approach, and $G(\rho, s)$ is the overlap function, related by unitarity to elastic scattering

$$Imh(\rho, s) = |h(\rho, s)|^2 + G(\rho, s). \tag{2}$$

where $h(\rho, s)$ is the elastic amplitude in the impact parameter representation. Unitarity, a key issue in this approach, enters both in the definition of the elastic amplitude and of the inelastic one (the overlap function).

In the $u-$ matrix unitarization (see [12] and references therein)

$$G_{in} = \frac{Imu}{1 + 2Imu + |u|^2}, \tag{3}$$

where u is the elastic amplitude (input, or the "Born term").

We use a dipole (DP) model for the elastic scattering amplitude, exibiting geometrical features and fitting the data. After u-matrix unitarization, the elastic amplitude reads (see [12])

$$h(\rho, s) = \frac{u}{1 - iu}, \tag{4}$$

where $u(y, s) = ige^{-y}$, $y = \frac{\rho^2}{4\alpha' L}$, and $L \equiv \ln s$.

Remarkably, the ratio of the elastic to total cross sections in this model,

$$\frac{\sigma_{el}}{\sigma_t} = 1 - \frac{g}{(1 + g)\ln(1 + g)} \tag{5}$$

fixes the (energy-dependent) values of the parameter g. Typical values of g for several representative energies are quoted in [12].

Rescattering corrections to $G_{in}(\rho, s)$ here will be accounted for phenomenologically according to the following prescription (see [12] and earlier reference therein).

$$G_{in}(\rho, s) = |S(\rho, s)|\tilde{G}_{in}(\rho, s), \tag{6}$$

where $S(\rho, s))$ is the S is the elastic scattering matrix, related to the u matrix by

$$S(\rho, s) = \frac{1 + iu(\rho, s)}{1 - iu(\rho, s)}. \tag{7}$$

This procedure is not unique. For example, it allows the following generalization (see [12] and earlier reference therein)

$$G_{in}(\rho, s) = |S(\rho, s)|^{\alpha}\tilde{G}^{\alpha}(\rho, s), \tag{8}$$

where α is a parameter, varying between 0 and 1.

We assume

$$< n(\rho, s) >= N(s)\tilde{G}^{\alpha}_{in}(\rho, s). \tag{9}$$

The moments are defined by (see [12] and earlier references therein)

$$< n^k(s) >= \frac{N^k(s) \int G_{in}(\rho, s)(G^{alpha}_{in}(\rho, s))^k d^2\rho}{\int G_{in}(\rho, s) d^2\rho} \tag{10}$$

Now we insert the expression for the DP with the u-matrix unitarization (4) into (10) to get

$$< n^k(s) >= \frac{N^k(s)(1+g)}{g} \int_0^g \frac{dx}{(1+x)^2} \left(\left(\frac{1+x}{1-x}\right)^{\alpha} \frac{x}{(1+x)^2} \right)^k. \tag{11}$$

The mean multiplicity $< n(s) >$ is defined as

$$< n(s) >= \frac{N(s)(1+g)}{g} \int_0^g \frac{x dx}{(1+x)^4} \left(\frac{1+x}{1-x}\right)^{\alpha} = \frac{N(s)}{a}. \tag{12}$$

For the distributions we have

$$P(n) = \frac{1+g}{g} \int_0^g \frac{dx}{(1+x)^2} \delta\left(n - N\left(\frac{1+x}{1-x}\right)^{\alpha} \frac{x}{(1+x)^2}\right). \tag{13}$$

Integration in (13) gives

$$\psi(z) = <n> P(n) = \frac{1+g}{g} \frac{x(1-x)}{z(1+x)[(1-x)^2 + 2\alpha x]},$$

where $z = n/ <n>$.

Since the above integral is non-zero only when the argument of the δ function vanishes,

$$n = N\left(\frac{1+x}{1-x}\right)^{\alpha} \frac{x}{(1+x)^2},$$

one gets a remarkable relation

$$z = \frac{ax}{(1+x)^{2-\alpha}(1-x)^{\alpha}}. \tag{14}$$

To calculate the distribution $\Psi(z)$ one needs the solution of equation (14). It can be found explicitly for two extreme cases, namely $\alpha = 0$ and $\alpha = 1$. Otherwise, it can be calculated numerically.

The maximal value of z, corresponding to $x = g$ (x varies between 0 and g), can be found as:

$$z_{max} = \frac{ag}{(1+g)^{2-\alpha}|(1-g)|^{\alpha}}. \tag{15}$$

It can be seen from (15) that z_{max} is a constant if g is energy independent. The experimentally observed ratio σ_{el}/σ_t varies between 53 Gev and 900 Gev from 0.174 to 0.225, implying the variation of g from 0.489 to 0.702, uniquely determined by the above ratio. This monotonic increase of g(s) in its turn pushes $z_{max}(s)$ outwards, terminating when g reaches unity (according to [12] this will happen around 10 TeV, i.e. at the future LHC), whenafter the term $|1-g|$ in (15) will start rising again, pulling $z_{max}(s)$ back to smaller values. I.e. $z_{max}(s)$ has its own maximum in s at $g = 1$.

The unusual behavior of $z_{max}(s)$ is not the only interesting feature of the present approach. This effect can be related to the behavior of the ratio σ_{el}/σ_t. As argued by Troshin and Tyurin (see [13]), σ_{el}/σ_t may pass the so-called black disc limit and continue rising in a new, "antishadowing" mode of the u-matrix unitarity approach (multiplicity distributions were not considered in that paper). According to the recent calculations [14] the transition from shadowing to antishadowing will also occur in the LHC energy region.

To summarize, we found a regularity connecting the geometrical properties in high-energy dynamics (GS and KNO scaling) with the dynamics of the high-multiplicity processes. We showed, in particular, that exact geometrical, or KNO scaling, implying constant g in our model, results in a cut-off at large z of the distribution function $\Psi(z)$. Any departure from scaling (energy dependence of g in our model) shifts the point z_m according to eq. (15). Within the present accelerator energy domain (ISR, SPS, Tevatron) g varies from about 0.5 to about 0.8. It will reach the critical value $g = 1$ at LHC, where we predict a change of the regime: $z_{max}(s)$ will start decreasing and the black disc limit will be exceeded (which, as shown in [13] and [14], is not equivalent to the violation of the unitarity limit, but means transition from shadowing to antishadowing [13] and [14]).

Finally, it should be noted that we use many model assumptions, decreasing the predictive power of our calculations. These assumptions concern mostly the way absorption corrections are introduced and the assumption of the local (δ function) dependence of multiplicities on the impact parameter. Both assumptions, as well as others can be modified. As a result we quantitive rather than qualitative changes in the results.

The most drastic approximation used in our calculations was the use in eq. (13) of a delta-function distribution in the impact parameter, making possible explicit calculations. The sharp (delta-function) dependence of the multiplicity on the impact paremeter resulted in an equally sharp and unrealistic cut-off in the multiplicity distributions at largest z. It is obvios that physics (multiplicity distributions) cannont be discontinuous. Actually, this cut-off is expected to transform, after smoothing the delta function in eq. (13), into a change of regime in the distribution $\Psi(z)$. In other words, replacing the delta function in (13) by a Gaussian or a Breit-Wigner-like dependence on the impact parameter, a mild asymptotic tail will appear in $\Psi(z)$. The relevant integrals are to be calculated numerically.

We thus predict an experimentally measurable change of $\Psi(z)'s$ slope near $z_{max}(s)$. This effect can be revealed by measuring the local slope $\frac{d\ln\Psi(z)}{d\ln z}$ within finite bins in z, close to $z_{max}(s)$.

Acknowledgments L.J. thank Professor A.N. Sissakian and his stuff for their hospitality at this inspiring meeting.

References

[1] J. Manjavidze and A. Sissakian, Phys. Rep. **346** (2001); J. Manjavidze and A. Sissakian, *Phenomenology of Very HIgh Multiplicity Hadron Processes*, arXiv: hep-ph/0204281.

[2] T. Alexopoulos et al. (E735 Collaboration), Phys. Lett. **B435** (1998) 453.

[3] G.J. Alner et al. (UA5 Collaboration), Physics Reports **154** (1987) 247; R.E. Ansorge et al. (UA5 Collaboration) Z. Phys. **C43** (1989) 357.

[4] I. Dremin, J.W. Gary, Physics Reports, **349** (2001) 301.

[5] A. Giovannini and R. Ugoccioni, *Global event properties in proton-proton phyisics wioth ALICE*, arXiv:hep-ph0203215 v1, 22 March 2002, and references therein.

[6] L. Jenkovszky, V. Kuvshinov, Z. Cicovani et al., Minijet production at the SPS collider and beyond, Torino Univ. preprint, DFTT 28/89, 1989.

[7] V.D. Rusov et al. Phys. Letters, **B504** (2001) 213.

[8] N.Giokaris, *Why do high-energy collisions contrive to produce so few particles most of the time?* CERN Courier, December 2001, p. 12.

[9] M.K.Aliev et al. ITF-84-74R preprint, Kiev, 1984 (in Russian).

[10] L.L. Jenkovszky, B.V. Struminsky, Z.E. Chikovani, ITF-86-55P preprint, Kiev, 1986 (in Russion).

[11] Z.E. Chikovani et al., ITP-87-145 preprint, Kiev, 1987.

[12] A.N.Vall, L.L. Jenkovszky, B.V. Struminsky, Sov. J. of Partciles and Nuclei **19** (1988) 77.

[13] S.M. Troshin and N.E. Tyurin, Phys. Letters, **B316** (1993) 175.)

[14] P. Desgrolard, L.L. Jenkovszky, B.V. Struminsky, Eur. Phys. J. C **11** (1999) 145.

Maximum Likelihood Method for Determination of Inelastic Interaction Cross-Sections in the Calorimeter

D. Garibashvili
Georgian Academy of Sciences

The ionization calorimeter designed as an equipment for cosmic ray particles [1] now is widely used as the device in the accelerator and the satellite experiments [2, 3].

Traditionally the ionization calorimeter is used as a device for energy determination, but it can be used also for studying inelastic interaction cross-sections of various particles with nuclei of different materials, absorbers of the ionization calorimeters. Statistical distribution of interaction points within the depth of the absorber of the calorimeter permits to determine the mean free path for an interaction λ - thickness, at which the number of particles decreases exponentially (by e-factor). The relation between the cross-section σ and λ is:

$$\sigma = \frac{1}{n\lambda},$$

where σ is measured in cm^2, λ in cm, and n is a number of nuclei in cm^3. If λ is measured in g/cm^2, then

$$\sigma = \frac{A}{N\lambda},$$

where A is an atomic weight of the absorber and N is the Avogadro number.

The Maximum Likelihood Method, proposed by M.Bartlett [4], and closely analyzed by G.Chikovani [5] for studying the unstable particles lifetime, can be used for determination of the Mean Free Path λ.

The brief description of this method for hadron interactions with iron nuclei on the Tskhra-Tskaro installation is given in our works [6, 7, 8].

The probability of interaction of a particle on the depth from x to $x+dx$ is [5]:

$$P(x)dx = \frac{\frac{1}{\lambda}e^{-\frac{x}{\lambda}}}{1-e^{-\frac{\Lambda}{\lambda}}}dx\,, \tag{1}$$

where Λ is the so-called potential path, the path of the particle on which the interaction can be detected (e.g., the whole thickness of a calorimeter).

It can be easily seen, that the probability (1) is normalized to 1 for $0 \le dx \le \Lambda$:

$$\int_0^{\Lambda} P(x)dx = 1.$$

The interaction points in the calorimeter can be registered with an error equal to thickness of a layer Δx, so (1) must be integrated over this thickness:

$$\int_x^{x+\Delta x} P(x)dx = \frac{e^{-\frac{x}{\lambda}}(1-e^{-\frac{\Delta x}{\lambda}})}{1-e^{-\frac{\Lambda}{\lambda}}}. \tag{2}$$

Let us have n interactions in the calorimeter with a set of x_i ($x_1, x_2, ..., x_n$), Δx_i ($\Delta x_1, \Delta x_2, ..., \Delta x_n$) and Λ_i ($\Lambda_1, \Lambda_2, ..., \Lambda_n$). The probability of determination of such selection is:

$$P(x_i, \Delta x_i) = \prod_{i=1}^{n} \frac{e^{-\frac{x_i}{\lambda}}(1-e^{-\frac{\Delta x_i}{\lambda}})}{1-e^{-\frac{\Lambda_i}{\lambda}}} . \tag{3}$$

The formula (3) contains only one unknown parameter - λ, therefore (3) is the Likelihood function [9] for λ parameter. $L(\lambda)=P(x_i, \Delta x_i)$.

According to the Bartlett Maximum Likelihood principle the value λ at which the equation (3) has maximum is the best estimation of the searching parameter λ_0.

It is more convenient to use a logarithmic likelihood function $lnL(\lambda)$, which has a maximum at the same value of λ.

The extremum condition gives:

$$F\left(\frac{1}{\lambda}\right) \equiv \frac{\partial \ln L(\lambda)}{\partial \lambda} = \frac{1}{\lambda^2}\sum_{i=1}^{n}\left[x_i - \frac{\Delta x_i}{\exp\left(\frac{\Delta x_i}{\lambda}\right)-1} + \frac{\Lambda_i}{\exp\left(\frac{\Lambda_i}{\lambda}\right)-1}\right] = 0 . \tag{4}$$

Solving this equation one can find λ, that is the best estimation of the parameter λ_0. The standard deviation of $F(1/\lambda_0)$ from zero is determined from the statement [10]:

$$D\left[F\left(\frac{1}{\lambda}\right)\right] = -\left[\frac{\partial^2 \ln L(\lambda)}{\partial \lambda^2}\right]_{\lambda=\lambda_0} = \frac{1}{\lambda^4}\sum_{i=1}^{n}\left[\frac{(\Delta x_i)^2 \exp\left(\frac{\Delta x_i}{\lambda}\right)}{\left(\exp\left(\frac{\Delta x_i}{\lambda}\right)-1\right)^2} - \frac{\Lambda_i^2 \exp\left(\frac{\Lambda_i}{\lambda}\right)}{\left(\exp\left(\frac{\Lambda_i}{\lambda}\right)-1\right)^2}\right] . \tag{5}$$

Bartlett proposed the so-called S - function:

$$S\left(\frac{1}{\lambda}\right) = \frac{\sum_{i=1}^{m} n_i \cdot \left(\frac{x_i}{\lambda} - a_i + b_i\right)}{\left[\sum_{i=1}^{m} n_i \left(a_i^2 \cdot \exp\frac{\Delta x_i}{\lambda} - b_i^2 \cdot \exp\frac{\Lambda_i}{\lambda}\right)\right]^{1/2}} , \tag{6}$$

that is a standardized deviation $F(1/\lambda)$ from zero. Here a_i and b_i are:

$$a_i = \frac{\frac{\Delta x_i}{\lambda}}{\exp\left(\frac{\Delta x_i}{\lambda}\right)-1} \quad \text{and} \quad b_i = \frac{\frac{\Lambda_i}{\lambda}}{\exp\left(\frac{\Lambda_i}{\lambda}\right)-1} , \tag{7}$$

m is a number of layers in the calorimeter and n_i is a number of interaction points in the i-th layer: $\sum_{i=1}^{m} n_i = n$

Bartlett showed that $S(1/\lambda)$ was a linear function near the λ_0. Therefore one can take some arbitrary values of λ and using experimental data plot a $S(1/\lambda)$ dependence on $1/\lambda$

(see Fig.1). Then from this diagram one can determine values of λ, corresponding to the conditions:

$$S(1/\lambda)=0 \quad \text{and} \quad S(1/\lambda)=\pm 1.$$

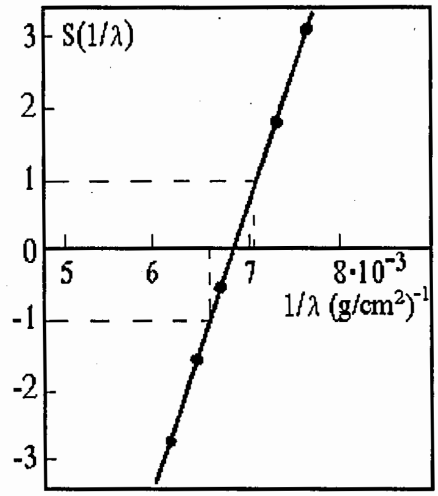

Fig.1. The Bartlett S-function

The $\lambda_{S=0}$ is the best estimation of λ_0, and $\lambda_{S=+1}$ and $\lambda_{S=-1}$ give the limits of reliability (standard deviation) of the experimentally determined value λ. So the problem of cross-section determination is reduced to the measurement of values x_i, Δx_i and Λ_i for each event of single particle interaction with the nucleus of the calorimeter absorber.

If the particles get into the calorimeter within the small angular cone, or their angular distribution is known with very high accuracy, all the particles can be taken as running with equal angles, and the determined λ must be multiplied by factor $\xi(\theta)$, which is calculated from the angular distribution of initial particles. In this case all the above equations are simplified:

The potential path for all particles is the same: $\Lambda_1 = \Lambda_2 = \ldots = \Lambda_n \equiv \Lambda$. ($\Lambda$ is the whole thickness of the calorimeter absorber). In this case: $b_1 = b_2 = \ldots = b_m \equiv b$

$$b = \frac{\frac{\Lambda}{\lambda}}{exp\left(\frac{\Lambda}{\lambda}\right) - 1}. \tag{8}$$

And the S-function comes to:

$$S\left(\frac{1}{\lambda}\right) = \frac{b \cdot n + \sum_{i=1}^{m} n_i \cdot \left(\frac{x_i}{\lambda} - a_i\right)}{\left[-b^2 \cdot n \cdot \exp\frac{\Lambda}{\lambda} + \sum_{i=1}^{m} n_i a_i^2 \cdot \exp\frac{\Delta x_i}{\lambda}\right]^{1/2}}. \tag{9}$$

If the layers of the calorimeter have equal thickness, e.g. $\Delta x_1 = \Delta x_2 = \ldots = \Delta x_m \equiv \Delta x$, then $a_1 = a_2 = \ldots = a_m \equiv a$ and the S-function is more simplified:

$$S\left(\frac{1}{\lambda}\right) = \frac{(b-a) \cdot n + \sum_{i=1}^{m} n_i \cdot \left(\frac{x_i}{\lambda}\right)}{\left(a^2 \cdot \exp\frac{\Delta x}{\lambda} - b^2 \cdot \exp\frac{\Lambda}{\lambda}\right)^{1/2} \cdot \sqrt{n}}. \tag{10}$$

with a and b:

$$a=\frac{\dfrac{\Delta x}{\lambda}}{\exp\left(\dfrac{\Delta x}{\lambda}\right)-1} \quad \text{and} \quad b=\frac{\dfrac{\Lambda}{\lambda}}{\exp\left(\dfrac{\Lambda}{\lambda}\right)-1} \tag{11}$$

It should be mentioned, that this method does not demand to know the whole flow of particles and, in spite of complexity of S-function, is easy for calculations. The method is very convenient, because it simultaneously gives the searching parameter and its errors.

The calculation procedure is as follows:

1) Calculation of the coefficients a_i ($a_1, a_2,..., a_m$) and b_i ($b_1, b_2,..., b_m$) for choosen values of λ_i ($\lambda_1, \lambda_2, ..., \lambda_k$) near the expected value λ_0. Since $S(1/\lambda)$ is a linear function, it is enough to choose only two values of λ (λ_1 and λ_2).

2) Calculation of values of S-function S_1 and S_2 corresponding to λ_1 and λ_2, as the experimental data are received and selection of n ($n_1, n_2, ..., n_m$) events is made.

3) Determination of values $1/\lambda$ and λ from the ploted diagram $S(1/\lambda)$ vs. $1/\lambda$, which correspond to conditions

$$S(1/\lambda)=0 \quad \text{and} \quad S(1/\lambda)=\pm 1.$$

4) Calculation (if necessary) of the coefficient $\xi(\theta)$ and multiplying the values λ_0, $\lambda_{S=+1}$ and $\lambda_{S=-1}$ on this coefficient.

5) Calculation of the cross-section and its errors using the formula $\sigma=\dfrac{A}{N}\cdot\dfrac{1}{\lambda}$.

If the angular distribution of particles does not allow to use the constant value of Λ, then the calculation procedure is more complicated:

1) Determination of values x_i ($x_1, x_2, ..., x_n$), Δx_i ($\Delta x_1, \Delta x_2, ..., \Delta x_n$) and Λ_i ($\Lambda_1, \Lambda_2, ..., \Lambda_n$) for each event of interaction.

2) Calculation of values of S-function for two or more values of λ, chosen near the expected one.

3) Determination of values $1/\lambda$ and λ from the ploted diagram $S(1/\lambda)$ vs. $1/\lambda$, which correspond to conditions

$$S(1/\lambda)=0 \quad \text{and} \quad S(1/\lambda)=\pm 1.$$

4) Calculation of the cross-section and its errors using the formula $\sigma=\dfrac{A}{N}\cdot\dfrac{1}{\lambda}$.

REFERENCES

1. *N.L.Grigorov, V.S.Murzin, I.D.Rappoport.* JETP, **34**, 1958, p.506 (Russian).
2. ATLAS Collaboration. ATLAS TDR1, TDR2, TDR3, CERN/LHCC 96-40, 96-41, 96-42, 1996.
3. *N.L.Grigorov, M.A.Kondratyeva, L.M.Poperekova, B.Y.Shestopalov.* Proc. 14th Intern. Conf. Cosmic Rays, **7**, p.2232, 1975; Izv. AN USSR, Phys. Ser., **37**, p.1386, 1973 (Russian).
4. *M.Bartlett.* Phil. Mag., **44**, p. 249, 1953.
5. *G.E.Chikovani.* Ph.D. Thesis, 1962 (Russian); Trudi Inst. Phys AN Gruzii. **8**, 1962 (Russian).
6. *E.L.Andronikashvili, G.E.Chikovani, D.I.Garibashvili et al.* Izv. AN USSR, Phys. Ser., **31**, 9, p.1455, 1967 (Russian).
7. *D.I.Garibashvili, D.B.Kakauridze.* Izv. AN USSR, Phys. Ser., **31**, 9, p.1458, 1967 (Russian).
8. *E.L.Andronikashvili, G.E.Chikovani, D.I.Garibashvili et al.* Canadian J. Phys., **46**, S689, 1968.
9. *D.J.Hudson.* Lectures on Elementary Statistics and Probability, Geneva, 1964.
10. *H.Cramer.* Mathematical Methods of Statistics, Stockholm University, 1946.

Multiple lepton pair production in relativistic ion collisions

E. Bartoš[1,2], S. R. Gevorkyan[1,3], E. A. Kuraev[1] and N. N. Nikolaev[4]

[1] *Joint Institute of Nuclear Research, 141980 Dubna, Russia*
[2] *Dept. of Theor. Physics, Comenius Univ., 84248 Bratislava, Slovakia*
[3] *Yerevan Physics Institute, 375036 Yerevan, Armenia*
[4] *Institut f. Kernphysik, Forshchungszentrum Jülich, D-52425 Jülich, Germany and L. D. Landau Institute for Theoretical Physics, 142432 Chernogolovka, Russia*

Abstract

We apply the Sudakov technique to description of the multiple production of lepton pairs in peripheral collisions of ultrarelativistic heavy ions. For heavy ions with $Z_1\alpha \sim Z_2\alpha \ll 1$ one needs a careful treatment of the multiple Coulomb exchange between colliding ions and screening effects, whereas interaction of real or virtual lepton pairs with colliding ions can be neglected. We demonstrate that while the inclusive spectra are modified by multiple Coulomb exchange between the colliding ions, the Coulomb corrections to the momentum integrated multiplicity distributions do vanish. After transformation to the impact parameter representation the probability of n lepton pair production is shown to obey the Poisson distribution. The relevant cross section is obtained.

1 Introduction

The multiplicity and the distribution of lepton pairs produced in the Coulomb fields of two colliding relativistic heavy ions are closely connected to the problem of unitarity. When heavy ions collide at relativistic velocities their Lorentz contracted electromagnetic fields are sufficiently intense to produce a large numbers of such pairs. Usually the process of lepton pairs production is considered as pair creation in the classic Coulomb potential of a charge moving along a straight line. Such an approach allows one [1] to investigate the impact parameter dependent total probability of the pair creation $P(b)$, which by definition is connected with the total cross section $\sigma = \int P(b)d^2b$. As was noticed in [2] the probability of single pair production calculated to lowest order in fine structure constant $\alpha = \frac{e^2}{4\pi} = \frac{1}{137}$ (throughout we use units for which $c = \hbar = 1$) at small impact parameters exceeds one, thus violating unitarity. This excess begins at impact parameters smaller than the Compton wavelength of the electron $\lambda_c = \frac{1}{m} = 386\,\mathrm{fm}$ and at energies of practical interest (RHIC & LHC).

Allowance for the finite size of colliding nuclei doesn't remedy the situation, because that would affect only the impact parameters comparable to t0he nuclei radii, which are much smaller than the Compton wavelength of the electron $R \ll \lambda_c$.

As was shown in [3] this problem can be solved by taking into account the possibility of multiple pair production, whose relative contribution grows with energy and dominates at small impact parameters. Since this early publication there has been much work has in this direction (see e.g. [4] and references therein) with the common for all statement: the probability to produce n lepton pairs in the Coulomb field of heavy ions colliding at fixed impact parameter b can be approximately represented as a Poisson distribution i.e. $P(b,n) = \frac{W^n(b)}{n!}e^{-W(b)}$, where W(b) is the average multiplicity of pairs at a fixed impact parameter.

Because of the somewhat controversial situation in the subject and its importance for the operation of relativistic heavy ion colliders (RHIC & LHC), in the present communication we revisit the multiple pair production based on the powerful Sudakov technique of calculation of high energy Feynman diagrams. Recently it has been applied [5] to the calculation of Coulomb corrections to single lepton pair production in relativistic heavy ion collisions. Here we extend the Sudakov approach to get the probability of multiple pair ($n \geq 2$) production in relativistic heavy ions collisions. For heavy ions with charge the numbers satisfy the conditions $Z_1\alpha \sim Z_2\alpha \ll 1$, $Z_1Z_2\alpha \gg 1$, one needs full allowance of multiple Coulomb interaction of colliding nuclei, whereas the secondary interaction of produced pairs (real or virtual) with the Coulomb fields of colliding ions can be neglected.

The paper is organized as follows. In section 2 we introduce the necessary definitions and discussed briefly the Sudakov'derivation of the Born amplitude for single pair creation. Then We show how one can sum the perturbative series to get the amplitude for the process of n pairs production in a compact analytical form.

In Section 3 we consider the Coulomb interaction between the colliding ions and show how it affects the amplitude and cross section of the process

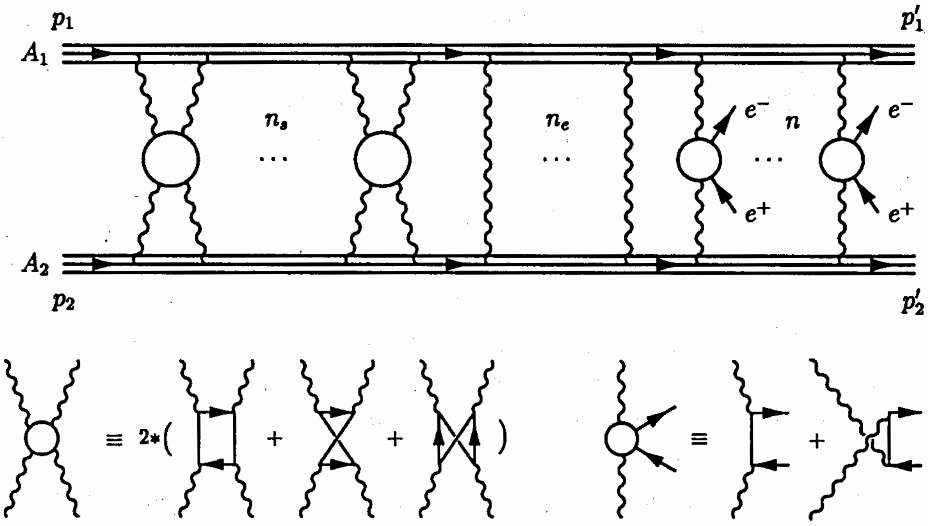

Fig. 1: The peripheral process of creation of n lepton pairs with n_e photon exchanges between nuclei A_1, A_2 and n_s light–by–light scattering blocks.

under consideration. Apart from the conventional multiple photon exchange between ions, this interaction include also the so called "screening corrections" which are the result of the ions interaction through the virtual lepton pairs and are responsible for the probability of vacuum–to–vacuum transition. In the language of the Abramovski–Gribov–Kancheli unitarity rules [6], the diagrams with lepton pair loops can be associated with the QED model for the pomeron, and the n-pair production amplitudes can be associated with the unitarity cuts through n exchanged pomerons. In section 4 we report the multiple production amplitudes in the impact representation in which the summation of the perturbation series for the n-pair production can be done in a compact closed form. Finally, using this amplitude we obtain the probability of n pair production which can be cast in the Poisson form, and the total cross section of all pair production process.

2 The amplitude of the n pairs production process.

The typical Feynman diagram (FD) describing the n lepton pairs production in the collision of relativistic nuclei with atomic numbers A_1, A_2, with n_e exchanged photons between colliding nuclei as well as screening effects e.g. the insertions of n_s light by light (LBL) scattering blocks is drawn in Fig. 1.

Upper and lower blocks in Fig. 1 describes many virtual photons interaction amplitudes with nuclei. They contain the complete set of $(n_e+n+2n_s)!$ Feynman diagrams. To avoid the multiple counting in what follows, we will multiply the relevant amplitude by the factor $1/(n_e!n_s!(2!)^{2n_s})$.

As was mentioned above we restrict ourselves to ions with charge numbers such that

$$Z_{1,2} \gg 1, \quad Z_1\alpha \sim Z_2\alpha \ll 1, \quad Z_1Z_2\alpha > 1, \tag{1}$$

which permits us to omit the multiphoton exchanges between the produced pairs and colliding ions. The dominant mechanism is a production of a single lepton pair per collision of equivalent photons, i.e., one lepton loop per two-photon ladder. The alternative mechanism of multiple pair production per collision of equivalent photons, i.e., multiple lepton loops per two-photon ladder, is suppressed by inverse powers of Z_1Z_2.

For the description of a peripheral process of n lepton pairs creation i.e. the process

$$A_1(Z_1,p_1)+A_2(Z_2,p_2) \to A_1(Z_1,p_1')+A_2(Z_2,p_2')+e_+e_-(r_1)+\cdots+e_+e_-(r_n),$$
$$r_i = q_+^i + q_-^i \tag{2}$$

It is convenient to use the Sudakov parameterization for the four-momentum of all exchanged photons (for details see [5])

$$k_i = \alpha_i\tilde{p}_2 + \beta_i\tilde{p}_1 + k_{i\perp}, \quad d^4k_i = \frac{s}{2}d\alpha_i d\beta_i d^2k_{i\perp}, \tag{3}$$

$$s = (p_1+p_2)^2, \quad s \gg p_i^2 = M_i^2 \gg m^2, \quad \tilde{p}_1 = p_1 - p_2\frac{p_1^2}{s}, \quad \tilde{p}_2 = p_2 - p_1\frac{p_2^2}{s},$$

$$\tilde{p}_1^2 = \tilde{p}_2^2 = O\left(\frac{m^6}{s^2}\right), \quad \tilde{p}_1 k_{i\perp} = \tilde{p}_2 k_{i\perp} = 0, \quad s = 2p_1p_2 = 2\tilde{p}_1\tilde{p}_2.$$

Here $\tilde{p}_i$ are light-like four-vectors build from p_i, M_i are the masses of colliding nuclei, m and s are the electron mass and the total center mass energy.

The denominators of intermediate states of the nucleon Green functions for upper and lower blocks are the same and have the following form

$$s\sum_i \alpha_i - \left(\sum_i \mathrm{k}_i\right)^2 + i0, \quad s\sum_i \beta_i - \left(\sum_i \mathrm{k}_i\right)^2 + i0. \tag{4}$$

Peripheral process is characterized by small values of longitudinal Sudakov parameters α_i, β_i and the transverse momenta of the order of electron mass

$$|\alpha_i| \sim |\beta_i| \ll 1, \quad -k_{i\perp}^2 \sim m^2. \tag{5}$$

Further simplification follows from the form of the nominators of the exchanged photons Green function (we work in the Feynman gauge). Using the Gribov's representation for the metric tensors

$$g_{\mu\nu} = g^{\perp}_{\mu\nu} + \frac{2}{s}\Big(\tilde{p_1}^{\mu}\tilde{p_2}^{\nu} + \tilde{p_1}^{\nu}\tilde{p_2}^{\mu}\Big). \tag{6}$$

it is easy to show that for the typical conversion of the nuclei currents $J_\mu(p_1)J^\mu(p_2)$ only one term, which contains the scalar products of a nucleus current with a four–momentum of another nucleus, becomes relevant (with power accuracy)

$$J_\mu(p_1)J^\mu(p_2) \approx \frac{2}{s}J_\lambda(p_1)p_2^\lambda J_\sigma(p_2)p_1^\sigma\left(1+O\Big(\frac{m^2}{s}\Big)\right). \tag{7}$$

It can be seen that the quantity $J_\mu(p_1)J^\mu(p_2)/s$ remains finite with the large values of s. This fact provides great simplification of the spinor structure of the amplitude

$$\begin{aligned}
&\bar{u}(p_1')\tilde{p}_2(p_1+\chi_1+M_1)\tilde{p}_2\ldots(p_2+\chi_N+M_1)\tilde{p}_2u(p_1) \approx s^{N+1}N_1, \\
&\bar{u}(p_2')\tilde{p}_1(p_2+\eta_1+M_2)\tilde{p}_1\ldots(p_2+\eta_N+M_2)\tilde{p}_1u(p_2) \approx s^{N+1}N_2, \\
&\qquad N_1 = \frac{1}{s}\bar{u}(p_1')\hat{p}_2u(p_1), \quad N_2 = \frac{1}{s}\bar{u}(p_2')\hat{p}_1u(p_2).
\end{aligned} \tag{8}$$

Besides we have $\sum|N_1|^2 = \sum|N_2|^2 = 2$ for the nuclei with the spin 1/2 and $|N_1|^2 = |N_2|^2 = 1$ for the scalar one. Using the identity

$$\sum_{perm}\frac{1}{\alpha_{i_1}}\frac{1}{\alpha_{i_1}+\alpha_{i_2}}\cdots\frac{1}{\sum\limits_{j=1}^{N}\alpha_{i_j}} = \prod_{i=1}^{N}\frac{1}{\alpha_i} \tag{9}$$

one can be convinced that the amplitude describing the upper and lower blocks in Fig. 1 can be put in the form

$$I_1 = N_1\prod_{i=1}^{N}\left(\frac{s}{-s\alpha_i+i0}+\frac{s}{s\alpha_i+i0}\right), \; I_2 = N_2\prod_{i=1}^{N}\left(\frac{s}{-s\beta_i+i0}+\frac{s}{s\beta_i+i0}\right) \tag{10}$$

with $N = n_e + 2n_s + n - 1$.

This expressions contain all dependence on Sudakov parameters α_i, β_i (the 4-momenta of exchanged photons in the peripheral kinematics in denominators of their Green functions can be considered as Euclidean two-vectors $k_i^2 = s\alpha_i\beta_i + k_{i\perp}^2 \approx k_{i\perp}^2 = -\mathbf{k_i}^2$).

At this stage the integration over Sudakov parameters can be done, because the dependence of the amplitude on α_i, β_i provides the convergence of the relevant integrals

$$\int I_1 \prod_{i=1}^{N} d\alpha_i = (2\pi i)^N N_1, \quad \int I_2 \prod_{i=1}^{N} d\beta_i = (2\pi i)^N N_2. \tag{11}$$

Let us now consider the single pair production. The amplitude of the process (1) in its lowest order (Born approximation) reads [5]

$$M_{(0)}^{(1)} = is(8\pi\alpha)^2 Z_1 Z_2 N_1 N_2 \frac{B_{\alpha\beta} p_1^\alpha p_2^\beta}{s \mathbf{q_1}^2 \mathbf{q_2}^2}, \quad B_{\alpha\beta} = \bar{v}(q_+) O_{\alpha\beta} u(q_-), \tag{12}$$

$B_{\alpha\beta}$ is the Compton tensor [5] for pair creation by two virtual photons with polarization vectors $e_1(q_1)$, $e_2(q_2)$. $q_{1(2)}$ are the 4–momenta of exchange photons and $r = q_+ + q_-$. Strictly speaking the squares of these 4–vectors q_i^2 do not vanish in the limit $\mathbf{q}_i^2 \to 0$. This fact becomes essential when one calculates the total cross section of a single pair production process. For the case of two or more pairs production (which is our case) the replacement $q_i^2 = -\mathbf{q_i}^2$ can safely be done.

Using the gauge invariance

$$q_1^\alpha B_{\alpha\beta} = q_2^\beta B_{\alpha\beta} = 0 \tag{13}$$

one can perform the replacement

$$\frac{B_{\alpha\beta} p_1^\alpha p_2^\beta}{s} = \frac{B_{\alpha\beta} e_1^\alpha e_2^\beta}{\tilde{s}_1} |\mathbf{q_1}||\mathbf{q_2}|, \quad e_i^\alpha = \frac{q_{i\perp}^\alpha}{|\mathbf{q_i}|}, \quad \tilde{s}_1 = s\alpha_2\beta_1, \tag{14}$$

The quantity $\tilde{s}_1$ is related to the square of the invariant mass of a pair

$$s_1 = (q_1 + q_2)^2 = \tilde{s}_1 - (\mathbf{q_1} + \mathbf{q_2})^2 = (q_+ + q_-)^2. \tag{15}$$

Two-dimensional vectors e_i can be interpreted as a polarization vectors of exchanged virtual photons.

Using (13-15) one can rewrite the Born amplitude (12) in a form

$$M_{(0)}^{(1)} = isN_1 N_2 B(q_1, q_2), \tag{16a}$$

$$B(q_1, q_2) = (8\pi\alpha)^2 Z_1 Z_2 \frac{B_{\alpha\beta} e_1^\alpha e_2^\beta}{\tilde{s}_1 |\mathbf{q_1}||\mathbf{q_2}|} \tag{16b}$$

Now we are able to construct the amplitude for the process of n pairs production. Bearing in mind the expressions (11) the matrix element of two pairs production can be represented as the convolution of two Born terms from expression (16b)

$$M^{(2)}_{(0)} = i^2 s N_1 N_2 \int B(k, k - r_1) B(q - k, q - r_2 - k) \frac{d^2\mathbf{k}}{8\pi^2}. \tag{17}$$

A straightforward generalization to the matrix element in the case of n pairs production reads

$$M^{(n)}_{(0)} = i^n s N_1 N_2 \int \prod_{i=1}^{n-1} \left(B(k_i, k_i - r_i) \frac{d^2 k_i}{8\pi^2} \right) B(h, h - r_n),$$

$$h = q - \sum_{i=1}^{n-1} k_i. \tag{18}$$

Thus one can see that the amplitude for multiple pair production is solely determined by the convolution of the amplitudes corresponding to single pair production.

In the language of the AGK unitarity rules, this result can be interpreted as unitarity cut through all exchanged pomerons.

3 The Coulomb exchanges between ions

Let us now consider the effect of m photon exchanges between nuclei A_1, A_2. The arguments given above leads to the following matrix element for the process of n pairs production with m photons exchanges among the colliding ions

$$M^{(n)}_{(m)} = \frac{i^n s N_1 N_2}{m!} \int \prod_{j=1}^{m} \left(\frac{-i\alpha Z_1 Z_2}{\chi_j^2 + \lambda^2} \frac{d^2\chi_j}{\pi} \right) \tag{19}$$

$$\cdot \int \prod_{i=1}^{n-1} \left(B(k_i, k_i - r_i) \frac{d^2\mathbf{k_i}}{8\pi^2} \right) B(k_n, k_n - r_n), \; k_n = q - \sum_{i=1}^{n-1} k_i - \sum_{i=1}^{m} \chi_i.$$

Another effect which we take into account is the possibility of the ion–ion interaction through the LBL blocks (screening effect in Fig. 1), which in the AGK language [6] is equivalent to the exchange by additional un–cut pomerons. It is associated with the iteration of a typical kernel

$$L \int Y(\mathbf{l}) d^2\mathbf{l}, \tag{20a}$$

$$Y(\mathbf{l}) = \frac{(\alpha^2 Z_1 Z_2)^2}{32\pi^4} \int \frac{P}{|\mathbf{l}_1||\mathbf{l}_2||\mathbf{l}_1 - \mathbf{l}||\mathbf{l}_2 + \mathbf{l}|} d^2\mathbf{l}_1 d^2\mathbf{l}_2 \frac{d\tilde{s}_1}{\tilde{s}_1^{\,2}}, \tag{20b}$$

$$P = \Pi^{\alpha\beta\gamma\delta} e_1^{\alpha}(l_1) e_2^{\beta}(l_1 - l) e_3^{\gamma}(l_2) e_4^{\delta}(l_2 + l), \tag{20c}$$

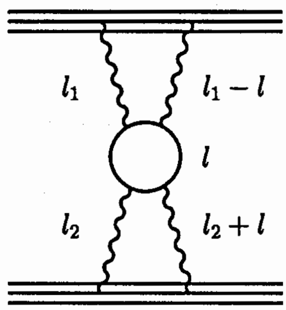

Fig. 2: Typical kernel of the ion–ion interaction through the LBL blocks.

where we rearrange the "extra" phase volume of longitudinal Sudakov parameters α_2, β_1 in terms of invariant mass square of LBL block and extract explicitly the boost degree of freedom of LBL block

$$\int \frac{d\alpha_2 d\beta_1}{s(\alpha_2\beta_1)^2} = \int \frac{d\beta_1}{\beta_1} \int \frac{d\tilde{s}_1}{\tilde{s}_1^2} = L \int \frac{d\tilde{s}_1}{\tilde{s}_1^2}, \tag{21}$$
$$L = \ln \gamma_1\gamma_2, \quad \tilde{s}_1 = (l_1 + l_2)^2 > 4m^2.$$

The structure (20) entered the matrix element (19) in the compact form

$$\frac{1}{n_s!} \prod_{i=1}^{n_s} \left(LY(\mathrm{l_i}) d^2\mathrm{l_i} \right) \tag{22}$$

Real part of (20c) (equal to one half of its s–channel discontinuity) is related with (16b)

$$\Re\Pi^{\alpha\beta\gamma\delta} e_1^\alpha(l_1) e_2^\beta(l_1 - l) e_3^\gamma(l_2) e_4^\delta(l_2 + l) = \frac{1}{2} \int B_{\alpha\beta}(l_1, r - l_1) e_1^\alpha(l_1) e_2^\beta(r - l_1)$$
$$\cdot B_{\gamma\delta}(l_1 - l, r + l - l_1) e_1^\gamma(l_1 - l) e_2^\delta(r + l - l_1) d\Phi_r, \tag{23}$$

where $d\Phi_r$ is the phase volume of the intermediate pair

$$d\Phi_r = \frac{\delta^4(r - q_+ - q_-) d^3q_+ d^3q_-}{(2\pi)^2 2\varepsilon_+ 2\varepsilon_-}. \tag{24}$$

We will show later that the imaginary part of P is irrelevant either for the total cross section or for the probability of n pairs production distribution.

4 The impact parameter representation for the amplitude

The last step in building the matrix element for the process of n real pairs creation consist in transformation of the obtained above expressions in the impact–parameter representation and summation over all eikonal photons and LBL blocks. For this we introduce the identity

$$\int \delta^2\Big(\mathbf{k_n} - \mathbf{q} + \sum_{i=1}^{n-1}\mathbf{k_i} + \sum_{i=1}^{n_s}\chi_\mathrm{i} + \sum_{i=1}^{n_v}\mathbf{l_m}\Big)d^2\mathbf{k_n} =$$

$$\frac{1}{4}\int e^{-i\mathbf{q}\rho}\exp\left[i\rho\Big(\mathbf{k_n} + \sum_{i=1}^{n-1}\mathbf{k_i} + \sum_{i=1}^{n_s}\chi_\mathrm{i} + \sum_{i=1}^{n_v}\mathbf{l_m}\Big)\right]\frac{d^2\mathbf{k_n}}{\pi}\frac{d^2\rho}{\pi} = 1\cdot \quad (25)$$

Using this expression the summation in n_e and n_s can be easily done with the result

$$M^{(n)} = \frac{i^n\pi s}{2}N_1N_2\int e^{-i\mathbf{q}\rho}e^{i\Psi(\rho\lambda)}e^{-L[A(\rho)/2+i\varphi(\rho)]}\prod_{i=1}^{n}\tilde{B}(\rho,\mathbf{r}_\mathrm{i})\frac{d^2\rho}{\pi}, \quad n\geq 2, \quad (26)$$

with

$$\frac{A(\rho)}{2} + i\varphi(\rho) = \int Y(\mathbf{l})e^{i\mathbf{l}\rho}\frac{d^2\mathbf{l}}{\pi}, \quad \tilde{B}(\rho,\mathbf{r}_\mathrm{i}) = \int B(\mathbf{k},\mathbf{k}-\mathbf{r}_\mathrm{i})e^{i\mathbf{k}\rho}\frac{d^2\mathbf{k}}{8\pi^2}, \quad (27)$$

$$\Psi(\rho\lambda) = -\alpha Z_1Z_2\int\frac{e^{i\chi\rho}}{\chi^2+\lambda^2}\frac{d^2\chi}{\pi} = -2\alpha Z_1Z_2K_0(\lambda\rho) \quad (28)$$

where $K_0(\lambda\rho)$ is modified Bessel function (Mac-Donald function).

The phase volume of final state which consists from the scattered nuclei and n pairs can be written in the following form

$$d\Gamma_{n+2} = \prod_{i=1}^{n}\left(\frac{d^3q_+d^3q_-}{(2\pi)^6 2\varepsilon_+2\varepsilon_-}\right)\frac{1}{(2\pi)^2}\frac{d^3p_1'd^3p_2'}{2\varepsilon_1'2\varepsilon_2'}\delta^4\Big(p_1+p_2-p_1'-p_2'-\sum_{i=1}^{n}r_i\Big)$$

$$= \prod_{i=1}^{n}\left(\frac{L}{(2\pi)^4}\frac{d^2\mathbf{r}_\mathrm{i}}{2}ds_id\Phi_i\right)\frac{d^2\mathbf{q}}{2s(2\pi)^2} \quad (29)$$

with $q = p'_{1\perp}$.

Cross section of n pairs production has the form

$$d\sigma_n = \frac{1}{8s}\frac{|M_n|^2}{n!}d\Gamma_{n+2}. \quad (30)$$

Statistical factor $1/n!$ is included to take into account the identity of pairs. Using the expressions (25)-(29) we get

$$\frac{d\sigma_n}{d^2\rho} = P_n(\rho), \quad P_n(\rho) = \frac{(LA_1(\rho))^n}{n!}e^{-LA_1(\rho)}, \quad n\geq 2 \quad (31)$$

with

$$A_1(\rho) = \frac{1}{2^5\pi^4}\int |B(\rho, r)|^2 ds_1 d^2\mathbf{r} d\Phi_r. \tag{32}$$

It can be easily recognized that for $A(\rho)$ from (27)

$$A(\rho) = A_1(\rho), \tag{33}$$

thus confirming the Poisson character of probability distribution in impact-parameter representation.

Let us mention that the effect of eikonal photons as well as the imaginary part of the amplitude corresponding to LBL blocks do not modify the total cross section as well as differential cross section integrated over phase volume of final nuclei. Really, integrating the square of the amplitude (26) over the phase volume one immediately obtains

$$\int e^{i\mathbf{q}(\rho_1-\rho_2)} e^{i\{[\psi(\rho_1)-\psi(\rho_2)]-L[\varphi(\rho_1)-\varphi(\rho_2)]\}} f(\rho_1) f(\rho_2) \frac{d^2\mathbf{q}}{\pi}\frac{d^2\rho_1}{\pi}\frac{d^2\rho_2}{\pi} = \int f^2(\rho)\frac{d^2\rho}{\pi}. \tag{34}$$

Nevertheless, the exclusive cross section is sensitive to both these factors.

Expression (32) can be simplified if one neglects the dependence of Compton tensor (14) on external photons virtualities

$$B_{\alpha\beta}(k, r)e^\alpha e^\beta \to B_{\alpha\beta}(0, r)e^\alpha e^\beta \tag{35}$$

and use the well known relation [7]

$$\int\limits_{4m^2}^{\infty} \sum \left|B_{\alpha\beta}(0, r)e^\alpha e^\beta\right|^2 \frac{ds_1 d\Phi_r}{s_1^2} = \frac{7}{36\pi m^2}. \tag{36}$$

As a result the expression (32) can be cast in the form

$$A(\rho) = \frac{7}{18\pi^2 m^2}(\alpha^2 Z_1 Z_2)^2 I(\rho), \tag{37}$$

$$\begin{aligned} I(\rho) &= \int^m \frac{e^{i\rho(\mathbf{k}_1-\mathbf{k}_2)}}{|\mathbf{k}_1||\mathbf{k}_1-\mathbf{r}||\mathbf{k}_2||\mathbf{k}_2-\mathbf{r}|}\frac{d^2\mathbf{r}}{\pi}\frac{d^2\mathbf{k}_1}{\pi}\frac{d^2\mathbf{k}_2}{\pi} \\ &= \int^m \frac{e^{i\chi\rho}}{|\mathbf{k}||\mathbf{k}-\chi||\mathbf{k}'||\mathbf{k}'+\chi|}\frac{d^2\chi}{\pi}\frac{d^2\mathbf{k}}{\pi}\frac{d^2\mathbf{k}'}{\pi} \\ &= \int e^{i\chi\rho}\ln^2\left(\frac{m^2}{\chi^2}\right)\frac{d^2\chi}{\pi} \approx \frac{16}{\rho^2}\left(\ln(\rho m) + O(1)\right), \end{aligned}$$

where we introduce the cut–off parameter $|k| < m$ as a result of the fast decreasing of matrix element of pair production by two photons. For the case of heavy leptons production (μ or τ) the upper limit must be replaced by quantity Q which can be associated with maximal momentum transferred to nucleus without its disintegration. For the case $\rho m \gg 1$ one has

$$A(\rho) \approx \frac{56}{9} \frac{(\alpha^2 Z_1 Z_2)^2}{\pi^2 (\rho m)^2} \left(\ln(\rho m) + O(1)\right) \tag{38}$$

which is in the agreement with [4].

Our formula (31) can be applied for the case $n = 0$ (the probability of elastic nuclei scattering). The case $n = 1$ needs a bit accurate consideration. The expression for σ_1 can be cast in the following form

$$\sigma_1 = \sigma_B + L \int A(\rho) \left(e^{-LA(\rho)} - 1\right) d^2\boldsymbol{\rho}. \tag{39}$$

First term σ_B corresponds to the leading order of the Racah formula (see for instance [2]) for the cross section in Born approximation. Inferring (39), one has to take into account the longitudinal components of momenta of exchanged photons which create the pair. The second term takes into account the unitarity corrections to the total cross section.

Conclusions

In conclusions let us enumerate very shortly the main results of the present work. In our paper we obtained the general form for the amplitude of n lepton pairs production, accounting for the mutual Coulomb interaction of relativistic ions. We get the probability of vacuum–vacuum transition in the closed analytic form. We confirmed that the probability of n pair production can be approximated by Poisson distribution. Although this result has been claimed before in a number of publications, the mutual interaction of ions has not been taken into account in these works. At last we have shown that the Coulomb interaction between the colliding nuclei, although important in the exclusive kinematics, does not affect the integral yield of lepton pairs.

Acknowledgements

We are grateful to Valery Serbo, Alexander Tarasov and Lev Lipatov for their interest to the subject and useful comments. The work is supported by INTAS 97-30494, INTAS-00366 and SR-2000 grants. E. K. is grateful to NCPI, JINR for support.

References

[1] K. Hencken, D. Trautmann, G. Baur, Phys. Rev. A51 (1995) 1874.

[2] C. A. Bertulani, G. Baur, Phys. Rep. 163 (1988) 299.

[3] G. Baur, Phys. Rev. A42 (1990) 5736.

[4] R. N. Lee, A. I. Milstein, V. G. Serbo, Phys. Rev. A65 (2002) 022102.

[5] E. Bartoš, S. Gevorkyan, E. Kuraev, N. Nikolaev, hep-ph/0109281.

[6] V. Abramovski, V. Gribov and O. Kancheli, Yad. Phys. 18 (1973) 595.

[7] E. Kuraev, L. Lipatov, Yad. Fiz. 16 (1972) 1060.

Proton–Proton Interaction with High Multiplicity at Energy 70 GeV (proposal).

E.A.Kuraev, I.D.Manjavize, V.A.Nikitin, I.A.Rufanov, A.N.Sissakian.
Joint Institute for Nuclear Research, Dubna.

P.F.Ermolov.
Institute of Nuclear Physics of Moscow State University, Moscow.

A.P.Meschanin.
State Science Center Institute of High Energy Physics, Protvino.

Abstract.

The goal of the proposed experiment is to investigate the collective behaviour of particles in the process of multiple hadron production in pp interaction $pp \to n_\pi \pi + 2N$ at the beam energy $E_{lab} = 70\ GeV$. The domain of high multiplicity $n_\pi = 30 \div 40$ or $z = n/\bar{n} = 4 \div 6$, will be studied. Near the threshold of reaction $n_\pi \to 69$, $z \to z_{th} = 8.2$, all particles get a small relative momentum $\Delta q < 1/R$, where R is the dimension of the particles production region. As a consequence of multiboson interference a number of collective effects may show up: a)- drastic increase of partial cross section $\sigma(n)$ of n identical particles production is expected, comparing with commonly accepted extrapolation; b) - the jets formation consisting of identical particles may occur as a result of multiboson BE effect; c) - large fluctuation of charged $n(\pi^+, \pi^-)$ and neutral $n(\pi^0)$ components, onset of centauros or chiral condensate effects are anticipated; d) - Increase of the rate of direct γ's as a result of the bremsstrahlung in partonic cascade and annihilation of $\pi^+\pi^- \to n\gamma$ in dense and cold pionic gas or condensate is expected. In the domain of high multiplicity $z \geq 5$, the major part of the centre of mass energy $\sqrt{s} = 11.6\ GeV$ is materialized leading to the high density thermalized hadronic system. Under this condition a phase transition to cold QGP may occur. The search for QGP signatures like large intermittency in the phase space particle distribution, an enhanced rate of direct photons will be performed. The experimental setup is designed for detection of rare high multiplicity events. The experiment is carried out at the extracted proton beam of IHEP U-70 accelerator. The required beam intensity is $\sim 10^7\ s^{-1}$. Assuming the partial cross section $\sigma(n_\pi = 35) = 10 \div 1\ nb$ the anticipated counting rate is $10 \div 1$ events per hour. The multiboson BEC enhancement may drastically increase the counting rate.

1. Introduction.

The investigation of multiple particles production at high energy is one of the fundamental problems of hadron physics. It is essentially a nonperturbative process. QCD gives only a qualitative picture of this phenomenon: hadron collision initiates a partonic cascade. The gluon strings that arise between colore partons eventually braek and produce quark-atiquark pairs. At the final stage of the cascade development when the energy is exhausted the partons join together creating hadrons. The mechanism of the colore confinement is unknown. As a consequence at present it is impossible to calculate theoretically even the main parameters of the process: multiplicity distribution, the energy and mass spectra of particles. Some features of the reaction are described by different models: thermodynamic, hydrodynamic, partonic cascade, Redge poles and so on. But none of these approaches are complete and their substantiation is far from being rigorous.

There exists an extensive literature on this subject. The theoretical approaches based on statistics and thermodynamics are reviewed in [1, 2]. The grounds for the phase transition search are presented in [3, 4]. The importance of the investigation of multiparticle production for understanding the hadron matter properties under extreme conditions, like high density and temperature, is stressed in [5]. Complete survey of the situation with particles correlation and intermittency can be find in [6]. Experimental data on multiplicity distribution and its phenomenological comprehension is given in [7].

The purpose of the proposed experiment "Thermalization"is to investigate the collective behaviour of particles in the process of multiparticle production in pp (or pN) interactions

$$pp \longrightarrow n_\pi \pi + 2N \tag{1}$$

at the proton energy $E_{lab} = 70\ GeV$. At present the multiplicity distribution at this energy is measured up to the number of charged particles $n_{ch} = 20$ [13]. The corresponding scaling variable $z = n_{ch}/\bar{n}_{ch} = 3.5$. The kinematics limit is $n_{\pi,thr} = 69$, $z_{thr} = 8.2$. Here $n_{\pi,thr}$ is the maximal number of charged and neutral pions allowed by energy-momentum conservation. We plan to study the events with multiplicity $n_\pi = 30-45$, $z = 5-6$. At large multiplicity and near the threshold of the process (1), where all particles have a small relative momentum, the high particle density $f = (2\pi)^3 d^6n/dp^3dr^3 \approx \pi^{3/2}N/(V_pV_r)$ in the 6-dimensional phase space is reached. Here N is number of particles in momentum-space volume V_pV_r. Note that in the system h=c=1 the value f is dimensionless. The authors of [8, 9, 10] argue that the parameter f indicates the importance of multiparticle effects. The value f is the mean number of pions that interfere with one given pion and build the Bose-Einstein (BE) enhancement in the two particle correlation function. So, if $f \ll 1$, only the two particle correlation may be observed. Typically $f \approx 0.1$ for the mid-rapidity region and $p_\perp \approx \bar{p}_\perp$. Even at LHC energy in Pb-Pb collisions $\bar{f}$ is expected to be small in spite of huge multiplicity. This is due to large phase space volume $V_pV_r \approx (\frac{4}{3})^2\bar{p}^3\bar{r}^3$ occupied by secondary particles: $\bar{p} \approx 0.5\ Gev/c$, $r \approx 10\ fm$. In contrast to high energy A-A collision in our case of the pp collision the volume V_pV_r is by three order of magnitude less, since we expect to have $\bar{p} \approx 0.07\ GeV/c$, $r \approx 2 \div 3\ fm$. So we anticipate to reach very high particle phase space density $f \gg 1$. As a consequence, one expects to observe the collective effects connected with multiboson interference: broadening of the multiplicity distribution, anomalous fluctuation of charged and neutral components, the jets formation and so on.

In the region $z \geq 4$ the major part of center of mass energy $\sqrt{s} = 11.6\ GeV$ is transferred into mass of produced particles. The density of the created hadron system may be rather high, $\rho/\rho_0 \approx 5 \div 10$. Here ρ_0 is the density of nuclear matter in the ground state. According to the common notion the system under such condition supposed to be quark-gluon plasma (QGP). Fig. 1 is taken from [11] to illustrate this statement.

The onset of QGP manifests itself, at least, by two signatures: large particles intermittency in phase space of rapidity - transverse momentum and an excess of the direct photons and lepton pairs. We plan to search for both of these signatures. The unique feature of QGP in our case is its low temperature. The closer we approach to the reaction threshold, the lower is the temperature and higher is the density of the system. The lower is the temperature the longer is life time of the system. The latter is especially important: the system must come to the equilibrium in order to reveal the QGP features.

The further progress in understanding the dynamics of the multiparticle production process will come from further development of the experiment.

For the purposes of this experiment we plan to improve the setup Spectrometer with Vertex Detector (SVD) installed at the extracted proton beam of IHEP (Protvino) U-70 accelerator. The beam intensity is $10^7\ c^{-1}$. It incidents on hydrogen (or light nuclei) target and generates $10^4\ c^{-1}$ pp (or pN) interaction. One should mention that it is difficult to make a reliable extrapolation of experimentally measured multiplicity distribution from the region $0 \leq z \leq 3.5$ to the region $z \geq 5$. We expect a partial cross section in the interval $4 \leq z \leq 5$ is about 10 nb $\div$ 1 nb. Then we can collect about 10 $\div$ 1 events per hour. However, there are theoretical arguments favoring BE enhancement of the identical pions production. Then the counting rate will be much higher.

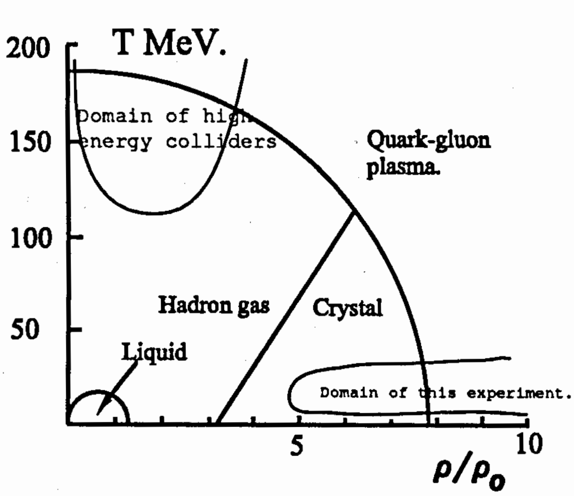

Fig. 1. Phase diagram of nuclear matter.

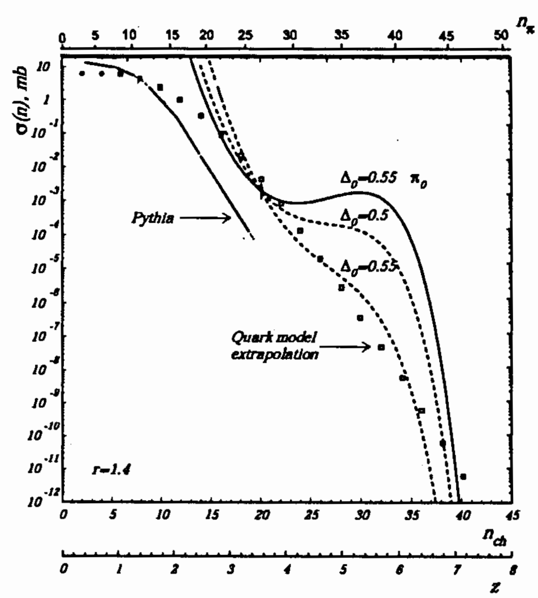

Fig. 2. Multiplicity distribution (partial cross-section) in pp interaction. For details see text.

2. Physics program.

Multiparticle process near kinematics limit.

Let us consider high enough multiplicity n_{crit} when in c.m.s. no energy remains for formation of the leading particles. Then all secondaries have equal energy $\sqrt{p_\perp^2 + p_l^2 + m^2}$ which we determine from the mean transverse momentum of pion $p_\perp \approx 0.3$ GeV/c as it was measured in soft hadron reactions. The longitudinal momentum is $p_l = \frac{1}{\sqrt{2}} p_\perp$. The critical multiplicity is determined by relation $\sqrt{\bar{p}_\perp^2 + m_\pi^2} = (\sqrt{s} - 2m_N)/(n_{crit} + n_N)$. Here n_N=2 is the nucleon multiplicity. We get $n_{crit} = 23$. In the region $n \geq n_{crit}$ the particles in c.m.s. should have isotropic angular distribution and their energy distribution is Maxwell or BE. The corresponding temperature is $T = \frac{2}{3} E_{kin}$; $E_{kin} = (\sqrt{s} - 2m_N - n_\pi \cdot m_\pi)/(n_\pi + n_N)$. Here n_π is pion multiplicity. T depends on pion multiplicity n_π and vanishes when $n_\pi \to n_{th}$. On this basis we develop the Monte Carlo event generator and calculated the angular and momentum distribution of the pion and nucleons. These data are necessary for the experiment planing. An example: at multiplicity n_π =50 mean c.m. energy of all particles is 50 MeV and mean lab. emission angle $\bar{\theta}_\pi$=90 mr, $\bar{\theta}_N$=40 mr. These numbers indicate remarkable feature of apparatus: having very modest angular acceptance $\theta = 2\bar{\theta}_\pi$=200 mr it will detect 95% of all secondary products.

There is the experimental indication on onset of the thermalization regime at multiplicity n_{ch}=18 [12].

Multiplicity distribution.

Topological cross section $\sigma(n_{ch})$ in pp interaction at 70 GeV at U-70 accelerator have been measured in two experiments [13], see fig. 2. The calculation by the MC Pythia code is shown. One can see that standard generator predicts cross section $\sigma(z)$ which is in reasonably good agreement with experimental data at $z < 2$ but it underestimates the value of $\sigma(z)$ by two order of magnitude at $z \geq 3.5$.

An important task is the extrapolation of the function $\sigma(z)$ from the domain $z \leq 3.5$ to the domain of our interest $z \geq 5$. One of the successful approximation of the data at moderate energy is suggested in [14]. Authors make use of the additive quark model. It is assumed one quark-quark collision is described by Poisson function. Two and three qq-collision is represented by the convolution of Poisson functions.

The models mentioned above do not take in to account the effect of identical particles interference. Generally, the account of the multi-boson effects is extremely difficult task. But there exists a simple analytically solvable model [8] allowing for a study of the characteristic features of multiboson systems under various conditions including those near the Bose condensation. The latter even is called some times as pion laser. The authors of [10] apply this model to study the influence of the BEC on pion multiplicity, spectra and two pion correlation function. Prediction of this model is shown in fig. 2. Free parameters are: r - space dimension of the system and Δ - characteristic mean momentum of the particles. We see that model strongly favours the production of π^0 (so called anticentauro event).

Multiboson jets.

We considered the influence of the BE statistics on pion multiplicity distribution. There is another interesting BEC effect which is widely discussed in literature. It is multiboson momentum (and angular) correlation. Reference [15] is devoted to the analysis of the multipionic system. It was found that requirement of wave function symmetrization leads to the formation of an interference maximum with the momentum dispersion d_{cor} and the angular width θ_{cor}: $d_{cor} = C/(r\sqrt{n})$; $\theta_{cor} = d_{cor}/p_0$, p_0 is the mean momentum of the pion. The meaning of these formulas is that at $n \gg 1$ there is monochromatization in momentum space and angular collimation of the particles within the interference maximum.

Qualitatively similar effect is discussed in [16] but on rather different ground. The authors point out the possibility that at high enough energy density $3 \div 6\ GeV/fm^3$ (which we hope will be easily achieved in our experiment) the produced pions can create certain coherent state - a classical pion field, the analog of the classical electromagnetic field. Thus one can expect rather characteristic picture: a large number of pion may emerge with almost the same momentum, creating a jet pattern in concrete collision. There may be jets consisting predominantly of the particles with only one sign (i.e. π^+, π^- or π^0). This effects resemble a laser without optical resonator. Another analogy is the electromagnetic coherent superemission in spin oriented system in magnetic field.

Thermodynamics of the hadron system.

The emphasis of this proposal is the study of multiparticle process (1) at high multiplicity $n \geq n_{crit}$, where the leading particles must vanish and it is reasonable to assume that the system approaches the thermodynamic equilibrium state. The onset of this regime may be checked directly by measuring the degree of isotropy of particle angular distribution in c.m.s. and by evaluation the temperature T_i corresponding to different species of the secondaries: $i = \pi,\ K,\ p,\ \bar{p},\ d$. The difference of the quantities T_i gives another criterion of equilibrium. The thermodynamics analysis of the hadron production is widely used for a long time. The main features of the multiparticle process seem to have got quantitative description. In particular the abundance of different particle species is explained from relativistic quantum molecular dynamics. The application of this kind of theories and models to the data analysis of the proposed experiment have a good ground since we plan to take a special measure to detect a multiparticle systems approaching the thermal equilibrium state. The deviation of the experimental observation from theoretical prediction will serve as a signal of a new physics.

Intermittency.

The secondary particles have a nonuniform distribution in the momentum space. The particle density has statistical and dynamical fluctuations, i.e. the distribution has an intermittent character. The intermittency depends on the particle production mechanism. For instance, the resonances and the clusters in intermediate state give rise to fluctuations in the final state of the system. The theoretical considerations show the rise of intermittency near the phase transition point. It also depends on the hadronization process (i.e. confinement) and QCD vacuum properties. Thus, the experimental study of the intermittency may throw light on the complicated and hidden mechanism of particle production at high energy. The present project certainly has a direct connection with this topic, since high statistics of the high multiplicity events makes it possible to carry out the precise investigation of the intermittency effect.

One should to distinguish stochastic and regular intermittency. The field source movement inside the medium with velocity greater than the phase velocity of the field quanta in this medium leads to wave production. In case of electromagnetic interactions it is a well known Cherenkov effect. Generalization of Cherenkov radiation to scalar and vector fields cases was developed in a number of papers. In particular, Cherenkov gluon radiation in QCD frames devised in [17]. The existence of color current, necessary for this phenomena, is confirmed by studying of hard processes. The Cherenkov type radiation can be emitted in the projectile and target particles. This leads to two peaks of dense groups of particles (spikes) distribution in rapidity phase-space. At the same time the particle distribution at the azimuthal angle is uniform. It is so called ring events. Indication on existence of such phenomenon was reported in a number of papers, see e.g. [18]. A double-peak shape in the pseudorapidity particle distribution for pp-collisions has been observed in agreement with the coherent gluon-jet emission model. Therefore high luminosity and high multiplicity trigger in "Thermalization"setup is very important to collect enough statistic for study the ring events. The accurate data will give possibility to determine confinement radius and refractive index of hadron matter.

Direct photons.

The direct photons (DP) as definition are not a decay product of any known particles. In accordance with quantum electrodynamics they may be emitted in the process of charged particle scattering. In particular quark-quark and quark-gluon interaction leads to photon emission. The higher is the density and longer is the system lifetime, the more of DP it should emit. This simple picture explains why so many experimental and theoretical efforts are devoted to the DP study. The phenomenon of the DP is discovered, but, it seems, nothing unusual has been found up to now: the DP rate agrees with general theoretical expectation. But there is one exception. It is low energy photons $p_\perp \leq 0.1\ GeV/c,\ x \leq 0.01$. One can cite at least three publications where the low energy photon spectrum is measured and the photon rate $5 \div 7$ times exceeds theoretical prediction. It is K^+p and $p\bar{p}$ interaction at 70 GeV and π^+p and K^+p interaction at 250 GeV [19]. The excess of DP may be connected with some unknown physical process. It is especially interesting to investigate DP in proposed experiment, since we are going to deal with a high density system. The quark-gluon cascade leading to high multiplicity final state has large number of steps (rescattering, loops and so on) and each of them is connected with bremsstrahlung. Apart of this at high density an additional source of $\gamma's$ is predicted

[20]: the charged pions annihilation $\pi^+\pi^- \to n\gamma$. This process if being discovered may serve as one of the tool of the density and temperature measurement.

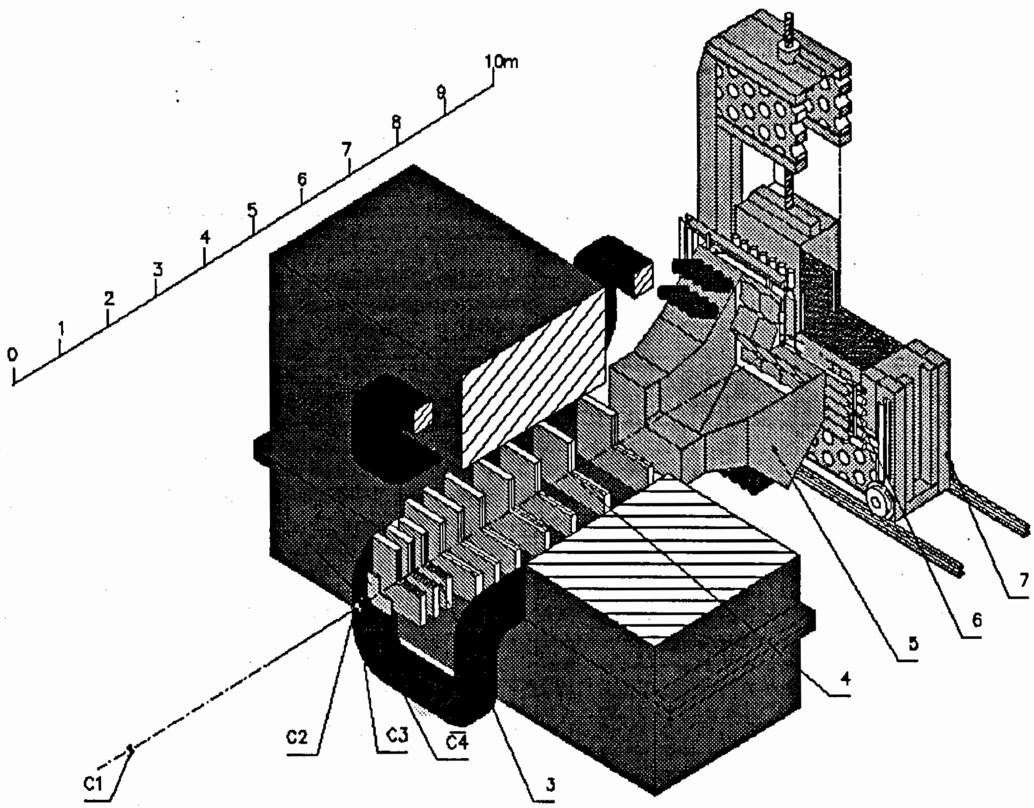

Fig. 3. Schematic of the experimental setup - Spectrometer with Vertex Detector (SVD). c1,c2 - beam monitor. c3 - nuclear and hydrogen targets. c4 - silicon vertex detector. 3, 4 - tracker of the magnetic spectrometer, drift tubes and proportional chambers. 5 - threshold Cherenkov counter. 6 - scintillation hodoscope. 7 - electromagnetic calorimeter.

3. Experimental setup.

The experiment will be carried out at improved setup SVD installed at the extracted proton beam of IHEP (Protvino) U-70 accelerator [21]. The physics program dictates the following requirements to the apparatus.

- The setup is capable to detect with high efficiency the events with large charged and (or) neutral multiplicity $20 \div 50$ particles. Photon multiplicity is up to 100. The energy threshold of γ's detection is 50 MeV.

- The trigger system is capable to select the rare events with multiplicity $n_\pi = 20 \div 50$. The coefficient of suppression of low multiplicity events $n_\pi < 20$ is 10^3.

- The magnetic spectrometer has resolution $\delta p/p \approx 1\%$ in the momentum interval $p = 0.3 \div 4.\ GeV/c$.

The setup schematic is presented in Fig. 3. The apparatus consists of the following main parts.

- The position sensitive beam monitor.

- The liquid hydrogen target has diameter 2 cm and length 2.5 cm. The apparatus test and some data collection may be done with nuclear target.

- The vertex detector consists of 10 planes of silicon strip detectors with space resolution 25 - 50 mcm.

- The trigger solution is obtained from combination of amplitude signals and number of hits in strip detectors and electromagnetic calorimeter signal.

-The magnet has the bending power 1.5 $T \cdot m$ and aperture X x Y = 130 x 160 cm^2.

- The tracker of the magnetic spectrometer consists of 25 planes of drift tubes and proportional chambers.

4. Conclusion.

The goal of the proposed experiment "Thermalization"is the investigation of collective behaviour of particles in the process of multiple hadron production in pp (or pN) interaction $pp \rightarrow n_\pi \pi + 2N$ at the beam energy $E_{lab} = 70\ GeV$. The domain of high multiplicity $n_\pi = 30 \div 50$ or $z = n/\bar{n} = 4 \div 6$, will be studied. Near the threshold of reaction $n_\pi \rightarrow 69$, $z \rightarrow z_{th} = 8.2$, all particles get small relative momentum $\Delta q < 1/R$, where R is the size of the particles production region. As consequence of multiboson interference a number of collective effects may show up.

The physics objectives of the experiment are as followers.

1. Search for a new phenomena.

- Drastic broadening of the multiplicity distribution $\sigma(z)$ is expected due to effect of BEC. In the region $n_\pi \geq 40$, $z \geq 5$ the actual cross section $\sigma(z)$ may exceed by 3 order of magnitude the extrapolated function $\sigma_{extr}(z)$. The latter is calculated on the basis of QCD or qq-collision model without inclusion of the BEC effect.

- The BEC may manifest itself by formation of narrow jets of identical particles or "cold spots"in momentum space. The other notions for this effect are pion laser, classical boson field, boson condensate.

- The particle sources may be two types: chaotic and coherent. The precision measurement of the two particle correlation function $R(q)$ makes possible to determine the sources parameters: chaoticity, space-time size, primordial correlation length and time. The latter is dynamic characteristics of the hadron matter.

- The large variation of the π^+, π^-, π^0 multiplicity is expected in framework of BEC. The multiplicity fluctuations may also manifest classical pionic field production or onset of chiral condensate.

2. The systematic and precision study of known phenomena.

- The direct photons especially with low energy $E_\gamma \leq 100\ MeV$ may manifest a new physics, in particular, existence of the QGP.

- The study of stochastic intermittency is the instrument for phase transition search and also search for BEC effect of the cold spot type.

- The existence of events with regular intermittency, so called ring events, is published. This effect is referred as a gluonic Cherenkov radiation. It needs confirmation. If it really exists it will be a genuine probe of the hadronic matter properties.

- The measurement of the production rate of the particles of different species π, K, p, d, $\bar{p}$ gives data for test and development of thermodynamics models. Simultaneous analysis of the differential cross section and BE correlation functions makes possible to disentangle the hadronic system size, temperature and expansion rate.

The experiment will be carried out at 70 GeV proton beam of IHEP U-70 accelerator. The apparatus design is essentially based on the fact that at high multiplicity the all secondary particles have sharp forward collimation. In spite of modest setup size it is expected that at least 70% of all particles drops in to apparatus aperture and will be detected.

The apparatus includes liquid hydrogen target, silicon vertex detector, magnetic spectrometer, electromagnetic calorimeter. The multilevel trigger system is designed to select the rare events with high charged and neutral multiplicity $n_\pi \geq 20$. The target luminosity is $10^{30}\ cm^{-2}s^{-1}$ at the beam intensity $10^7\ s^{-1}$.

The magnet spectrometer provides high momentum resolution $\delta p \leq 5\ MeV/c$ which is crucially important for BEC investigation.

The counting rate of the events with total multiplicity 40 is expected to be 10 events per hour. If scenario of BEC is realized, than counting rate will be essentially higher.

References

[1] R.Hagedorn. La Revista del Nuovo Cimento, v. 6, N 10, p. 1, (1983).

[2] I.D.Manjavidze. El. Part. and At. Nucl., v. 16, N 1, p. 101, (1985).
J.D.Manjavidze, A.Sissakian. JINR preprint E2-2000-217, Dubna,(2000).
Phys. Rep. 346 (2001) 1.

[3] J.D.Bjorken Phys. Rev. D27, p. 140, (1983).

[4] I.L.Rosental, Yu.A.Tarasov. Uspekhi Phys. Nauk., v. 163, N. 1, p. 29, (1993).

[5] E.L.Feinberg et. al., Uspekhi Phys. Nauk, v. 104, p. 539, (1971).

[6] I.M.Dremin. Uspekhi Phys. Nauk, v. 164, N 8, p. 785, (1994).
A.E.De Wolf et al. Phys.Rep. v. 270, p.1, (1996).

[7] A.I.Golokhvastov. JINR preprint p2-98-181 , Dubna, (1998).

[8] S.Pratt. Phys. Rev., C50, p. 469, (1994).

[9] G.F.Bertch. Phys. Rev. Lett., v. 72, p.2349, (1994).

[10] R.Lednitsky et al. Phys. Rev. C61, N 3, p. 034901, (2000).

[11] V.G.Boiko et al. El. Part. and Atomic Nucl., v. 22, p. 675, (1991).

[12] P.F.Ermolov. Proceedings of 21 session of IHEP PAC, p. 67, Serpukhov, (1977).

[13] V.V.Babintsev et al., IHEP preprint M-25, Protvino, (1976). M.Yu.Bogolyubsky et al. IHEP preprint 97-50, Protvino, (1997).

[14] O.G.Chikilev, P.V.Shliapnikov. Jadernaja Phis., v. 55, p. 820, (1992).

[15] M.I.Podgoretsky. JINR preprint P2-85-240 (in Russian) , Dubna, 1985.

[16] A.A.Anselm and M.G.Ryskin. Phys. Lett., B266, p. 482, (1991).

[17] I.M.Dremin, JETP Lett. v. 30, p. 140, (1979); Elem. Part. and Atom. Nucl. v. 18, p. 31, (1987).

[18] I.M.Dremin et al., Jorn. of Nucl. Phys., v. 52, N 3(9), p. 840, (1990).

[19] P.V.Chlapnikov et al., Pys. Lett., B141, p. 276, (1984). M.N.Ukhanov et al., IHEP preprint 86-195, Protvino, (1986). F.Botterwerk et al., Z. Phys.,C51, p. 541, (1991).

[20] M.K.Volkov and E.Kuraev. Phys. Lett., B424, p. 235, (1998); Yad. Fis., v. 62, p. 133, (1999).

[21] S.G.Basiladze, P.F.Ermolov et al. Proposal of an experiment for studying mechanisms of charmed particle production and decay in pA interaction at 70 GeV. SVD collaboration. Preprint INP MSU 99-28/586, Moscow.

Moments of the Very High Multiplicity Distributions.

V.A. Nechitailo

Lebedev Physical Institute, Moscow 119991, Russia

Abstract

In experiment, the multiplicity distributions of inelastic processes are truncated due to finite energy, insufficient statistics or special choice of events. It is shown that the moments of such truncated multiplicity distributions possess some typical features. In particular, the oscillations of cumulant moments at high ranks and their negative values at the second rank can be considered as ones most indicative on specifics of these distributions. They allow to distinguish between distributions of different type.

1 Introduction

Studies of multiplicity distributions of high-energy inelastic processes have produced many important and sometimes unexpected results (for the reviews, see, e.g., [1, 2, 3]). The completely new region of very high multiplicities will be opened with the advent of RHIC, LHC and TESLA accelerators.

Theoretical approaches to multiplicity distributions in high-energy processes have usually to deal with analytic expressions at (pre)asymptotic energies which only approximately account for the energy-momentum conservation laws or with purely phenomenological expressions of the probability theory. The multiplicity range extends in this case from zero to infinity.

In experiment, however, one has to consider distributions truncated at some multiplicity values in one or another way. These cuts could appear due to energy limitations, low statistics of experimental data or because of special conditions of an experiment. Energy limitations always impose the upper cutoff on the tail of the multiplicity distributions. Low statistics of data can truncate these distributions from both ends if it is insufficient to detect rare events with very low and/or very high multiplicity. Similar truncations appear in some specially designed experiments [4], when events within some definite range of multiplicities have been chosen.

It would be desirable even in these cases to compare the distributions within those limited regions with underlying theoretical distributions. The straightforward fits are sometimes not accurate enough to distinguish between various possibilities because the probability values vary by many orders of the magnitude. More rigorous approach is to compare different moments of the truncated distributions. The simple-minded χ^2-fits are less sensitive and provide less information. The cumulant moments K_q seem to be most sensitive to slight variations (and, especially, cuts and shoulders) of the distributions. They often reveal such tiny details of the distributions which otherwise are hard to notice.

In particular, QCD predicts quite peculiar behaviour of cumulant moments as functions of their rank q. According to solutions of the equations for the generating functions of the multiplicity distributions in the asymptotic energy region, the ratio of cumulant moments K_q to factorial moments F_q usually denoted as $H_q = K_q/F_q$ behaves as q^{-2} and at preasymptotic energy values reveals the minimum [5] at $q \approx 5$ with subsequent oscillations at higher ranks [6, 7]. Such a behaviour has been found in experiment at presently available energies [8, 9]. The solutions of the corresponding equations for the fixed coupling QCD also indicate on similar oscillations [10]. At asymptotics, the oscillations should disappear and H_q becomes a smoothly decreasing and positively definite function of q, as mentioned above.

Neither of the distributions of the probability theory possesses these features. Among them, the negative binomial distribution (NBD) happens to be one of the most successful ones in the description of global features of the multiplicity distributions [11]. Let us remind that the negative binomial distribution is defined as

$$P_n = \frac{\Gamma(n+k)}{\Gamma(n+1)\Gamma(k)} a^n (1+a)^{-n-k}, \tag{1}$$

where $a = \frac{\langle n \rangle}{k}$, $\langle n \rangle$ is the mean multiplicity, k is an adjustable parameter, and the normalization condition reads

$$\sum_{n=0}^{\infty} P_n = 1. \tag{2}$$

Its generating function is

$$G(z) = \sum_{n=0}^{\infty} P_n (1+z)^n = \left(1 - z\frac{\langle n \rangle}{k}\right)^{-k}. \tag{3}$$

The integer rank factorial and cumulant moments, and their ratio are

$$F_q = \frac{1}{\langle n \rangle^q} \frac{d^q G(z)}{dz^q}|_{z=0} = \frac{\Gamma(q+k)}{\Gamma(k) k^q}, \tag{4}$$

$$K_q = \frac{1}{\langle n \rangle^q} \frac{d^q \ln G(z)}{dz^q}|_{z=0} = \frac{\Gamma(q)}{k^{q-1}}, \tag{5}$$

$$H_q = \frac{\Gamma(q)\Gamma(k+1)}{\Gamma(k+q)}. \tag{6}$$

H_q-moments at the parameter $k = 2$ behave as $2/q(q+1)$, i.e. with the power-law decrease reminding at large q that of QCD, however, with a different weight factor. Therefore, at first sight, it could be considered as a reasonably good analytic model for asymptotic behaviour of multiplicity distributions. It has been proclaimed [12, 13, 14, 15] that the superposition of two NBDs with different parameters and their cutoff at high multiplicities can give rise to oscillations of H_q and better fits of experimental data at preasymptotic energies. Nevertheless, the fits have not been perfect enough.

Let us compare first the asymptotic QCD predictions with NBD fits at different values of the adjustable parameter k. The values of $D_q = q^2 H_q$ are plotted in Fig. 1 as functions of q for the asymptotic QCD are identically equal to 1. For NBD at $k = 2$, they exceed 1 tending to 2 at large q. At larger values of k, all D_q are less than 1 except $D_2 = 1$ at $k = 3$. Surely, the identity $D_1 \equiv 1$ is valid for any k due to the normalization condition.

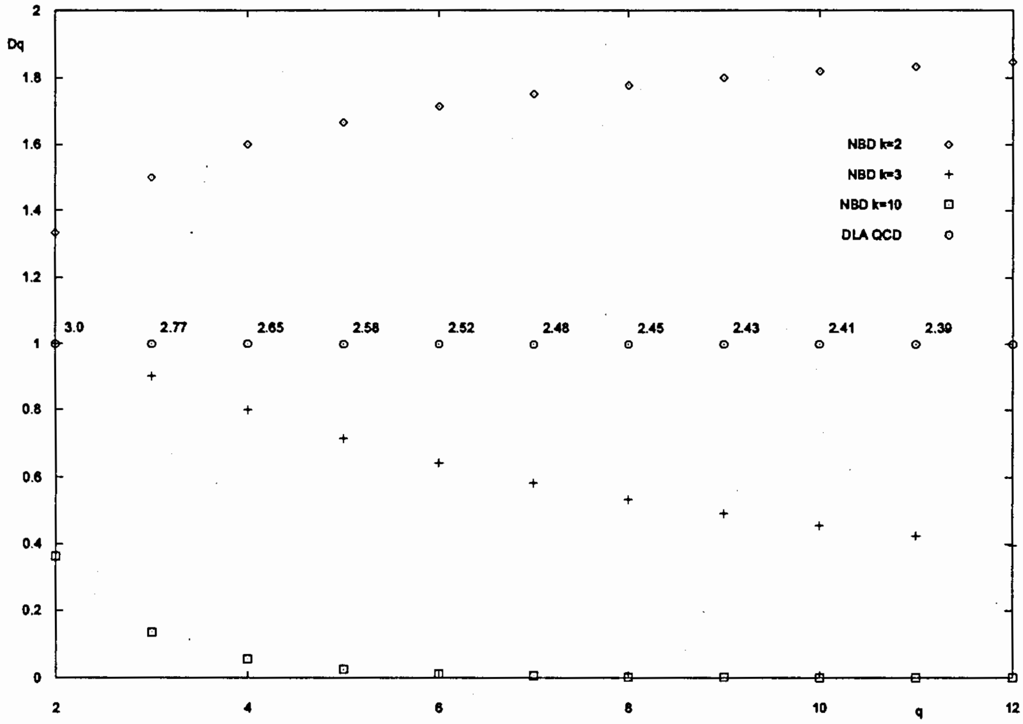

Fig. 1. $D_q = q^2 H_q$ are shown for asymptotical QCD by circles ($D_q^{QCD} \equiv 1$) in comparison with NBD-predictions at different values of the parameter k=2 (diamonds), 3 (crosses), 10 (squares). The numbers near the QCD values show which values of k one would need to use for NBD to fit $D_q = 1$ at the corresponding q.

To get asymptotic QCD results with all $D_q \equiv 1$ from the expressions similar to NBD, one would need to modify NBD in such a way that the parameter k becomes a function of n. Thus some effective values of k should be used to get QCD moments $D_q = 1$ at various q. They are obtained as the solutions of the equation

$$\prod_{n=1}^{q-1} \left(1 + \frac{k(q)}{n}\right) = q^2, \tag{7}$$

which follows from Eq. (6) for $H_q = q^{-2}$. They show that k somewhat decreases from 3 to some values exceeding 2 with increase of q. This reflects the well known fact that the tails of distributions are underestimated in NBD-fits [14] compared to experimental data in the preasymptotic region. Also, the amplitude of oscillations and their periodicity are not well reproduced by a single truncated NBD [14], and one has to use the sum of at least two NBDs to get a better fit. However, rather large values of k were obtained in these fits. It implies, in fact, that the fit is done with the help of two distributions very close to Poissonian shapes because the Poisson distribution is obtained from NBD in the limit $k \to \infty$. Therefore, the tails are suppressed very strongly.

Here, we will focuse our efforts on qualitative changes of moments when NBD is truncated, especially, as applied to studies of very high multiplicities.

In QCD considerations based on the equations for the generating functions for quark and gluon jets, the preasymptotic (next-to leading order etc) corrections give rise to oscillations of H_q. Even though they are of the higher order in the coupling strength, they appear mainly due to account of energy conservation in the vertices of Feynman diagrams but not due to considering the higher order diagrams which are summed in the modified perturbation theory series (see [3]). In the phenomenological approach, this would effectively correspond to the cutoff of the multiplicity distribution at some large multiplicity. Therefore, we intend here to study how strongly such a cutoff influences the NBD-moments, whether it produces oscillations of the cumulant moments, how strong they are, and, as a more general case, consider the moments of NBD truncated both at low and high multiplicities. This would help answer the question if the shape of the distribution in the limited region can be accurately restored from the behaviour of its moments. It could become especially helpful if only events with very high multiplicities are considered in a given experiment because of the above mentioned underestimation of tails in the NBD-fits.

2 Truncated NBD and its moments

In real situations, the multiplicity distribution is sometimes measured in some interval of multiplicities and one can try to fit by NBD the data available only in the restricted multiplicity range. Therefore, we shall consider the negative binomial distribution within the interval of multiplicities $m \leq n \leq N$ called $P_n^{(c)}$ and normalized to 1 so that

$$\sum_{n=m}^{N} P_n^{(c)} = 1. \tag{8}$$

Moreover, due to above reasoning and to simplify formulas we consider here only the case of $k = 2$. The generalization to arbitrary values of k is straightforward.

The generating function of the truncated distribution $G_c(z)$ can be easily found as

$$G_c(z) = \sum_{n=m}^{N} P_n^{(c)}(1+z)^n = G(z)(1+z)^m \frac{f(z)}{f(0)}, \tag{9}$$

where

$$f(z) = 1 + m(1-x) - [1 + (N+1)(1-x)]x^{N-m+1}, \tag{10}$$

$$x = b(1+z), \quad b = \frac{a}{1+a}. \tag{11}$$

Correspondingly,

$$f(0) \equiv f(z=0) \equiv f(x=b). \tag{12}$$

Using the above formulas for the factorial moments, one gets the following formula for the moments of the truncated distribution expressed in terms of the NBD-moments (4):

$$F_q^{(c)} = \left(\frac{\langle n \rangle}{\langle n \rangle_c}\right)^q F_q \left\{ 1 + \frac{1}{f(0)(q+1)} \sum_{r=1}^{q} \frac{a^{-r}}{r!}(q+1-r) \times \right.$$
$$\left[\left(\frac{m}{1+a} + 1 - r\right)\theta(m+1-r) \prod_{i=1}^{r}(m+2-i) \right.$$
$$\left.\left. - \left(\frac{N+1}{a+1} + 1 - r\right) b^{N-m+1} \prod_{i=1}^{r}(N+3-i) \right] \right\} \tag{13}$$

where $\langle n \rangle_c$ is the mean multiplicity of the truncated distribution. It is related to the mean multiplicity $\langle n \rangle$ of the original distribution as

$$\langle n \rangle - \langle n \rangle_c = \frac{(1-b)[(N+1)(N+2)b^{N-m+1} - m(m+1)]}{1 + m(1-b) + b^{N-m+1}[(N+1)b - N - 2]}. \tag{14}$$

These expressions can be used also for the distributions truncated at one side by setting $m = 0$ or $N = \infty$.

The cumulant moments can be calculated after the factorial moments are known from Eq. (13) according to the identities

$$F_q = \sum_{m=0}^{q-1} \frac{\Gamma(q)}{\Gamma(m+1)\Gamma(q-m)} K_{q-m} F_m. \tag{15}$$

This formula is a simple relation between the derivatives of a function and of its logarithm (see Eqs (4) and (5)). Therefore it is valid for both original and truncated distributions.

For the Poisson distribution, the ratios H_q are identically equal to zero, and are given by Eq. (6) for NBD while truncation induces new features. In Figures we show the behaviour of the ratios H_q as functions of the rank q for the truncated Poisson and negative binomial distributions.

At the beginning, we consider the abrupt cutoff only of the very high multiplicity tail, i.e., the case $m = 0$ and $N > \langle n \rangle$. This mimics the energy-momentum conservation limits. In Figs 2 and 3, it is shown that such a cutoff induces oscillations of H_q. The farther is the cutoff from the mean multiplicity, the weaker are oscillations. This quite expected result is known from long ago [12, 13]. It is demonstrated in Fig. 2 for $\langle n \rangle = 10$ and different cutoffs at $N = 30, 40, 50$. Another representation of the same result is seen in Fig. 3 where the constant cutoff $N = 30$ has been chosen for different $\langle n \rangle$ equal to 5, 10 and 15. The closer is the cutoff to $\langle n \rangle$, the stronger the low-rank moments are damped. For the faraway cutoff $N = 50$, the period of oscillations increases. This increase is larger for lower mean multiplicity (see Fig. 4). At $N/\langle n \rangle$=const, one observes the approximate scaling of H_q as seen in Fig. 5.

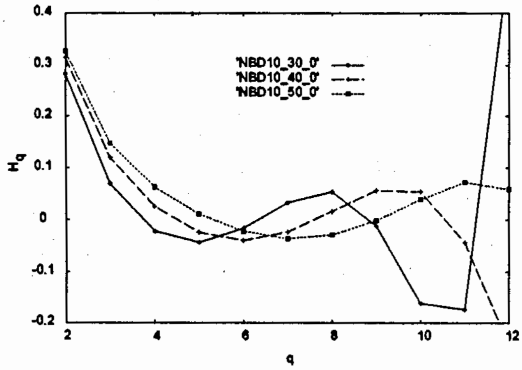

Fig.2. H_q-moments for NBD with $\langle n \rangle$=10 truncated at $N = 30$ (diamonds), 40 (crosses), 50 (squares) at $m = 0$.

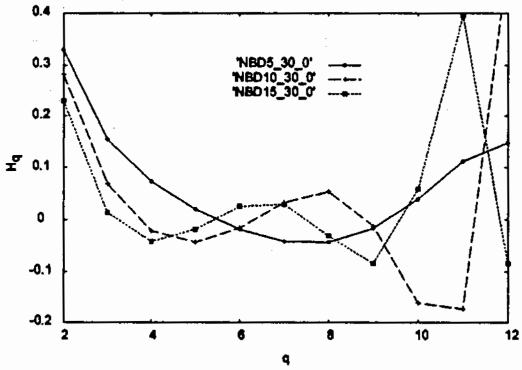

Fig.3. H_q-moments for NBD with $\langle n \rangle$=5 (diamonds), 10 (crosses), 15 (squares) truncated at $N = 30$ at $m = 0$.

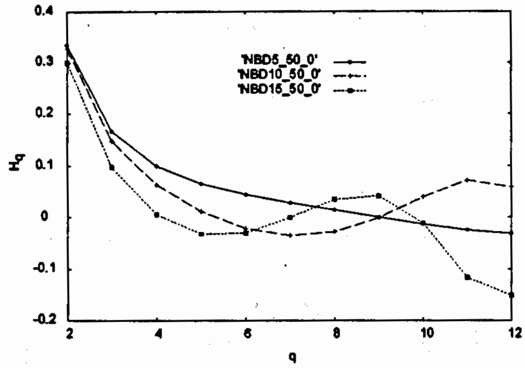

Fig.4. H_q-moments for NBD with $\langle n\rangle$=5 (diamonds), 10 (crosses), 15 (squares) truncated at $N = 50$ at $m = 0$.

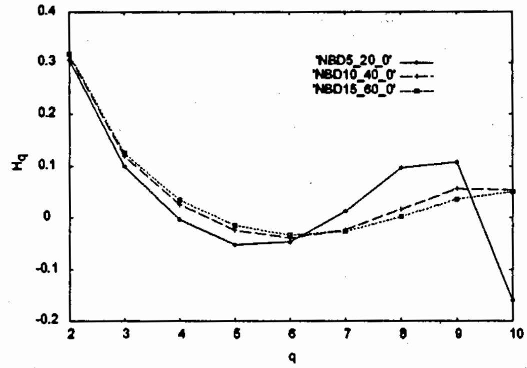

Fig.5. Approximate scaling of H_q-moments for NBD with $N/\langle n\rangle$=const.

3 Very high multiplicities

With the advent of RHIC, LHC and TESLA we are approaching the situation when average multiplicities become very high and the tails of multiplicity distributions reach the values which are extremely large. These events with extremely high multiplicities at the tail of the distribution can be of a special interest. The tails of particular channels die out usually very fast, and a single channel dominates at the very tail of the distribution. Mostly soft particles are created in there. Thus one hopes to get the direct access to very low-x physics. QCD-interpretation in terms of BFKL-equation (or its generalization) can be attempted. Also, the hadronic densities are rather high in such events, and the thermodynamical approach can be applied [16].

However, these events are rather rare and the experimental statistics is quite poor until now. The Poisson distribution has the tail which decreases mainly like an inverse factorial. According to NBD (1), the tail is exponentially damped with the power-increasing preexponential factor. At the same time, QCD predicts even somewhat slower decrease as it is seen in Fig. 1 from the behaviour of the moments. This is important for future experiments in the very high multiplicity region.

To study these events within the truncated NBD with $k = 2$ according to Eq (13), let us choose the multiplicity interval of the constant length $N - m = 20$ and place it at various distances from the mean multiplicity $\langle n\rangle = 10$ as in Fig. 2. The resulting H_q are shown in Fig. 6.

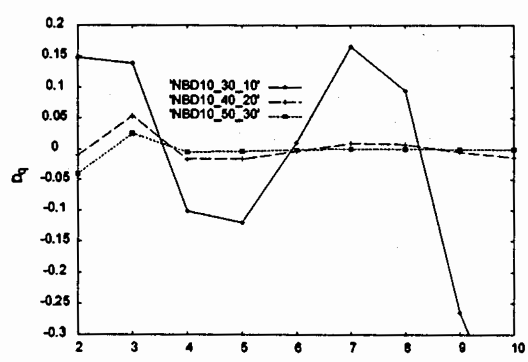

Fig. 6. D_q-moments for NBD with $\langle n\rangle$=10 truncated at $m = 10, N = 30$ (diamonds), 20-40 (crosses), 30-50 (squares).

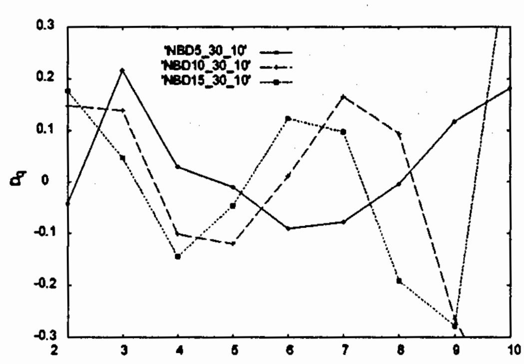

Fig. 7. D_q-moments for NBD with $\langle n\rangle$=5 (diamonds), 10 (crosses), 15 (squares) truncated at $m = 10, N = 30$.

The most dramatic feature is the negative values of H_2 and the subsequent change of sign of H_q at each q in the case when the lower cutoff m is noticeably larger than $\langle n\rangle$ ($m/\langle n\rangle \geq 2$). This reminds of the behaviour of H_q for the fixed multiplicity distribution and shows that the NBD-tail decreases quite fast so that the multiplicity m dominates in the moments of these truncated distributions. This is not so dramatic if one considers the flat multiplicity distribution within the window $N - m$ (see the circles in Fig. 6).

The same features have been demonstrated in Figs 7 and 8 for different average multiplicities and different positions of the fixed window $N - m = 20$. In Fig. 7, the window is rather close to $\langle n\rangle$ or even contains it inside (for $\langle n\rangle$=15). Therefore $H_2 < 0$ only for $\langle n\rangle$=5. In Fig. 8, it is very far from $\langle n\rangle$. Thus all H_2 are negative, the more the lower is $\langle n\rangle$. Again, the sign-changing characteristics remind those for the fixed multiplicity distribution.

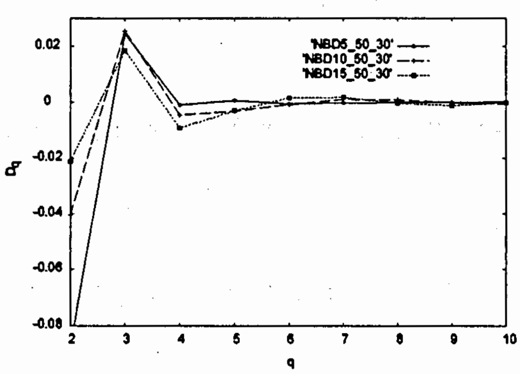

Fig. 8. D_q-moments for NBD with $\langle n\rangle$=5 (diamonds), 10 (crosses), 15 (squares) truncated at $m = 30, N = 50$.

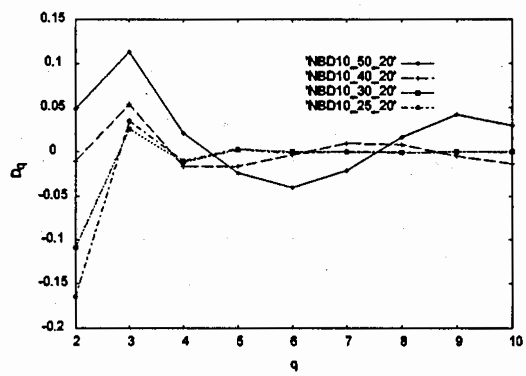

Fig. 9. D_q-moments for NBD with $\langle n\rangle$=10 truncated at $m = 20, N = 50$ (diamonds), 20-40 (crosses), 20-30 (squares), 20-25 (circles).

Another possibility to study the tail of the distribution with the help of H_q-ratios is their variation with the varying length of the tail chosen. At the same mean multiplicity $\langle n\rangle$=10, we calculate moments for the intervals starting at $m = 20$ and ending at $N = 50$, 40, 30, 25. The values of H_q at rather low ranks $q = 2$, 3, 4, 5 are very sensitive to the interval length (as it is shown in Fig. 9) and vary by the order of magnitude.

4 Conclusions

In connection with some experiments planned, our main concern here was to learn if H_q-ratios can be used to judge about the behaviour of the tail of the multiplicity distribution. Using NBD as an example, we have shown that H_q behave in a definite way depending on the size of the multiplicity interval chosen and on its location. Comparing the corresponding experimental results with NBD-predictions, one would be able to show whether the experimental distribution decrease slower (as predicted by QCD) or faster than NBD.

In particular, the negative values of H_2 noted above are of special interest because they show directly how strong is the decrease of the tail. NBDs at different k values would predict different variations of H_2 with more negative H_2 for larger k. Also, the nature of oscillations of H_q-moments at larger values of q reveals how steeply the tail drops down.

Let us stress that the choice of high multiplicities for such a conclusion could be better than the simpleminded fit of the whole distribution. As one hopes, in this case there is less transitions between different channels of the reaction (e.g., from jets with light quarks to heavy quarks), and the underlying low-x dynamics can be revealed.

Acknowledgements

This work is supported by the RFBR grants N 00-02-16101 and 02-02-16779.

References

[1] I.M. Dremin, Phys.-Uspekhi **37**, 715 (1994).

[2] E.A. DeWolf, I.M. Dremin and W. Kittel, Phys. Rep. **270**, 1 (1996).

[3] I.M. Dremin and J.W. Gary, Phys. Rep. **349**, 301 (2001).

[4] V.A. Nikitin, Talk at III International workshop on Very High Multiplicities, Dubna, June 2002.

[5] I.M. Dremin, Phys. Lett. B **313**, 209 (1993).

[6] I.M. Dremin and V.A. Nechitailo, Mod. Phys. Lett. A **9**, 1471 (1994); JETP Lett. **58**, 881 (1993).

[7] S. Lupia, Phys. Lett. B **439**, 150 (1998).

[8] I.M. Dremin, V. Arena, G. Boca et al, Phys. Lett. B **336**, 119 (1994).

[9] SLD Collaboration, K. Abe et al, Phys. Lett. B **371**, 149 (1996).

[10] I.M. Dremin and R.C. Hwa, Phys. Rev. D **49**, 5805 (1994); Phys. Lett. B **324**, 477 (1994).

[11] A. Giovannini, Nuovo Cim. A **15**, 543 (1973).

[12] R. Ugoccioni, A. Giovannini and S. Lupia, in M. M. Block, A.R. White (Eds.) Proc. XXIII Int. Symposium on Multiparticle Dynamics, Aspen, USA, 1993, WSPC, Singapore, 1994, p. 297.

[13] B.B. Levtchenko, in B.B. Levtchenko (Ed.), Proc. VIII Workshop on High Energy Physics, Zvenigorod, Russia, 1993, MSU, 1994, p. 68.

[14] A. Giovannini, S. Lupia and R. Ugoccioni, Phys. Lett. B **388**, 639 (1996); **342**, 387 (1995).

[15] R. Ugoccioni and A. Giovannini, Nucl. Phys. Proc. Suppl. **71**, 201 (1999).

[16] J. Manjavidze and A. Sisakian, Phys. Rep. **346**, 1 (2001).

Wavelets applied to very high multiplicity events.

I.M. Dremin

Lebedev Physical Institute, Moscow 119991, Russia

Abstract

Wavelets are widely used now for the analysis of local scales (or frequencies) important in physical events, biological objects, natural phenomena etc. They provide unique information about scales at different locations. In particular, they are used for analysis of patterns in the phase space of very high multiplicity events.

1 Introduction

Wavelets have become a necessary mathematical tool in many investigations. They are used in those cases when the result of the analysis of a particular *signal*[1] should contain not only the list of its typical frequencies (scales) but also knowledge of the definite local coordinates where these properties are important, i.e., the size and location of its fluctuations. In particular, the secondary particle distributions within the available phase space for the very high multiplicity events can be studied and the corresponding patterns defined by the particle correlations found.

The wavelet basis is formed by using dilations and translations of a particular function defined on a finite interval. Its finiteness is crucial for the locality property of the wavelet analysis . Commonly used wavelets generate a complete orthonormal system of functions with a finite support. That is why by changing the scale (dilations) they can distinguish the local characteristics of a signal at various scales, and by translations they cover the whole region in which it is studied. Due to the completeness of the system, they also allow for the inverse transformation to be properly done. That is why, e.g., one can ask such a question as how the high multiplicity event would look like if only correlations of a definite scale are left in this event. This is demonstrated below.

The locality property of wavelets gives a substantial advantage over Fourier transform which provides us only with knowledge of the global frequencies (scales) of the object under investigation because the system of the basic functions used (sine, cosine or imaginary exponential functions) is defined over an infinite interval.

It has been proven that any function can be written as a superposition of wavelets, and there exists a numerically stable algorithm to compute the coefficients for such an expansion. Moreover, these coefficients completely characterize the function, and it is possible to reconstruct it in a numerically stable way by knowing these coefficients. The discrete wavelets can not be represented by analytical expressions (except for the simplest one) or by solutions of some differential equations, and instead are given numerically as solutions of definite functional equations containing rescaling and translations. Moreover, in practical calculations their direct form is not even required, and only the numerical values of the coefficients of the functional equation are used. This is a very important procedure called multiresolution analysis which gives rise to the multiscale local analysis of the signal and fast numerical algorithms. Each scale contains an independent non-overlapping set of information about the signal in the form of wavelet coefficients, which are determined from an iterative procedure called the fast wavelet transform. In combination, they

[1]The notion of a signal is used here for any ordered set of numerically recorded information about some processes, objects, functions etc. The signal can be a function of some coordinates, would it be the time, the space or any other (in general, n-dimensional) scale.

provide its complete *analysis* and simplify the *diagnosis* of the underlying processes. The extended review on wavelets see in [1].

2 Wavelets for beginners

Each signal can be characterized by its averaged (over some intervals) values (trend) and by its variations around this trend. Actually, physicists dealing with experimental histograms analyze their data at different scales when averaging over different size intervals. This is a particular example of a simplified wavelet analysis treated in this Section. To be more definite, let us consider the situation when an experimentalist measures some function $f(x)$ within the interval $0 \le x \le 1$, and the best resolution obtained with the measuring device is limited by 1/16th of the whole interval. Thus the result consists of 16 numbers representing the mean values of $f(x)$ in each of these bins and can be plotted as a 16-bin histogram. It can be represented by the following formula

$$f(x) = \sum_{k=0}^{15} s_{4,k}\varphi_{4,k}(x), \tag{1}$$

where $s_{4,k} = f(k/16)/4$, and $\varphi_{4,k}$ is defined as a step-like block of the unit norm (i.e. of height 4 and widths 1/16) different from zero only within the k-th bin. For an arbitrary j, one imposes the condition $\int dx|\varphi_{j,k}|^2 = 1$, where the integral is taken over the intervals of the lengths $\Delta x_j = 1/2^j$ and, therefore, $\varphi_{j,k}$ have the following form $\varphi_{j,k} = 2^{j/2}\varphi(2^j x - k)$ with φ denoting a step-like function of the unit height over such an interval. The label 4 is related to the total number of such intervals in our example. At the next coarser level the average over the two neighboring bins is taken. Up to the normalization factor, we will denote it as $s_{3,k}$ and the difference between the two levels as $d_{3,k}$. To be more explicit, let us write down the normalized sums and differences for an arbitrary level j as

$$s_{j-1,k} = \frac{1}{\sqrt{2}}[s_{j,2k} + s_{j,2k+1}]; \quad d_{j-1,k} = \frac{1}{\sqrt{2}}[s_{j,2k} - s_{j,2k+1}], \tag{2}$$

or for the backward transform (synthesis)

$$s_{j,2k} = \frac{1}{\sqrt{2}}(s_{j-1,k} + d_{j-1,k}); \quad s_{j,2k+1} = \frac{1}{\sqrt{2}}(s_{j-1,k} - d_{j-1,k}). \tag{3}$$

Since, for the dyadic partition considered, this difference has opposite signs in the neighboring bins of the previous fine level, we introduce the function ψ which is 1 and -1, correspondingly, in these bins and the normalized functions $\psi_{j,k} = 2^{j/2}\psi(2^j x - k)$. This allows us to represent the same function $f(x)$ as

$$f(x) = \sum_{k=0}^{7} s_{3,k}\varphi_{3,k}(x) + \sum_{k=0}^{7} d_{3,k}\psi_{3,k}(x). \tag{4}$$

One proceeds further in the same manner to the sparser levels 2, 1 and 0 with averaging done over the interval lengths 1/4, 1/2 and 1, correspondingly. The most sparse level with the mean value of f over the whole interval denoted as $s_{0,0}$ provides

$$f(x) = s_{0,0}\varphi_{0,0}(x) + d_{0,0}(x)\psi_{0,0}(x) + \sum_{k=0}^{1} d_{1,k}\psi_{1,k}(x) \\ + \sum_{k=0}^{3} d_{2,k}\psi_{2,k}(x) + \sum_{k=0}^{7} d_{3,k}\psi_{3,k}(x). \tag{5}$$

The functions $\varphi_{j,k}(x)$ and $\psi_{j,k}(x)$ are normalized by the conservation of the norm, dilated and translated versions of them. In the next Section we will give explicit formulae for them in a particular case of Haar scaling functions and wavelets. In practical signal processing, these functions (and more sophisticated versions of them) are often called low and high-pass filters, correspondingly, because they filter the large and small scale components of a signal. The subsequent terms in Eq. (5) show the fluctuations (differences $d_{j,k}$) at finer and finer levels with larger j. In all the cases (1)–(5) one needs exactly 16 coefficients to represent the function. In general, there are 2^j coefficients $s_{j,k}$ and $2^{j_n} - 2^j$ coefficients $d_{j,k}$, where j_n denotes the finest resolution level (in the above example, $j_n = 4$).

All the above representations of the function $f(x)$ (Eqs. (1)-(5)) are mathematically equivalent. However, the latter one representing the wavelet analyzed function directly reveals the fluctuation structure of the signal at different scales j and various locations k present in a set of coefficients $d_{j,k}$ whereas the original form (1) hides the fluctuation patterns in the background of a general trend. In practical applications the latter wavelet representation is preferred because for rather smooth functions, strongly varying only at some discrete values of their arguments, many of the high-resolution d-coefficients in relations similar to Eq. (5) are close to zero (compared to the "informative" d-coefficients) and can be discarded. Bands of zeros (or close to zero values) indicate those regions where the function is fairly smooth.

At first sight, this simplified example looks somewhat trivial. However, for more complicated functions and more data points with some elaborate forms of wavelets it leads to a detailed analysis of a signal and to possible strong compression with subsequent good quality restoration. This example also provides an illustration of the very important feature of the whole approach with successive coarser and coarser approximations to f called the multiresolution analysis and discussed in more detail below.

3 Basic notions and Haar wavelets

To analyze any signal, one should, first of all, choose the corresponding basis, i.e., the set of functions to be considered as "functional coordinates". In most cases we will deal with signals represented by the square integrable functions defined on the real axis. For nonstationary signals, e.g., the location of that moment when the frequency characteristics have abruptly been changed is crucial. Therefore the basis should have a compact support, i.e. it should be defined on the finite region. The wavelets have this property. Nevertheless, with them it is possible to span the whole space by translation of the dilated versions of a definite function. That is why every signal can be decomposed in the wavelet series (or integral). Each frequency component is studied with a resolution matched to its scale.

Let us try to construct functions satisfying the above criteria. An educated guess would be to relate the function $\varphi(x)$ to its dilated and translated version. The simplest linear relation with $2M$ coefficients is

$$\varphi(x) = \sqrt{2} \sum_{k=0}^{2M-1} h_k \varphi(2x - k) \tag{6}$$

with the dyadic dilation 2 and integer translation k. At first sight, the chosen normalization of the coefficients h_k with the "extracted" factor $\sqrt{2}$ looks somewhat arbitrary. Actually, it is defined *a'posteriori* by the traditional form of fast algorithms for their calculation (see Eqs. (20) and (21) below) and normalization of functions $\varphi_{j,k}(x), \psi_{j,k}(x)$. It is used in all the books cited above.

For discrete values of the dilation and translation parameters one gets discrete wavelets. The value of the dilation factor determines the size of cells in the lattice chosen. The integer M defines the number of coefficients and the length of the wavelet support. They are interrelated because from the definition of h_k for orthonormal bases

$$h_k = \sqrt{2} \int dx \varphi(x) \bar{\varphi}(2x-k) \tag{7}$$

it follows that only finitely many h_k are nonzero if φ has a finite support. The normalization condition is chosen as

$$\int_{-\infty}^{\infty} dx \varphi(x) = 1. \tag{8}$$

The function $\varphi(x)$ obtained from the solution of this equation is called a scaling function[2]. If the scaling function is known, one can form a "mother wavelet " (or a basic wavelet) $\psi(x)$ according to

$$\psi(x) = \sqrt{2} \sum_{k=0}^{2M-1} g_k \varphi(2x-k), \tag{9}$$

where

$$g_k = (-1)^k h_{2M-k-1}. \tag{10}$$

The simplest example would be for $M = 1$ with two non-zero coefficients h_k equal to $1/\sqrt{2}$, i.e., the equation leading to the Haar scaling function $\varphi_H(x)$:

$$\varphi_H(x) = \varphi_H(2x) + \varphi_H(2x-1). \tag{11}$$

One easily gets the solution of this functional equation

$$\varphi_H(x) = \theta(x)\theta(1-x), \tag{12}$$

where $\theta(x)$ is the Heaviside step-function equal to 1 at positive arguments and 0 at negative ones. The additional boundary condition is $\varphi_H(0) = 1$, $\varphi_H(1) = 0$. This condition is important for the simplicity of the whole procedure of computing the wavelet coefficients when two neighboring intervals are considered.

The "mother wavelet " is

$$\psi_H(x) = \theta(x)\theta(1-2x) - \theta(2x-1)\theta(1-x). \tag{13}$$

with boundary values defined as $\psi_H(0) = 1$, $\psi_H(1/2) = -1$, $\psi_H(1) = 0$. This is the Haar wavelet known since 1910 and used in the functional analysis . Namely this example has been considered in the previous Section for the histogram decomposition. This is the first one of a family of compactly supported orthonormal wavelets ${}_M\psi$: $\psi_H ={}_1 \psi$. It possesses the locality property since its support $2M-1 = 1$ is compact.

The dilated and translated versions of the scaling function φ and the "mother wavelet" ψ

$$\varphi_{j,k} = 2^{j/2}\varphi(2^j x - k), \tag{14}$$

$$\psi_{j,k} = 2^{j/2}\psi(2^j x - k) \tag{15}$$

form the orthonormal basis as can be (easily for Haar wavelets) checked[3].

[2]It is often called also a "father wavelet " but we will not use this term.

[3]We return back to the general case and therefore omit the index H because the same formula will be used for other wavelets.

The Haar wavelet oscillates so that

$$\int_{-\infty}^{\infty} dx \psi(x) = 0. \tag{16}$$

This condition is common for all the wavelets. It is called the oscillation or cancellation condition. From it, the origin of the name wavelet becomes clear. One can describe a "wavelet" as a function that oscillates within some interval like a wave but is then localized by damping outside this interval. This is a necessary condition for wavelets to form an unconditional (stable) basis. We conclude that for special choices of coefficients h_k one gets the specific forms of "mother" wavelets, which give rise to orthonormal bases.

The wavelet coefficients $s_{j,k}$ and $d_{j,k}$ can be calculated as

$$s_{j,k} = \int dx f(x) \varphi_{j,k}(x), \tag{17}$$

$$d_{j,k} = \int dx f(x) \psi_{j,k}(x). \tag{18}$$

However, in practice their values are determined from the fast wavelet transform described below.

These coefficients are referred as sums (s) and differences (d), thus related to mean values and fluctuations. If only the terms with d-coefficients in (5) are considered, the result is called as the wavelet expansion. For the histogram interpretation, this procedure would imply that one is not interested in average values but only in the histogram shape determined by fluctuations at different scales.

4 Multiresolution analysis and Daubechies wavelets

Though the Haar wavelets provide a good tutorial example of an orthonormal basis, they suffer from several deficiences. One of them is the bad analytic behavior with the abrupt change at the interval bounds, i.e., its bad regularity properties. By this we mean that all finite rank moments of the Haar wavelet are different from zero - only its zeroth moment, i.e., the integral (16) of the function itself is zero. This shows that this wavelet is not orthogonal to any polynomial apart from a trivial constant. The Haar wavelet does not have good time-frequency localization. Its Fourier transform decays like $|\omega|^{-1}$ for $\omega \to \infty$.

The goal is to find a general class of those functions which would satisfy the requirements of locality, regularity and oscillatory behavior. Note that in some particular cases the orthonormality property sometimes can be relaxed. They should be simple enough in the sense that they are of being sufficiently explicit and regular to be completely determined by their samples on the lattice defined by the factors 2^j.

The general approach which respects these properties is known as the multiresolution approximation. This works in practice when applied to the problem of finding out the coefficients of any filter h_k and g_k. They can be directly obtained from the definition and properties of the discrete wavelets. These coefficients are defined by relations (6) and (9). The orthogonality of the scaling functions, of wavelets to the scaling functions, of wavelets to all polynomials up to the power $(M-1)$ and the normalization condition can be written as equations for h_k which uniquely define them (see [1]). In case $M=2$ they lead to following values of coefficients:

$$h_0 = \frac{1}{4\sqrt{2}}(1+\sqrt{3}), \quad h_1 = \frac{1}{4\sqrt{2}}(3+\sqrt{3}), \quad h_2 = \frac{1}{4\sqrt{2}}(3-\sqrt{3}), \quad h_3 = \frac{1}{4\sqrt{2}}(1-\sqrt{3}). \tag{19}$$

These coefficients define the simplest D^4 (or ${}_2\psi$) wavelet from the famous family of orthonormal Daubechies wavelets (D^{2M}) with finite support. For the filters of higher order in M, i.e., for higher rank Daubechies wavelets, the coefficients can be obtained in the same manner. The wavelet support is equal to $2M-1$. It is wider than for the Haar wavelets. However the regularity properties are better. The higher order wavelets are smoother compared to D^4.

5 Fast wavelet transform

Fast wavelet transform allows to proceed with all the computation within short time interval because it uses the simple iterative procedure. Therefore it is crucial for all work with wavelets.

The coefficients $s_{j,k}$ and $d_{j,k}$ carry information about the content of the signal at various scales and can be calculated directly using the formulas (17), (18). However this algorithm is inconvenient for numerical computations because it requires many (N^2) operations where N denotes a number of the sampled values of the function. We will describe a faster algorithm. In practical calculations the coefficients h_k are used only without referring to the shapes of wavelets.

In real situations with digitized signals, we have to deal with finite sets of points. Thus, there always exists the finest level of resolution where each interval contains only a single number. Correspondingly, the sums over k will get finite limits. It is convenient to reverse the level indexation assuming that the label of this fine scale is $j = 0$. It is then easy to compute the wavelet coefficients for more sparse resolutions $j \geq 1$. Multiresolution analysis naturally leads to an hierarchical and fast scheme for the computation of the wavelet coefficients of a given function. In general, one can get the iterative formulas of the fast wavelet transform

$$s_{j+1,k} = \sum_m h_m s_{j,2k+m}, \tag{20}$$

$$d_{j+1,k} = \sum_m g_m s_{j,2k+m} \tag{21}$$

where

$$s_{0,k} = \int dx f(x)\varphi(x-k). \tag{22}$$

These equations yield fast algorithms (the so-called pyramid algorithms) for computing the wavelet coefficients, asking now just for $O(N)$ operations to be done. Starting from $s_{0,k}$, one computes by iteration all other coefficients provided the coefficients h_m, g_m are known. The explicit shape of the wavelet is not used in this case any more.

The remaining problem lies in the initial data. If an explicit expression for $f(x)$ is available, the coefficients $s_{0,k}$ may be evaluated directly according to (22). But this is not so in the situation when only discrete values are available. In the simplest approach they are chosen as $s_{0,k} = f(k)$.

6 The Fourier and wavelet transforms

As has been stressed already, the wavelet transform is superior to the Fourier transform, first of all, due to the locality property of wavelets. The Fourier transform uses sine, cosine or imaginary exponential functions as the main basis. It is spread over the entire real axis whereas the wavelet basis is localized. An attempt to overcome these difficulties and improve time-localization while still using the same basis functions is made by the so-called windowed Fourier transform. The signal $f(t)$ is considered within some time interval (window) only. However, all windows have the same width.

In contrast, the wavelets ψ automatically provide the time (or spatial location) resolution window adapted to the problem studied, i.e., to its essential frequencies (scales). Namely, let t_0, δ and ω_0, δ_ω be the centers and the effective widths of the wavelet basic function $\psi(t)$ and its Fourier transform. Then for the wavelet family $\psi_{j,k}(t)$ (15) and, correspondingly, for wavelet coefficients, the center and the width of the window along the t-axis are given by $2^j(t_0 + k)$ and $2^j\delta$. Along the ω-axis they are equal to $2^{-j}\omega_0$ and $2^{-j}\delta_\omega$. Thus the ratios of widths to the center position along each axis do not depend on the scale. This means that the wavelet window resolves both the location and the frequency in fixed proportions to their central values. For the high-frequency component of the signal it leads to a quite large frequency extension of the window whereas the time location interval is squeezed so that the Heisenberg uncertainty relation is not violated. That is why wavelet windows can be called Heisenberg windows. Correspondingly, the low-frequency signals do not require small time intervals and admit a wide window extension along the time axis. Thus wavelets well localize the low-frequency "details" on the frequency axis and the high-frequency ones on the time axis. This ability of wavelets to find a perfect compromise between the time localization and the frequency localization by automatically choosing the widths of the windows along the time and frequency axes well adjusted to their centers location is crucial for their success in signal analysis . The wavelet transform cuts up the signal (functions, operators etc) into different frequency components, and then studies each component with a resolution matched to its scale providing a good tool for time-frequency (position-scale) localization. That is why wavelets can zoom in on singularities or transients (an extreme version of very short-lived high-frequency features!) in signals, whereas the windowed Fourier functions cannot. In terms of traditional signal analysis , the filters associated with the windowed Fourier transform are constant bandwidth filters whereas the wavelets may be seen as constant relative bandwidth filters whose widths in both variables linearly depend on their positions.

The wavelet coefficients are negligible in the regions where the function is smooth. That is why wavelet series with plenty of non-zero coefficients represent really pathological functions, whereas "normal" functions have "sparse" or "lacunary" wavelet series and easy to compress. On the other hand, the Fourier series of the usual functions have a lot of non-zero coefficients, whereas "lacunary" Fourier series represent pathological functions.

Thus these two types of analysis can be considered as complementary rather than overlapping ones.

One can already start the signal analysis with above procedures. However, there are several technical problems which will not be mentioned here. At some length they are described in the cited review paper.

7 Applications

Wavelets become widely used in pure and applied science. Here we describe just two examples of wavelet application to analysis of one- and two-dimensional objects (see [1]).

The single variable example is provided by the time variation of the pressure in an aircraft compressor. The goal of the analysis of this signal is motivated by the desire to find the precursors of a very dangerous effect (stall+surge) in engines leading to their destruction. It happened that the dispersion of the wavelet coefficients can serve as a precursor of this effect. Let us mention that the similar procedure has been quite successful in analysis of other engines, of heartbeat intervals and diagnosis of a disease.

The two-dimensional wavelet analysis can be used in for recognition of objects shapes. It has been applied, e.g., for pattern recognition of the finger prints (this helped save a lot of computer memory, in particular), of the erythrocytes and their classification. It was used also for analysis of patterns in very high multiplicity events. Lead-lead collisions at 158 GeV/c with multiplicities exceeding 1000 charged particles were analyzed in the two-dimensional phase space and wavelet coefficients for low scales $j < 6$ were omitted. Then the long-range images of events were obtained by the inverse transform. They showed some quite peculiar features of long-range correlations, in particular, the ring-like structure reminding that of Cherenkov rings.

Many other examples can be found in the cited literature and in Web sites.

8 Conclusions

The beauty of the mathematical construction of the wavelet transformation and its utility in practical applications attract researchers from both pure and applied science. Moreover, the commercial outcome of this research has become quite important. We have outlined a minor part of the activity in this field.

References

[1] Dremin I M, Ivanov O V, Nechitailo V A *Physics-Uspekhi* 44 447 (2001)

New effects in finite-temperature Bose-Einstein distribution functions of identical particles

G.A. Kozlov
Bogoliubov Laboratory of Theoretical Physics,
Joint Institute for Nuclear Research,
141980 Dubna, Moscow Region, Russia

Abstract

We study the evolution properties of propagating identical particles (bosons) produced at finite temperature in a randomly distributed environment. The lower bound on the space-time size of the multiparticle production region as well as the correlation chaoticity are derived. We have estimated the effect due to the random source contribution to the distribution functions.

1 Introduction

The investigation of particle collisions with high multiplicity is a central feature of modern particle physics. Interest in (charged) particles "moving" in an environment of quantum fields taking into account the relations between quantum fluctuations and chaoticity is attracted by particle physicists.

One of the most important tasks of multiparticle studies is to analyze fluctuations and correlations such as the Bose-Einstein correlation (BEC) [1,2] of produced particles. This is a rather instructive tool to study high multiplicity hadron processes in detail. The most recent reviews of the presentation of the BEC can be found in [3]. We understand the multiparticle production as the process of colliding particles where the kinetic energy is dissipated into the mass of produced particles [4]. We consider the incident energy $\sqrt{s} \gg \Lambda$, where Λ means the quantum chromodynamics scale. Phenomenological models [5-9] describing the crucial properties of multiparticle correlations are very useful for systematic investigations of the properties caused by fluctuations and correlations. By considering them, one can obtain the characteristic properties of the internal structure of disordering of produced particles in order to extract the information on the space-time size of the multiparticle production region, to estimate the lifetime of the particle emitter, etc. There was used the analysis of correlation functions and distribution functions in [7] to understand the possible view on the quark-gluon plasma formation.

In this paper, we present the model to describe high multiplicity effects at finite temperature. The most characteristic point of our model is that both distribution and correlation functions are taken into account on the quantum level (the operators of production and annihilations are used) with the random source contributions coming from the environment. It is well-known that the cross-section of the production of N particles at a given center of mass energy $\sqrt{s}$ of two colliding particles with the momenta p and $\bar{p}$ is defined as

$$\sigma_N(s) = \int d\Omega_N \, \delta^4(p + \bar{p} - \sum_{j=1}^{N} q_j) |A_N(p, q)|^2 ,$$

where A_N is the N particle production amplitude, q_j are the 4-momenta of produced particles and Ω_N is a phase space. In the simple nonrelativistic case, the multiplicity N depends on the mean kinetic energy $\epsilon = \frac{3}{2} k T$ at the temperature T as $N = (\sqrt{s} + \epsilon)/(m + \epsilon)$, where k is the Boltzmann constant and m is a mass of a particle. We define the average mean multiplicity $\langle \bar{N} \rangle$ (as a natural scale of the produced particle multiplicity N) via the multiparticle correlation function $w(\vec{k})$ as $\langle \bar{N} \rangle = \int d_3 \, \vec{k} \, w(\vec{k})$, where $\vec{k}$ is the spatial momentum of a particle. Following a natural way we suppose $\langle \bar{N} \rangle \ll N$, while $N \ll N_0 = \sqrt{s}/M$, where $M \sim O(0.1 \; GeV)$. The main object in this investigation is the multiparticle thermal distribution function $\tilde{W}(k_\mu)$ related to $\langle N \rangle$ as

$$\tilde{W}(k_\mu) = \langle N \rangle \, f(k_\mu) = \langle N \rangle \langle b^+(k_\mu) \, b(k_\mu) \rangle_\beta \, , \tag{1}$$

where $\langle N \rangle$ is defined as the scale of the multiplicity N at four-momentum k_μ (μ is the Lorenz index), the normalized distribution function $f(k_\mu)$ is finite, i.e. $\int d_4k\, f(k_\mu) < \infty$ and the label β in (??) means the temperature T (of the phase space occupied by operators $b^+(k_\mu)$ and $b(k_\mu)$) inverse. The nature of operators $b^+(k_\mu)$ and $b(k_\mu)$ will be clarified in Sec. 3.

At present, for BEC no a (phenomenological) model can fit the experimental data and no analysis from first principles is in sight. As a new theoretical idea, we use the method combined different fields of physics to describe the BEC in multiparticle production processes:
i) a semiphenomenological transport theory which is formulated by means of an operator-field evolution equation of the Langevin type [10,7-9];
ii) an axiomatic quantum field theory [11] in terms of distributions (generalized functions) [12];
iii) a statistical distribution theory.
We formulate an evolution model of dual representation in Sec. 2. In this work, we claim that the observation of the space-time size effect in a multiparticle production is derived via the multiparticle correlation and distribution functions as well as the so-called chaoticity which will be introduced in Sec. 3. The multiparticle correlation function formalism concerns the statistical physics based on the Langevin-type equation. This equation to be introduced in Sec. 3 is considered as a basis for studying the approach to equilibrium of the particle(s). It is assumed that the heat bath being in essence infinite in size remains for all times in equilibrium as well. We use the method applied to the model where a relativistic particle moving in the Fock space is described by the number representation underlying the second quantization formulation of the canonical field theory. We deal with the microscopic look at the problem with the elements of quantum field theory at the stochastic level with the semiphenomenological noise embedded into the evolution dissipative equation of motion. The statistical distribution of the particles will be discussed in Sec. 4. We conclude in Sec. 5.

2 The model of dual representation within the dissipative dynamics

Let us suppose that the evolution of particles produced at high energies is described by the solutions of the model Hamiltonian where any physical system of particles is described by the doublet of field operators. We introduce the dual states in the eigenbasis $\{|k\rangle, |k(\epsilon)\rangle\}$ of the Hamiltonian H, where $0 \leq \epsilon < \infty$ is identified as the frequency representing the energy of the object and $|k\rangle$ is a discrete eigenstate. We consider the simple dual model where H is given within the damped harmonic oscillator

$$H = H_0 + H_i \ , \tag{2}$$

where

$$H_0 = \epsilon_0 |k\rangle\langle k| + \int_0^\infty d\epsilon \, \epsilon \, |k(\epsilon)\rangle\langle k(\epsilon)| \ , \tag{3}$$

$$H_i = \rho \int_0^\infty d\epsilon \, g(\epsilon) \, [|k(\epsilon)\rangle\langle k| + |k\rangle\langle k(\epsilon)|] \ , \tag{4}$$

$$\langle k|k\rangle = 1 \, , \, \langle k|k(\epsilon)\rangle = \langle k(\epsilon)|k\rangle = 0 \, , \, \langle \epsilon|\epsilon'\rangle = \delta(\epsilon - \epsilon') \, .$$

Here, we identify $|k\rangle$, $|k(\epsilon)\rangle$ and $\langle k|$, $\langle k(\epsilon)|$ with the special mode operators of annihilation $a, b(\epsilon)$ and creation $a^+, b^+(\epsilon)$, respectively, e.g., for "quarks" and "gluons" or their combinations. In the interaction Hamiltonian (??), ρ is the coupling constant, while $g(\epsilon)$ provides the transition between discrete and continuous states.

The equations of motion obeying (??) with (??) and (??) are

$$i \, d_t a_k(t) = \epsilon_0 \, a_k(t) + \rho \int_0^\infty d\epsilon \, g(\epsilon) \, b_k(\epsilon, t) \, ,$$

$$i \, d_t b_k(\epsilon, t) = \epsilon \, b_k(\epsilon, t) + \rho \, g(\epsilon) \, a_k(t) \, ,$$

where the label k means $|\vec{k}|$ as the momentum. We demand that $a_k(t)$ and $b_k(\epsilon, t)$ satisfy the following natural conditions:

$$a_k(t) \, a_k^+(t) + \int_0^\infty d\epsilon \, b_k(\epsilon, t) \, b_k^+(\epsilon, t) < \infty \, ,$$

$$[a_k^+(t)]^+ = a_k(t) \quad , [b_k^+(\epsilon, t)]^+ = b_k(\epsilon, t) \, .$$

The next step is to give the relations between the variables and couplings of the model (??) and the phenomenological constants, e.g., the frequency E and the damping constant κ involved into the dissipative dynamics given by the Boltzmann-type equations in the relaxation time approximation:

$$\frac{d_t \langle a_k(t) \rangle}{\langle a_k(t) \rangle} = -(i \, E + \kappa) \, , \tag{5}$$

$$d_t w_k(t) = d_t\langle a_k^+(t) a_k(t)\rangle = -2\,\kappa\,[w_k(t) - n(\beta)]\,. \tag{6}$$

Here,

$$d_t\langle a_k(t)\rangle = -i\,\epsilon_0\,\langle a_k(t)\rangle - \rho^2 \int_0^\infty d\epsilon\, g^2(\epsilon) \int_\tau^t ds\,\langle a_k(s)\rangle \exp[-i\epsilon(t-s)]\,,$$

$$\langle a_k(z)\rangle = -i\,\rho \int_\tau^z dx\,\langle \sigma_k(x)\rangle \exp[-i\epsilon_0(z-x)]\,,$$

$$\sigma_k(t) = \int_0^\infty d\epsilon\, g(\epsilon)\, b_k(\epsilon, t)\,,$$

$$n(\beta) = [\exp(\epsilon_0\,\beta) \pm 1]^{-1}$$

as $\tau \to -\infty$. One can conclude that the phenomenological constants E and κ in (??) and (??) are nothing else but ϵ_0 and $2\,\pi\,\rho^2\,g^2(\epsilon_0)$, respectively, i.e. the microscopic parameters coming from the model Hamiltonian (??).

3 The model

The investigation of BEC is one of the most challenging topics in modern physics to analyze theoretically such the phenomena based of the general principles of quantum field theory (QFT) at finite temperature. However, such complicated phenomena are rather far from the basic features of QFT to be connected to each other. Hence, one needs to introduce an approximate semiphenomenological model which enables one to clarify the details of correlations in terms of basic variables and some parameters embedded into this model.

Suppose that the phase space of produced hadrons consists of many "quantum" cells where some number of the (canonical) operators $a(k_\mu)$ and its Hermitian conjugate $a^+(k_\mu)$ are localized . Since the nature of the operators $a(k_\mu)$ and $a^+(k_\mu)$ is unknown one can consider them as some mode operators which can in principle be composed of any other operators. Hence, the operator $a(k_\mu)$ $(a^+(k_\mu))$ describes a special matter mode which is excited in a cell. For simplicity, one can identify the operator $a(k_\mu)$ with a single boson or fermion operator. The system of "quantum" cells interacts with more extended system which is supposed to be a thermal bath where the energy of a system containing "quantum" cells are dissipated in. In a simple version, a heat bath is considered as a large number of independent harmonic oscillators given by the operators $\hat{c}$ ($\hat{c}^{+}$) obeying the standard Hamiltonian $H_\beta = \sum_i \omega_i\,(\hat{c}_i^{+}\hat{c}_i + 1/2)$. On the semiphenomenological level, we suppose that rather complicated multiparticle interaction process is replaced with a single-particle operator $b = a + R$ propagation derived by a systematic operator A and disturbed by a random force $F_1 = F + P$. R is a random source operator while P gives a stationary external force.

Considering the "propagation" of a particle with the momentum $\vec{k}$ in the quantum equilibrium phase space under the influence of a random force coming from surrounding particles, the dissipative dynamics of the relevant system is described by the equation containing only the first order time derivatives of the dynamic degrees of freedom, the operators $b(\vec{k},t)$ and $b^{+}(\vec{k},t)$ [7-9]:

$$i\ \partial_t b(\vec{k},t) = F_1(\vec{k},t) - A(\vec{k},t)\ , \tag{7}$$

Here, the interaction of particles under consideration with surroundings as well as providing the propagation is given by the operator $A(\vec{k},t)$ defined as the one closely related to the dissipation force:

$$A(\vec{k},t) = \int_{-\infty}^{+\infty} K(\vec{k},t-\tau)\ b(\vec{k},\tau)\ d\tau\ .$$

An interplay of particles with surroundings is embedded into the interaction complex kernel $K(\vec{k},t)$, while the real physical transitions are provided by the random source operator $F(\vec{k},t)$ with the zeroth value of the statistical average, $\langle F\rangle = 0$. The random evolution field operator $K(\vec{k},t)$ stands for the random noise and it is assumed to vary stochastically with a δ- like equal time correlation function

$$\langle K^{+}(\vec{k},\tau)\ K(\vec{k}',\tau)\rangle = 2\ (\pi l)^{1/2}\ \xi\ \delta(\vec{k}-\vec{k}')\ ,$$

where both the strength of the noise ξ and the positive constant $l \to \infty$ define the effect of the Gaussian noise on the evolution of particles in the thermalized environment.

The formal solution of Eq. (??) in the operator form in the four-momentum space-time $S(\Re_4)$ ($k^\mu = (\omega = k^0, k_j)$) is $\tilde{b}(k_\mu) = \tilde{a}(k_\mu) + \tilde{R}(k_\mu)$ where the operator $\tilde{a}(k_\mu)$ is expressed via the Fourier transformed operator $\tilde{F}(k_\mu)$ and the Fourier transformed kernel function $\tilde{K}(k_\mu)$ as $\tilde{a}(k_\mu) = \tilde{F}(k_\mu)\cdot[\tilde{K}(k_\mu) - \omega]^{-1}$, while the function $\tilde{R}(k_\mu) \sim P \cdot [\tilde{K}(k_\mu) - \omega]^{-1}$. In our model, we suppose that a heat bath (an environment) is an assembly of damped oscillators coupled to the produced particles which in turn are distributed by the random force $\tilde{F}(k_\mu)$. In addition, there is the assumption that the heat bath is statistically distributed. The random force operator $F(\vec{k}, t)$ can be expanded by using the Fourier integral

$$F(\vec{k}, t) = \int_{-\infty}^{+\infty} \frac{d\omega}{2\pi}\, \psi(k_\mu)\, \hat{c}(k_\mu)\, e^{-i\omega t} ,$$

where the form $\psi(k_\mu) \cdot \hat{c}(k_\mu)$ is just the Fourier operator $\tilde{F}(k_\mu) = \psi(k_\mu) \cdot \hat{c}(k_\mu)$, and the canonical operator $\hat{c}(k_\mu)$ obeys the commutation relation

$$\left[\hat{c}(k_\mu), \hat{c}^+(k'_\mu)\right]_\pm = \delta^4(k_\mu - k'_\mu) .$$

The function $\psi(k_\mu)$ is determined by the condition (the canonical commutation relation with the operators $\hat{c}(k_\mu), \hat{c}^+(k'_\mu)$ is taken into account)

$$\int_{-\infty}^{+\infty} \frac{d\omega}{2\pi} \left[\frac{\psi(k_\mu)}{\tilde{K}(k_\mu) - \omega}\right]^2 = 1 .$$

We formulate distribution functions of produced particles in terms of a point-to-point equal-time temperature-dependent thermal correlation functions of two operators

$$w(\vec{k}, \vec{k}', t; T) = \langle a^+(\vec{k}, t)\, a(\vec{k}', t)\rangle_\beta = Tr[a^+(\vec{k}, t)\, a(\vec{k}', t) e^{-H\beta}]/Tr(e^{-H\beta}).$$

The standard canonical commutation relation

$$\left[a(\vec{k}, t), a^+(\vec{k}', t)\right]_\pm = \delta^3(\vec{k} - \vec{k}')$$

at every time t is used as usual for Bose (-) and Fermi (+)-operators.

The probability to find the particles in the multiparticle production region with momenta $\vec{k}$ and $\vec{k}'$ in the same event at the time t is:

$$C_2(\vec{k}, \vec{k}', t) = W(\vec{k}, \vec{k}', t)/[W(\vec{k}, t) \cdot W(\vec{k}', t)] .$$

Here, the one-particle thermal distribution function in a simple version fluctuates only its normalization, e.g., the mean multiplicity $\langle N\rangle$, $W(\vec{k}, t) =$

$\langle N\rangle \cdot f(\vec{k},t)$ defining the single spectrum, while $W(\vec{k},\vec{k}',t) = \langle N(N'-\delta_{ij})\rangle \cdot f(\vec{k},\vec{k}',t)$ for i-and j-types of particles. Here, $\delta_{ij} = 1$ if $i = j$ and 0 otherwise. Distribution functions $f(\vec{k},t)$ and $f(\vec{k},\vec{k}',t)$ look like

$$f(\vec{k},t) = \langle b^{+}(\vec{k},t)\, b(\vec{k},t)\rangle$$

and

$$f(\vec{k},\vec{k}',t) = \langle b^{+}(\vec{k},t)\ b^{+}(\vec{k}',t)\ b(\vec{k},t)\ b(\vec{k}',t)\rangle\,,$$

respectively.

The ratio function C_2 leads to the enhanced probability for emission of identical particles which is given in $S(\Re_4)$ as follows:

$$C_2(k_\mu,k'_\mu;T) = \xi(N)\,[1 + D(k_\mu,k'_\mu;T)]\,, \tag{8}$$

where

$$\xi(N) = \frac{\langle N\,(N'-\delta_{ij})\rangle}{\langle N\rangle\,\langle N'\rangle}$$

.

The 2-particle BEC function $\Xi(k_\mu,k'_\mu)$ looks like

$$\Xi(k_\mu,k'_\mu) = \langle \tilde{a}^{+}(k_\mu)\ \tilde{a}(k'_\mu)\rangle = \frac{\psi^{*}(k_\mu)\cdot\psi(k'_\mu)}{[\tilde{K}^{*}(k_\mu)-\omega]\cdot[\tilde{K}(k'_\mu)-\omega']}\cdot\langle \hat{c}^{+}(k_\mu)\ \hat{c}(k'_\mu)\rangle\ .$$

Taking into account the trick with $\delta^4(k_\mu - k'_\mu)$-function to be replaced by the δ-like consequence like $\Omega(r)\cdot\exp[-(k-k')^2r^2]$ [12], one can get the following expression for D-function

$$\begin{gathered} D(k_\mu,k'_\mu;T) = \lambda(k_\mu,k'_\mu;T)\cdot\exp(-q^2/2) \\ \times[n(\bar{\omega},T)\Omega(r)\exp(-q^2/2) + \tilde{R}^{*}(k'_\mu)\tilde{R}(k_\mu) + \tilde{R}^{*}(k_\mu)\tilde{R}(k'_\mu)]\,, \end{gathered} \tag{9}$$

where

$$\lambda(k_\mu,k'_\mu;T) = \frac{\Omega(r)}{\tilde{f}(k_\mu)\cdot\tilde{f}(k'_\mu)}\cdot n(\bar{\omega},T)\ ,\ \bar{\omega} = \frac{1}{2}(\omega+\omega')\ ,$$

while $q^2 \equiv Q^2\,r^2$ and the function $\Omega(r)\cdot n(\omega;T)\cdot\exp(-q^2/2)$ in (??) describes the space-time size of the multiparticle production region. Choosing the z-axis along the pp or $\bar{p}p$ collision axis one can put

$$q^2 = (r_0\cdot Q_0)^2 + (r_z\cdot Q_z)^2 + (r_t\cdot Q_t)^2\ ,$$

$$Q_\mu = (k-k')_\mu, Q_0 = \epsilon_{\vec{k}} - \epsilon_{\vec{k}'}, Q_z = k_z - k'_z, Q_t = \left[(k_x - k'_x)^2 + (k_y - k'_y)^2\right]^{1/2},$$

$$\Omega(r) = \frac{1}{\pi^2} r_0 \cdot r_z \cdot r_t^2 ,$$

where r_0, r_z and r_t are time-like, longitudinal, and transverse "size" components of the multiparticle production region. To derive (??), the Kubo-Martin-Schwinger condition

$$\langle a(\vec{k}', t')\; a^+(\vec{k}, t)\rangle = \langle a^+(\vec{k}, t)\; a(\vec{k}', t - i\beta)\rangle \cdot \exp(-\beta\; \mu)$$

has been used (μ is the chemical potential), and the thermal statistical averages for the $\hat{c}(k_\mu)$-operator should be represented in the following form

$$\langle \hat{c}^+(k_\mu)\; \hat{c}(k'_\mu)\rangle = \delta^4(k_\mu - k'_\mu) \cdot n(\omega, T),$$

$$\langle \hat{c}(k_\mu)\; \hat{c}^+(k'_\mu)\rangle = \delta^4(k_\mu - k'_\mu) \cdot [1 \pm n(\omega, T)]$$

for Bose (+)- and Fermi (-)-statistics, respectively; $n(\omega, T) = \{\exp[(\omega - \mu)\beta] \pm 1\}^{-1}$. Formula (??) indicates that the chaotic multiparticle source emanating from the thermalized multiparticle production region exists. It is easy to see that the correlation functions containing the random force functions $F(\vec{k}, t)$ carry the quantum features in the thermalized stationary equilibrium, namely

$$\langle F(\vec{k}, t)\, F^+(\vec{k}', t')\rangle = \delta^3(\vec{k} - \vec{k}'))\, \Gamma_1(\vec{k}, -\Delta t),$$

$$\Gamma_1(\vec{k}, -\Delta t) = \int \frac{d\omega}{2\pi}\, |\psi(k_\mu)|^2\, [1 \pm n(\omega, \beta)]\, \exp(-i\,\omega\,\Delta t),$$

$$\Delta t = t - t';$$

$$\langle F^+(\vec{k}, t)\, F^+(\vec{k}', t')\rangle = \delta^3(\vec{k} - \vec{k}'))\, \Gamma_2(\vec{k}, \Delta t),$$

$$\Gamma_2(\vec{k}, \Delta t) = \int \frac{d\omega}{2\pi}\, |\psi(k_\mu)|^2\, n(\omega, \beta)\, \exp(i\,\omega\,\Delta t).$$

The quantitative information (longitudinal r_z and transverse r_t components of the multiparticle production region, the temperature T of the environment) could be extracted by fitting the theoretical formula (??) to the measured D-function and estimating the errors of the fit parameters. Hence, the measurement of the space-time evolution of the multiparticle source would provide information of the multiparticle process and the general reaction mechanism.

The temperature of the environment enters into formula (??) through the two-particle correlation function $\Xi(k_\mu, k'_\mu; T)$. Formula (??) looks like the fitting C_F-ratio using a source parameterizations:

$$C_F(r) = const\,[1 + \lambda_F(r) \cdot \exp(-r_t^2 \cdot Q_t^2/2 - r_z^2 \cdot Q_z^2/2)] \ ,$$

where $r_t(r_z)$ is the transverse (longitudinal) radius parameter of the source with respect to the beam axis, λ_F stands for the effective intercept parameter (chaoticity parameter) which has a general dependence of the mean momentum of the observed particle pair. Here, the dependence on the source lifetime is omitted. The chaoticity parameter λ_F is the temperature-dependent and the positive one defined by

$$\lambda_F(r) = \frac{|\Omega(r)\; n(\bar\omega; T)|^2}{\tilde f(k_\mu) \cdot \tilde f(k'_\mu)} \ .$$

The correlation function $\Xi(k_\mu, k'_\mu)$

$$\Xi(k_\mu, k'_\mu) = \Omega(r) \cdot n(\bar\omega; T) \cdot \exp(-q^2/2) \ ,$$

defines uniquely the size r of the multiparticle production region. There is no satisfactory tool to derive the precise analytic form of the random source function $\tilde R(k_\mu)$, but one can put [13,8,9] that

$$\tilde R(k_\mu) = [\alpha \cdot \langle \tilde a^+(k_\mu)\; \tilde a(k_\mu)\rangle]^{1/2} \ ,$$

where α is of the order $O\left(P^2/n(\omega, T) \cdot |\psi(k_\mu)|^2\right)$. Finally, one can obtain

$$D(q^2; T) = \frac{\tilde\lambda^{1/2}(\bar\omega; T)}{(1+\alpha)(1+\alpha')} e^{-q^2/2} \left[\tilde\lambda^{1/2}(\bar\omega; T) e^{-q^2/2} + 2(\alpha\alpha')^{1/2}\right] \ , \qquad (10)$$

where $\tilde\lambda(\bar\omega; T) = n^2(\bar\omega; T)/[n(\omega; T) \cdot n(\omega'; T)]$. It is easy to see that, in the vicinity of $q^2 \approx 0$, one can get the full correlation if $\alpha = \alpha' = 0$ and $\tilde\lambda(\bar\omega; T)$=1. Putting $\alpha = \alpha'$ in (??), we find the formal lower bound on the space-time dimensionless size of the multiparticle production region of the bosons

$$q^2 \geq \left(\frac{1}{1 + \frac{1}{2}\sqrt{\frac{\tilde\lambda}{\alpha \cdot \alpha'}}}\right) \left\{ \ln \left[\frac{2\sqrt{\tilde\lambda \cdot \alpha \cdot \alpha'}}{B\,(1+\alpha)\,(1+\alpha')}\right]^2 + \sqrt{\frac{\tilde\lambda}{\alpha \cdot \alpha'}} \right\}$$

at $(k-k')^2 \leq 2/r^2$ where B means the maximal value of C_2 at Q=0, otherwise

$$q^2 \geq 2 \ln \left[\frac{2\sqrt{\tilde{\lambda}} \cdot \alpha \cdot \alpha'}{B\,(1+\alpha)\,(1+\alpha')} \right]$$

at $(k-k')^2 >> 2/r^2$.

4 Statistical distributions

¿From a widely accepted point of view, at high energies, there are two channels, at least, for multiparticle production where produced particles occupy the multiparticle production region consisting of i elementary cells. These main channels are a) a direct channel assuming that all particles p_j are produced directly within the quark (q)-antiquark ($\bar{q}$) annihilation or the gauge-boson fusion, e.g., $q\bar{q} \rightarrow p_j p_j ...$; b) an indirect channel which means that the particles are produced via the decays of intermediate vector bosons χ^* in both heavy and light sectors in the kinematically allowed region, e.g., $q\bar{q} \rightarrow \chi^* \chi^* ... \rightarrow p_j p_j ...$ All the particles produced are classified by the like-sign constituents that are labeled as p^+, p^-, p^0-subsystems, where $p : \mu, \pi, K...$ The mean multiplicity $\langle N \rangle$ and the mean energy $\langle E \rangle$ of the p_j subsystem are defined as [5] $\langle N \rangle = \sum_j \sum_{m_j} m_j \, \zeta_j^{(m_j)}$ and $\langle E \rangle = \sum_j \sum_{m_j} m_j \, \epsilon_j \, \zeta_j^{(m_j)}$, where ϵ_j is the energy of a p-particle in the jth elementary cell and $\zeta_j^{(m_j)}$ stands for the probability of finding m_j p particles in the jth cell and is normalized as $\sum_{m_j=0}^{\infty} \zeta_j^{(m_j)} = 1$. In the direct channel, for charged produced mesons $\langle N \rangle$ is defined uniquely for a given β as

$$\langle N \rangle = 2 \sum_j [\exp(\epsilon_j \, \beta) - 1]^{-1}$$

while $\langle E \rangle$ looks like

$$\langle E \rangle = \frac{1}{3} \sqrt{s} = \sum_j \frac{\epsilon_j}{\exp(\epsilon_j \, \beta) - 1}$$

. Going into y-rapidity space in the longitudinal phase space with a lot of cells of equal size δy, the energy ϵ_j should be expressed in terms of the transverse mass $m_t = \sqrt{\langle k_t \rangle^2 + m_p^2}$ ($\langle k_t \rangle$ and m_p are the transverse average momentum and the mass of a p-particle):

$$\epsilon_j(s) = \frac{m_t}{2}\left[g_j(\tilde{s}) + g_j^{-1}(\tilde{s})\right], \tilde{s} = \frac{s}{4\, m_t^2},$$

$$g_j(\tilde{s}) = (\sqrt{\tilde{s}} + \sqrt{\tilde{s}-1})\, \exp[-(j-1/2)\, \delta y].$$

Here, the four-momentum of p-particle is given as

$$k^\mu = (\sqrt{\langle k_t \rangle^2 + m_p^2}\, \cosh y, k_t\, \cos\varphi, k_t\, \sin\varphi, \sqrt{\langle k_t \rangle^2 + m_p^2}\, \sinh y),$$

where the azimuthal angle is in the range $0 < \varphi < 2\,\pi$. Our model produces an enhancement of $C_2(Q,\beta)$ in the small enough region of Q where C_2 is defined only by the model parameters α and α' and the mean multiplicity $\langle N(s) \rangle$ at fixed value of β, namely (α=α'):

$$C_2(Q,\beta) \simeq \xi(\langle N \rangle)\left\{1 + \frac{\sqrt{\tilde{\lambda}(\bar{\omega},\beta)}}{(1+\alpha)^2}\left[\sqrt{\tilde{\lambda}(\bar{\omega},\beta)}\right.\right.$$
$$\left.\left. +2\,\alpha - (\sqrt{\tilde{\lambda}(\bar{\omega},\beta)} + \alpha) Q^2\, r^2\right]\right\}. \tag{11}$$

It is clear that $C_2(Q,\beta)$-function at $Q^2 = 0$

$$C_2(Q,\beta) \simeq \xi(\langle N(s) \rangle) \cdot \left[2 - \left(\frac{\alpha}{1+\alpha}\right)^2\right]$$

cannot exceed 2 because of $\alpha \neq 0$ and $\xi(N(s)) < 1$ even at large multiplicity. The Boltzmann behaviour should be realized in the case when $\alpha \to \infty$, i.e. the main contribution to the fluctuating behaviour of the $C_2(Q,\beta)$-function should come from the random source contribution (see (??) and (??)). We found that the enhancement of the $C_2(Q,\beta)$-function, mainly, the shape of this function, strongly depends on the transverse size r_t of the phase space and has a very weak dependence of the δy size of a separate elementary cell. The increasing of r_t makes that the shape of the $C_2(Q,\beta)$-function becomes more crucial.

Obviously, $\xi(\langle N(s) \rangle)$ is the normalization constant in (??), where $\langle N(s) \rangle$ should be derived at the origin of Q^2 precisely from $C_2(Q=0,\beta) \equiv C_{2_0}(s)$ as $\langle N(s) \rangle \simeq \frac{1}{\varepsilon}$ where

$$\varepsilon = 1 - \frac{C_{2_0}(s)}{2 - \left(\frac{\alpha}{1+\alpha}\right)^2}$$

can be extracted from the experiment at some chosen value of α ($\alpha = 0$ should be taken into account as well). On the other hand, the $C_2(Q, \beta)$-function allows one to measure $\alpha = \alpha'$ which parameterizes the random source contribution as well as the splitting between α and α'. Neglecting the random source contribution (i.e., putting $\alpha = \alpha' = 0$) we can estimate the chaoticity $\tilde{\lambda}(\bar{\omega}, \beta)$ by measuring $C_2(Q, \beta)$ as $Q^2 \to 0$.

In fact, the theoretical prediction that $D(Q, \beta) > 1$ means that in the multiparticle production region one should select the single boson "dressing" of some quantum numbers, and the particles suited near it in the phase space are "dressed" with the same set of quantum numbers. The amount of such neighbor particles has to be as many as possible. This allows to form a cell in the space-time occupied by equal-statistics particles only. Such a procedure can be repeated while all the particles will occur in the multiparticle production region. This leads to the space-time distribution of produced particles in the phase-space cells formed only for bosons. In fact, there is no restriction of the number of bosons occupying the chosen elementary cells. It means that $D(Q, \beta)$-function are defined for all orders.

5 Summary and discussion

We investigated the finite temperature BEC of identical particles in the multiparticle production using the solutions of the operator field Langevin-type equation in $S(\Re_4)$, the quantum version of the Nyquist theorem and the quantum statistical methods. There was presented the crucial role of the model in describing the BEC via calculations of distribution functions as the functions of the mean multiplicity and chaoticity at each four-momentum $\sqrt{Q_\mu^2}$. Based on this model, one can compare the effects on single particle spectra and multiparticle distribution caused by multiparticle correlations. There are several parameters in the model: $\beta, \delta y, \alpha(\alpha')$. One can focus on the statement that the deviation of the $D(Q, \beta)$-function from zero at finite values of the physical variables q^2 and the model parameter α indicates that the multiparticle production region should be considered as the phase-space consisting of the elementary cells (with the size δy of each) which are occupied by the particles of identical statistics. The Boltzmann behaviour of C_2-function (??) is available only at large enough values of α which means the leading role of the random source contribution to the distribution function.

An important feature of the model is getting the information on the space-time structure of the multiparticle production region. We are able to predict the source size and the intercept parameter -the chaoticity λ as well. We have found that the distribution function $C_2(Q,\beta)$ depends on the number of elementary cells defined by the equal size δy in the rapidity y-space.

Of course, the best check of any model could be done if various kinds of high energy experimental data on the multiparticle correlations would be well reproduced by the model in consideration.

6 Acknowledgements

I gratefully acknowledge G. Wilk for a useful discussion concerning the Bose-Einstein correlation nature.

References

[1] R. Hanbury-Brown and R.Q. Twiss, Nature 178, 1046 (1956).

[2] G. Goldhaber et al., Phys. Rev. 120, 300 (1960).

[3] U.A. Wiedermann and U. Heinz, Phys. Rep. 319, 145 (1999); R. Weiner, Phys. Rep. 327, 249 (2000).

[4] J.D. Manjavidze and A.N. Sissakian, Phys. Rep. 346, 1 (2001) .

[5] T. Osada, M. Maruyama, and F. Tagaki, Phys. Rev. D 59, 014024 (1998).

[6] O.V. Utyuzh, G. Wilk and Z. Wlodarczyk, hep-ph/0102275; Phys. Rev. C 64, 027901 (2001); Phys. Lett. B 522, 273 (2001).

[7] G.A. Kozlov, Phys. Rev. C 58, 1188 (1998).

[8] G.A. Kozlov, Journ. of Math. Phys. 42, 4749 (2001).

[9] G.A. Kozlov, New Journ. of Phys. 4, 23 (2002).

[10] M. Mizutani, S. Muroya, and M. Namiki, Phys. Rev. D 37, 3033 (1988).

[11] N.N. Bogoliubov, A.A. Logunov, A.I. Oksak, I.T. Todorov, General principles of quantum field theory (Nauka, Moscow, 1987).

[12] M. Gelfand and G.E. Shilov, Generalized Functions, Vol. I (N.Y., 1964).

[13] M. Namiki and S. Muroya, Theory of particle distribution-correlation in high energy nuclear collisions, in Proc. of RIKEN Symp. on Physics of High Energy Heavy Ion Collisions, 1992 Ed. by S. Date and S. Ohta (Saitama, Japan), p. 91.

Toward VHM events generator

J.Manjavidze, V.Voronyuk

JINR, Dubna

Contents

Generating functional

The unitary condition: $\mathbf{S}\,\mathbf{S}^{+} = \mathbf{I}$

$$\mathbf{S} = \mathbf{I} + i\mathbf{A} \quad \Rightarrow \quad 2i\,\mathbf{A}\,\mathbf{A}^{*} = \mathbf{A} - \mathbf{A}^{*}$$

We consider the quantity

$$\rho(\alpha, z) = \sum_{m,n=1}^{\infty} \frac{1}{m!\,n!} \int d\omega_m(p;\alpha_i, z_i)\, d\omega_n(q;\alpha_f, z_f)\, |a_{m,n}(p,q)|^2$$

where

$$d\omega_m(p;\alpha,z) = \prod_{k=1}^{m} \frac{d^3p_k\, e^{i\alpha\, p_k}\, z(p_k)}{(2\pi)^3 2\epsilon(p_k)}, \qquad \epsilon(p) = \sqrt{\vec{p}^2 + m^2}$$

invariant phase space, $z(p)$ is some weight function.

The generating functional $\rho(\alpha, z)$ can be used as the events generator

$$\rho_{m,n}(p,q;\alpha) = \prod_{k=1}^{m} \frac{\delta}{\delta z_i(p_k)} \prod_{k=1}^{n} \frac{\delta}{\delta z_f(q_k)} \rho(z,\alpha)\Big|_{z=0}$$

$$\sigma_n(a_1 + a_2 \to f) = \frac{1}{J(s)} \int \frac{d^4\alpha_i}{(2\pi)^4} \frac{d^4\alpha_f}{(2\pi)^4} e^{i\,P(\alpha_i+\alpha_f)} \rho_{2\to n}(p_1, p_2; q_1, \ldots, q_n; \alpha) \prod_{k=1}^{n} d^3q_k$$

The reduction formula for the amplitude looks

$$a_{m,n}(p_1,\ldots,p_m;q_1,\ldots,q_n) = (-i)^{m+n} \prod_{k=1}^{m} \hat{\phi}(p_k) \prod_{k=1}^{n} \hat{\phi}^*(q_k)\, Z[\phi]\Big|_{\phi=0}$$

where

$$\hat{\phi}(p) = \int dx\, e^{-ipx} \frac{\delta}{\delta\phi(x)}$$

$$Z[\phi] = \int DuD\varphi\, e^{iS_{C_+}(u)+iS_{0\,C_+}(\varphi)-iV_{C_+}(u,\varphi+\phi)}$$

where C_+ is the Mills complex time contour:

$$t \to t+i\epsilon, \quad \epsilon \to +0,\ -\infty \le t \le +\infty$$

$$\rho(\alpha,z) = \exp\Big[\int \frac{d^3p\, e^{i\alpha_i p} z_i(p)}{(2\pi)^3 2\epsilon(p)} \hat{\phi}_+(p)\hat{\phi}^*_-(p) + \int \frac{d^3q\, e^{i\alpha_f q} z_f(q)}{(2\pi)^3 2\epsilon(q)} \hat{\phi}^*_+(q)\hat{\phi}_-(q)\Big]\, Z[\phi_+]Z^*[\phi_-]$$

Denote

$$\rho_0[\phi] = Z[\phi_+]Z^*[\phi_-]$$

The model

The model: **scalar $\lambda\varphi^4$ conformal theory**

$$\mathcal{L} = \left[\frac{1}{2}(\partial_\mu u)^2 - \frac{g}{4}u^4\right] + \left[\frac{1}{2}(\partial_\mu \varphi)^2 - \frac{m^2}{2}\varphi^2\right] - \dot{\kappa}\, u\, \varphi^2$$

Zero order over φ

$$\rho_0[\phi] = \int Du_+ \, e^{iS_{C_+}(u_+) - iV_{C_+}(u_+,\phi)} \int Du_- \, e^{-iS_{C_-}(u_-) + iV_{C_-}(u_-,\phi)}$$

The boundary condition

$$\int_{C_+} dx\, \partial_\mu(u_+ \partial^\mu u_+) = \int_{C_-} dx\, \partial_\mu(u_- \partial^\mu u_-)$$

$$\rho_0[\phi] = e^{-i\hat{K}(je)} \int \prod_{t,\mathbf{x}} du(x)\, \delta\left(\frac{\delta S(u)}{\delta u} - \kappa\phi^2 + j\right) e^{i\tilde{S}(u,e)}$$

where

$$\hat{K}(je) = \int_{C_+} dx\, \hat{j}\hat{e} + \int_{C_-} dx\, \hat{j}\hat{e}$$

$$\tilde{S}(u,e) = S_{C_+}(u+e) - S_{C_-}(u-e) - 2Re \int dx\, \frac{\delta S(u)}{\delta u} e$$

Factor space

$$u_c : (u,p)(\mathbf{x},t) \to (\xi,\eta)(t)$$

$$DM(u,p) = DM(\xi,\eta) = d\Omega \prod_t d\xi d\eta\, \delta\left(\dot{\xi} - \frac{\delta h_j}{\delta \eta}\right) \delta\left(\dot{\eta} + \frac{\delta h_j}{\delta \xi}\right)$$

The equation

$$\Box u + g\, u^3 = 0$$

has the $O(4) \times O(2)$ invariant solution (deAlfaro Fubini Furlan)

$$u_c = \sqrt{\frac{(v - v*)^2}{g(x+v)^2(x+v*)^2}}$$

There is exist transformation $\{x\} \to \{\zeta\}$

$$\begin{cases} \zeta_1^2 + \zeta_2^2 + \zeta_3^2 + \zeta_5^2 = \zeta_0^2 + \zeta_6^2 \\ \zeta_5 + \zeta_6 = 1 \end{cases}$$

such that

$$\sqrt{-g}\, u_c = (\zeta_0^2 + \zeta_6^2)^{-1/2}$$

Splitting sources

$$\rho_0(\phi) = e^{-i\,\hat{K}(j,e)} \int d\Omega \prod_t d\xi d\eta\, \delta\left(\dot{\xi} - \frac{\delta h_j}{\delta \eta}\right) \delta\left(\dot{\eta} + \frac{\delta h_j}{\delta \xi}\right) e^{i\,\tilde{S}(u_c,e)}$$

Mapping sources

$$\rho_0(\phi) = e^{-i\,\hat{K}(j_{\xi,\eta},e_{\xi,\eta})} \int d\Omega \prod_t d\xi d\eta \delta\left(\dot{\xi} - 1 - j_\xi\right) \delta\left(\dot{\eta} - j_\eta\right) e^{-2i\kappa\, Re \int dx\, \phi^2 e_c} e^{i\,\tilde{S}(u_c,e_c)}$$

where

$$e_c = e_\eta \frac{\partial u_c}{\partial \xi} - e_\xi \frac{\partial u_c}{\partial \eta}$$

Performing integration we find

$$\rho_0(\phi) = e^{-i\,\hat{K}(j,e)} \int d\Omega d\xi_0 d\eta_0\, e^{-2i\kappa\, Re \int dx\, \phi^2 e_c} e^{i\,\tilde{S}(u_c,e_c)}$$

where

$$u_c = u_c(\mathbf{x}; \xi_0 + t + \int dt'\, \theta(t-t')\, j_\xi(t');\ \eta_0 + \int dt'\, \theta(t-t')\, j_\eta(t'); \lambda)$$

Finally we have

$$\rho(\alpha, z) = e^{-i\,\hat{K}(j,e)} \int d\Omega d\xi_0 d\eta_0\, e^{-\mathrm{N}(\alpha_i,z_i) - \mathrm{N}^*(\alpha_f,z_f)} e^{i\,\tilde{S}(u_c,e_c)}$$

$$\mathrm{N}(\alpha, z) = \kappa \int \frac{d^3p\, e^{i\,\alpha\, p} z(p)}{(2\pi)^3 2\epsilon(p)} \left| \int dx\, e^{-i\,p\,x}\, 2\, e_c \right|^2$$

Elastic scatering

The simple example: $2 \to 2$ scatering.

$$\rho_{2\to 2}(p_1, p_2; q_1, q_2) = \frac{2^4 \kappa^4 e^{i\,\alpha_i(p_1+p_2)} e^{i\,\alpha_f(q_1+q_2)}}{(2\pi)^{12}\epsilon(p_1)\epsilon(p_2)\epsilon(q_1)\epsilon(p_2)} \times$$

$$\times\, e^{-i\,\hat{K}(j,e)} \int dx_0\, d\xi_0\, d\lambda\, d\eta_0\, |\Gamma(p_1, e_c)|^2\, |\Gamma(p_2, e_c)|^2\, |\Gamma(q_1, e_c)|^2\, |\Gamma(q_2, e_c)|^2 \times$$

$$\times\, e^{-2i\,g \int dx\, u_c\, e_c^3}$$

where

$$\hat{K}(je) = \int dt\, \left(\hat{j}_\xi \hat{e}_\xi + \hat{j}_\eta \hat{e}_\eta\right)$$

$$\Gamma(p, e_c) = \int d^4x\, e^{-i\,p\,x}\, e_c, \qquad e_c = e_\eta \frac{\partial u_c}{\partial \xi_0} - e_\xi \frac{\partial u_c}{\partial \eta_0}$$

$$u_c = u_c(\mathbf{x}; \xi_0 + t + \int dt'\, \theta(t-t')\, j_\xi(t');\, \eta_0 + \int dt'\, \theta(t-t')\, j_\eta(t'); \lambda)$$

$$\sqrt{-g}\, u_c(\mathbf{x} - \mathbf{x_0}, \xi, \eta, \lambda) = \left\{ \frac{4\eta^2 \varrho^2}{(\eta^2(\xi^2 - \mathbf{x}^2) - \varrho^2)^2 + 4\eta^2\varrho^2(\xi\sqrt{1+\lambda^2} - \mathbf{x}_i\lambda^i)^2} \right\}^{1/2}$$

where $\varrho = \frac{\pi^2}{2}\sqrt{1+\lambda}$

$$u_c \sim \sqrt{\frac{1}{-g}} \quad \Rightarrow \quad \rho_{2\to 2} = \frac{C_1}{g^4} + \frac{C_2}{g^5} + \frac{C_3}{g^6} + \ldots$$

150р 00к.

Научное издание

Very High Multiplicity Physics

Proceedings of the Third International Workshop

Физика очень больших множественностей

Труды III международного совещания

E1,2-2003-29

Сборник отпечатан методом прямого репродуцирования
с оригиналов, предоставленных оргкомитетом.

Ответственный за подготовку сборника к печати *Н. И. Шубитидзе.*

Подписано в печать 05.03.2003.
Формат 60 × 84/8. Бумага офсетная. Печать офсетная.
Усл. печ. л. 30,4. Уч.-изд. л. 38,48. Тираж 150 экз. Заказ № 53777.

Издательский отдел Объединенного института ядерных исследований
141980, г. Дубна, Московская обл., ул. Жолио-Кюри, 6.